UCRL-52825

THE NUCLEAR STRUCTURE OF TELLURIUM 133 VIA BETA DECAY AND SHELL MODEL CALCULATIONS IN THE DOUBLY MAGIC TIN 132 REGION

Stephen Mark Lane
(Ph. D. Thesis)

August 1979

Work performed under the auspices of the U S Department of Energy by the UCLLL under contract number W-7405-ENG-48

LAWRENCE LIVERMORE LABORATORY
University of California Livermore California 94550

UCRL-52825

THE NUCLEAR STRUCTURE OF TELLURIUM 133 VIA BETA DECAY AND SHELL MODEL CALCULATIONS IN THE DOUBLY MAGIC TIN 132 REGION

Stephen Mark Lane
(Ph. D. Thesis)

MS. date: August 1979

THE NUCLEAR STRUCTURE OF TELLURIUM 133 VIA BETA DECAY AND SHELL MODEL CALCULATIONS IN THE DOUBLY MAGIC TIN 132 REGION

By

Stephen Mark Lane
A.B. (San Jose State University) 1971
M.S. (University of California, Davis) 1973

DISSERTATION

Submitted in partial satisfaction of the requirements for the degree of

DOCTOR OF PHILOSOPHY

in

Engineering-Applied Science

in the

GRADUATE DIVISION

of the

UNIVERSITY OF CALIFORNIA

DAVIS

Abstract

An experimental investigation of the level structure of $^{133}_{52}Te_{81}$ has been performed by spectroscopy of gamma-rays following the beta-decay of 2.7 min ^{133}Sb. Antimony isotopes were separated from gross fission products by antimony hydride production at the Lawrence Livermore Laboratory Fast Chemistry Facility. Multiscaled gamma-ray singles spectra and $2.5X10^7$ gamma-gamma coincidence events were used in the assignment of 105 of the approximately 400 observed gamma-rays to ^{133}Sb decay and in the construction of the ^{133}Te level scheme with 29 excited levels. One hundred twenty-two gamma-rays have been identified as originating in the decay of other isotopes of Sb or their daughter products. The remaining gamma-rays have been associated with the decay of impurity atoms or have as yet not been identified.

A new computer program based on the Lanczos tridiagonalization algorithm using an uncoupled m-scheme basis and vector manipulations has been written by R. F. Hausman and S. D. Bloom. It was used to calculate energy levels, parities, spins, model wavefunctions, neutron and proton separation energies, and some electromagnetic transition probabilities for the following nuclei in the $^{132}_{50}Sn_{82}$ region: ^{128}Sn, ^{129}Sn, ^{130}Sn, ^{131}Sn, ^{130}Sb, ^{131}Sb, ^{132}Sb, ^{133}Sb, ^{132}Te, ^{133}Te, ^{134}Te, ^{134}I, ^{135}I, ^{135}Xe, and ^{136}Xe. The results are compared with experiment and the agreement is generally good. For non-magic nuclei: the $1g_{7/2}$, $2d_{5/2}$, $2d_{3/2}$, $1h_{11/2}$, and $3s_{1/2}$ orbitals are

available to valence protons and the $2d_{5/2}$, $2d_{3/2}$, $1h_{11/2}$, and $3s_{1/2}$ orbitals are available to valence neutron holes. The present CDC7600 computer code can accommodate 59 single particle states and vectors comprised of 30,000 Slater determinants. The effective interaction used was that of Petrovich, McManus, and Madsen, a modification of the Kallio-Kolltveit realistic force. Single particle energies, effective charges and effective g-factors were determined from experimental data for nuclei in the ^{132}Sn region.

Contents

List of Tables

List of Figures

1. Introduction

There has been much interest lately in the structure of nuclei in the region around the nucleus ^{132}Sn as witnessed by the survey of recent experimental and theoretical publications shown in figure 1.1. This interest stems, ultimately, from the fact that, in the language of the nuclear shell model, ^{132}Sn is a doubly closed nucleus; all of the available neutron and proton orbitals are completely filled, the total ground state angular momentum is zero and the next available orbitals are 3 MeV above the last filled orbitals (see figure 1.2). Thus, physicists interested in making microscopic calculations for nuclei having additional nucleons or nucleon holes can treat ^{132}Sn as an inert core providing a spherical potential well in which these "excitons" can move.

There is, however, a difficulty. The number of nuclei whose structure can be determined by conventional shell model techniques is limited by the ability to account for a sufficient number of orbitals to reproduce the desired nuclear properties. The following example will make this clear. The $1g_{7/2}$, $2d_{3/2}$, $2d_{5/2}$, $3s_{1/2}$, and $1h_{11/2}$ subshells comprise the "gddsh" major shell and provide 32 distinct orbitals for excitons in the ^{132}Sn potential well. Thus, if one were to consider the nucleus with a single valence proton, ^{133}Sb, and limit the states accessible to that proton to the major shell mentioned above, one would have to account for 32 separate states. Now, if one considered the one valence proton, one valence neutron-hole nucleus, ^{132}Sb, $32^2 = 1024$ multiparticle states should be dealt with. Finally, to consider the two valence proton, two valence neutron-hole nucleus, ^{132}Te would require

Figure 1.1. Recent experimental (E) and theoretical (T) publications concerning nuclei in a region around doubly magic tin-132. References and publication dates are given.

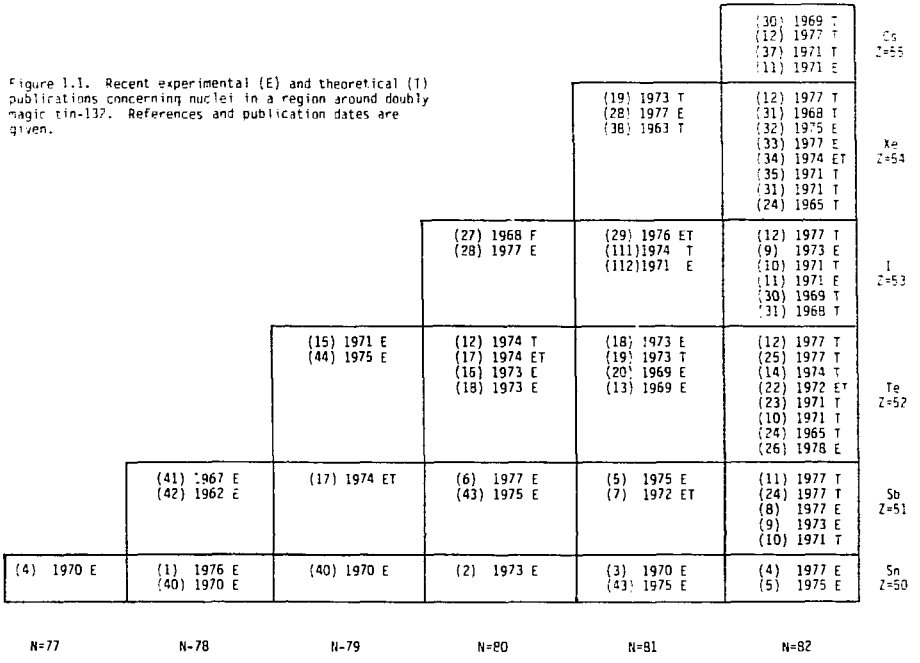

Figure 1.2. Nuclear shell model energy levels. Spectroscopic level notation is shown along with the maximum number of nucleons which can occupy each subshell. The magic numbers due to completely filled major shells are shown on the right.

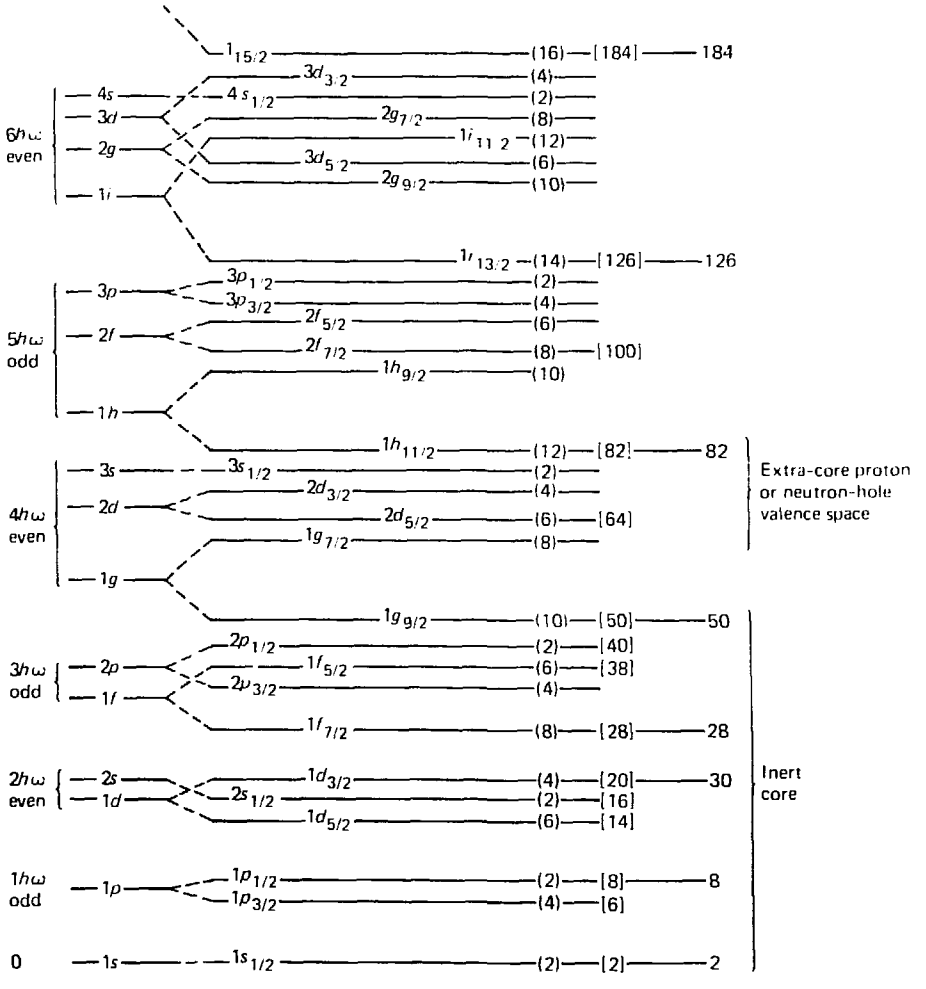

$\frac{32 \times 31}{2}^2$ = 246,016 states be allowed for. Although there are various schemes whereby the appropriate choice of representation partially diagonalizes the Hamiltonian matrix, it is obvious that as more excitons are considered, the number of multiparticle states rapidly overwhelms the available computing power.

Many ways have been discovered to avoid this problem and still describe the structure of spherical nuclei in this region. The most common way is the effective interaction scheme whereby the valence space is kept small but the principal effects that would be seen if a larger valence space were used are included by renormalizing the interaction between valence particles. In most cases, however, there is no simple way of telling a priori what the principal effects are. Another approach is to abandon microscopic models in favor of models that describe the nucleus with collective coordinates such as vibrations of the nuclear surface. Yet another approach results from a combination of collective and independent particle models where the motion of a few (one or two) valence nucleons are coupled to the correlated motion of the nuclear surface. Much success has also been achieved with a model that treats the nucleus as a superfluid system of nucleon pairs.

It is possible to circumvent these problems in still another way and retain the attendant advantages of a microscopic calculation. This can be accomplished by the application of a powerful numerical method of diagonalizing very large vector spaces. One such method, the Lanczos algorithm, tridiagonalizes in an iterative fashion large sparse matrices and does so in such a way that the lowest eigenvalues converge fastest.

Following the lead of Whitehead [45,46] and others [47,48], R. F. Hausman and S. D. Bloom at Lawrence Livermore Laboratory (LLL) have written a computer program for solving the nuclear shell model eigenvalue problem which makes use of the Lanczos method. By employing an m-scheme multiparticle basis description, this program dispenses with unwieldly coupling formalisms involving seniority and coefficients of fractional parentage and makes it possible to cast the algorithms in a vector form suitable for execution on parallel processing computers. Hausman refers to this technique as the "vector method"[49]. The program presently has the capacity to handle 30,000 multiparticle basis states and 59 single particle states. In a valence space consisting of the full gddsh shell, with the restriction that neutron-holes are excluded from the $1g_{7/2}$ subshell, detailed properties of nuclei having as many as five excitons may be calculated in this way.

This study presents results of calculations using the above described method applied to those nuclei shown in figure 1.3. The potential well in which the valence particles moved was approximated by a harmonic oscillator well and matched in size to the radius of ^{132}Sn. The interaction between valence nucleons was one due to Petrovich, McManus, and Madsen[50]. This force, which is a modified form of the realistic Kallio-Kolltveit interaction [51], has been used successfully for structure calculations in other regions of spherical nuclei.[100,101] The single particle energies were obtained from the ^{131}Sn one neutron-hole spectrum (the $1h_{11/2}$ energy was readjusted in a few cases). When it is kept in mind that these calculations were made without the freedom of adjustable

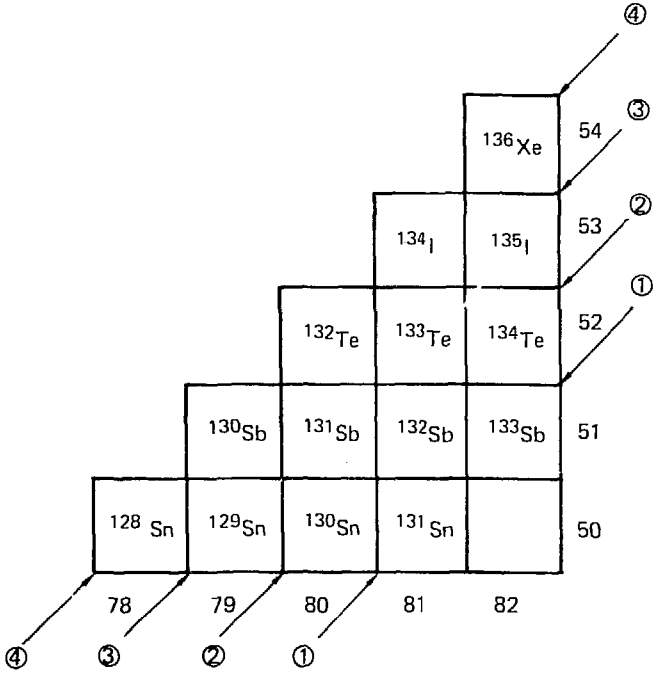

Figure 1.3. Nuclides in the tin 132 region whose properties were investigated in this study. The number of excitons involved are circled. The incomplete 5 exciton calculation, xenon-135, is not shown.

parameters, the agreement with experiment is shown to be suprisingly good.

Once realistic calculations are feasible it is desirable to have as much experimental data as possible to use for verification. Unfortunately, acquisition of spectroscopic information in the ^{132}Sn region is particularly difficult. The only practical way of producing these nuclides is by the fission reaction, but, even though the nuclide yields are high (see figure 1.4), the species of interest have short half-lives and must be rapidly separated from the other interfering fission products.

The separations can be performed in either of two ways: by fast chemistry or by an online isotope separator (ISOL). ISOLs produce a source of isobars while chemical separations give a source consisting of isotopes of a single element. When a chain of isobars is produced in fission, the subsequent decay produces daughters that are also members of that chain. On the other hand, when a sample of isotopes produced in fission is isolated, the decay produces species not present in the original sample. This is an obvious advantage of ISOL separations; the number of contaminating nuclides in the separated sample remains small. Furthermore, for each element studied, a new procedure must be developed when chemical separations are employed, whereas a simple adjustment on an ISOL is usually all that is needed to produce a sample of different isobars. Unfortunately, ISOLs are rare devices; only the LOHENGRIN, ISOLDE, JOSEF, and OSIRIS machines in Europe are currently in use. (The author's first years of graduate study at LLL involved the development, with Drs. P. C. Stevenson and J. T. Larsen, of an ISOL of unique design having several potential

advantages over existing machines[52,53]. After promising initial results, there was insufficient funding to produce a completely workable prototype.)

Lacking an ISOL, the separations required for this study were done chemically at the LLL Fast Chemistry Facility. Specifically, this study involved the determination of the 2.7 min ^{133}Sb decay scheme from gamma-rays observed in the decay of a separated sample of antimony fission products. The decay schemes for 2.8 min ^{132}Sb^{g} and 4.2 min ^{132}Sb^{m} were also determined (with E. A. Henry) but will be discussed elsewhere[54].

In designing a separation procedure for short lived antimony isotopes there are several general requirements that are common to separations involving nuclides with half-lives in the 1s-10min range. 1)The procedure must produce good yields (>1-10%). This is not a critical requirement for ^{133}Sb since its independent thermal neutron fission yield is quite high; however, it is important for other nuclides whose fission yields are much lower. 2)To prevent the washing out of weak gamma-rays of interest by gamma-rays from interfering species, the decontamination factor should be >100. 3)Concern must be given to reaction rates; the chemical reactions used in the separation must proceed to near completion in time scales comparable to the separation time. 4)The separation should be automatable. The following example will indicate why this is so. Spectroscopic data from the ^{133}Sb experiment were collected only during a 3 min period starting 50 s after the antimony sample was separated from the other fission products. This allowed time for 11.0s ^{134}Sb and 1.7s ^{135}Sb to decay substantially but not enough

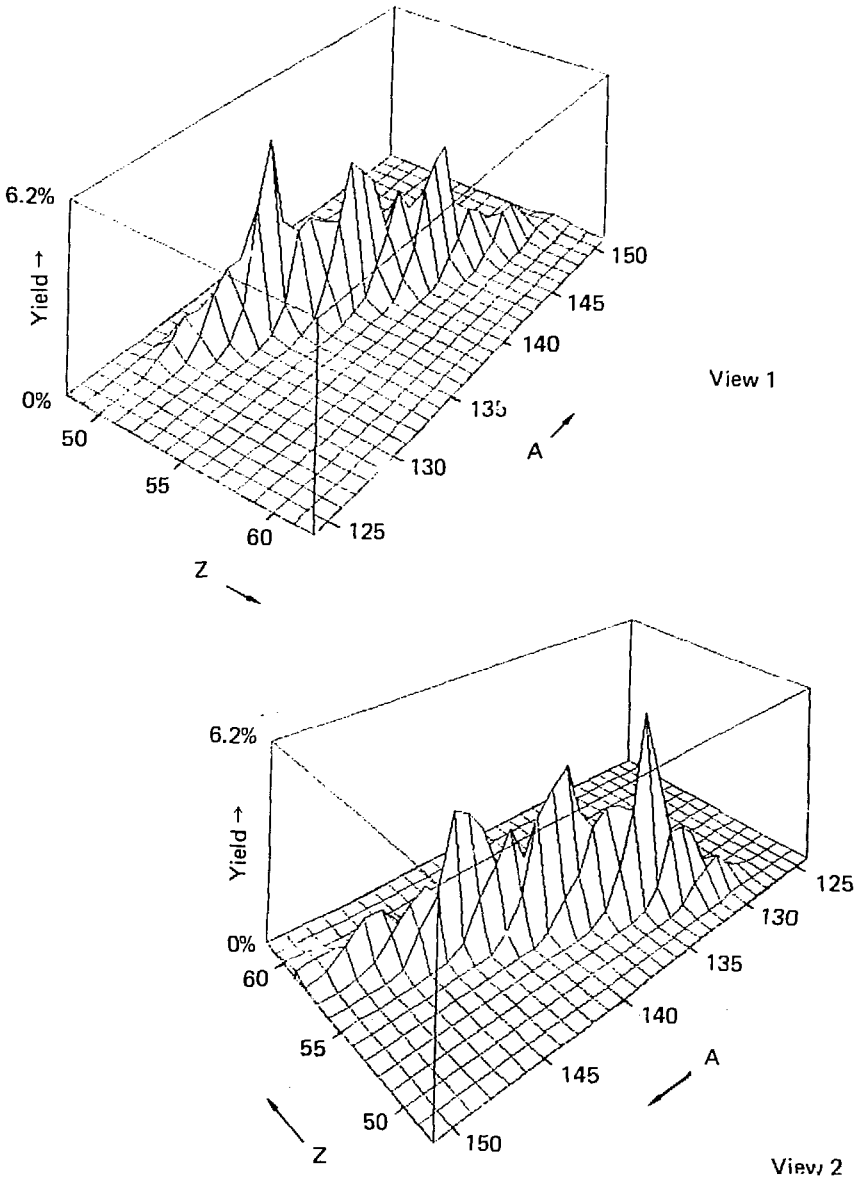

Figure 1.4. Independent yields of fission products in the tin-132 region from the thermal neutron fission of uranium-235.

time for the longer 23 min ^{131}Sb, 6.3 min $^{130}Sb^{m}$, 40 min $^{130}Sb^{g}$ or 12.5 min ^{133}Te to become serious contaminants. Because the maximum count rate of the coincidence spectrometer was 200 events/s and a total of $2.5X10^{7}$ events were required by statistical considerations, more than 700 samples needed to be processed.

Once a separation was found that satisfied the above requirements there still remained the problem of interference from gamma-rays emitted by other isotopes of antimony and from antimony daughters. For 2.7 min ^{133}Sb, the principal interference came from 2.8 min $^{132}Sb^{g}$ and 4.2 min $^{132}Sb^{m}$ and to a lesser extent from 23 min ^{134}Sb, 6.3 min $^{130}Sb^{g}$, and 12.5 min $^{133}Te^{m}$ Two spectroscopic techniques were used to identify gamma-rays with the proper nuclide: multiscaling and gamma-gamma coincidence spectroscopy. Multiscaling was used to assign half-lives to the stronger gamma-rays which should match the half-lives of the parent nuclides. Gamma-gamma coincidence spectroscopy determined the energies of gamma-rays that were emitted nearly coincident in time. Once two such gamma-rays were found it was assumed that they had been emitted from the same nuclear cascade. This information was useful in placing gamma-rays between the proper levels in a decay scheme. As an additional benefit, since the time interval between the coincidence events was recorded, the existence of isomeric states with lifetimes in the range 1-1000 ns could be discovered.

The material contained in this thesis was organized in the following way. Chapter 2 discusses the experimental techniques used: the fast chemistry procedure, an analysis of the interfering species present in a source produced by this method, a description of the

gamma-ray spectrometers, and the methods of data reduction. Chapter 3 gives examples of the gamma-ray spectra taken, a compilation of the gamma-ray energies and intensities measured, assignments to specific nuclides of these gamma-rays, and the details of the ^{133}Sb decay scheme. In chapter 4 the methods used to make large scale shell model calculations are covered. Also discussed are the PMM two-body force and its relationship to a few other effective interactions as well as the determination of single particle energies for the gddsh shell. The results of shell model calculations in the ^{132}Sn region (including energy levels, spins, parities, model wavefunctions, neutron and proton separation energies for those nuclides shown in figure 1.3) are presented in chapter 5. The calculation of electromagnetic transition probabilities is discussed in chapter 6. Results of these calculations are compared to experiment and to the results of calculations done by others. Chapter 7 contains some concluding remarks and recommendations for further work. The appendix gives the details of the interfering activity calculation.

Chapter 2

2. Experimental Apparatus and Techniques

2.1 Fast Chemistry

2.2 Interfering Species

2.3 Gamma-ray Spectroscopy

2.4 Data Analysis

2. Experimental Apparatus and Techniques

The nuclear level structure of ^{133}Te was determined by measuring gamma-ray spectra from the decay of excited ^{133}Te states populated by the beta-decay of 2.7 min ^{133}Sb. Antimony-133 is a high yield fission product of the thermal neutron fission of ^{235}U. A computer-controlled rapid chemical separation was used to isolate the antimony isotopes from the other fission products. The antimony samples were available for counting within 50 s and the separation was repeated every 3 min. A discussion of the chemical procedure and apparatus is given in section 2.1.

A model used to predict the activity of antimony isotopes and antimony daughters present in the sample at counting time is presented in section 2.2. The model was also used to estimate the degree of separation of the ^{133}Sb activity from the activities of several possible contaminants.

Gamma-rays emitted from excited states of other tellurium isotopes, from tellurium daughters, and from a few other contaminant nuclei present in the separated sample, served to make the spectra extremely complex. It was found that only 23% of the observed transitions belonged to the ^{133}Sb beta-decay. Identification of gamma-rays associated with the ^{133}Sb decay, therefore, required the collection of several different types of spectra. In addition to the simple single parameter spectra, several spectra were taken at consecutive time intervals (multiscaled spectra) so that the growth and decay of various gamma-rays could be observed. Other workers have also collected similar data [18,20] but that information has proven

to be insufficient to make unambiguous identifications, partially because the half-lives of some of the interfering species are very close to that of ^{133}Sb. These workers have also performed gamma-gamma coincidence experiments but with poor resolution and insufficent statistics. Thus, the central part of this experiment became the collection of 25 million gamma-gamma coincidence events with large-volume high-resolution Ge(Li) detectors to overcome the inadaquacies of prior work.

Three singles gamma-ray spectrometers, one of which operated in a multiscale mode, and a gamma-gamma three-parameter coincidence spectrometer (the two gamma-ray energies and the time between their detection being the three parameters) were used to accumulate the data for this experiment. Although some of the features of the single parameter spectrometers will be mentioned, section 2.3 deals mainly with the three-parameter system.

Several computer programs were used to reduce the large amount of data. In particular, GAMANAL[56] was useful since it automated the analysis of the single parameter and the multiscaled spectra and could be used to unfold the large number of gamma-ray multiplets present. The three-parameter coincidence data were analyzed by 3PSORT[57], a Nova 1200 minicomputer program. These two programs are discussed in section 2.4.

2.1 Fast Chemistry

Although several radiochemical procedures for the separation of antimony from a solution of mixed fission products are known [58], the first rapid separation (<1 min) was developed by Greendale and Love [59]. They produced hydride gases (SbH_3, H_2Te, H_2Se, AsH_3, GeH_4, and SnH_4) by reduction with zinc metal in hydrochloric acid and then thermally decomposed the SbH_3 at a temperature of 600°C. Since this method was not one that could be automated easily, several major modifications were made by J. Landrum at LLL[60]. These changes included the generation of the hydride gases with sodium borohydride solution[61] instead of zinc granules because a liquid is much easier to handle via a system of remotely-controlled valves. The hydrides were decomposed in a bromine solution which was passed through an ion exchange column under conditions that were very specific for the adsorption of antimony.

Further streamlining and simplification of this procedure, following H. Folger, J. V. Kratz, H. Franz and G. Herrmann[62,63,64], were made at LLL by O. G. Lien, P. C. Stevenson, and H. G. Hicks. They removed the SnH_4, GeH_4, and some of the H_2Te by passing the hydride gases through a $CaSO_4$ drying tube. The H_2Se and the remaining H_2Te were trapped in a NaOH solution. A filter made of glass wool soaked in a saturated solution of KOH in methanol provided the final step in the separation by absorbing the SbH_3 but allowing the only remaining hydride, AsH_3, to pass through. Although the Landrum separation was used in some of the experiments, the focus of this section will be on the newer separation since it was used to

acquire the bulk of the data.

A schematic diagram of the automated chemistry apparatus, whose construction was due mainly to O. G. Lien, is given in figure 2.1. This system consisted of three reagent reservoirs, 8 computer controlled pneumatic valves, 2 one-way check valves, an extraction needle, a 50ml reaction vessel, a 40 X 1.5cm $CaSO_4$ drying tube, a NaOH trap, and a glass wool filter. Sources of compressed nitrogen and of vacuum were provided along with a removable waste container. All component parts were connected with 1/4 inch I.D. polyethylene tubing except the lines connected to the extraction needle which were 1/16 inch I.D. PVC tubing.

The fissile samples were 1 mg of uranium, enriched to 93.5% in ^{235}U, dissolved in .75 ml of .01 M H_2SO_4, and doubly encapsulated in heat sealed polyethylene vials. The vials were placed in polyethylene containers (rabbits) which could be pneumatically propelled through a 3.13 cm ID flexible polyethylene tube. Each sample was irradiated by sending a rabbit into the core of the Livermore Pool Type Reactor (LPTR) where it was exposed to a thermal neutron flux of 1.9×10^{13} n/cm^2sec [65] for 0.5 to 3.0 seconds. After irradiation, the rabbit was pneumatically transported to the chemistry station, a fume hood in a chemistry lab about 60 meters away, in 2.2 seconds.

Upon receipt of a rabbit at the chemistry station the automatic control sequence was initiated by an MCS-8 microcomputer having an internal clock. This sequence is summarized in table 2.1. The MCS-8 was programmed to open or close any of the 8 valves shown in figure 2.1 and could, via pressure actuated rams, pierce the rabbit with the extraction needle, withdraw the needle, and discard the rabbit. The controlling

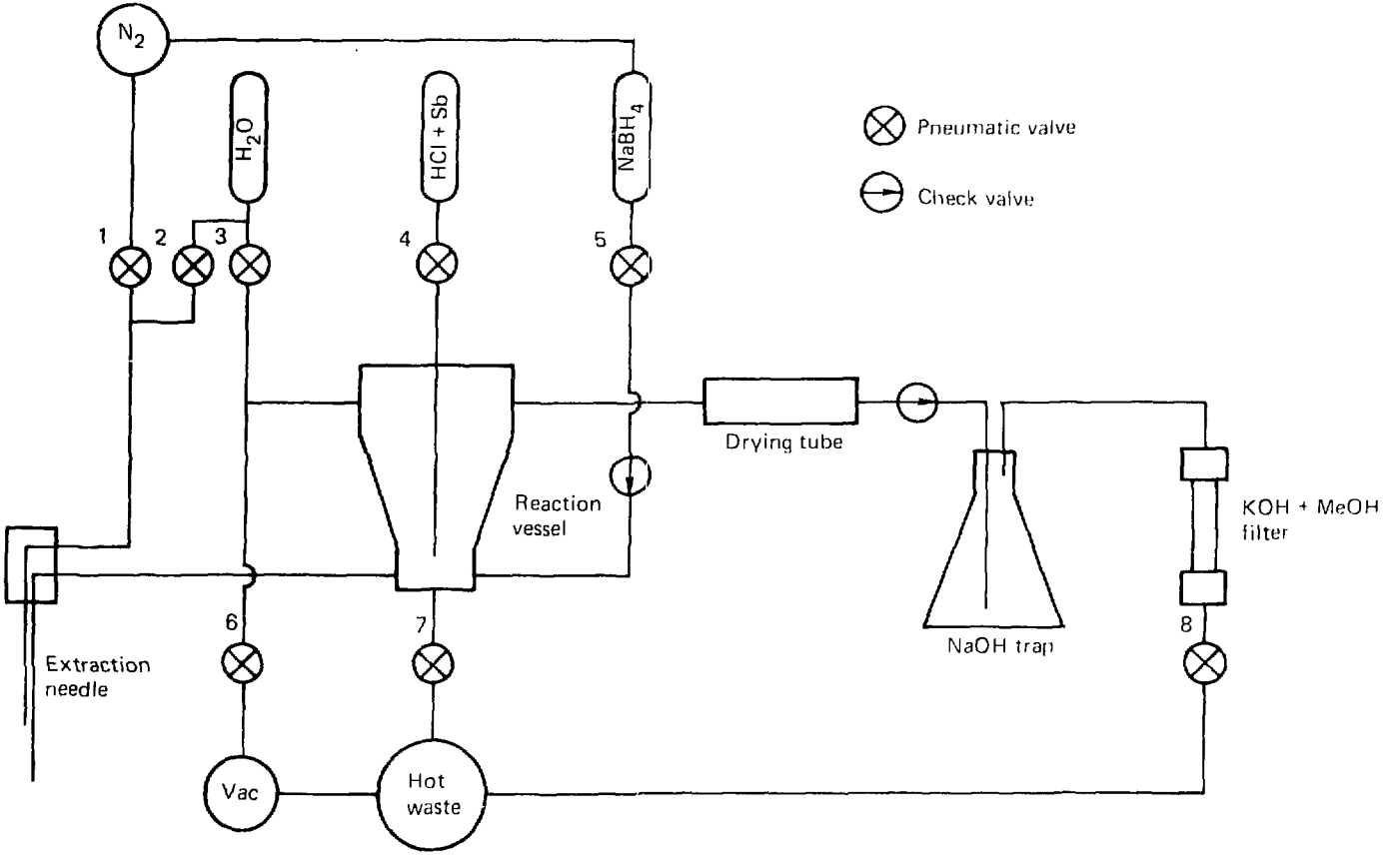

Figure 2.1. Schematic diagram of the fast chemistry apparatus.

program was loaded from a teletype, so it was a simple matter to change parameters such as the length of time a certain valve was to remain open.

The first step of the separation cycle was the removal of the mixed fission product solution from the rabbit by the insertion of the extraction needle and transfer to the reaction vessel. Ten milliliters of 6 M HCl containing 1.5 mg antimony carrier were then injected into the reaction vessel. The next step allowed noble gas fission products to be pumped away through the vacuum line attached to the top of the reaction vessel. This step was followed by hydride gas generation from the injection of 10ml of a solution containing .08 g/ml $NaBH_4$ and .1 ml concentrated NaOH. The chemical yields of Sb and Sn were found by Landrum to be 60% - 70%. The probable reactions that convert antimony in either the +5 or the +3 oxidation state to stibine gas are

$$3H_2O + Sb^{+5} + BH_4^- \rightarrow SbH_3 + H_3BO_3 + 4H^+$$

or

$$3H_2O + Sb^{+3} + BH_4^- \rightarrow SbH_3 + H_2 + H_3BO_3 + 2H^+$$

respectively. These hydride gases were drawn through the $CaSO_4$ drying tube to absorb the spray from the reaction vessel, the SnH_4, and some of the H_2Te. The gases then passed through a trap containing .5 N NaOH which removed the H_2Te and H_2Se. The remaining hydrides, SbH_3 and AsH_3, were passed through a 5 cm length of 1/4 in I.D. polyethylene tubing containing a small plug of glass wool which had been soaked in a saturated solution of KOH in methanol. While the Sb adhered to the glass wool, the AsH_3 passed through and was pumped away. After a 45 sec wait to allow short

Table 2.1. Computer Control Sequence for the Antimony Separation

Step	Operation	Valves Opened[a)]	Elapsed Time (s)
1	Extract sample from rabbit and transfer to reaction vessel.	1,6	0.0
2	Transfer HCl+Sb to reaction vessel.	1,4,6	0.3
3	Purge rare gas fission products.	1,6	1.9
4	Inject $NaBH_4$ into reaction vessel.	1,5,6	2.2
5	Draw hydrides through drying tube, NaOH trap, and KOH + MeOH filter. (Sample is now available for counting.)	8	2.7
6	Flush system with N_2.	1,8	5.1
7	Wash needle with H_2O.	2,7	8.3
8	Purge needle with N_2.	1,7	9.9
9	Wash reaction vessel and flush with H_2O.	1,3	12.3
10	Drain reaction vessel and flush with Sb + HCl.	4,7	13.1
11	Drain reaction vessel.	7	14.7
12	Ready for next sample.		15.2

a) Solution volumes were controlled by the amount of time a valve stayed open. All valves used in each step were closed before proceeding to the next step.

lived species time to decay, the short length of tubing was removed by hand and placed before the gamma-ray detectors.

The remainder of the computer-controlled cycle purged the system with N_2, washed the needle and reaction vessel with water and finally rinsed the reaction vessel with the HCl and Sb carrier solution. The sample was separated in 5 seconds after its arrival at the chemistry station and the total cycle time was 15 seconds. Sample strength was adjusted by varying the irradiation time to optimize the coincidence count rate at 200 counts/sec. During the course of this experiment, samples were continually processed in this manner at a rate of 1 every 3 minutes for ten eighteen hour days. About one fourth of the time was needed to maintain the mechanical system.

2.2 Interfering Species

The interfering species present in the separated sample can be placed in two categories: (1) daughters of ^{133}Sb ($^{133}Te^{m,g}$, $^{133}I^{m,g}$), other antimony isotopes ($^{128}Sb^{m}$, ^{129}Sb, $^{130}Sb^{mg}$, ^{131}Sb, $^{132}Sb^{m,g}$, ^{134}Sb), and their daughters ($^{131}Te^{g}$, ^{134}Te, $^{134}I^{m,g}$, $^{134}Xe^{m}$); and (2) all other contaminants. If a perfect separation was achieved all of the interfering species in the first category would still be present while those in the second category would not.

A model can be formulated, using the information given in a compilation by Meek and Rider[55], which predicts the number of disintegrations of the species in category one relative to the number of ^{133}Sb disintegrations in a 3 minute counting interval. The model assumes that at 5 sec after fission a perfect separation of antimony isotopes occurred and at 50 sec the counting was started. This model can obviously be of aid in identifying unknown gamma-rays by indicating those species most likely to be present. The effectiveness of the separation can be estimated by predicting the activities of contaminants, assuming no separation was performed, and comparing with observed contaminant activities. The details of the model, including input parameters, are given in the appendix.

Identification of interfering species came from the gamma-gamma coincidence data. The arbitrary criterion for establishing the presence of a contaminant was that at least one previous known coincidence be found. Contaminating species are listed in table 2.2 along with the coincidence evidence. The amounts of the contaminants were derived from singles spectra photopeak intensities and are given in table 2.2 with references to the decay schemes from which the

Table 2.2 Contaminants Present in Counting Sample

Contaminant Nuclide	Coincidence Evidence	E (I)[a (keV)	Reference	Observed[b Activity	Calculated Activity[c No Sep	Sep
^{89}Rb	1032/1248/998 1032/1538,2196	1031.88(64)	66	.6	24	0
$^{90}Rb^{m+g}$	832/824,1061,1375,2753	831.69(100)	67	.8	240	0
$^{130}Sn^{g}$	192/435,550,780 229/550,743	779.8(59)	68	4	37	0
$^{130}Sn^{m}$	145/544,899		68	Trace	--	--
$^{130}Sb^{g}$	839/793/182,468	732.0(22)	68	2	4.3	1.3
$^{130}Sb^{m}$	839/793/349,697,816	1017.5(30)	68	7	16	8.2
^{131}Sn	1226/450	1226.2(100)	69	1	40	0
^{131}Sb	933/943/642	933.1	6	20	1[illegible]	14
^{132}Sn	340/652,899 992/248	898.5(42)	70	2	21	0
$^{132}Sb^{g}$	974/697,1134,1516	635.6(9.9)	70, 71		72	59
$^{132}Sb^{m}$	974/697/103/150		70, 71		36	28
$^{133}Te^{g}$	312/408,1000,1021	407.9(31)	72	1	26	8.6

$^{133}Te^{m}$	913/647,864	912.58(100)	72	1	11	1.5
$^{134}Sb^{g}$	1279/297/115/706		71	Trace	.89	.89
^{134}Te	277/435,566		73	Trace	29	.83
$^{138}Cs^{g}$	1436/463,1009	1435.86(100)	74	2	4.9	0
^{140}Cs	602/528,908,1200	602(100)	75	.9	300	0

a) Tabulated energy and intensity of photopeak used to determine observed number of disintegrations.

b) Percentage of contaminant disintegrations relative to the number of Sb-133 disintegrations observed in the 3 min counting period. Sb-133 disintegrations were inferred from the 1096 keV photopeak.

c) Calculated percentage of contaminant disintegrations relative to Sb-133 disintegrations, assuming no chemical separation and assuming a perfect Sb separation 5 s after fission. Details of calculations are given in the appendix.

coincidence relationships and absolute photopeak intensities were obtained. Amounts are given as the percent disintegrations in the 3 min counting interval relative to the number of Sb^{133} disintegrations observed in that same period. The number of Sb^{133} disintegrations was derived by multiplying the efficiency-corrected 1096 keV photopeak area by 2.5 (see chapter 3). In columns 6 and 7 the model predictions are given, first assuming no separation, then assuming a perfect separation. Model results for category one species are shown in figure 2.2.

Most category-two fission products have decontamination factors of 100 or better and hence are not observed. Notable exceptions are Sn and the noble gas daughters, Rb and Cs. Tin is present because it forms a hydride gas that is not as efficiently removed as the other hydrides. Rubidium and cesium are seen because the noble gases, Xe and Kr, were not completely pumped away and flowed freely through the system until their decay. Category-one species are shown to be present in about
the amounts predicted and are dominated by ^{130}Sb, ^{131}Sb, $^{132}Sb^{mg}$, and $^{133}Te^{mg}$.

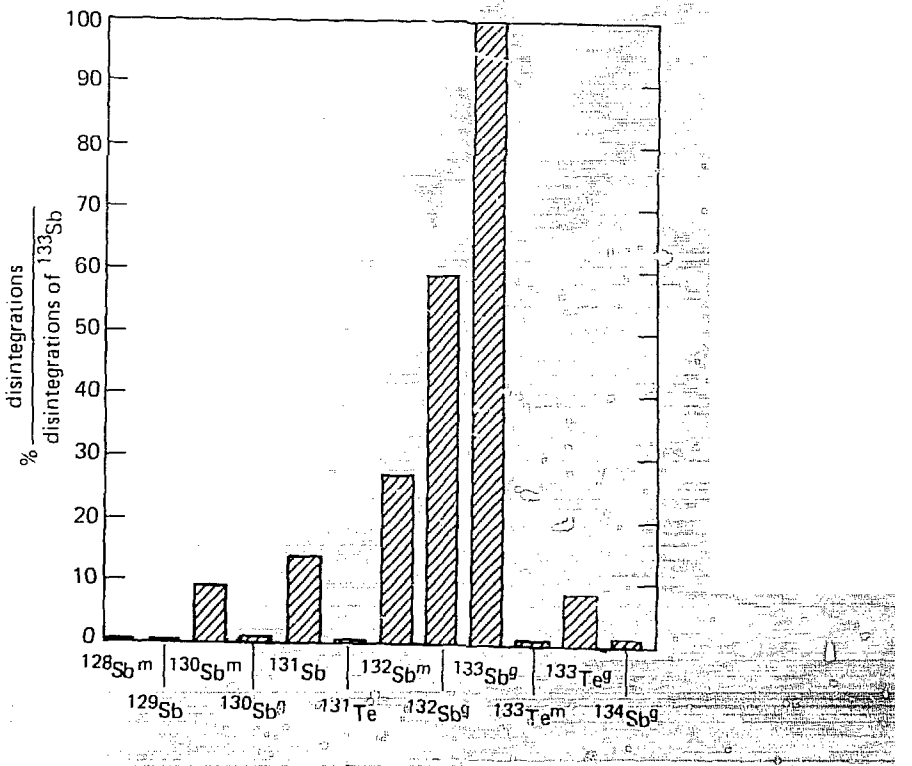

Figure 2.2. Integrated activities of species predicted to be found in a pure antimony sample separated 5 s after fission and counted for a 3 min period beginning 50 s after fission.

2.3 Gamma-ray Spectroscopy

All of the gamma-ray spectra reported in this work were obtained with high-resolution, high-efficiency Ge(Li) detectors. Three types of gamma-ray spectra were taken: single-parameter, multiscaled single-parameter, and three-parameter. The single-parameter spectra are counts versus energy collected by a multichannel analyzer. Much care was taken to calibrate the gamma-ray spectrometers to obtain very accurate energies and intensities. The multiscaled single-parameter data are a collection of singles spectra taken during consecutive time intervals. For example, one set of multiscaled spectra were taken beginning at times 1.67, 2.83, 4.00, 5.47, 6.33, 7.50, 8.67, and 9.83 minutes after the sample became available for counting. The growth and decay of all but the weakest gamma-rays were followed by comparing their intensities at each time interval. A half-life could then be assigned to each gamma-ray to help identify the emitting nucleus.

The three-parameter spectra, also called gamma-gamma coincidence spectra, were obtained using two detectors. To record an event, a gamma-ray observed by one of the detectors must be followed by another gamma-ray observed in the other detector within 200 nsec. The gamma-ray energies from each detector were digitized by 8192 channel analog-to-digital converters (ADCs) and the time interval between receipt of the two signals was digitized by a 512 channel ADC. For each coincidence event a triplet of channel values was stored in a minicomputer data buffer. Once the buffer was filled the information was written onto magnetic recording tape. At the end of the experiment the data were analyzed for events of interest by playing back the magnetic tape.

Since the lifetimes of excited states subject to electromagnetic decay are, with the exception of isomeric states, in the sub-nanosecond region, gamma-rays belonging to the same cascade are emitted essentially simultaneously. Because of the finite charge collection times in the detectors and statistical fluctuations in the electronics, gamma-rays emitted simultaneously may appear separated in time by several nanoseconds. The time spectrum for this experiment, for example, contained a gaussian peak whose full width at 1/10 maximum was 19 ns, on an almost flat background. Thus, those pairs of events detected within a 23 ns window about the peak, excepting random chance coincidences, were considered to have been emitted by the same nuclear cascade.

Random chance coincidences occur when a pair of events that are not emitted from the same nuclear cascade arrive at the detectors at nearly the same time and are taken to be valid coincidences. Unlike the case for true coincidences, the distribution of time intervals between chance events is not peaked, but rather contributes a flat background to the time spectrum. Therefore, one can set two windows in the time spectrum, the first containing the true coincidence peak and the second, of the same width, in the flat chance coincidence region to one side of the peak. It is assumed that the number of chance coincidences in both windows is the same, so the coincidences seen in the chance window can be subtracted from the coincidences in the true-plus-chance window resulting in only true coincidences being taken into account.

The energy signal from one of the detectors starts the time-to-amplitude (TAC) converter while the signal from the other

detector is delayed 200 ns and stops the TAC. If a pair of gamma-rays are in "prompt" coincidence, they will appear separated in time by 200 ns in the time spectrum. Suppose, however, that a certain level has a lifetime greater than 1nsec. Then gamma-rays cascading into that level are in "delayed" coincidence with those cascading out of it. If a gamma-ray that populates the delayed state is detected in the start detector and a gamma-ray depopulating that state is detected in the stop detector, the event will appear at a later time relative to the prompt peak in the timing spectrum. On the other hand, if the depopulating gamma-ray is detected in the start dectector and the populating gamma-ray in the stop detector, the event will appear earlier in the time spectrum than the prompt peak. The lifetime of the delayed level can be measured (if it is in the range 1-1000 ns) from the slope of the locus of points produced by these delayed events.

The gamma-gamma coincidence data were accumulated using two ORTEC Ge(Li) solid state detectors. They were true coaxial right circular cylinders of active volumes greater than 50 cm^3. Photopeak widths obtained by observing the 1332 keV gamma-ray of ^{60}Co were approximately 2.1 keV FWHM for both detectors. The detectors were placed 1.5 cm apart on opposite sides of a lead sample holder as shown in figure 2.3. Two ports were cut in the holder to allow a direct line of sight from the source by the detectors. The lead sample holder placed between and the lead bricks placed around the two detectors minimized the occurrence of gamma-rays scattering out of one detector and depositing their remaining energy in the other detector. Thin (1/16-inch) sheets of copper and cadmium were placed between the

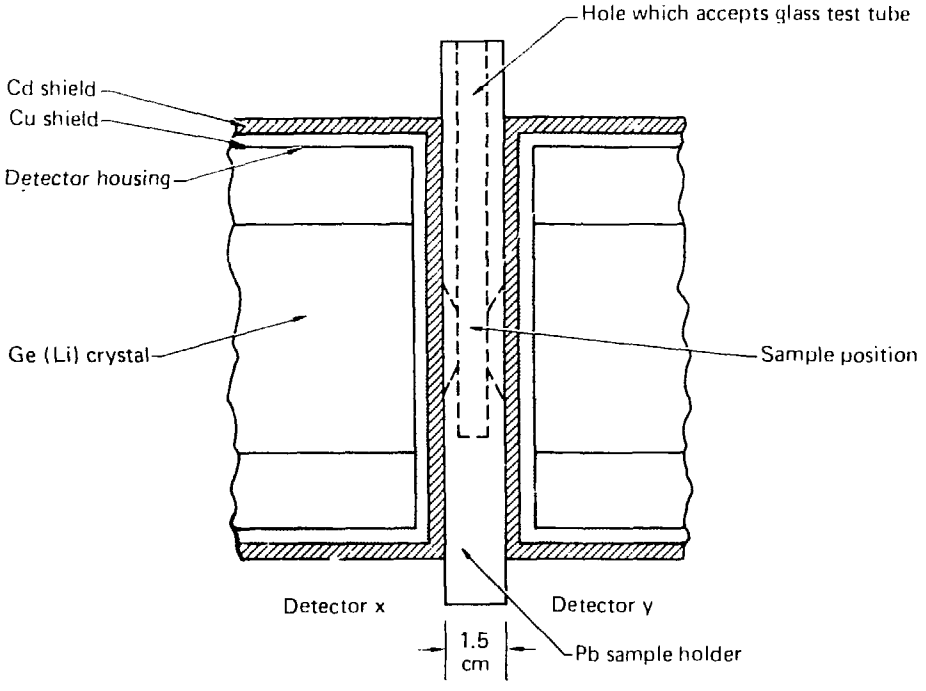

Figure 2.3. Coincidence counting geometry and sample holder.

detectors and the source to reduce the fluorescent Pb X-ray background.

Figure 2.4 is a block diagram of the coincidence system electronics. The pulses from the Ge(Li) crystals were first amplified by FET preamplifiers and the outputs split to give both energy and timing signals. The energy signals were further amplified by ORTEC 472 spectroscopy amplifiers and then fed to ORTEC 442 linear gate stretchers. The stretchers delayed the signals and shaped them to be accepted by the Northern NS623 8192 channel ADCs.

The timing signals from the preamplifiers were sent to timing filter amplifiers where the pulses were appropriately shaped and amplified to be analyzed by ORTEC 473 constant fraction discriminators (CFD). The pulses were amplified well past saturation to minimize timing walk due to different rise-times and achieve a timing resolution of 8 nsec FWHM.

The output of one CFD provides the start pulse for an ORTEC 437 time-to-amplitude converter while the other CFD output was delayed by 200 nsec to provide the stop pulse. The TAC pulses, whose amplitudes were proportional to the time interval between reception of the start and stop pulses, were sent to another Northern NS623 set to act as a 512 channel ADC.

The NS623 module used as the time ADC contained a single channel analyzer which produced a square pulse at the arrival of a signal from the TAC. This pulse was delayed and stretched by an ORTEC 416 gate and delay generator to provide a properly timed signal to the linear gates of the energy ADCs thus ensuring that only the two energy events corresponding to that TAC event were digitized by the ADC's. The triplet of events was then stored in a 2k data buffer of a Data

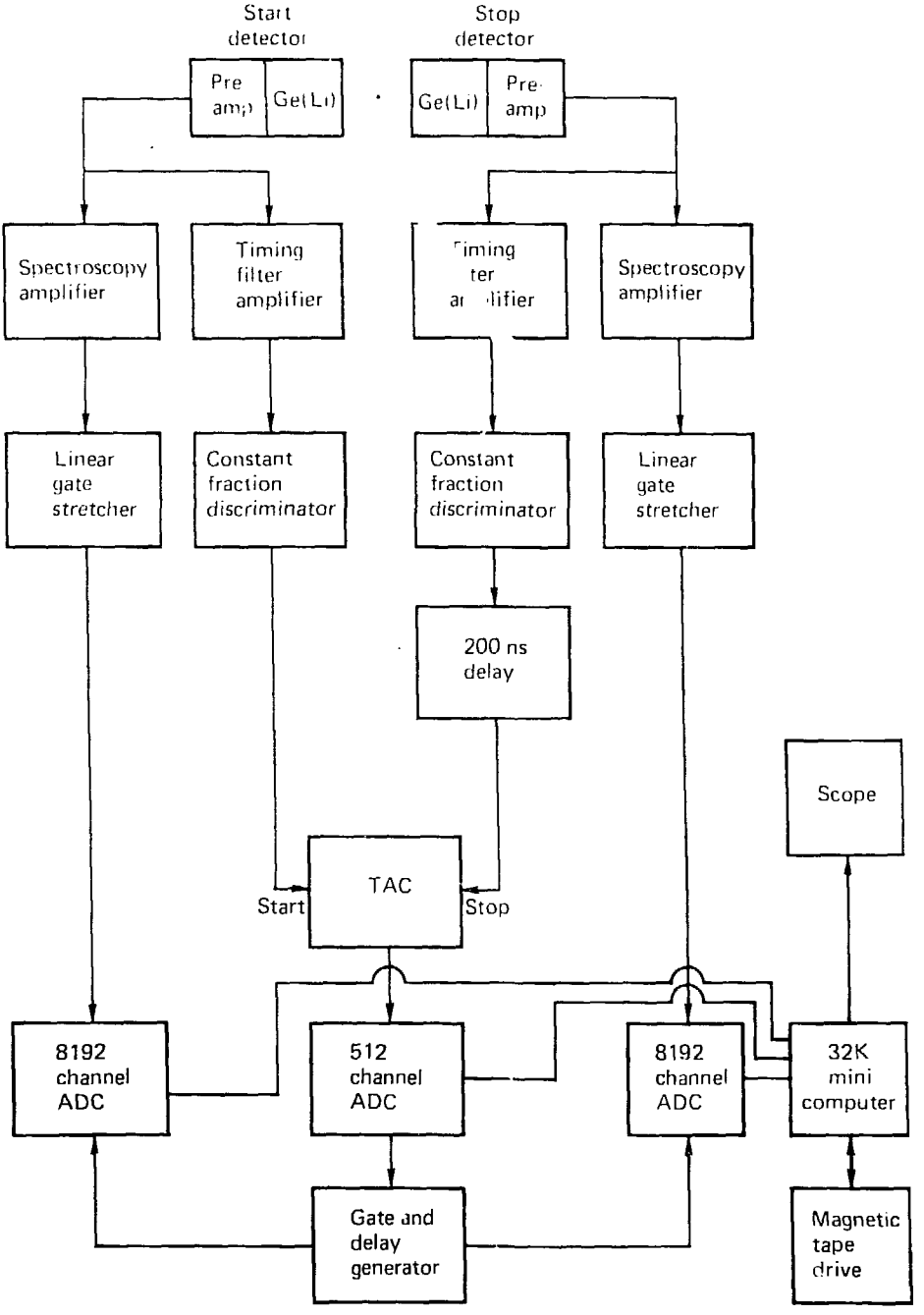

Figure 2.4. Block diagram of the three-parameter coincidence electronics system.

General Nova 1200 minicomputer until it was filled. Then the buffer contents were written to magnetic tape while the data continued to be accumulated in another buffer.

Two single-parameter multiscaled experiments were done prior to the present investigation. These experiments, performed by R.A. Meyer, J. Larsen, and J. Landrum of LLL,[76] were unpublished and of a preliminary nature. They were done in order to determine isomer branching characteristics for the A=133 isobaric chain.

The first of these experiments was done using the automated gamma counting facility at LLL[77]. This system has several Ge(Li) solid state detectors with associated ND 2200 multichannel analyzers and automatic sample changers all controlled by a DEC PDP-8/I computer having 32k of core memory, 3.2 million words of disk storage and two Ampex magnetic tape drives. The particular detector was a Canberra five sided coaxial type with a volume of 42 cm^3 and a resolution of 1.1 keV FWHM at 122 keV and 1.91 keV FWHM at 1332 keV. The energy nonlinearity and the detection efficiency of each detector was carefully checked to ensure that this system is very stable in order to obtain accurate energies and intensities. In some cases the uncertainties in the energies and intensities are as small as .005% and 5% respectively.

A major difficulty with the isomeric branching experiment was the distance between the counting facility and the chemical separation station, 1/4 km. Transporting samples by hand meant that, including separation time, they reached the counter 4 minutes or $\approx$1.5 half-lives of ^{133}Sb after irradiation. Therefore, some of the weaker lines could not be detected. Spectra were taken beginning at 1.67, 2.83,

4.00, 5.47, 6.33, 7.50, 8.67 and 9.83 minutes after the beginning of the first counting period.

The experiment was repeated in the chemistry laboratory where the separation occurred. Now the samples could be counted 45 seconds after irradiation. A 30 cm^3 Ge(Li) true coaxial detector was used that had a resolution of 2.2 keV FWHM at 1332 keV. The data were collected with an ND-160 multichannel analyzer system. Spectra were collected beginning at 75, 15, 155, 195, 235, 305, and 375 seconds after the end of the irradiation. There was a 10 second interval after each counting period during which the data were written on magnetic tape.

Finally, two single-parameter experiments were performed with a 50 cm^3 Ge(Li) true coaxial detector, resolution of 2.1 keV FWHM at 1332 keV. In the first experiment the data were acquired in the presence of a ^{56}Co source of comparable strength to the antimony sample. Since only the higher energy gamma-rays were of interest in this part of the experiment, a 1.6 cm thick lead absorber was placed between the detector and the source to attenuate the low energy components. The sources for this experiment were 3.67 min old Sb samples that had just finished a 3 min count in the coincidence spectrometer. The ^{56}Co lines were then used to calibrate the energy of some of the stronger Sb peaks which in turn were used for calibration in the other singles experiment where 60 sec old Sb samples were counted with no ^{56}Co external standard.

2.4 Data Analysis

This section describes briefly two of the computer codes that were employed in the gamma-ray spectral analysis.

A version of the program GAMANAL was used to analyze all of the single parameter gamma spectra. This code performs the following tasks:

(1) Compton continuum subtraction

(2) peak search

(3) peak fitting including resolution of complex multiplets

(4) exact energy determination

(5) relative intensity determination

The Compton continuum is obtained from the original spectrum by repeated smoothings. Wherever the original spectrum exceeds the smoothed spectrum by a specified number of standard deviations the original values are replaced by the smoothed values. The process is repeated but on each successive pass the allowable number of standard deviations is reduced. A point by point comparison of the channel values and the first and second derivatives of these values is now made between the original and the final smoothed version in order to find the peak regions.

Under these peak regions the background is adjusted so that it resembles a smoothed step function. Individual peak shapes are fitted with a Gaussian function to which has been added a low energy tailing term,

$$Y_i = Y_o e^{A(X_i-X_o)^2} + C\, Y_o e^{B(X_i-X_o)} \left(1 - e^{.4A(X_i-X_o)^2}\right)\delta$$

where

Y_i = net data counts

Y_o = peak height

$A = \frac{-1}{2\sigma^2}$ (FWHM = 2.355σ)

X_i = channel value of ith point

X_o = peak position

B and C are parameters used in describing the tailing component

$$\delta = \begin{cases} 1 & (X_i-X_o)<0 \\ 0 & (X_i-X_o)>0 \end{cases}$$

The parameters A and C are individually determined from a least squares fit of isolated standard peaks deemed characteristic and of good quality by the user. Values for these parameters are then fitted as a function of energy, E, by

$$-(2.773/A + .46)\ \text{Gain}^2 = k_1 + k_2 E$$

$$\ln C = k_3 + k_4 E$$

where the k_1, k_2, k_3, and k_4 are free parameters. The skewness parameter, B, is taken only from the highest energy standard peak. All of the peaks in the spectrum, including the standard peaks, are then fitted with this parameter set.

The code can accommodate up to twelve peaks in a multiplet by using an iterative least squares procedure. If the value of the residues at a certain point plus the sum of the residues of the two

neighboring points exceed 4 standard deviations, an additional peak is inserted and the iterative procedure repeated.

Exact photopeak energies are calculated from the peak location determined via the functional fit and from the user-provided gain, channel 1 energy, and energy non-linearity curve. Relative intensities are found by combining the calculated area of a fitted peak with an efficiency vs. energy curve.

The output is in an easy-to-read tabular form, listing, for each recognized peak, the peak channel number, energy, energy uncertainty, peak area, efficiency corrected peak intensity, % intensity error, and a parameter indicating the goodness of the fit.

The 3-parameter data took the form of 25 million channel value triplets; each coincidence event was recorded as a channel value from both energy ADCs and a channel value from the TAC ADC. These triplets can be viewed as the indices of a 4096 X 4096 X 512 array where the 8192 energy channels have been compressed by summing adjacent channels. The content of a given cell is just the number of events collected having the triplet of indices associated with that cell.

Various coincidence relationships are obtained by choosing window limits for two of the indices and searching the tapes to produce a spectrum of the number of events as a function of the third index. In this manner the gamma-rays in prompt coincidence with a particular gamma-ray can be found by setting a window about the prompt timing peak and about the gamma-ray peak of interest. Likewise, delayed coincidences can be investigated by setting the time window at shorter or longer times relative to the prompt peak as explained above. It is also possible to obtain the spectrum of time intervals between the

detection of two particular gamma-rays by setting energy channel window limits to include only those two gamma-rays.

When a window is set about a gamma-ray peak, there are not only photoelectric events in that window, but also Compton scattering events from other gamma-rays. These scattered events can be taken into account by introducing two additional windows, one on each side of the peak energy window, whose cumulative size is the same as the peak window. We then assume that the Compton background underneath the photopeak is the same as the average background on either side of the peak. Whereas events that are found to fall in the peak window are added to the resultant spectrum, events that fall in the background windows are subtracted. In principle, the net counts in the finished spectrum are due only to full energy events.

Random chance events are handled in a similar fashion; a background time window in the flat region adjacent to the gaussian peak in the time spectrum compensates for the chance events in the peak window.

A NOVA 1200 minicomputer having 32k of core memory, two 1.2 megaword disk packs and a 9-track magnetic tape drive was used for the 3-parameter data reduction. The NOVA program used, called 3PSORT, was written by J. Carlson at LLL. For each of the 478 gamma-rays observed, a coincidence spectrum was generated by searching through 14 magnetic tapes containing 25 million triplets (a feat which took one month of continuous running).

Once these spectra were created they were transferred via magnetic tape to the Livermore Time Sharing System (LTSS)[78] where they were individually photographed on microfiche for ease in viewing

and handling. Because the peak shapes were of a non-standard form (this is in part due to the windows not containing entire peaks), peak fitting programs such as the one in GAMANAL were of no use and these spectra had to be scanned by eye.

Chapter 3

3. The Decay Scheme of ^{133}Sb

3.1 Gamma-ray Singles Spectroscopy

3.2 Gamma-gamma Coincidence Spectroscopy

3.3 Spin and Parity Assignments

3. The Decay Scheme of Antimony-133

Antimony-133 was first investigated by Abelson[79] in 1939. He measured the half-lives of what were later identified as ^{133}I, ^{133}Te, and ^{133}Sb to be 22 h, 60 min, and 10 min respectively. G. B. Cook[80] in 1951 made the first unambiguous identification of ^{133}Sb, a result confirmed later by A. C. Pappas.[81] Strom et al.[82] remeasured the half-life of ^{133}Sb to be 2.67 $\pm$ .33 min and determined the cumulative yield in thermal neutron fission of ^{235}U to be 3.05 $\pm$ .39%. Using gamma-ray singles spectra, Ge(Li) - NaI(T) gamma-gamma coincidence spectra, and beta-gamma coincidence spectra, Treytl[20] assigned gamma-rays of energies 700 keV, 818 keV, 979 keV, 1097 keV, and 2776 keV to ^{133}Sb and placed them in a proposed decay scheme. Blachot and Carraz[21] assigned gamma-rays of energies 104 keV, 382 keV, 698 keV, 815 keV, 975 keV, 990 keV, and 1098 keV to the decay of ^{133}Sb or ^{132}Sb. Erten and Blachot[18] measured the half-lives of the 1096.4 keV, 1728.2 keV, and 2751.7 keV gamma-rays to be 2.3 $\pm$ .2 min and associated them with the ^{133}Sb decay. With Ge(Li) - Ge(Li) gamma-gamma coincidence studies, they also assigned to the ^{133}Sb decay gamma-rays of energies 423.5 keV, 631.8 keV, 816.5 keV, 935.5 keV, 1025.0 keV, 1305.0 keV, 1490.0 $\pm$ 1.0 keV, and 1655.2 $\pm$ 1.0 keV and presented a partial decay scheme containing 12 gamma-rays. In addition, they found 60 gamma-rays in the decay of antimony fission products that they could not assign to a particular nucleus.

A 334.14 keV gamma-ray was identified by Alvager and Oelsner[83] as an M4 isomeric transition in ^{133}Te on the basis of K/L conversion electron ratios and systematics of M4 transitions in

other nearby nuclei. They proposed an isomeric state, $^{133}Te^{m}$, at 334.14 keV with a spin and parity of $11/2^{-}$. The half-lives of this isomeric state and of the ^{133}Te ground state have been measured to be 55.4 ± 4 min[84] and 12.45 ± .28 min[27,85,86], respectively. Meyer[87] has found that 82% of the ^{133}Sb decays populate the ^{133}Te ground state while the remaining 18% populate the isomeric state and the isomeric state then decays 83% by beta-decay. He also determined the energy of the isomeric level to be 334.19 keV.

Rudstam et al.[88] have measured the Q-beta value to be 3950 ± 200 keV based on the beta-gamma coincidence with the gated 2750 keV gamma-ray assumed to be a ground-state transition following the decay of ^{133}Sb.

Only the 334.19 keV isomeric level has been adopted by Nuclear Data Sheets[72] because of experimental difficulties due partly to ^{133}Sb and ^{132}Sb both having half-lives near 2.7 min[17] and partly because a source of chemically separated antimony fission products produces spectra having a high density of peaks.

One need only inspect the two previous attempts to construct a decay scheme for ^{133}Sb to see these difficulties. None of Treytl's newly proposed levels can be confirmed by this study and only 3 of the 6 gamma-rays placed in his scheme are now thought to belong to the ^{133}Sb decay. Only 4 of the 5 levels in Erten and Blachot's proposed decay scheme and 7 of the 11 gamma-rays therein could be verified.

The present study has circumvented these problems by using preliminary gamma-ray spectra now available from mass-separated sources produced by the on-line mass separators LOHENGRIN[89] in Grenoble and JOSEF[90] in Julich. The A=133[4] and A=132[5]

^{235}U fission chain results eliminate the confusion brought about by the like half-lives of ^{133}Sb and ^{132}Sb, at least for the stronger transitions. The LOHENGRIN gamma-ray spectra from the A=133 and A=132 chains are shown in figures 3.1 and 3.2. Tables 3.1 and 3.2 identify the gamma-rays and give approximate energies.

Another improvement over past experiments which was made use of here was the combination of an automated chemical separation and high-volume, high-efficiency Ge(Li) detectors. This allowed the collection of a much larger number of coincidence events compared to the previous works -- enough to resolve close multiplets and to clearly observe coincidences involving gamma-rays of intensities as low as .1% of the strongest ^{133}Sb line (1096 keV).

Energies and intensities were determined by gamma-ray singles spectroscopy and are given in section 3.1. Approximately 400 gamma-rays, listed in table 3.3, were observed of which 227 have been assigned to specific nuclides. The 440 gamma-gamma coincidence slices made are discussed in section 3.2 and summarized in table 3.4. From this information, the ^{133}Sb decay scheme, shown in figure 3.3, was found to have 29 excited levels and 105 gamma-rays. The spin and parity assignments of these levels are discussed in section 3.3. Also, 18 new levels were discovered in the ^{132}Sb scheme and 64 gamma-rays were placed. The ^{132}Sb data were analyzed with E. A. Henry and will be reported elsewhere [54]

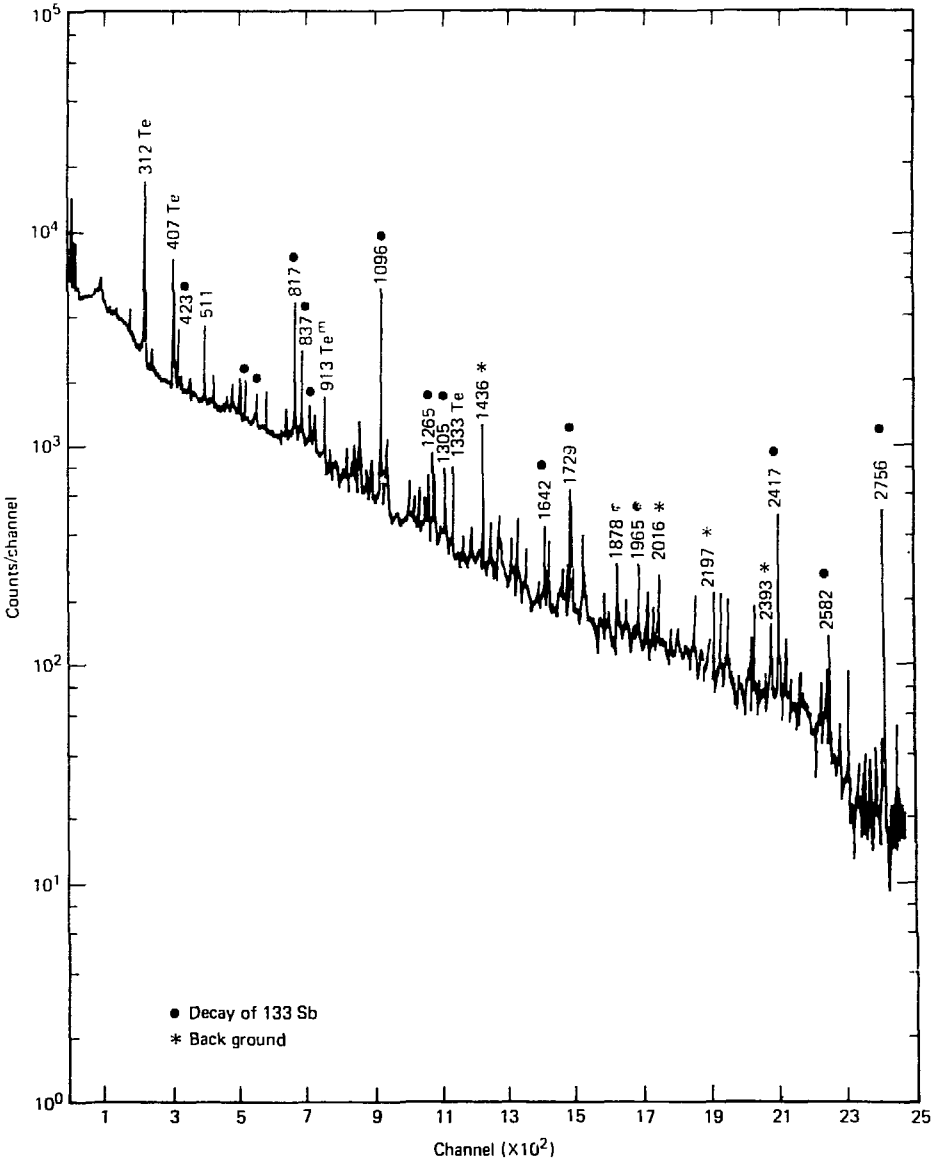

Figure 3.1. Gamma-ray spectrum of the A=133 decay chain from the LOHENGRIN online mass separator.

Table 3.1 Gamma-rays observed in the A=133 LOHENGRIN spectrum.(*)

Approximate Energy (keV)						
74 D	437	720 C	1021 BC	1306 BCD	1706 B	2252
85	456 B	773	1027 B	1312 BC	1718 C	2304
95 D	463 BD	787 C	1032	1333 CD	1728 B	2332 B
113	475 C	794 D	1048 B	1394	1733	2363 C
160	502	799 D	1060 B	1401	1768	2391 A
169 D	511 ANN	809 B	1066 B	1436 A	1775 B	2416 BC
202 D	527 C	817 B	1096 B	1460 AD	1801	2441 B
214 B	531 D	827 B	1115 B	1477	1807	2447 B
218	539 B	832	1120	1484 B	1837	2458
261 D	547 C	837 B	1184 B	1489 BC	1877 B	2481 BD
267 B	555	845 C	1189	1529 B	1896 C	2543 C
275 B	586 CD	853	1192	1552 B	1904	2671
298 B	603 B	864 BD	1202 B	1572	1944 BC	2744 B
308 B	613 C	881 B	1218	1579 B	1965 B	2790
313 C	622 D	912 D	1236 B	1589 D	1976 B	2794 B
335 B	632 B	931 C	1249 B	1635	2004 D	2978
345 D	648 CD	938	1265 B	1642 B	2015 A	3295
408 C	679	987	1272	1654 B	2132 B	3383
414 B	687	1001 C	1278	1659 B	2195 AC	3437
424 B	703 D	1010	1293 AB	1697 BC	2218	3853
					2244 C	4071

(*)

A = Background
B = ^{133}Sb
C = $^{133}Te^{g}$
D = $^{133}Te^{m}$

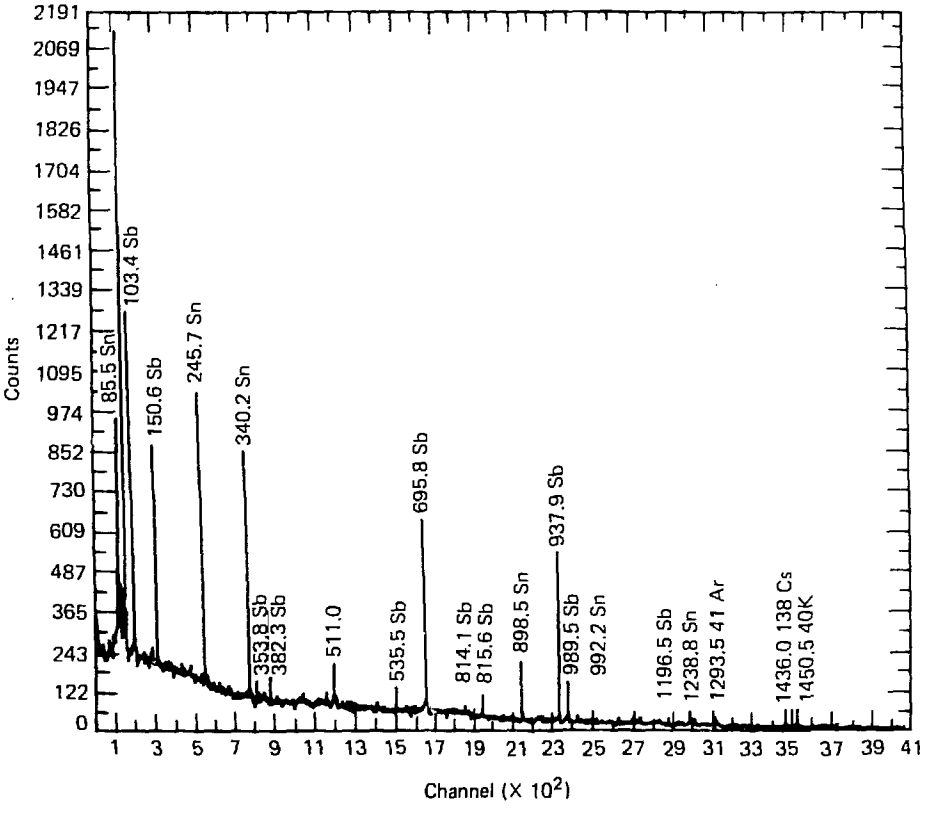

Figure 3.2. Gamma-ray spectrum of the A = 132 decay chain from the LOHENGRIN online mass separator.

Table 3.2. Gamma-rays observed in the A=132 LOHENGRIN spectrum.(*)

Approximate Energy (keV)					
85.5 A	340.4 A	548.7 A	814.1 B	974.6 B	1196.5 B
103.4 B	353.8 B	635.6 B	816.6 B	989.6 B	1238.9 A
150.6 B	382.3 B	651.8 A	898.5 A	992.2 A	
246.7 A	528.4 A	696.8 B	937.9 B	1077.8 A	

(*) A = ^{132}Sn
B = ^{132}Sb

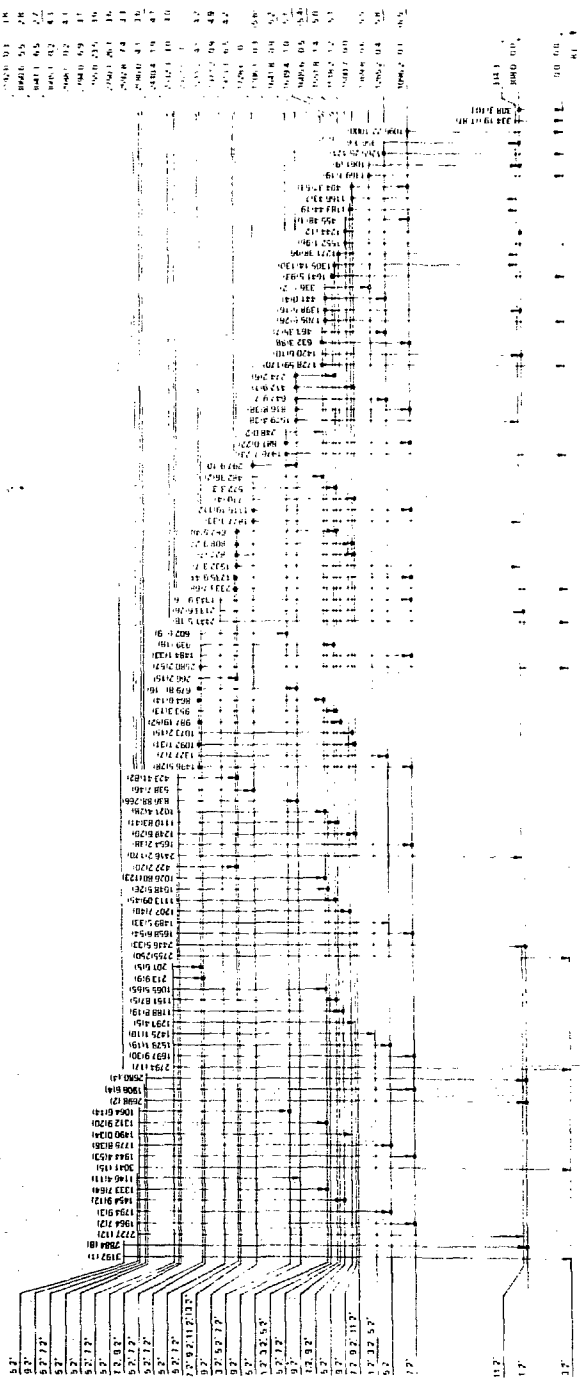

Figure 3.3. The ^{133}Sb decay scheme.

3.1 Gamma-ray Singles Spectroscopy

Table 3.3 presents a compilation of gamma-rays observed in two composite spectra, each constructed by summing 50 singles spectra obtained from chemically separated Sb fission product sources. The first composite spectrum covers 0-2 MeV and is shown in figures 3.4-3.19. The last 2300 channels of the second spectrum, which has a 0-4 MeV energy range, are shown in figures 3.20-3.27. Individual spectra were taken at times ranging from 75 s to 375 s after fission with counting times of 30-60 s. The energies and intensities given in the table were obtained from GAMANAL peak fits of the summed spectrum.

Preliminary spectra were taken with known energy standards (^{56}Co, ^{125}Sb, ^{182}Ta, ^{54}Mn, ^{137}Cs, ^{113}Sn) to determine the energies of the stronger peaks in the Sb spectrum. These peaks were then used as internal calibrations in obtaining energies of the weaker peaks in spectra taken without energy standards. The energy uncertainties reported in table 3.3 represent the error due to the peak fit added in quadrature to the error in the calibration energies. The relative intensity errors are the quadrature sums of the peak fitting errors and the error in the relative efficiency curve. Intensities have been normalized to the 1096 keV ^{133}Sb photopeak intensity which has been set equal to 1000. To obtain gamma rays per 100 beta decays, multiply by 0.0386. The comparison of intensities of peaks belonging to different nuclides is meaningless; the intensities have been obtained from the sum of several spectra taken at many different times.

The approximate half-lives were determined for several gamma-rays by multiscaling techniques. One component decay curves were fitted to the 7 data points obtained for each gamma-ray. In cases where several components were present the given half-life can be completely erroneous. In all cases the accuracy is never better than $\pm$ 0.5 min.

The identification of a decaying nuclide with a certain gamma-ray, when possible, was noted in table 3.3. These gamma-ray assignments were made on the basis of coincidence data, half-lives, energies, and intensities.

Table 3.3 Gamma-rays observed in the decay of chemically separated Sb fission products.(*)

E(ΔE) (keV)	I(ΔI)	$t_{1/2}$ (min)	Nuclide
85.3 (3)			($^{130}Sn^{m}$), (^{132}Sn)
95.1 (4)			
96.9 (4)			
103.6 (2)	390 (50)	3.3	$^{132}Sb^{mg}$
123.6 (2)	2 (2)		($^{132}Sb^{m}$)
135.1 (3)	11 (2)	10	^{131}Sb
138.3 (2)	10 (2)	12	
142.7 (4)	3 (2)		
145.0 (2)	17 (3)		$^{130}Sn^{m}$
150.6 (2)	430 (60)	6.5	$^{132}Sb^{m}$
160.6 (2)	12 (2)	2.7	^{133}Sb
169.4 (3)	6 (2)		
172.6 (3)	2 (1)		
176.4 (2)	44 (5)		
182.3 (1)	260 (30)	9.8	$^{130}Sb^{m}$
192.5 (2)	300 (30)	6.1	^{130}Sn
197.3 (2)	19 (3)		
201.6 (3)	5 (2)	1.8	^{133}Sb
213.9 (3)	9 (2)		^{133}Sb
229.2 (2)	94 (10)	7.2	$^{130}Sn^{g}$
243.6 (3)	3 (2)		
246.8 (2)	36 (4)		^{132}Sn
248. (1)	2 (2)		^{133}Sb

E(ΔE) (keV)	I(ΔI)	$t_{1/2}$ (min)	Nuclide
251.4 (4)	3 (2)		
255.2 (2)	14 (2)		
258.1 (2)	13 (2)		$^{132}Sb^{ms}$, ^{138}Xe
261.0 (2)	10 (2)		^{133}Sb
266.2 (2)	15 (3)		^{133}Sb
271.6 (3)	5 (2)		
274.2 (2)	18 (3)	2.8	^{133}Sb, ^{131}Sb
276.6 (2)	16 (2)		$^{132}Sb^{g}$
279.2 (2)	5 (2)		
286.5 (3)	5 (2)		
293.8 (2)	11 (2)		$^{132}Sb^{m}$
296.3 (2)	19 (2)		^{134}Sb
297.9 (2)	10 (5)		^{133}Sb
301.0 (2)	12 (2)		^{131}Sb
304.3 (2)	16 (3)		
307.9			
308.3 (2)	103 (9)	2.5	^{133}Sb
312.1 (2)	550 (50)	Daughter	$^{133}Te^{g}$
314.0 (2)	14 (3)	Daughter	$^{128}Sb^{m}$
321.3 (2)	8 (2)		
324.2 (2)	7 (2)		^{131}Sb
331.1 (2)	60 (6)	10	$^{130}Sb^{g}$
334.23			(^{133}Sb)
336. (1)	2 (2)		^{133}Sb
340.3 (2)	35 (10)		^{132}Sn

E(ΔE) (keV)	I(ΔI)	$t_{1/2}$ (min)	Nuclide
341.3 (2)	23 (7)		$^{130}Sn^{g}$
348.5 (2)	32 (4)		$^{130}Sb^{m}$
353.7 (2)	61 (6)	2.4	$^{132}Sb^{gm}$
363.8 (2)	6 (3)		
368.4 (2)	35 (4)		$^{132}Sb^{m}$
369.9 (2)	17 (3)		
380.7 (1)	39 (6)		$^{132}Sb^{mg}$
382.64 (9)	140 (10)		$^{132}Sb^{mg}$
384.6 (1)	15 (4)		
403.2 (4)	7 (4)		
404.37 (6)	53 (6)	2.8	^{133}Sb
407.62 (1)	250 (20)	Daughter	$^{133}Te^{g}$
412.9 (2)	7 (2)		^{133}Sb
422.2 (2)	20 (4)		^{133}Sb
423.41 (5)	82 (7)	2.3	^{133}Sb
434.70 (5)	74 (6)		
436.65 (6)	68 (6)	2.3	$^{132}Sb^{g}$
441.0 (1)	12 (3)	2.8	^{133}Sb, $^{132}Sb^{m}$
445.02 (7)	25 (5)	2.5	$^{132}Sb^{g}$
450.05 (6)	68 (5)	2.4	
452.31 (8)	24 (3)		
455.48 (7)	25 (3)		^{133}Sb
463.35 (5)	80 (9)		^{133}Sb
468.02 (6)	47 (4)		$^{130}Sb^{mg}$
472.4 (2)	9 (2)		

E(ΔE) (keV)	I(ΔI)	$t_{1/2}$ (min)	Nuclide
474.8 (2)	12 (2)		
482.36 (9)	9 (2)		^{133}Sb
491.2 (2)	11 (3)		
496.99 (9)	47 (4)	4.8	$^{132}Sb^{m}$
500.0 (2)	8 (3)		$^{132}Sb^{g}$
511.0 (5)	160 (20)		$^{132}Sb^{m}$, Annihilation
517.9 (2)	5 (2)		
522.3 (3)	6 (3)		$^{132}Sb^{gm}$
529.4 (3)	5 (3)		
538.7 (1)	46 (5)	2.0	^{133}Sb
544.1 (5)	6 (3)		
550.4 (3)	9 (3)		
558.3 (2)	10 (2)		
560.9 (2)	8 (2)		$^{132}Sb^{mg}$
564.7 (4)	3 (2)		
572.3 (3)	3 (2)		^{133}Sb
586.5 (3)	5 (3)		
591.0 (2)	10 (3)		$^{132}Sb^{mg}$
602. (1)	9 (6)		^{133}Sb, ^{140}Cs
606.7 (2)	25 (4)		
611.5 (2)	31 (5)	2.8	$^{132}Sb^{g}$
619.9 (2)	15 (5)		
625.3 (2)	22 (6)		^{131}Sb
632.3 (2)	88 (6)	2.4	^{133}Sb
635.90 (2)		2.8	$^{132}Sb^{g}$

E(ΔE) (keV)	I(ΔI)	$t_{1/2}$ (min)	Nuclide
642.38 (7)	213 (10)	10	^{131}Sb
645.2 (2)	90 (6)		
647.9 (2)	43 (8)		^{133}Sb, $^{130}Sb^{m}$, $^{133}Te^{m}$
654.4 (2)	14 (3)	10	
658.2 (2)	47 (4)	20	
669.1 (2)	41 (3)	28	
671.5 (2)	11 (3)		
679.8 (2)	16 (4)		^{133}Sb
687.5 (2)	40 (4)	2.5	^{133}Sb
691.1 (2)	64 (3)	3.3	$^{132}Sb^{mg}$
695.5 (2)	34 (6)	3.4	
697.02 (9)	2160 (90)	2.9	$^{132}Sb^{mg}$
706.8 (3)	5 (3)		
710. (1)	4 (3)		^{133}Sb
719.6 (2)	65 (5)	Daughter	$^{133}Te^{g}$
723.1 (2)	11 (3)		
726.5 (2)	33 (3)	33	^{131}Sb
732.3 (2)	51 (6)	12	
740. (1)			$^{132}Sb^{mg}$
743.2 (2)	106 (6)		$^{130}Sn^{g}$, ^{128}Sb
748.7 (2)	26 (3)	5.8	$^{130}Sb^{m}$
754.0 (2)	23 (5)		^{128}Sb
760.2 (2)	40 (4)		
776.4 (2)	29 (4)		$^{132}Sb^{mg}$
780.03 (8)	290 (20)	3.0	

E(ΔE) (keV)	I(ΔI)	$t_{1/2}$ (min)	Nuclide
786.93 (9)	46 (4)	Daughter	$^{133}Te^{g}$
793.51 (8)	610 (30)	11	$^{130}Sb^{m}$
798.52 (9)	60 (4)	1.1	
808.9 (1)	27 (3)	2.5	^{133}Sb
813.3 (2)	84 (5)	3.4	$^{132}Sb^{g}$
816.8 (2)	730 (42)	2.9	^{133}Sb, $^{132}Sb^{g}$, $^{130}Sb^{m}$
822.9			$^{132}Sb^{g}$
824.7 (5)	7 (5)		^{131}Sb
827. (1)	21 (6)		^{133}Sb
836.88 (7)	266 (9)	2.4	^{133}Sb
839.49 (7)	720 (30)	10	$^{130}Sb^{mg}$
844.26 (9)	34 (3)	Daughter	$^{133}Te^{g}$
847.0 (2)	15 (3)		
849.4 (3)	5 (2)		
854.7 (2)	22 (3)	6.5	
864.0 (2)	29 (3)	3.5	^{133}Sb, $^{133}Te^{m}$
881.0 (2)	82 (10)	2.0	^{133}Sb, $^{132}Sb^{g}$
884.1 (2)	28 (6)		
889.8 (2)	7 (2)		
898.7 (2)	60 (30)		^{132}Sn, $^{130}Sn^{m}$
902.5 (3)	6 (3)		
912.5 (2)	53. (5)		$^{133}Te^{m}$
914.7 (2)	14 (4)		
920.9 (2)	25 (3)	6.8	$^{130}Sb^{m}$
927.7 (1)	32 (4)		$^{132}Sb^{m}$

E(ΔE) (keV)	I(ΔI)	$t_{1/2}$ (min)	Nuclide
642.38 (7)	213 (10)	10	^{131}Sb
645.2 (2)	90 (6)		
647.9 (2)	43 (8)		^{133}Sb, $^{130}Sb^{m}$, $^{133}Te^{m}$
654.4 (2)	14 (3)	10	
658.2 (2)	47 (4)	20	
669.1 (2)	41 (3)	28	
671.5 (2)	11 (3)		
679.8 (2)	16 (4)		^{133}Sb
687.5 (2)	40 (4)	2.5	^{133}Sb
691.1 (2)	64 (3)	3.3	$^{132}Sb^{mg}$
695.5 (2)	34 (6)	3.4	
697.02 (9)	2160 (90)	2.9	$^{132}Sb^{mg}$
706.8 (3)	5 (3)		
710. (1)	4 (3)		^{133}Sb
719.6 (2)	65 (5)	Daughter	$^{133}Te^{g}$
723.1 (2)	11 (3)		
726.5 (2)	33 (3)	33	^{131}Sb
732.3 (2)	51 (6)	12	
740. (1)			$^{132}Sb^{mg}$
743.2 (2)	106 (6)		$^{130}Sn^{g}$, ^{128}Sb
748.7 (2)	26 (3)	5.8	$^{130}Sb^{m}$
754.0 (2)	23 (5)		^{128}Sb
760.2 (2)	40 (4)		
776.4 (2)	29 (4)		$^{132}Sb^{mg}$
780.03 (8)	290 (20)	3.0	

E(ΔE) (keV)	I(ΔI)	$t_{1/2}$ (min)	Nuclide
786.93 (9)	46 (4)	Daughter	$^{133}Te^{g}$
793.51 (8)	610 (30)	11	$^{130}Sb^{m}$
798.52 (9)	60 (4)	1.1	
808.9 (1)	27 (3)	2.5	^{133}Sb
813.3 (2)	84 (5)	3.4	$^{132}Sb^{g}$
815.8 (2)	730 (42)	2.9	^{133}Sb, $^{132}Sb^{g}$, $^{130}Sb^{m}$
822.9			$^{132}Sb^{g}$
824.7 (5)	7 (5)		^{131}Sb
827. (1)	21 (6)		^{133}Sb
836.88 (7)	266 (9)	2.4	^{133}Sb
839.49 (7)	720 (30)	10	$^{130}Sb^{mg}$
844.26 (9)	34 (3)	Daughter	$^{133}Te^{g}$
847.0 (2)	15 (3)		
849.4 (3)	5 (2)		
854.7 (2)	22 (3)	6.5	
864.0 (2)	29 (3)	3.5	^{133}Sb, $^{133}Te^{m}$
881.0 (2)	82 (10)	2.0	^{133}Sb, $^{132}Sb^{g}$
884.1 (2)	28 (6)		
889.8 (2)	7 (2)		
898.7 (2)	60 (30)		^{132}Sn, $^{130}Sn^{m}$
902.5 (3)	6 (3)		
912.5 (2)	53. (5)		$^{133}Te^{m}$
914.7 (2)	14 (4)		
920.9 (2)	25 (3)	6.8	$^{130}Sb^{m}$
927.7 (1)	32 (4)		$^{132}Sb^{m}$

E(ΔE) (keV)	I(ΔI)	$t_{1/2}$ (min)	Nuclide
930.48 (9)	49 (4)		$^{132}Sb^{mg}$, $^{133}Te^{g}$
932.83 (7)	237 (6)	24	^{131}Sb
934.9			
936.33 (9)	22 (3)		$^{132}Sb^{g}$
939. (1)	18 (6)		^{133}Sb
943.29 (4)	470 (10)	23	^{131}Sb
950.3 (2)	11 (3)		
953.3 (2)	13 (3)		^{13}?$^{}$b
956.9 (3)	6 (3)		^{133}Sb
963.8 (2)	8 (3)		$^{132}Sb^{m}$
972.2 (2)	30 (7)		
974.29 (3)	2720 (50)	3.1	$^{132}Sb^{mg}$
976.7 (2)	11 (6)		
987.19 (9)	52 (3)	2.6	^{133}Sb
989.64 (9)	350 (6)	2.7	$^{132}Sb^{g}$
992.1 (2)	26 (3)		^{132}Sn
995.3 (4)	2 (2)		
1000.74 (9)	39 (4)	Daughter	$^{133}Te^{g}$
1009.6 (3)	4 (2)		
1014.4 (2)	17 (2)		
1017.78 (4)	180 (4)	12	$^{130}Sb^{m}$
1021.4 (5)	39 (7)		^{133}Sb, $^{133}Te^{g}$
1026.80 (7)	123 (4)	2.7	^{133}Sb
1042.1 (1)	97 (3)	4.0	$^{132}Sb^{m}$
1048.5 (2)	26 (5)	2.3	^{133}Sb

E(ΔE) (keV)	I(ΔI)	$t_{1/2}$ (min)	Nuclide
1056.5 (2)	10 (2)		$^{132}Sb^{m}$
1061. (1)	9 (3)		^{133}Sb
1062. (1)	11 (3)		$^{133}Te^{g}$
1064.6 (5)	14 (4)	2.2	^{133}Sb
1065.5 (1)	65 (3)		^{133}Sb
1073.2 (2)	15 (4)		^{133}Sb
1079.6 (2)	13 (2)		
1083.8 (2)	7 (2)		
1088.1 (2)	15 (3)		
1092.1 (2)	31 (9)	2.7	^{133}Sb
1093.3 (1)	89 (9)	2.7	^{132}Sb
1096.22 (3)	1000 (5)	2.5	^{133}Sb
1098. (1)	17 (3)		^{132}Sb
1103. (1)	9 (2)		
1107.6 (6)	2 (2)		
1110.83 (7)	41 (3)		^{133}Sb
1113.09 (9)	45 (3)	2.6	^{133}Sb
1115.19 (6)	112 (3)	2.4	^{133}Sb
1123.50 (6)	72 (3)	22	^{131}Sb
1126.0 (3)	9 (3)		
1128.39 (8)	39 (3)		
1132. (1)			
1133.71 (7)	126 (3)	3.0	$^{132}Sb^{mg}$
1141.82 (6)	44 (3)	2.3	$^{130}Sb^{m}$
1146.4 (2)	11 (2)		(^{133}Sb)

E(ΔE) (keV)	I(ΔI)	$t_{1/2}$ (min)	Nuclide
1151.87 (7)	82 (3)	2.3	^{133}Sb, $^{132}Sb^{g}$
1161.30 (9)	36 (3)	3.9	
1166.43 (9)	64 (5)	4.4	^{133}Sb, ($^{132}Sb^{m}$)
1170.5 (2)	24 (3)		$^{132}Sb^{m}$
1177. (1)			($^{130}Sb^{m}$)
1180.3 (2)	18 (5)		
1181.5 (5)			$^{132}Sb^{m}$
1183.44 (8)	75 (6)	1.9	^{133}Sb
1188.8 (2)	19 (3)	3.6	^{133}Sb
1196.7 (2)	66 (3)	2.4	$^{132}Sb^{g}$
1200.0 (2)	20 (3)		
1202.7 (2)	40 (3)	1.7	^{133}Sb
1207.3 (2)	44 (3)	39	^{131}Sb
1213.5 (2)	59 (3)	2.3	$^{132}Sb^{g}$
1218.6 (2)	42 (3)	2.2	
1225.0 (2)	87 (3)	.9	
1229.2 (2)	16 (3)	1.4	
1233.4 (2)	20 (3)		^{131}Sb
1235.9 (2)	41 (3)	3.4	^{133}Sb
1239.6 (2)	18 (2)	1.0	
1244. (1)	12 (6)		^{133}Sb
1249.6 (2)	20 (3)	6.8	^{133}Sb
1252.4 (2)	29 (4)	3.2	$^{133}Te^{g}$
1265.25 (4)	121 (5)	2.1	^{133}Sb
1267.6 (2)	23 (4)	2.5	

E(ΔE) (keV)	I(ΔI)	$t_{1/2}$ (min)	Nuclide
1271.38 (4)	96 (5)	2.9	^{133}Sb
1274.5 (2)	15 (3)		$^{132}Sb^{g}$
1279.2 (4)	5 (2)		^{134}Sb
1293.4 (3)	5 (2)		(^{133}Sb)
1299.9 (2)	20 (3)	2.6	$^{132}Sb^{g}$
1305.14 (4)	130 (5)	2.3	^{133}Sb
1309.6 (2)	19 (2)		($^{132}Sb^{m}$)
1312.7 (1)	7 (1)		
1312.9 (2)	20 (3)		^{133}Sb
1313.2 (5)	51 (10)		
1321.5 (2)	19 (3)	2.1	
1327.7 (2)	7 (2)		^{133}Sb
1330.0 (2)	94 (4)	Daughter	^{133}Sb
1343.9 (3)	6 (3)		^{133}Sb
1343.9 (3)			$^{132}Sb^{g}$
1354.2 (3)	5 (2)	4.2	
1360.0 (3)	7 (3)		
1368.2 (2)	19 (3)	3.6	
1370. (1)			^{133}Sb
1377.9 (9)	2 (2)		
1380.6 (2)	17 (2)	7.8	
1389.7 (3)	5 (2)		
1393.7 (2)	12 (2)	3.1	
1398.5 (2)	16 (3)	6.6	^{133}Sb
1405.4 (6)	2 (2)		

E(ΔE) (keV)	I(ΔI)	$t_{1/2}$ (min)	Nuclide
1410.0 (2)	9 (3)		
1414.3 (5)	2 (2)		
1420.6 (3)	10 (3)	1.9	^{133}Sb
1425.1 (2)	10 (3)	1.6	^{133}Sb, ^{132}Sb^{g}
1436.3 (2)	66 (5)	2.7	^{132}Sb^{g}
1443.3 (4)	4 (2)		
1448.8 (4)	3 (2)		
1454.9 (2)	12 (3)		^{133}Sb
1462.4 (2)	5 (2)		
1462.9 (2)	2 (3)		
1470.1 (2)	11 (3)	8.3	
1481.0 (2)	12 (2)	.5	
1484.1 (2)	33 (3)	2.1	^{133}Sb
1489.5 (5)	34 (3)	2.5	^{133}Sb
1490.0 (5)	33 (3)	2.5	^{133}Sb
1496.5 (2)	28 (3)	2.2	^{133}Sb
1513.6 (2)	47 (5)	2.9	^{132}Sb^{mg}
1529.1 (2)	19 (3)		^{133}Sb
1540.1 (2)	16 (2)	1.8	^{132}Sb^{g}
1543.6 (2)	11 (2)		
1552.1 (2)	96 (6)	2.7	^{133}Sb
1558.6 (2)	12 (2)	2.0	
1573.4 (2)	41 (5)	2.8	^{132}Sb^{mg}
1579.4 (2)	38 (3)	2.3	^{133}Sb
1580.8 (4)	20 (8)		^{132}Sb^{m}

E(ΔE) (keV)	I(ΔI)	$t_{1/2}$ (min)	Nuclide
1588.7 (2)	8 (2)	Daughter	
1596.9 (2)	18 (3)		
1609.2 (2)	11 (3)	2.2	
1613.7 (6)	2 (2)		
1633.9 (2)	34 (3)	2.5	$^{132}Sb^{g}$
1641.5 (2)	93 (6)	2.6	^{133}Sb
1644.5 (2)	39 (3)	2.5	$^{132}Sb^{g}$
1654.2 (2)	38 (3)	2.5	^{133}Sb
1658.6 (2)	54 (4)	2.8	^{133}Sb
1664.9 (5)	4 (2)		^{90}Rb
1668.0 (2)	28 (3)	8.3	($^{132}Sb^{m}$)
1682.8 (3)	4 (2)		
1691.0 (5)	2 (2)		
1697.9 (2)	30 (3)	2.3	^{133}Sb
1705.5 (2)	26 (4)	2.4	^{133}Sb
1717.8 (1)	26 (3)	Daughter	
1722.0 (2)	18 (3)	22	
1728.59 (7)	170 (12)	2.3	^{133}Sb
1732.82 (9)	45 (4)	2.1	
1737.9 (5)	2 (2)		
1756.2 (2)	8 (2)	2.2	
1763.1 (2)	10 (2)		
1767.0 (1)	22 (3)	3.3	
1775.8 (1)	36 (7)	1.9	^{133}Sb
1787.7 (1)	59 (6)	2.7	

E(ΔE) (keV)	I(ΔI)	$t_{1/2}$ (min)	Nuclide
1789.4 (4)	14 (5)		$^{132}Sb^{g}$
1794.9 (4)	3 (2)		
1821.8 (2)	11 (3)		
1837.5 (3)	5 (2)		
1854.44 (7)	52 (8)	8.4	
1877.3 (2)	33 (4)	1.9	^{133}Sb
1887.2 (3)	5 (2)	1.4	
1894.5 (2)	15 (2)		
1897.0 (2)	5 (2)		
1904.9 (2)	11 (2)	2.4	
1908.6 (6)	4 (2)	Daughter	^{133}Sb
1931.4 (3)	4 (2)	1.0	
1935.0 (3)	3 (2)		
1944.4 (2)	53 (6)	2.5	^{133}Sb
1946.7 (2)	4 (2)	2.5	
1964.7 (2)	43 (6)	3.0	^{133}Sb
1976.7 (2)	23 (4)	2.4	^{133}Sb
1992.3 (3)	7 (2)	2.9	^{133}Sb
2004.9 (3)	7 (3)		
2018.6 (2)	9 (2)		
2040. (1)	3 (3)	.9	
2068.8 (9)	13 (6)		
2079.4 (9)	11 (6)		
2116.7 (8)	5 (2)		
2133.6 (9)	26 (5)	2.5	^{133}Sb

E(ΔE) (keV)	I(ΔI)	$t_{1/2}$ (min)	Nuclide
2148.6 (9)	15 (5)	10	$^{132}Sb^{mg}$
2167.6 (9)	11 (4)	10	
2179.9 (8)	36 (7)	3.7	
2197.0 (9)	9 (3)	1.9	^{90}Rb
2229. (1)	3 (2)		
2243.4 (9)	45 (9)	2.5	
2270. (1)	4 (2)		
2280.4 (9)	65 (10)	3.1	
2290.9 (8)	10 (3)	2.4	
2310. (2)	3 (3)	3.0	$^{132}Sb^{mg}$
2317.2 (8)	16 (3)	3.3	
2332.7 (8)	68 (12)		^{133}Sb
2336.6 (9)	17 (6)		
2363.4 (8)	14 (4)	3.6	
2384.2 (8)	14 (3)	3.9	
2398.9 (8)	15 (4)		
2416.2 (8)	170 (30)	2.4	(^{133}Sb)
2441.5 (8)	18 (4)	2.4	(^{133}Sb)
2446.5 (8)	33 (6)	2.2	^{133}Sb
2468.4 (9)	9 (4)		
2479.0 (8)	16 (5)	3.6	$^{132}Sb^{mg}$
2515.5 (9)	8 (3)	2.1	
2551.0 (1)	5 (3)		
2563.1 (9)	7 (2)	1.8	
2580.2 (8)	57 (10)	2.5	(^{133}Sb)

E(ΔE) (keV)	I(ΔI)	$t_{1/2}$ (min)	Nuclide
2588.3 (8)	28 (6)	3.4	$^{132}Sb^{g}$
2633.8 (8)	12 (3)	2.3	
2662.0 (8)	23 (5)	3.2	
2665. (1)	25 (5)		
2672. (1)	5 (2)	3.4	
2680. (1)	4 (2)		^{133}Sb
2705. (1)	2 (1)	13	
2711. (2)	3 (2)	2.3	^{133}Sb
2727. (1)	12 (3)	2.4	^{133}Sb
2755. (1)	250 (40)	2.4	^{133}Sb
2781. (1)	4 (2)	4.1	
2795. (1)	17 (4)	2.4	(^{133}Sb)
2800. (1)	7 (2)		
2831. (1)	8 (2)	2.6	
2868. (2)	1 (1)		
2872. (2)	1 (1)		
2884. (2)	8 (2)	2.7	^{133}Sb
2898. (2)	3 (1)		
2913. (2)	14 (3)	3.5	$^{132}Sb^{mg}$
2920. (2)	5 (2)		$^{132}Sb^{mg}$
2949. (2)	4 (2)	3.7	
2979. (2)	6 (2)	1.0	
3003. (2)	8 (2)	5.1	
3041. (2)	15 (3)	2.2	(^{133}Sb)
3054. (2)	1 (1)		

E(ΔE) (keV)	I(ΔI)	$t_{1/2}$ (min)	Nuclide
3083. (2)	2 (1)		
3101. (2)	7 (2)	2.7	
3135. (2)	1 (1)		
3161. (2)	2 (1)		
3193. (2)	1 (1)		
3263. (2)	1 (1)		
3270. (2)	2 (1)	2.6	
3331. (2)	1 (1)		$^{132}Sb^{mg}$
3342. (2)	1 (1)		
3353. (2)	2 (1)	3.7	^{132}Sb
3408. (2)	1 (1)	2.0	^{132}Sb
3461. (2)	4 (1)	2.2	
3559. (2)	8 (2)	2.3	$^{132}Sb^{mg}$
3611. (2)	2 (1)	4.5	$^{132}Sb^{mg}$
3700. (2)	1 (1)		
3718. (2)	1 (1)		

(*) 1) Intensities are normalized to I(1096 keV) = 1000

2) Nuclides given in parenthesis indicate that there are no coincidence data to support the gamma-ray assignment.

3) If the activity was observed to increase with time, the word "Daughter" was written in the $t_{1/2}$ column.

Figures 3.4 - 3.19 0-2 MeV gamma ray singles spectrum of chemically separated Sb fission products.

Figures 3.20 - 3.27 Channels 1780 - 4096 of a 0-4 MeV gamma ray singles spectrum of chemically separated Sb fission products.

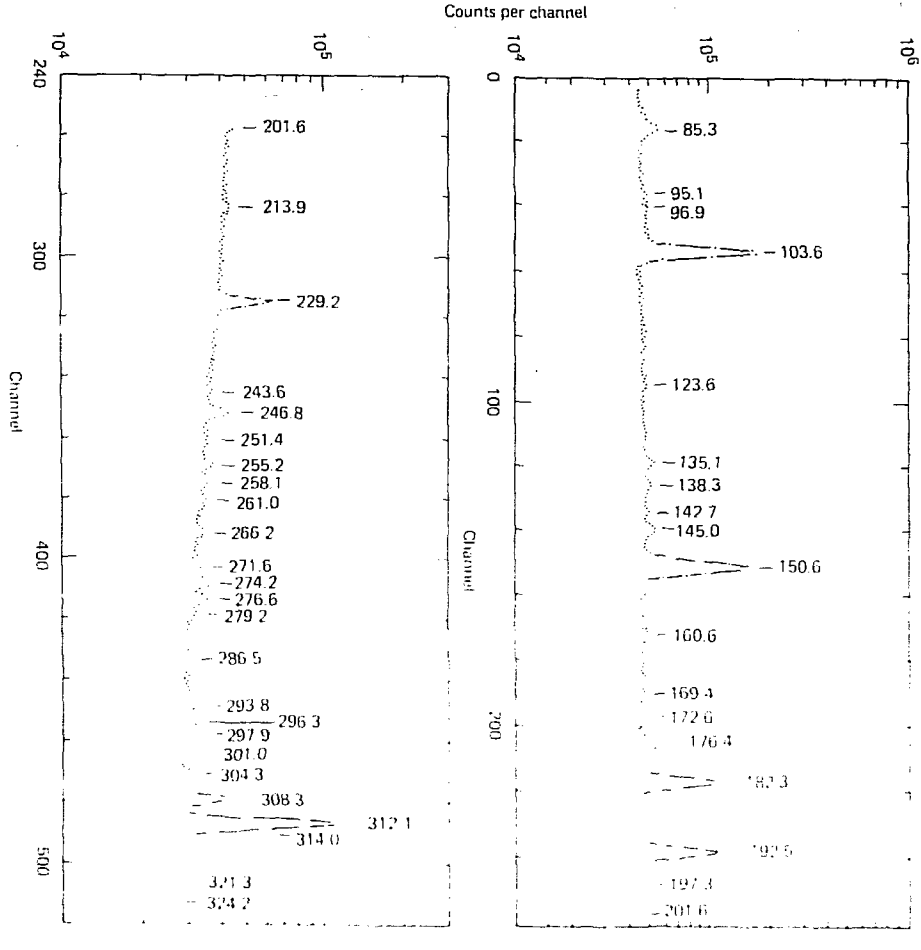
Counts per channel
Channel
240
300
400
500
0
100
200
201.6
213.9
229.2
243.6
246.8
251.4
255.2
258.1
261.0
266.2
271.6
274.2
276.6
279.2
286.5
293.8
296.3
297.9
301.0
304.3
308.3
312.1
314.0
321.3
324.2
85.3
95.1
96.9
103.6
123.6
135.1
138.3
142.7
145.0
150.6
160.6
169.4
172.6
176.4
182.3
193.5
197.3
201.6

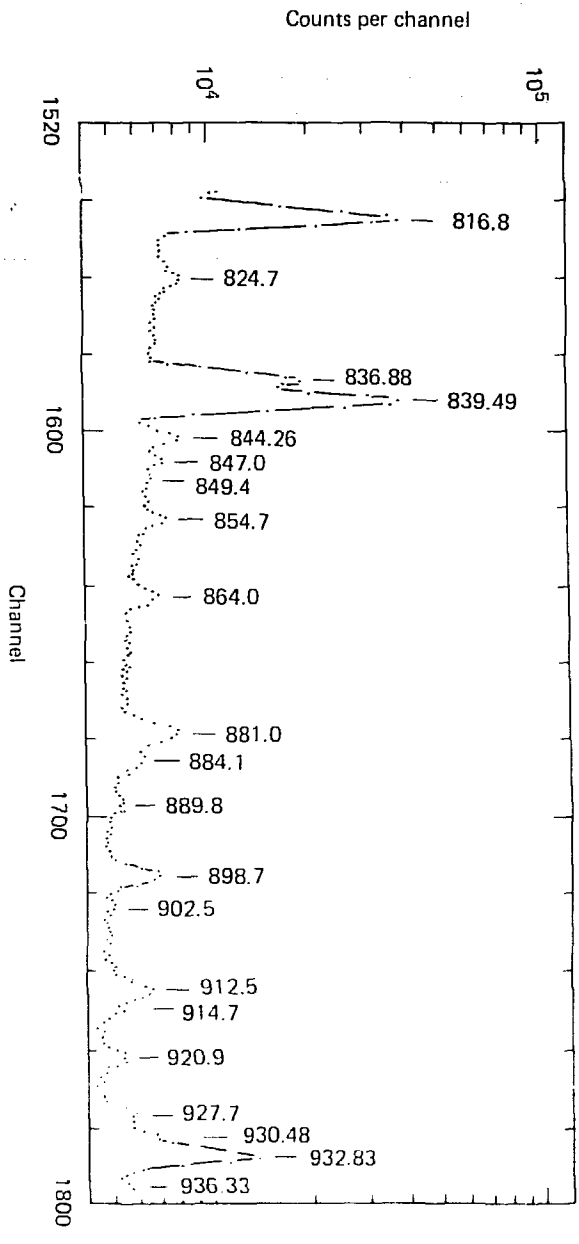
Counts per channel
10^4
10^5
1520
1600
1700
1800
Channel
816.8
824.7
836.88
839.49
844.26
847.0
849.4
854.7
864.0
881.0
884.1
889.8
898.7
902.5
912.5
914.7
920.9
927.7
930.48
932.83
936.33

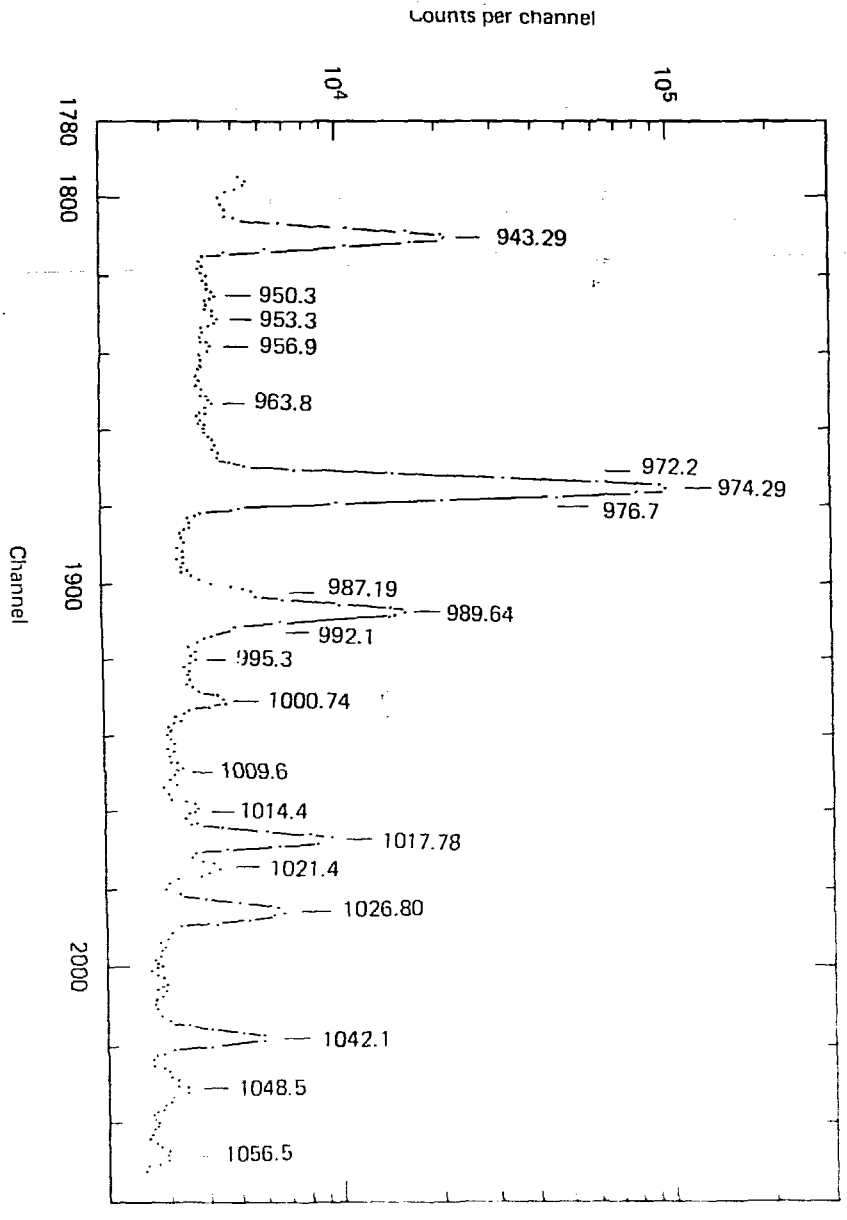
Counts per channel
10^4
10^5
Channel
1780
1800
1900
2000
943.29
950.3
953.3
956.9
963.8
972.2
974.29
976.7
987.19
989.64
992.1
995.3
1000.74
1009.6
1014.4
1017.78
1021.4
1026.80
1042.1
1048.5
1056.5

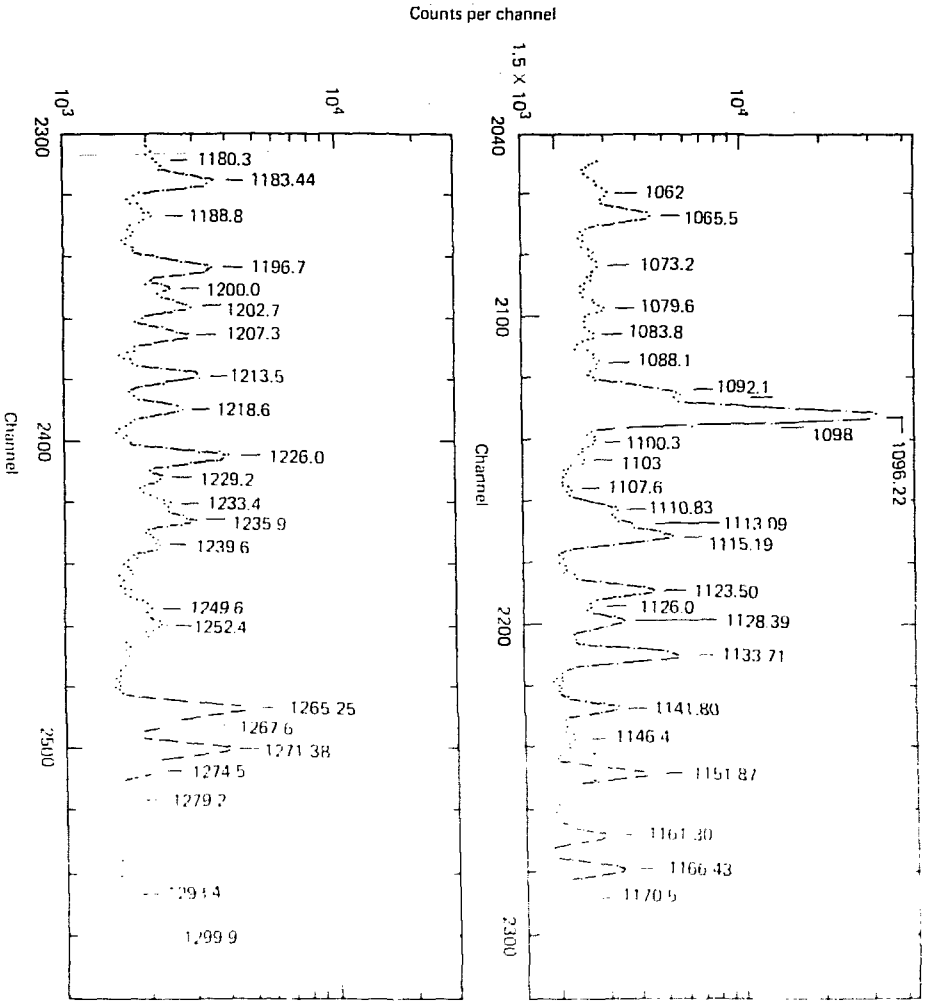
Counts per channel
1.5 X 10^3
10^4
2040
2100
2200
2300
Channel
1062
1065.5
1073.2
1079.6
1083.8
1088.1
1092.1
1098
1096.22
1100.3
1103
1107.6
1110.83
1113.09
1115.19
1123.50
1126.0
1128.39
1133.71
1141.80
1146.4
1151.87
1161.30
1166.43
1170.9
10^3
10^4
2300
2400
2500
Channel
1180.3
1183.44
1188.8
1196.7
1200.0
1202.7
1207.3
1213.5
1218.6
1226.0
1229.2
1233.4
1235.9
1239.6
1249.6
1252.4
1265.25
1267.6
1271.38
1274.5
1279.2
1294.4
1299.9

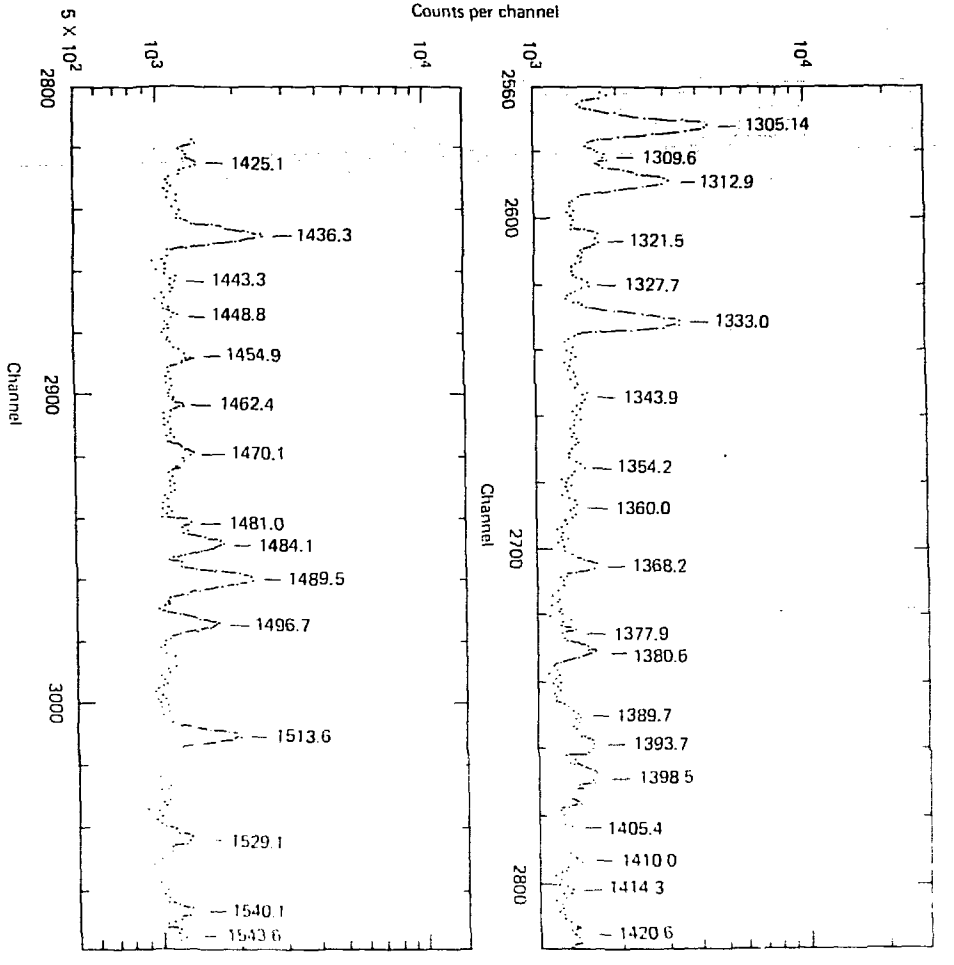
Counts per channel
5 X 10²
10³
10⁴
2800
2900
3000
Channel
1425.1
1436.3
1443.3
1448.8
1454.9
1462.4
1470.1
1481.0
1484.1
1489.5
1496.7
1513.6
1529.1
1540.1
1543.6
10³
10⁴
2560
2600
2700
2800
Channel
1305.14
1309.6
1312.9
1321.5
1327.7
1333.0
1343.9
1354.2
1360.0
1368.2
1377.9
1380.6
1389.7
1393.7
1398.5
1405.4
1410.0
1414.3
1420.6

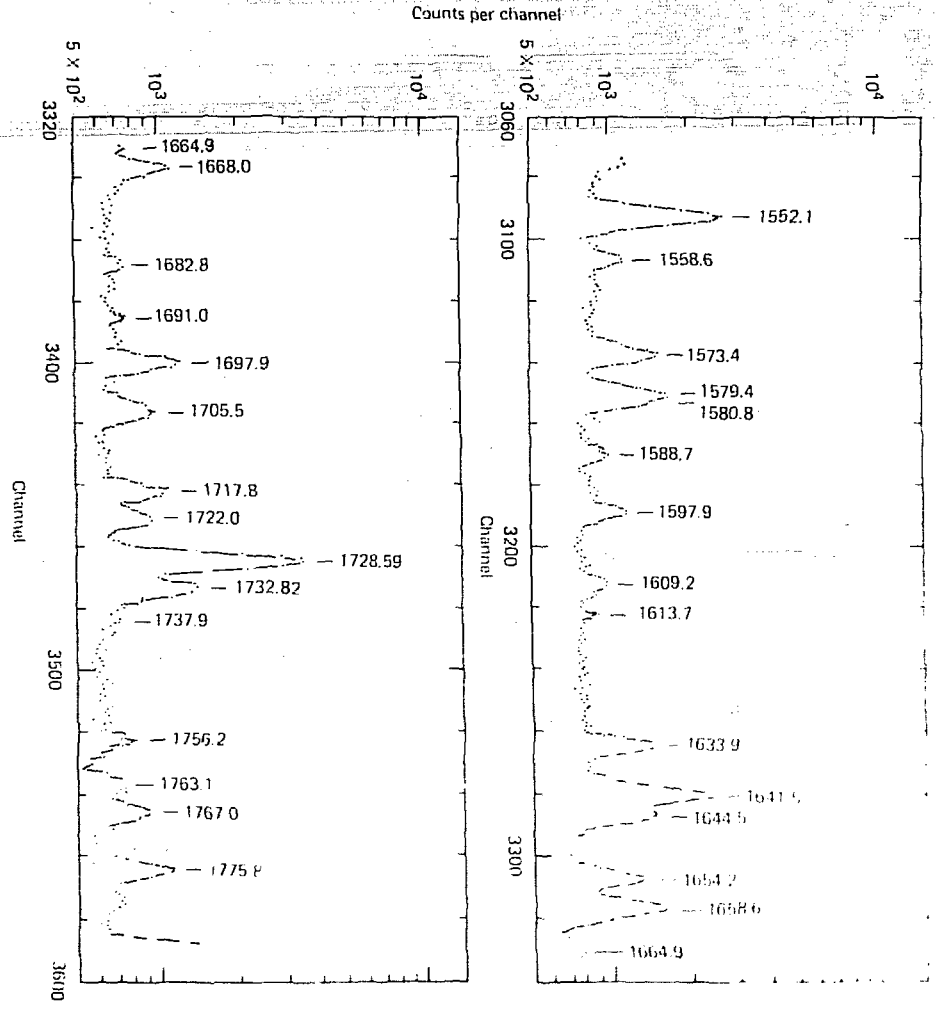
Counts per channel
5 X 10²
10³
10⁴
Channel
3320
3400
3500
3610
1664.9
1668.0
1682.8
1691.0
1697.9
1705.5
1717.8
1722.0
1728.59
1732.82
1737.9
1756.2
1763.1
1767.0
1775.8
3060
3100
3200
3300
1552.1
1558.6
1573.4
1579.4
1580.8
1588.7
1597.9
1609.2
1613.7
1633.9
1644.5
1654.2
1658.6
1664.9

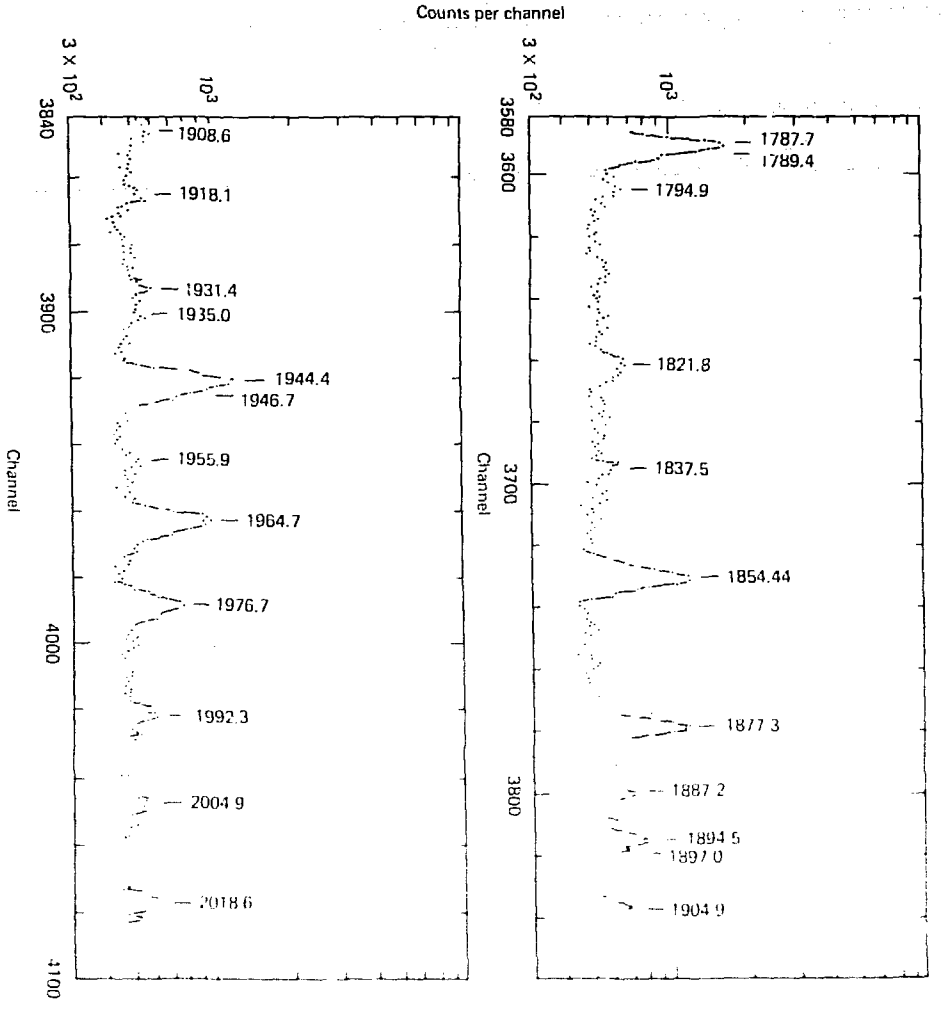
Counts per channel
3 X 10²
10³
3840
3900
4000
4100
Channel
1908.6
1918.1
1931.4
1935.0
1944.4
1946.7
1955.9
1964.7
1976.7
1992.3
2004.9
2018.6
3 X 10²
10³
3580
3600
3700
3800
Channel
1787.7
1789.4
1794.9
1821.8
1837.5
1854.44
1877.3
1887.2
1894.5
1897.0
1904.9

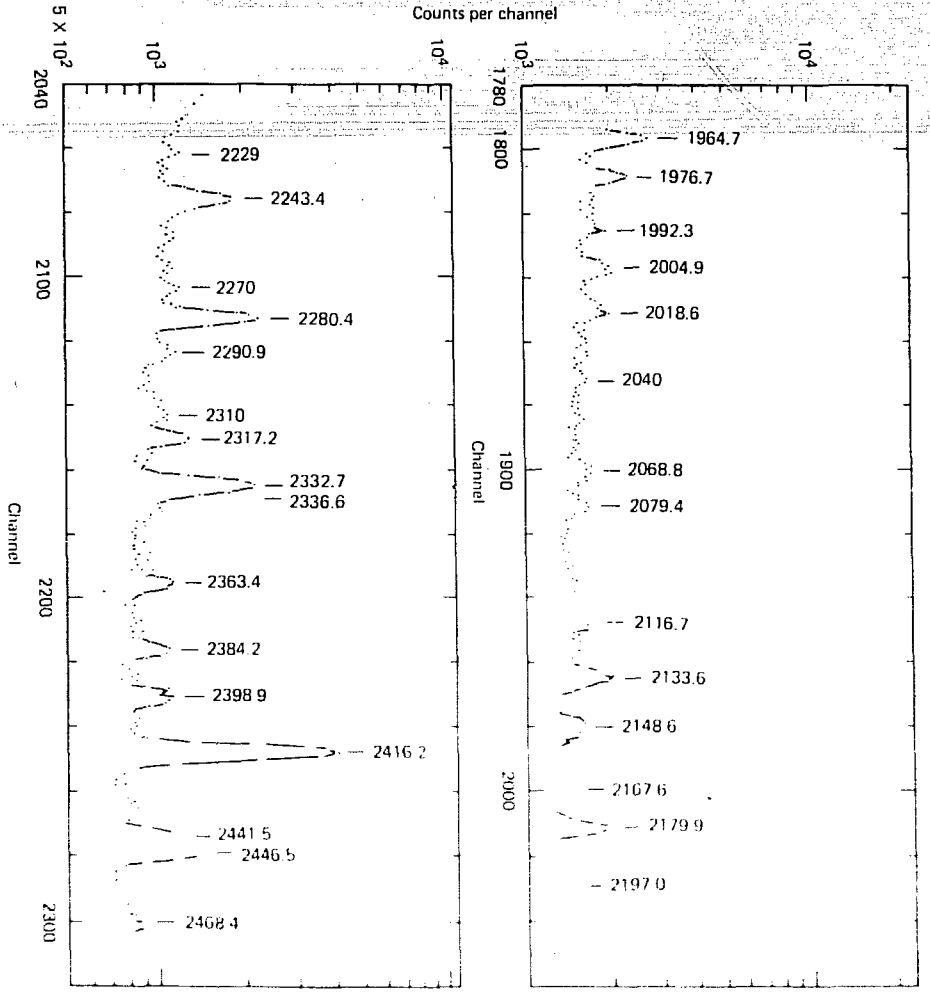
Counts per channel
5 X 10²
10³
10⁴
Channel
2040
2100
2200
2300
2229
2243.4
2270
2280.4
2290.9
2310
2317.2
2332.7
2336.6
2363.4
2384.2
2398.9
2416.2
2441.5
2446.5
2468.4
1780
1800
1900
2000
1964.7
1976.7
1992.3
2004.9
2018.6
2040
2068.8
2079.4
2116.7
2133.6
2148.6
2167.6
2179.9
2197.0

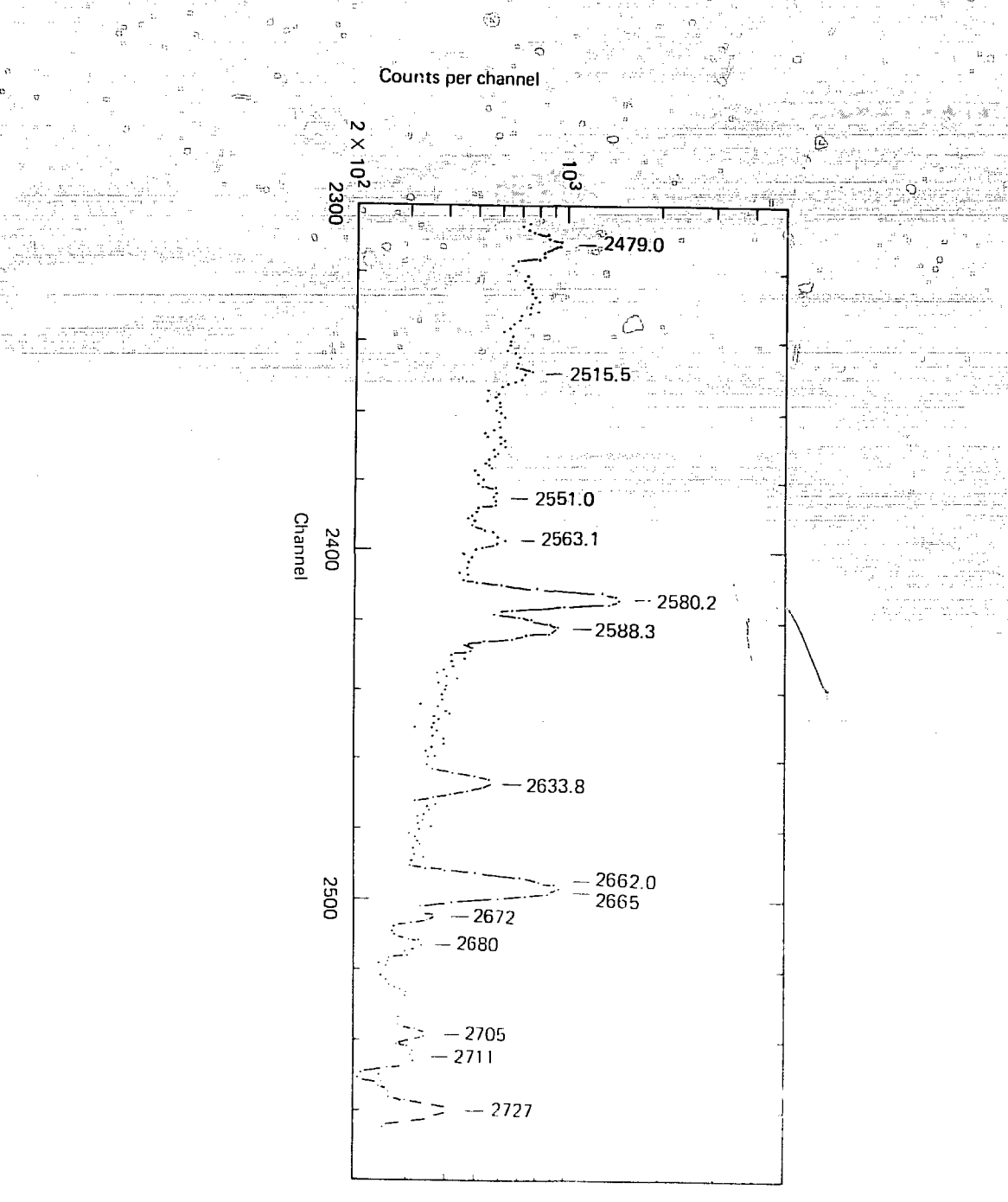
Counts per channel
2 X 10²
10³
2300
2400
2500
Channel
2479.0
2515.5
2551.0
2563.1
2580.2
2588.3
2633.8
2662.0
2665
2672
2680
2705
2711
2727

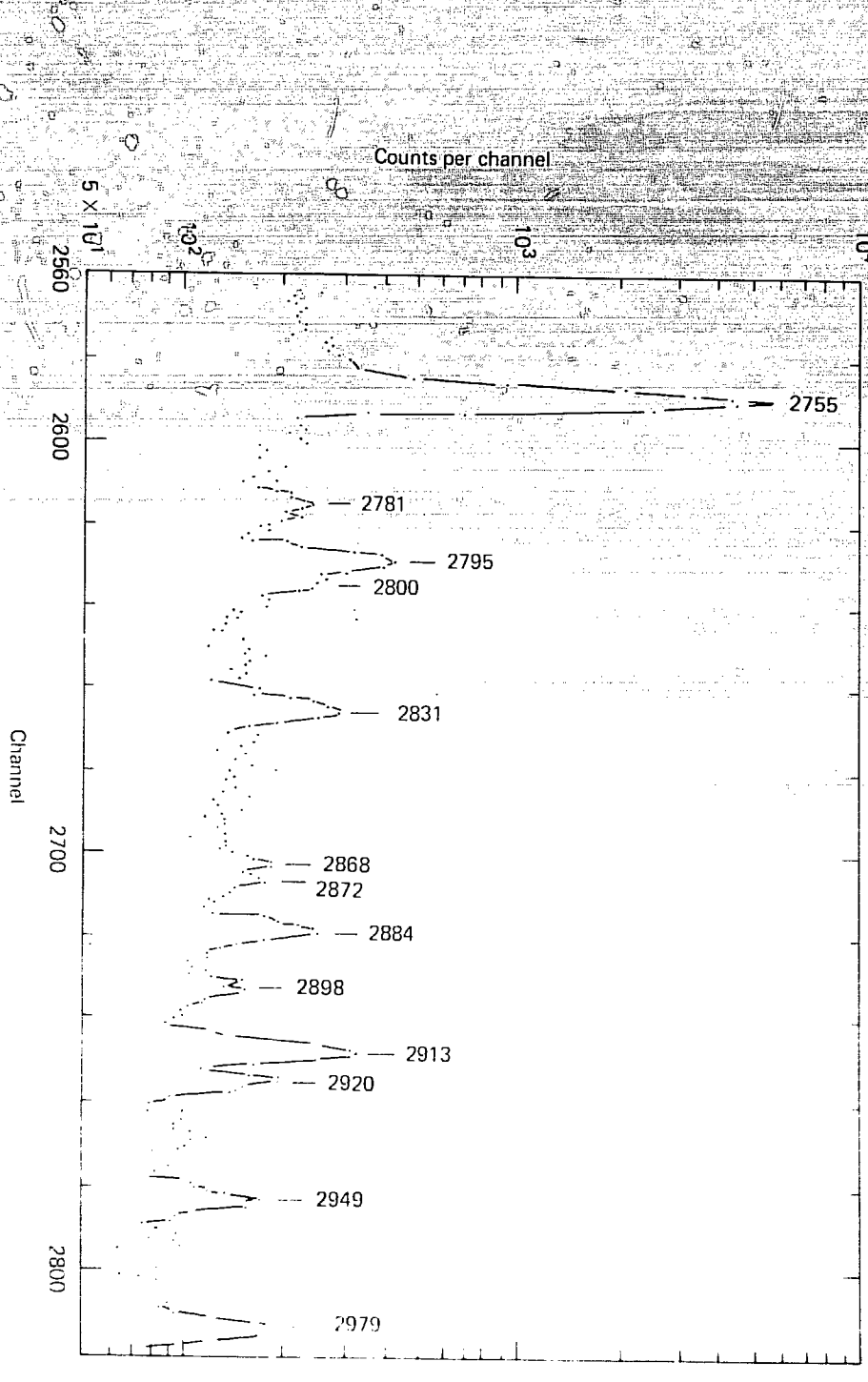
Counts per channel
5 × 10¹
10²
10³
10⁴
Channel
2560
2600
2700
2800
2755
2781
2795
2800
2831
2868
2872
2884
2898
2913
2920
2949
2979

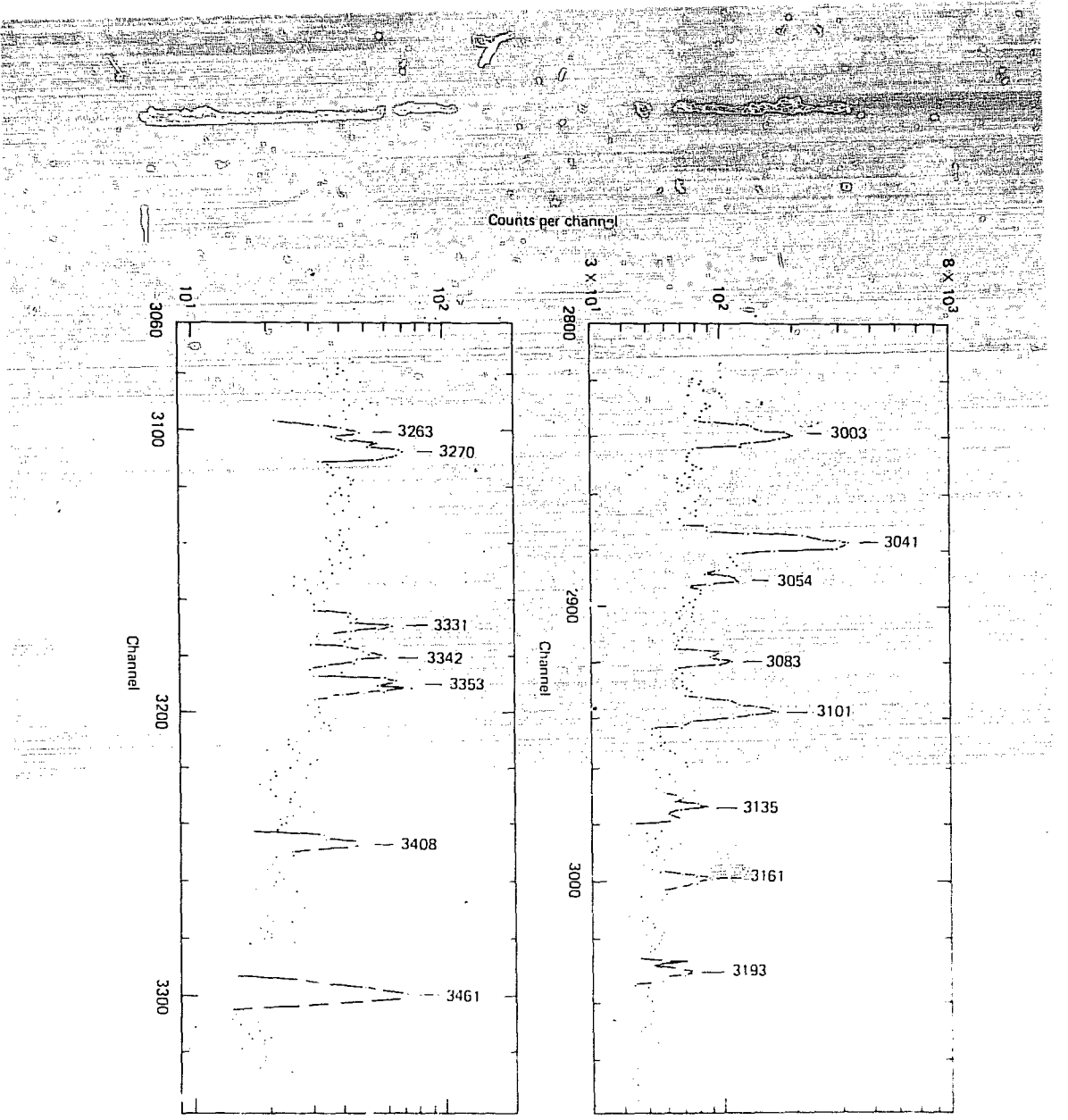
Counts per channel
Channel
3060
3100
3200
3300
3263
3270
3331
3342
3353
3408
3461
Channel
2800
2900
3000
3003
3041
3054
3083
3101
3135
3161
3193

Counts per channel
2 × 10⁰
10¹
10²
5 × 10²
3320
3400
3500
3600
Channel
3559
3611
3700
3718

3.2 Gamma-Gamma Coincidence Spectroscopy

Table 3.4 gives the results of the Ge(Li)-Ge(Li) gamma-gamma coincidence experiment. A gate was set for each peak in the coincidence profile spectrum. This spectrum contained all of the prompt coincidence events seen by one of the detectors. The width of the time window, 19 ns, was set at the full width at 1/10 maximum (FWTM) of the timing peak. Gates were also set in which the timing window was later and earlier than the timing peak. These gates are denoted in table 3.4 by an L or an E, respectively, appended to the gate energy. The width of each gate was set equal to the FWHM of stronger peaks and FWTM of weaker peaks. The approximate energy of each gate is given in column one. Known gamma-rays falling within the gate are given in column two along with a code letter designating the associated decaying nuclide. Column three displays the energies of gamma-rays observed to be in coincidence with those falling in the energy gate. If the gamma-rays in column three are consistent with the appropriate decay scheme listed at the end of the table, they are so labeled. When the coincidence is tenuous the energy is given parenthetically. Antimony-133 gamma-rays are underlined.

The coincidence data were used in the identification of gamma-rays belonging to the ^{133}Sb decay, confirmation of their placement, and in the determination of the intensities of ^{133}Sb components in multiplets not resolved in the singles spectra. Illustrations of these uses will be presented in the following examples of interesting problems encountered during construction of the decay scheme.

Table 3.4 Gamma-gamma coincidences(*)

Gate (keV)	Known Gamma-rays in gate (keV)	Coincident Gamma-rays (keV)
104	103.6QP	697QP, 973QP
116	115R	297R, 1280R
135	135.1N	642N, 826N
139		382
145	145.0G	544G, 900G
151		
151E		
151L	150.6QP	697QP, 973QP, 1672QP
161	160.6	404, 950, 985, 1071, 1075, 1092, 1096, 1185, 1271, 1308, (1496)
183	182.3M	96, 119, 121, 332M, 370M,428, 512, 793M, 839M, 1019M, 1096
183E	182.3M	332M, 370M, 400, 460, 731, 743, 855, 921M, 936, 1019M, 1600M
183L		
192	192.5F	230F, 436F, 515, 552F, 781F
202	201.6	772, 862, 988, 1092, 1096, 1272, 1308, 1498
211		278, 435
214	213.9	882, 1096, 1166, 2580
223		180, 1015, 1180, 1705
230	229.2F	192F, 341F, 551F, 612, 743F
236	234.5	538, 882, 1979
247	246.8I 248.	272, 342I, 529I, 550I, 652I, 992I, 2333
252		247, 272, 817, 1097, 1232

Gate (keV)	Known Gamma-rays in gate (keV)	Coincident Gamma-rays (keV)
259	257.9QP 258.1X	292QP, 697, 817, 974, 1042QP, 1097, 1411, 1768X
261	261.0	312, 382, 439, 512, 697, 817, 839, 974, 1096, 1137, 1184, 1215, 1821, 2333
267	266.2	512, 689, 697, 809, 827, 974, 1096, 1185, 1307, 1500, 1992
275	274.2 274.2N	642N, 697, 822, 839, 943, 973, 1041, 1308, 1700, 2481
277	276.6P	190, 210, 437, 567, 697P, 817P, 1096, 1515P, 1825
279		436, 1304, 1472
286		122, 973, 2023
291		973, 989, 1098, 1309, 1889
293	293.8Q	145, 258, 440, 448, 740, 1042Q, 1182, 1348
297	297.0R 297.9	116R, 381, (421), (539), 559, 818, 1096, 1280R, 2256
297E	297.0R	512, 550R, 708R, 990, 1792R, 2322R
297L		
302	301.0N	641N, 932N
305		(342), 382, 511, 697, 819, 839, 886, 973, 1097, 1330, 1552
308	308.3	311, 382, 438, 512, 697, 818, 832, 839, 958, 974, 1049, 1061, 1097, 1111, 1135, 1205, 1242, 1274, 1398, 1426, 1492, 1553, 1731, 1780, 1939, 2011, 2133, 2448, (2680), 2695, 2882
312	312.1S 314.0J	242, 308, 408S, 473S, 612S, 732, (741)J (752)J, 844S, 932S, 1000S, 1021S, 1062S, 1252S, 1403S, 1827S, 1882S, 2132, 2231S, 2443

Gate (keV)	Known Gamma-rays in gate (keV)	Coincident Gamma-rays (keV)
326	324.2N	697, 885, 942N, 973, 1092, 1331
332	331.1L	182L, 792L, 839L, 973
332E	331.1L	451, 731L, 937L, 989, 993
332L	331.1L	182L, 697, 793L, 840L
337	336	1096, (1369), 2028, 2333
338		697, 899, 973, 1042
341	340.3I	231, 383G, 497, 512, 652I, 697, 819, 899I, 973, 1096, 1136, 1267, 1843
346		192, 312, 382, 512, 603, 697, 818, 839, 973, 1096, 1237, 1554, 1618, 1628, 2926, 3602, 3638
349	348.5M	468, 793M, 840M, 973, 1097, 1308
354	353.7QP	512, 638QP, 697, 819, 839, 974, 1096
357		674, 697, 974, 1081, 1096, 1185, 1216
364		171, 192, 973, 1637
369	368.4Q	382Q, 649, 697Q, 930, 973Q
380	380.7QP	697QP, 973QP, 1096, 1135QP
383	382.QP	139, 369QP, 523QP, 612QP, 697QP, 910, 930, 973QP, 1015, 1043, 1171, 1181Q, 1315, 1355, 1999, (2069), 2413, 2632QP
405	404.4	161, 312, 412, 423, 711, 828, 1091, 1097, 1251, 1256
408	407.62S	312S, 845S, 973, 1635
413	412.9	404, 839, 1098
423	422.2 423.4	404, 512, 688, 697, 810, 818, 827, 942, 973, 1097, 1185, 1237, 1308, 1730, 1822, 1994, 2333

Gate (keV)	Known Gamma-rays in gate (keV)	Coincident Gamma-rays (keV)
437	436.6QP	192, 211, 309, 380QP, 446QP, 498QP, 512, 698P, 778, 974P, 1092, 1096, 1457, 1554,(1948)QP, 2011, 2131, 2200, 2320, 2480
441	441.0 441.0Q	293Q, 340, 697, 741Q, 818, 840, 974, 1035Q, 1043Q, 1050, 1098, 1267, 1308
445	445.0P	382, 438P, 511, 697, 795, 818, 839, 974, 1096, 1135, 1576
450		1228
456	455.5	382, 511, 698, 818, 839, 974, 1097, 1238
463	463.35	382, 512, 698, 818, 839, 974, 1097, 1268, 1438, 1731, 2333
469	468.0ML	331, 350, 792ML, 840ML, 1093, 1143
497	497.0Q	812, 850, 929Q, 1055Q, 1171Q, 1239, 1380, 1689
511	511.Q	189, 308, 511, 602, 697, 832, 966, 974, 1042Q, 1097, 1133, 1267, 1735, 1823, 1908, 2245, 3852
511E		973, 1019
513		185, 308, 312, 440, 511, 602, 832, 973, 1042, 1097, 1333, 1395, 1733, 2245
518		440, 974, 1015
523	523.3QP	382QP, 496, 697QP, (973)QP
528		602, 673, 973
539	538.7	297, 754, 819, 1097, 1118, 1308, 1879
545		978
550		750, 973, 1212
561	560.9QP	636QP, 979

Gate (keV)	Known Gamma-rays in gate (keV)	Coincident Gamma-rays (keV)
570		
591	591.0QP	973QP, 1198QP
591E		151
603	602. 602.Z	346, 512, 529Z, 671, 882, 909Z, 974, 1098, 1131Z, 1202Z, 1222Z, 1393, 1618, 1636, 1710, 1854, 1860, 1979, 2103, 2270, 2332, 3053, 3434
612	611.53QP	382QP, 697QP, 792, 818, 839, 975QP, 1097
625	625.3N	642N
632	632.3	(201), 482, 849, 866, 1022, 1028, 1068, 1098, 1312
636	635.9QP	353QP, 561QP, 697QP, 975QP, 1153QP, 1532, 1647QP, 1766, 1896QP, 1996, 2127, 2196
643	642.4N	136N, 275N, 301N, 626N, 758, 826N, 932, 1236N, 1759N, 1822, 1857N, 1958N, 1969, 2119N, (2150)
648	647.9 647.9M 647.9T	(290), 793M, 839M, 912T, (951)M, 1268, 1792
648E		637
658		(182), (273), (300), (433), (539), 760, 944, 974, 1032, 1198, (1668), 2571
680	679.8	202, 382, 698, 818, 839, (841), 975, 1098, 1581
688	687.5	267, 423, (697), (732), (766), (810), (870), 1308, (1705)
691	691.1QP	556, 822QP, (882), 939, 976QP, 1098QP, (1102), (1220), (1824), 1978, (2222), 2921QP

Gate (keV)	Known Gamma-rays in gate (keV)	Coincident Gamma-rays (keV)
697	697.0QP	103QP, 278, (358), 369, 382QP, 438QP, 512, 523, 611, 818QP, 882, 930, 938, 975QP, 1079, 1093QP, (1172), 1184, 1216, 1301, 1344QP, (1356), (1504), 1541, 1575,1792, 1890, (2190), 2384QP, 2635, 2666, 2704, 2712QP, (2765), 2800, (2885)
697E	697.02QP	151QP, 353QP, (492), 512, 560, 592, 637QP, 929, 991QP, 1001, 1152, 1199QP, 1439, 1545, 1648QP, 1790, 1856, 1966, 2006, 2117, 2169, 2194, 2282, 2782, 2831, (2869), 2899
697L		977, 1098
707		
720	719.6S	(843)S, 973, 1098, (1185)
724		818, 973
727	726.5N	943N, (973), (1098)
732		312, (975), (1439)
741	740.Q	293, 441Q, 697, 819, 1042
744	743.2F 743.2J	230F, (314)J, (754)J, (1040)J
750	748.7M	(454), (551), (697), 840M, 931
755	754.0J	(272), (297), (314)J, 743J, 973, (1100)
761		(384), (433), 658, 698, 974, 1162
766		(210), 697, (973), (1552)
774		881, 978, 1097, (1220), 1979
777	776.4QP	(197), 439QP, 975QP, 1135QP
781		192, (1098)
788	786.9S	931S, (1659), (1900)

Gate (keV)	Known Gamma-rays in gate (keV)	Coincident Gamma-rays (keV)
794	793.5ML	182ML, 331L, 349M, 469L, (508)L, (649)M, 698M, 819M, 840ML, 922M, (942), 1019M, 1101M, 1201M, (1268), (1418), 1600M
794E	793.5ML	331L, 456, 649, (688), 732, 936, 1019M, 1601M
794L		973
799		973, 1075, 1208, 1266, 1506, 1766, 2141, 2181, 2472
810	808.9	(260), 267, 422, 1186, 1441, 1948
814	813.3QP	498, 512, 699QP, 812QP, 839, 975QP, 1098,1846, 1989, 2071, (2100), 2589, (2594)
818	816.8 816.8QP 816.8M	278QP, 299, 697QP, 793M, 838, 881, 975QP, 1098, (1401), (1641), (1672), (1801), (1819), 1889, 1932, 1978
818E		(510), (636), 975, 1096
818L		(697)
832	832.1C	512, 824C, 1062C, (1244), 1378C, 1668C, 2130, 2242, 2297, 2512, 2753C, 2809, 3022, 3293, (3294), 3303C, 3318C, 3360, 3533C,(3571)C, (3811)C
837	836.9	(182), (229), 274, (308), (404), (412), (620), (649), 793, 818, 1098, (1268), 1307, 1581, 1914Sum
837E		
837L		(697)
840	839.49ML	182ML, 331L, 349M, 469ML, (625), (649)M, (680)L, 699M, 749M, 793ML, 818M, 1019, 1101M, 1142ML, 1202M, 1582, 1600M, 1896M, 1929, 2119, (3004)
840E	839.49ML	(163), (259)L, 332, 649, 732L, (921)M, (936)L, 1019M, (1601)M

Gate (keV)	Known Gamma-rays in gate (keV)	Coincident Gamma-rays (keV)
840L		(361), (973)
845	844.3S	312S, 409S, (635), (720)S, 943, 976, 1439, (1541)
850		(491), 1171, 1670, (1946)
864	864.0 864.0[illegible]	632, 699, 912T, 1098, (1136), 1582), 1730
881	881.0 881.02QP	(233), (509), 602, 693, 697QP, 772, 819, 975QP, (1049), (1066), 1086, 1098, (1339), 1502, 1576, (1582), (1796), (1948)
899	(898.7)G (898.7)I	(146)G, (178), (188), 341I, (383), (978), (1553)
908	907.0P	603, 698QP, 839, 973QP, (1136)QP, (1947)
913	912.[illegible]	649T, 864T, (1140), (1682)
921	920.9M	(182)M, 793M, 840M
928	927.67Q	312, 369Q, 382Q, 498Q, (612), 698, 912, 975, (1015), (1093), (1139), (1148), (1307), 1661, 1950
931	930.5QP 930.5S	228, 312S, 474S, 698QP, 788S, 943, 974QP, (1122), 301, 642, 943
933	932.8N	301N, 642N, 943N
936	936.3QP 936.8QP	692QP, 697QP, 974QP
943	943N	273, 325N, 659, 729N, 844, 934N, (1098), 1125N, (1392)N, 1458N, 1519, 1557N, 1575, 1610N, (1658), 1854
943E		
943L		(974)
948		(838), 1032, 1250

Gate (keV)	Known Gamma-rays in gate (keV)	Coincident Gamma-rays (keV)
953	953.3	(852), 1308, (1582)
957	956.9	308, (1097), (1778)
964	963.8Q	(512), (1042)Q, 1554
970		698, 973, (1097), (1111), (1253)
974	974.23QP	103, 278, 369, 382, 438, 445, 500, 511, 612, 692QP, 697QP, 778, 814QP, 818, (823), 882, 9031, 938, 977, (1003), 1094QP, 1135QP, 1184, 1215, 1278, 1301, 1322, 1343QP, 1381, 1391, 1422, 1516QP, 1542, 1575, 1636, 1781, 1790QP, 1890, 1847, (2022), (2120), (2271), 2386QP, 2479, 2517, (2539), 2589QP, 2634, 2663, 2711, (2746), 2801, (2843), 2883, 2913, 2920QP, (3101), (3408)QP, 3460, 3558, 3610QP
974E	974.23QP	152QP, 353QP, 512, 561, 592, 637QP, (731), 928, 992QP, 1081, 1153, 1198QP, 1333, 1438QP, 1484, 1648Qg, 1689, (1765), (1771), 1790, 1858, 2119, 2282, 2832
974L		1097
987	987.2	(510), (749), 1272
990	989.6QP 992.1I	248I, 422, 698QP, 974QP, 1058, (1097), (1129), 1272, (1473)
996		240, (973)
1001	1000.7S	312S, (818)
1009		1238, 1438
1015		498, (508), 698, 1172, (1308), 1402, 1670
1018	1017.8M	182M, 793M, 840M, (1184)
1022	1021.4 1021.4S	312S, (510), 632, 637, 794, 1098, 1730, 1932

Gate (keV)	Known Gamma-rays in gate (keV)	Coincident Gamma-rays (keV)
1027	1026.8	(494), (512), 632, (642), (693), 1042, 1098, 1221, 1268, 1730, 1932
1042	1042.1Q	(259), 273, 293Q, 339, 382, 441, 450, 494, 512, 552, 741, (911), 965Q, 1029, (1038)Q, (1092), (1349), 1478, (1619)
1049	1048.5	309, 441, (1268), 1400, 1709
1057	1056.4Q	(497)Q, 991, (1696)
1061	1061. 1062.0C 1062.0S	308, 312S, (439), 832C, (1636), (2475)C, (3149)
1064	1064.6	308
1066	1065.5	(512), 632, 1098, (1267), 1730, (1979)
1075		698, 799, 818, 974, (2156)
1080		(1088)
1080E		
1080L		(400), 698, 974
1084		881, 1098, (1778), 1979
1089		161, (384), 404, 698, 818, 974, (988), 1081, 1098, 1183
1093	1092.1 1093.3QP	382, 404, 498, 501, 698QP, 818, 838, 928, 974QP, 1042, 1096, 1382, 1428, 1946
1096	1096.22 1098.QP	(161), 298, 404, 412, 422, 512, 539, 632, 680, 691QP, (772), 818, 825, 839, 882, 944QP, 1028, 1067, (1092), 1118, 1149, 1231, 1239, 1251, (1278), 1486, 1499, 1574, 1658, 1661, 1700, 1788, 1911, 1948, 1966, 2010
1112	1110.8 1113.	973, (1096), (1268), 1308, 1642
1116	1115.2	539, (880), 1098, (1333), 1643

Gate (keV)	Known Gamma-rays in gate (keV)	Coincident Gamma-rays (keV)
1116E		
1116L		
1124	1123.5N	(181), (277), (301)N, (642)N, 698, 943N, 975, 1582
1126E		
1129		(498), 512, 602, 781, 1202, 1208, 1556
1134	1133.71QP	380QP, (439), 446QP, 500QP, (638), 656, 696, 778, 909, 975, (1104)QP, (1322), 1382, (1409), 1432, 1457, 1523, 1578QP, 1949QP, 2021QP, (2148), (2200), (2308)QP, (2363), 2479
1143	1141.8M	469, 840M, 1839
1147		
1152	1151.9QP 1151.9	(205), (374), 637QP, (697), (966), 975, 1642, (1789)
1156	1158QP	974QP, 1200QP, (1268), (1321)
1162		509, 698, 761, 974, (1096), (1158)
1167	1166.4	(161), (215), (382), (405), (429), 472, (502), (512), 1092, 1171, (1251), 1353, 1423, (1922)
1171	1170.5Q	(182), (369)Q, 382, 498Q, 698, 850, 974, 1016, 1168
1182	1181.5Q	(222), 382Q, (698)Q, 1238, 1354
1184	1183.4	(161), (267), 358, 422, 650, 698, 810, 975, 1072, 1089, (1202), 1235, (1482)
1189	1188.8	1272
1192		
1197	1196.7QP	591QP, 697QP, 973QP, 1158QP, (1552)

Gate (keV)	Known Gamma-rays in gate (keV)	Coincident Gamma-rays (keV)
1201		(511), (531), 602, 793, 840, (973), 1132, 1553, 1854
1203	1202.7	309, (697), (802), 974, (1072), 1098, 1220, (1246), (1269), 1553, 1778
1208	1207.3N	(382), 670N, 698, 861, 974, (1042), 1098, (1129), (1268)
1214	1213.5QP	(328), 697QP, 973QP, 1098, (1230), 1268, (1532)
1219		697, 973, 1029, 1098, 1200, 1204, 1242, 1552
1224		(302), (333), 642, 1184, (1490), (1632)
1227		450, (697), 973, 1097, (1898), (2032), 2083, 2189
1234E		
1236	1233.4N 1235.9	422, 455, 642N, 976, 1011, 1098, 1182, 1184, (1226), 1492
1241		698, (816), 974, 1222
1241E		
1250	1249.6	404, (698), 949, 1033, 1097
1253	1252.4S	312S, (1552)
1253E		
1257		
1265	1265.3	441, 463, 511, 649, (757), (837), 1028, 1049, 1179, 1216, (1258), (1266), (1275), 1329, 1492, 1530, 1739, 1777, 1797, 1840, 1900
1271	1271.4	310, 608, (974), 989, 1064, 1190, (1400), 1438, 1457
1275	1274.6QP	974QP, 1640QP, 2128, (2168)

Gate (keV)	Known Gamma-rays in gate (keV)	Coincident Gamma-rays (keV)
1279	1279.2R	116R, 298R, (1554)
1279E	1279.2R	(512), 708R
1279L		
1283		
1300	1299.9QP	698QP, 840, 975QP
1305	1305.1	266, 273, 422, 571, 687, 735, 837, 952, 1111
1312	1312.9	632, (973), (1552), 1730
1322		(382), 698, (794), 974, 1098, 1134, (1555)
1328	1327.7	(306), (639), 1268
1333	1333	(382), 697, 974, (1029), (1098), (1112), 1269, 1730
1338		697, 974, (1098)
1344	1343.9 1343.9QP	(698)QP, (782), (974)QP, (1096), (1112) (1489)
1354		382, (698), (1182), 1312, (1490)
1368		(512), 1429, 1637, 1797, (2789)
1376	1377.0C	(306), 831C, (977), (1379)C, 2130C
1381		(688), (697), 974, 1098, 1136, 1209, (1305)
1390		(189), 602, 944, 974, 1526, 1566, (1731)
1399	1398.5	309, (975), 1050, (1458), (1489), (1643)
1402		1016
1410		258, (991), (1015), (1096)

Gate (keV)	Known Gamma-rays in gate (keV)	Coincident Gamma-rays (keV)
1415		(698), 974, 1097
1416		
1420		1268, 1646
1421	1420.6	(308), (603), 976, 1168, 1308
1426	1425.1	(241), 309, (1092), 1370
1436	1436QP	462, 698QP, 731, (844), 976QP, 1011, 1273
1444		(839)
1448		
1455	1454.9	(239), (243), (872), 974, 1098, (1268), 1272
1456		
1463		(1092), 1642
1470		(231), (381), (644), 698, 975, 1029, 1098, (1113)
1481		(636), (793), 974, 1097, 1183
1484	1484.1	(698), 975, 1098, (1267)
1490	1489.5 1490.0	309, (502), (958), (977), (1096), 1244, 1268, 1553
1497	1496.5	(202), (582), 1098
1503		(445), (699), 882, (974)
1514	1513.7QP	277QP, (849), 975QP, (1212)
1522		(975), 1136
1530	1529.1	1268
1540	1540QP	697QP, 975QP
1544		(739), 855

Gate (keV)	Known Gamma-rays in gate (keV)	Coincident Gamma-rays (keV)
1544E		
1552	1552.1	(178), (890), 1204, 1490, 1554, 1612
1552L		
1560		(308), (642), 698, (944), (973), (1098)
1565		(625), (642), (976), (2750)
1574	1573.4QP	(445)QP, 698, 882, 943, 975QP, 1098, 1135QP
1574L		
1580	1579.4 1580.8Q	498Q, (539), (753), 839, 1128, (1575)
1594		(799)
1598		181, 794, (839)
1609		854, 1553
1615		(439), 602, 644, (950), (1136), (1182), (1639)
1634	1633.9QP	(182), (364), (408), (602), (929), 974QP, (1118), 1370
1634L		(699)
1642	1641.5	(637), (852), 940, (973), 1114, 1154, (1349), (1402), 1421
1645	1644.6QP	636QP, (695), 697, (1113), (1117)
1654	1654.2	1098
1659	1658.6	(378), (442), (697), (884), 1098
1666	1664.9C	832C, (973)
1666E		
1666L		

Gate (keV)	Known Gamma-rays in gate (keV)	Coincident Gamma-rays (keV)
1668		(665), (782), 832, 850, (921), (973), 1016
1668L		
1672		(372), (382), 816, (974), (1096), 1216
1672E		150, 636, 991
1672L		698
1686		(242), (425), (852)
1686E		
1693		
1698	1697.9	(973), 1098
1706	1705.5	(498), (602), (698), 1050
1722		(377), (382), (831), (1097)
1729	1728.6	482, (852), 865, 1024, 1028, 1068, (1278), 1314, 1333, (1437)
1729E		
1729L		(698)
1763		(463), 637, (698), 976
1763E		
1767		569, (752), (973)
1767E		
1776	1775.8	(280), 310, 699, (974), 1097, 1205, 1268
1780		(192), (636), 698, 974, (1136), 1268
1795	1794.9	309, (381), (510), (698), 710, 974, 1098, (1135), 1268, 1370

Gate (keV)	Known Gamma-rays in gate (keV)	Coincident Gamma-rays (keV)
1544E		
1552	1552.1	(178), (890), 1204, 1490, 1554, 1612
1552L		
1560		(308), (642), 698, (944), (973), (1098)
1565		(625), (642), (976), (2750)
1574	1573.4QP	(445)QP, 698, 882, 943, 975QP, 1098, 1135QP
1574L		
1580	1579.4 1580.8Q	498Q, (539), (753), 839, 1128, (1575)
1594		(799)
1598		181, 794, (839)
1609		854, 1553
1615		(439), 602, 644, (950), (1136), (1182), (1639)
1634	1633.9QP	(182), (364), (408), (602), (929), 974QP, (1118), 1370
1634L		(699)
1642	1641.5	(637), (852), 940, (973), 1114, 1154, (1349), (1402), 1421
1645	1644.6QP	636QP, (695), 697, (1113), (1117)
1654	1654.2	1098
1659	1658.6	(378), (442), (697), (884), 1098
1666	1664.9C	832C, (973)
1666E		
1666L		

Gate (keV)	Known Gamma-rays in gate (keV)	Coincident Gamma-rays (keV)
1668		(665), (782), 832, 850, (921), (973), 1016
1668L		
1672		(372), (382), 816, (974), (1096), 1216
1672E		150, 636, 991
1672L		698
1686		(242), (425), (852)
1686E		
1693		
1698	1697.9	(973), 1098
1706	1705.5	(498), (602), (698), 1050
1722		(377), (382), (831), (1097)
1729	1728.6	482, (852), 865, 1024, 1028, 1068, (1278), 1314, 1333, (1437)
1729E		
1729L		(698)
1763		(463), 637, (698), 976
1763E		
1767		569, (752), (973)
1767E		
1776	1775.8	(280), 310, 699, (974), 1097, 1205, 1268
1780		(192), (636), 698, 974, (1136), 1268
1795	1794.9	309, (381), (510), (698), 710, 974, 1098, (1135), 1268, 1370

Gate (keV)	Known Gamma-rays in gate (keV)	Coincident Gamma-rays (keV)
1807		309, 312, (512), (539), (603), (634), 698, (834), (841), (853), (881), 974, 1098, 1134
1815		(292), (697), (973)
1822		642, 692
1838		1142, 1268
1850		309, (497), 698, 974
1854		602, 642, 942
1862		(310)
1867		693
1877	1877.3	539
1882		142, 312
1887		309, 382, 698, 818, 974, 1516
1895	1896QP	637QP, (788), (818), 840, 1228, 1268
1895E		
1909	1908.6	309, 642, 974, 1098
1918		1142
1927		602, 974
1931		309, 818, 935, 973, 1022
1944	1944.4	(485), (511), (521), (590), 975, 1098, (1134), (1670)
1944E		
1944L		
1956		974, 1097, (1670)
1965	1964.7	316, 642, 1098

Gate (keV)	Known Gamma-rays in gate (keV)	Coincident Gamma-rays (keV)
1965E		
1965L		698
1970		
1977	1976.7	222, 235, (382), 603, 692, 772, 818, 1065, 1086
1983		235, 309, (437), (538), 603, 692, 697, 772, 818, (842), 975, 1066, 1086, 1098
1989		382, 812
1994	1992.3	262, 422
2019	2018.6QP	(312), (692), 698QP, (942), 973QP, 1136QP
2031		1231
2042		974, 1231
2048		
2054		(697), (922)
2069		(495), 974, (1096)
2073		818, (1790)
2084		1228
2103		602, 813
2112		(182), (602), (831), 974
2119		
2129	2129C	309, (339), (639), 698, 832C, 975, 1134, 1276, 1377C
2135	2133.6	309, 312, (600), (698), 973
2148	2148.6QP	280, (341), (639), (698)QP, 1134QP
2170		296, 309, (814), 1202, 1278

Gate (keV)	Known Gamma-rays in gate (keV)	Coincident Gamma-rays (keV)
2183		235, 309, 799, (1392)
2189		(230), (235), 309, (602), 698, (795), 974, 1228
2197		309, (382), 439, 639, (658), 698, 974, 1032, 1134
2197E		
2209	2209C	(602), 832C
2221		192, (309), (312), (439), (512), 602, 697, (832), 974, (1135)
2229		(381), (439)
2239		
2281		280, (312), 698, 973
2246		
2271		603, 698, 973
2310	2310.QP	974QP, (1062), 1135QP
2320		438, 976
2323		699, (832)
2334	2332.7	(249), 261, 338, 422, 462, 602, 709, 758, 832, (912), 974
2342		(832), (976)
2365		400, 441, 974, 1135, (1359), 1524
2384	2384QP	698QP, 976QP, (1012)
2384E		
2401		
2401E		
2416		(382), 697, 833, 976

Gate (keV)	Known Gamma-rays in gate (keV)	Coincident Gamma-rays (keV)
2416L		
2431	2431QP	977QP
2447	2446.5	309
2457	2457QP	975QP
2473	2473C	(1062)C
2478	2479.0QP	312, 436QP, 698QP, 975QP, 1134QP
2478E		
2491		
2497		
2507		1138
2515		(242), 602, 698, 832, 975
2539		347, 832, 975
2564		(698)
2571		659
2582		(308), (346), (513), (832), 974
2588	2588.3QP	813, 975QP, 1790Sum
2588E		
2588L		
2596	2596QP	974QP
2605	2605QP	698QP, 975QP
2634	2633.8QP	383QP, 698QP, 975QP
2655		(268), (312), (506), 698, 974
2680	2680	309
2698	2698	309, (697), (975)

Gate (keV)	Known Gamma-rays in gate (keV)	Coincident Gamma-rays (keV)
2711	2711QP	698QP, 974QP
2725	2725C	(832)C
2744	2744QP	974QP
2755	2755C	832C, (974), (1060), 1566
2755E		
2755L		
2764		698, 1061
2782E		
2800		(698), (812), (974), 1790Sum
2831		831
2831E		
2841		
2872		512, 832, 974
2884	2884	308, (561), (697), 974
2913	2913QP	974QP
2920	2920QP	(692)QP, 975QP
2926		346, (439), (1138)
3024		832, (1062)
3041		832
3049	3049QP	973QP
3054		602, (832), (974)
3101		832, 975
3115		(831)
3149	3149C	(832)C, 1062C

Gate (keV)	Known Gamma-rays in gate (keV)	Coincident Gamma-rays (keV)
3159		
3170		(832), (975)
3182		
3205	3205C	(832)C
3217		
3223		
3253		
3270		(832)
3295	3295C	(832)C
3305	3305C	832C
3317	3317C	832C
3330	3331QP	(831), 974QP
3341		(512), (602)
3353	3353QP	974QP
3362	3362C	(832)C, 1062C
3370		602
3384		
3408	3408QP	974QP
3461		974
3484		
3504	3504C	832C
3535	3535C	832C
3559	3559QP	976QP
3601		(345), (832)

Gate (keV)	Known Gamma-rays in gate (keV)	Coincident Gamma-rays (keV)
3611	3611QP	(439), 974QP
3625		(512)
3638		346, 439
3643		
3664		
3701		
3789		
3808		
3813	3813C	832C
4011		

(*)

1) The energies given in the first column are the approximate centroids of the start detector energy gates.

2) Except those gates ending in E or L, slices from weak peaks were taken with the time gate set at FWTM of the timing peak and FWHM for strong peaks. Gates with an E(L) appended had a time window containing times shorter (longer)than those represented by the timing peak. Therefore, a gamma-ray that deexcites a delayed level would have the gamma-rays feeding that level appearing in its E gate. Likewise, a gamma-ray feeding a delayed level would have the gamma-rays deexciting that level appear in its L gate.

3) Gamma-rays belonging to ^{133}Sb decay are underlined. Other nuclides are identified using the following code:

^{85}As	-	A
^{89}Rb	-	B
^{90}Rb	-	C
$^{129}Sn^{g}$	-	D
$^{129}Sn^{m}$	-	E
$^{130}Sn^{g}$	-	F
$^{130}Sn^{m}$	-	G
^{131}Sn	-	H
^{132}Sn	-	I
$^{128}Sb^{m}$	-	J
^{129}Sb	-	K
$^{130}Sb^{g}$	-	L
$^{130}Sb^{m}$	-	M
^{131}Sb	-	N
$^{132}Sb^{g}$	-	P
$^{132}Sb^{m}$	-	Q
^{134}Sb	-	R
$^{133}Te^{g}$	-	S
$^{133}Te^{m}$	-	T
^{134}Te	-	U
^{135}Te	-	V
^{135}I	-	W
^{138}Xe	-	X
^{138}Cs	-	Y
^{140}Cs	-	Z

4) Coincident gamma-rays given in parenthesis are weak coincidences.

5) Coincident gamma-ray energies may have errors as large as 3 keV.

1096 keV

Figure 3.28 shows the GAMANAL fit of the 1093 - 1096.22 - 1098 keV multiplet. The 1096.22 gamma-rays has been assigned to the ^{133}Sb beta-decay while the 1098 keV gamma-ray was associated with the $^{132}Sb^{m}$ beta-decay. From the coincidence information, the 1093 gamma-ray was found to be a doublet with a 1092.1 component belonging to the ^{133}Sb decay and a 1093.3 keV component belonging to $^{132}Sb^{m}$. The 1092.1 transition has been placed between the 2593 keV and 1501 keV ^{133}Te levels on the basis of its coincidences with the 404.37 keV, 1096.22 keV and the 1166.4 keV gamma-rays (see figures 3.29-3.31).

The 1092.1 keV gamma-ray appears clearly in the 1166 keV slice as shown in figure 3.32. The 1096.22 keV gamma-ray has been assigned to the ^{133}Sb decay on the basis of its intensity, its 2.7 min half-life, its presence in the A=133 and its absence in the A=132 LOHENGRIN spectra. The 1098 keV and 1093.3 keV gamma-rays both deexcite the 2764.4 keV level in $^{132}Sb^{g}$ and feed the 1665.3 keV and 1671.31 keV levels, respectively. This requires the 1098 keV gamma-ray be in coincidence with the 691.08 keV gamma-ray as shown in figure 3.33 and the 1093.3 keV gamma-ray to appear in the 697.08 slice as shown in figure 3.34. The 1092.1 was chosen to be the lowest energy component of the multiplet on the basis of its energy in the 1166 keV slice relative to the $^{132}Sb^{m}$ gamma-ray's energy in the 697 keV slice. The intensities of each component were obtained from GAMANAL peak fits. Relative intensities of the unresolved components were approximated by the peak areas in the coincidence spectra and an approximate efficiency curve. The efficiency curve was defined from

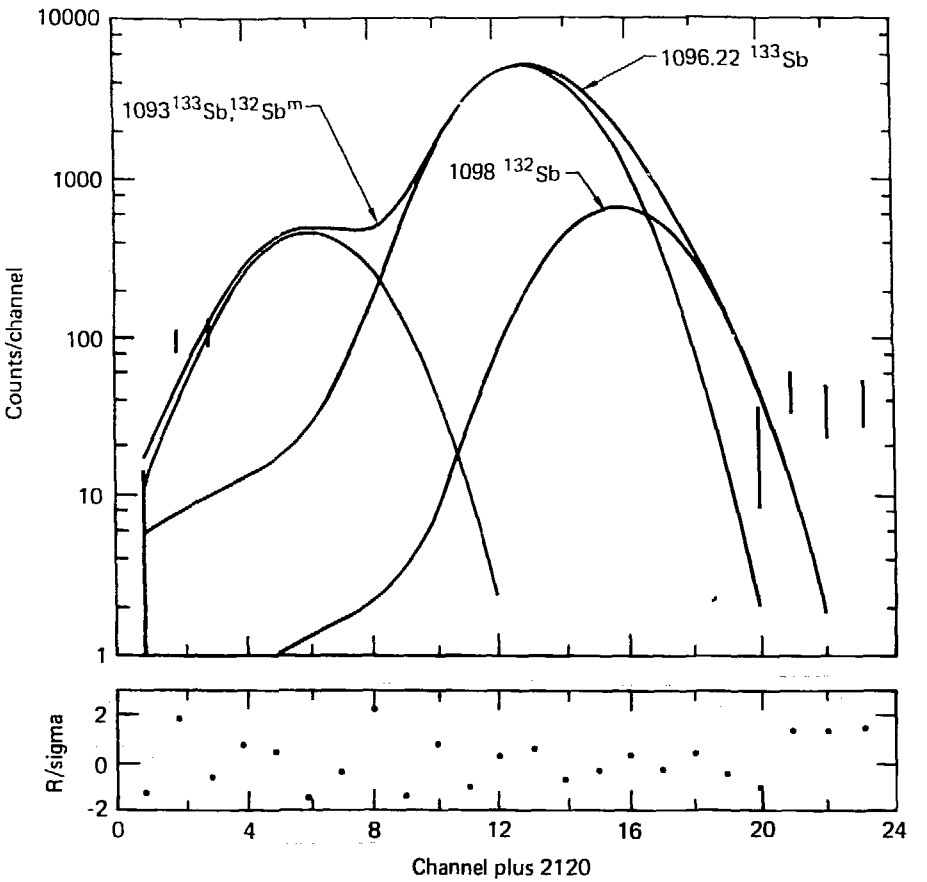

Figure 3.28. The GAMANAL fit to the 1092-1093-1096-1098 multiplet.

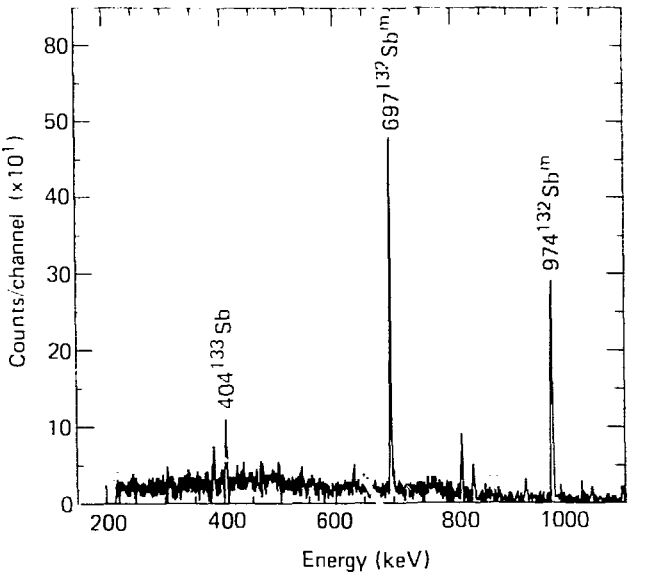

Figure 3.29. A portion of the 1093 keV slice showing coincidences with the 404 keV ^{133}Sb gamma ray and the 697 keV and 974 keV $^{132}Sb^{m}$ gamma rays.

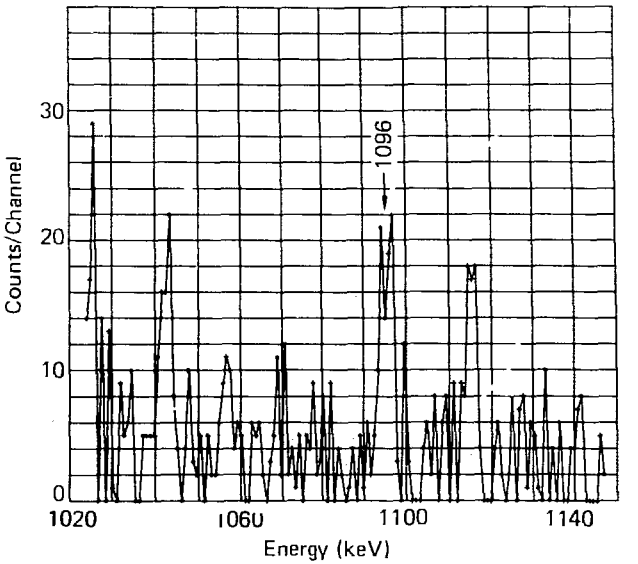

Figure 3.30. Part of the 1093 keV slice showing the 1092/1096 ^{133}Sb coincidence.

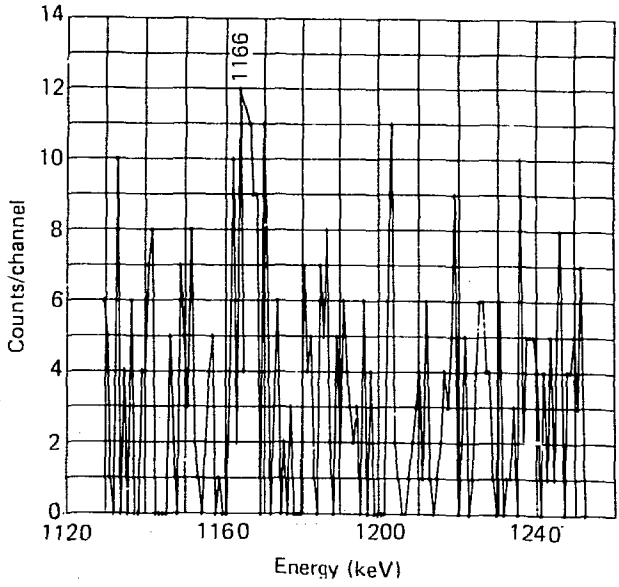

Figure 3.31. The ^{133}Sb 1166 keV gamma-ray appearing in the 1092 keV slice.

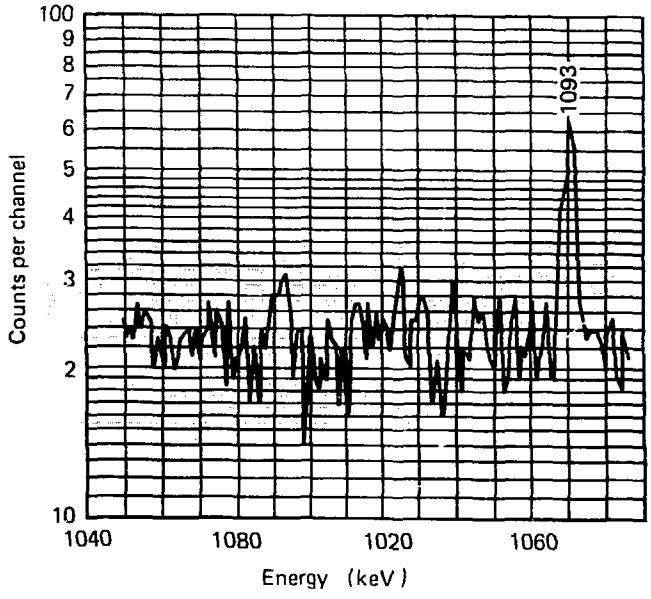

Figure 3.32. The 1093 keV peak in the 1166 keV slice.

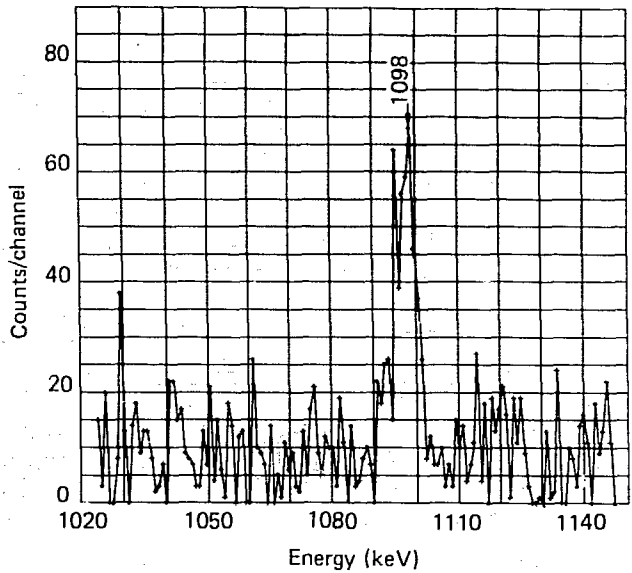

Figure 3.33. The $^{132}Sb^{m}$ 1098 keV gamma-ray in the 691 keV slice.

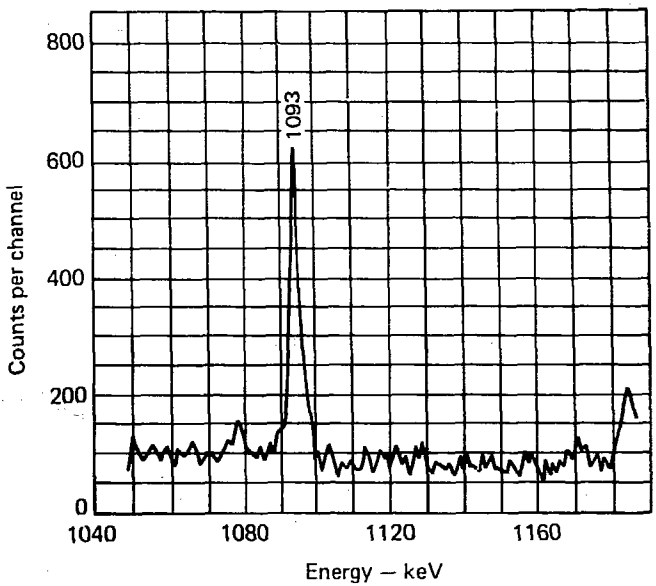

Figure 3.34. The $^{132}Sb^{m}$ 1093 keV gamma-ray in the 697 keV slice.

10 million ^{56}Co coincidence events by assuming identical detector efficiencies and assuming there was no angular correlation between coincident gamma-rays.

817 keV

Coincidence data indicate the peak at 816.8 keV is a triplet. The portion of the 817 keV coincidence slice in figure 3.35 shows $^{132}Sb^{g}$ peaks at 277 keV, 696 keV and 974 keV, ^{133}Sb peaks at 298 keV, 680 keV, and 837 keV, and the 793 keV peak belonging to $^{130}Sb^{m}$.

The intensity of the ^{133}Sb component was determined from the coincidence data using an approximate relative efficiency curve.

An intensity of 390 (39% of the 1096 photopeak intensity for the ^{133}Sb 817 keV component) was found by comparison with the intensities of the 837 keV and 632 keV peaks in the 1096 keV slice.

836 - 839 keV Doublet

The GAMANAL fit of the 836.88 keV - 839.49 keV doublet is shown in figure 3.36. The 836.88 keV component has been assigned to the ^{133}Sb decay on the basis of its presence in the A=133 and its absence in the A=132 LOHENGRIN spectra, its 2.4 min half-life, and certain coincidence data. It has been placed between the 2750.1 keV and 1913.3 keV levels in the ^{133}Sb decay scheme because it was observed to be in coincidence with the 1579.4, 816.5, 647.9, 412.9, and 273.1 keV gammas that de-excite the 1913.3 keV level (figures 3.37 and 3.38). A 839.4 keV gamma-ray has been reported in the $^{130}Sb^{m}$ decay scheme[68] and this identification has been confirmed from its

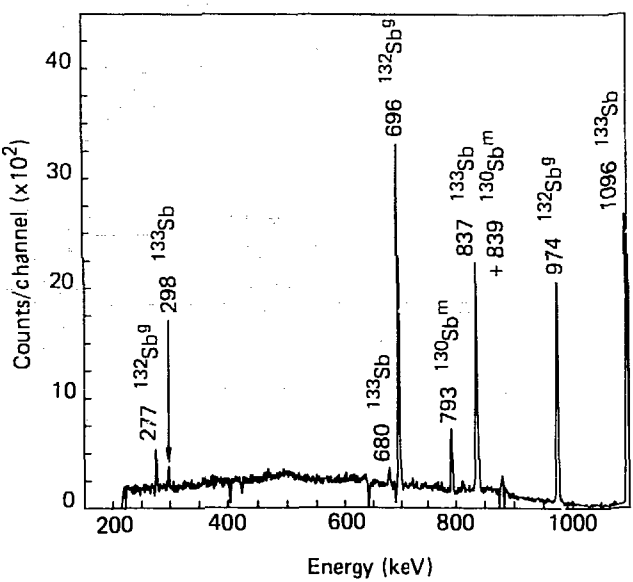

Figure 3.35. The 817 keV slice showing coincidences with ^{133}Sb peaks: 680 keV, 1096 keV, and 936 keV; $^{132}Sb^{g}$ peaks: 277 keV, 696 keV, and 974 keV; and $^{130}Sb^{m}$ peaks: 793 keV and 839 keV.

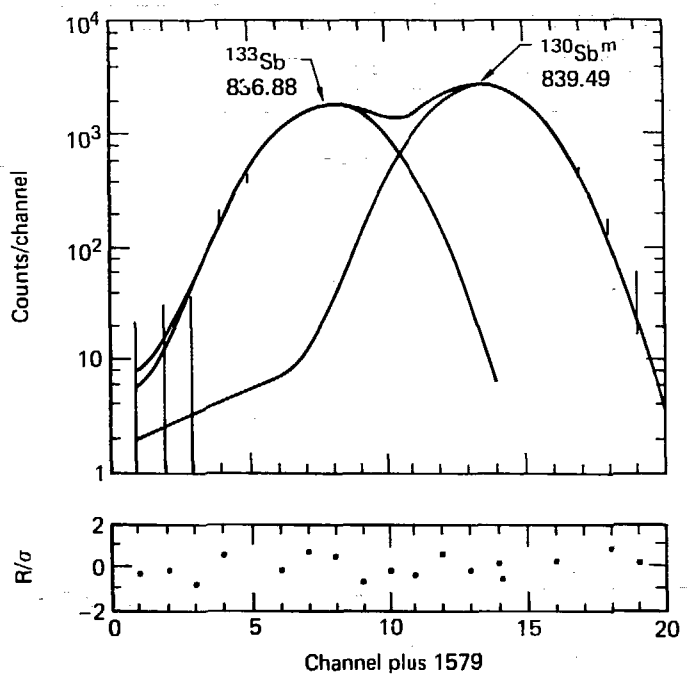

Figure 3.36. GAMANAL fit of the 836.88 - 839.49 doublet.

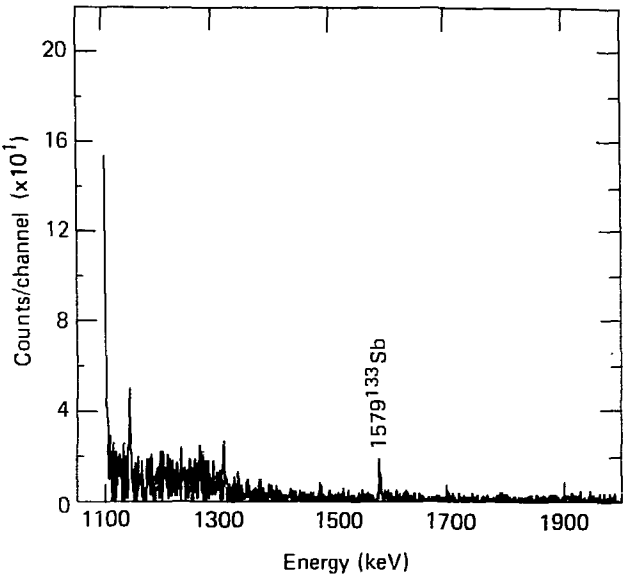

Figure 3.37. Part of the 836 keV slice showing the 836/1579 coincidence.

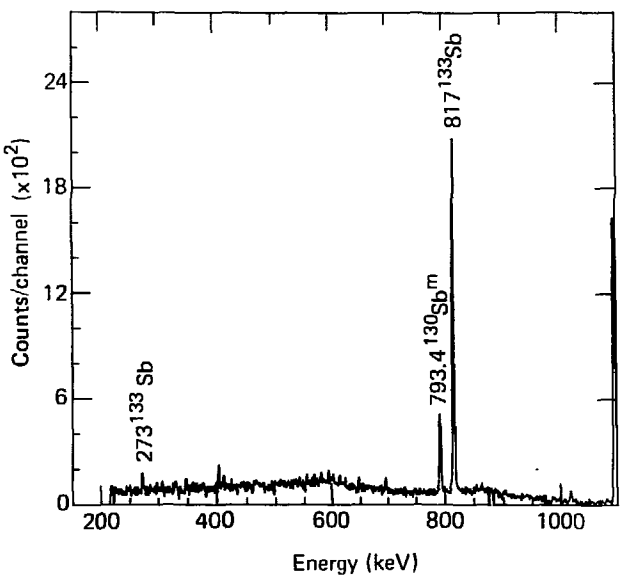

Figure 3.38. The 836 keV slice showing coincidences with the 273 keV and the 817 keV ^{133}Sb gamma rays and a 793 keV $^{130}Sb^{m}$ gamma ray.

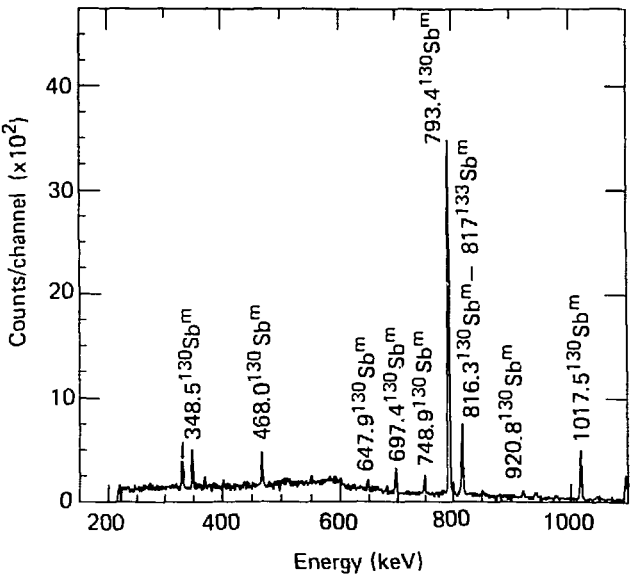

Figure 3.39. A portion of the 839 keV slice showing several coincidences with $^{130}Sb^{m}$ gamma rays.

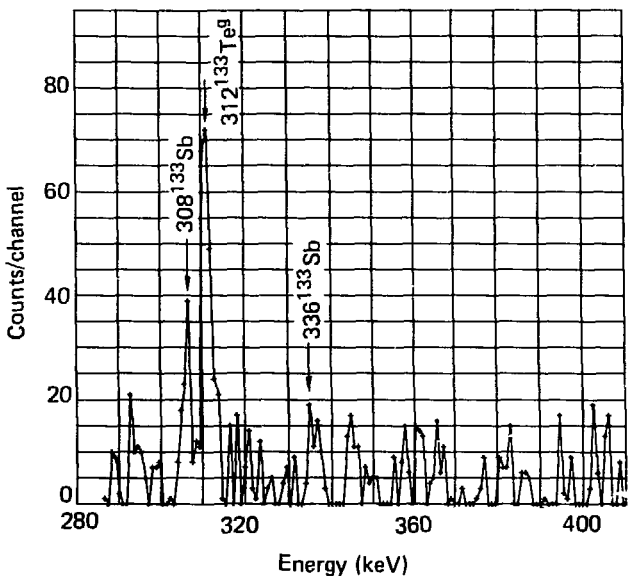

Figure 3.40. The 308/1062 and a possible 336/1062 coincidence are seen in this portion of the 1062 keV slice. The 1062/312 $^{133}Te^{g}$ coincidence is also seen.

coincidences with the gamma-rays labeled in figure 3.39. Relative intensities of the 836 keV - 839 keV component were taken from the GAMANAL fit.

1062

The peak labeled 1062 keV in the singles spectrum was found to be an unresolved doublet from its coincidences with ^{133}Sb and $^{133}Te^{g}$ gamma-rays. Accordingly, a 1061 keV gamma-ray was placed in the ^{133}Sb decay scheme between the 1369 keV level and the 308 keV level on the basis of the 308 keV/1061 keV coincidence and a possible 336 keV/1061 keV coincidence (figure 3.40). A 1061.6 keV gamma-ray has been found by Meyer in the $^{133}Te^{g}$ decay[91] and was confirmed here by the 1062 keV/312 keV coincidence. The intensity of the $^{133}Te^{g}$ component was estimated from the relative efficiency curve to be .9%.

1489

The 1489.5 keV peak in the singles spectrum has been determined from the coincidence data to be a doublet with energies 1489.5 $\pm$ .5 keV and 1490.0 $\pm$ .5 keV. The 1489.5 keV transition was placed between the 3041.1 keV and 1551.8 keV ^{133}Te levels due to its coincidences with the 1552.1 keV and 1244 keV gamma-rays (see figures 3.41 and 3.42). The 1490.0 keV gamma-ray was placed between the 2755.0 keV and the 1265.2 keV ^{133}Te levels because of its coincidence with the 126[illegible] keV transition. The intensities of the two components were found from coincidence peak areas to be approximately equal.

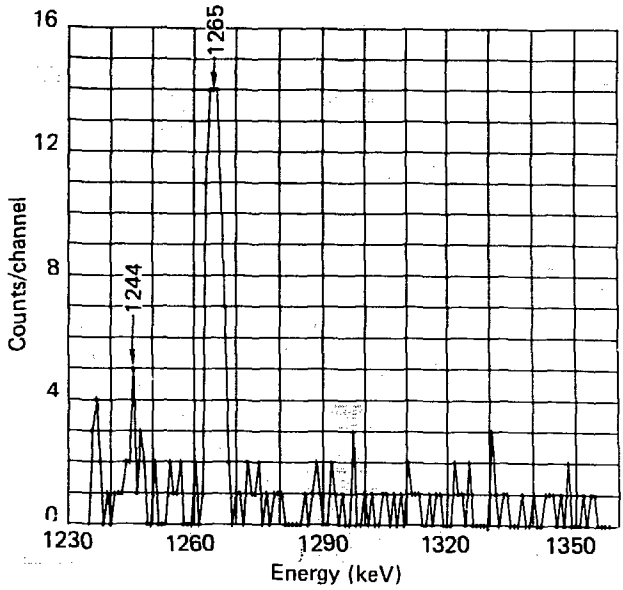

Figure 3.41. The 1244/1490 coincidence is seen on the 1490 keV slice.

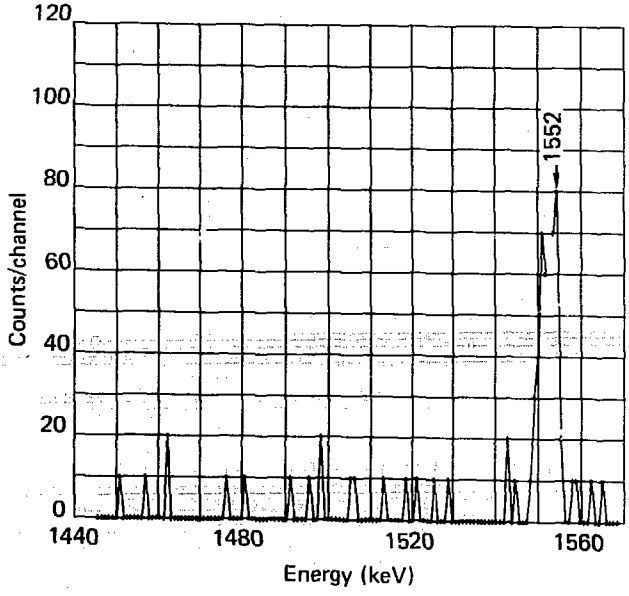

Figure 3.42. The 1490 keV slice shows a coincidence with the 1552 keV gamma ray.

Using the techniques illustrated in the above examples; the energies, relative intensities and placements for gamma-rays belonging to the decay of ^{133}Sb were determined and are presented in Table 3.5.

Table 3.5. Gamma-rays placed in the ^{133}Sb decay scheme(*)

E (ΔE) (keV)	I (ΔI)	Placement (from/to)
201.6 (3)	5 (2)	2794/2593
213.9 (3)	9 (2)	2794/2580
248. (1)	2 (2)	1977/1729
261.0 (2)	10 (2)	2593/2332
266.2 (2)	15 (3)	2593/2327
274.2 (2)	6 (3)	1913/1639
297.9 (2)	10 (5)	2211/1913
308.3 (2)	103 (9)	308/0
334.19 (5)	IT 380 (4)	334/0
336. (1)	<2 (2)	1706/1370
404.37 (6)	53 (6)	1501/1096
412.9 (2)	7 (2)	1913/1639
422.2 (2)	20 (4)	2755/2332
423.41 (5)	82 (7)	2750/2327
441.0 (1)	4 (2)	1706/1265
455.48 (7)	<3 (3)	1552/1096
463.35 (5)	7 (4)	1729/1265
482.36 (9)	2 (2)	2211/1729
538.7 (1)	46 (5)	2750/2211
572.3 (3)	3 (2)	2211/1639
602. (1)	<9 (6)	2580/1977
632.3 (2)	88 (6)	1729/1096
647.9 (2)	7 (7)	1913/1265

E (ΔE) (keV)	I (ΔI)	Placement (from/to)
679.8 (2)	<16 (4)	2593/1913
687.5 (2)	40 (4)	2327/1639
710. (1)	4 (3)	2211/1501
808.9 (1)	27 (3)	2327/1639
816.8 (4)	390 (30)	1913/1096
827. (1)	7 (3)	2327/1501
836.88 (7)	266 (9)	2750/1913
864.0 (2)	14 (2)	2593/1729
881.0 (2)	22 (10)	1977/1096
939. (1)	18 (6)	2580/1642
953.3 (2)	13 (3)	2593/1639
956.9 (3)	6 (3)	1265/308
987.19 (9)	52 (3)	2593/1606
1021.4 (5)	28 (6)	2750/1729
1026.80 (7)	123 (4)	2755/1729
1048.5 (2)	26 (5)	2755/1706
1061. (1)	9 (4)	1370/308
1064.6 (5)	14 (4)	3041/1977
1065.5 (1)	65 (3)	2794/1729
1073.2 (2)	15 (4)	2593/1518
1092.1 (2)	31 (8)	2593/1501
1096.22 (3)	1000 (5)	1096/0
1110.83 (7)	41 (3)	2750/1639
1113.09 (9)	45 (3)	2755/1639

E (ΔE) (keV)	I (ΔI)	Placement (from/to)
1115.19 (6)	112 (3)	2211/1096
1146.4 (2)	11 (2)	3061/1913
1151.87 (7)	5 (3)	2794/1642
1166.43 (9)	7 (5)	1501/334
1183.44 (8)	75 (6)	1518/334
1188.8 (2)	19 (3)	2794/1606
1202.7 (2)	40 (3)	2755/1552
1235.9 (2)	41 (3)	2332/1096
1244. (1)	12 (6)	1552/308
1249.6 (2)	20 (3)	2750/1501
1265.25 (4)	121 (5)	1265/0
1271.38 (4)	96 (5)	1606/334
1293.4 (3)	5 (2)	2794/1501
1305.14 (4)	130 (5)	1639/334
1312.9 (2)	20 (3)	3041/1729
1327.7 (2)	7 (2)	2593/1265
1333.7 (3)	64 (8)	3061/1729
1343.9 (3)	<6 (3)	2440/1096
1369.1 (5)	19 (3)	1370/0
1398.5 (2)	16 (3)	1706/308
1420.6 (3)	10 (3)	1729/308
1425.1 (2)	10 (3)	2794/1370
1454.9 (2)	12 (3)	3061/1606
1484.1 (2)	33 (3)	2580/1096

E (ΔE) (keV)	I (ΔI)	Placement (from/to)
1489.5 (5)	33 (3)	2755/1265
1490.0 (5)	34 (3)	3041/1552
1496.5 (2)	28 (3)	2593/1096
1529.1 (2)	19 (3)	2794/1265
1552.1 (2)	96 (6)	1552/0
1579.4 (2)	38 (8)	1913/334
1641.5 (2)	93 (6)	1642/0
1654.2 (2)	38 (3)	2750/1096
1658.6 (2)	54 (4)	2755/1096
1697.9 (2)	30 (3)	2794/1096
1705.5 (2)	26 (4)	1706/0
1728.59 (7)	170 (12)	1729/0
1775.8 (1)	36 (7)	3041/1265
1794.9 (4)	3 (2)	3061/1265
1877.3 (2)	33 (4)	2211/334
1908.6 (6)	4 (2)	3005/1096
1944.4 (2)	53 (6)	3041/1096
1964.7 (2)	43 (6)	3061/1096
1976.7 (2)	23 (4)	1977/0
1992.3 (3)	7 (2)	2327/334
2133.6 (8)	26 (5)	2440/308
2332.7 (8)	68 (12)	2332/0
2416.2 (8)	170 (30)	2750/334
2441.5 (8)	18 (4)	2440/0

E (ΔE) (keV)	I (ΔI)	Placement (from/to)
2446.5 (8)	33 (6)	2755/308
2580.2 (8)	57 (10)	2580/0
2680. (1)	4 (2)	2988/1096
2698. (1)	2 (1)	3005/308
2727. (1)	12 (3)	3061/334
2755. (1)	250 (40)	2755/0
2794. (1)	17 (4)	2794/0
2884. (2)	8 (2)	3192/308
3041. (2)	15 (3)	3041/0
3192. (1)	1 (1)	3192/0

* Intensities are normalized to I(1096) = 1000

3.3 Spin and Parity Assignments

The spin and parity assignments (J^{π}) for the levels populated in ^{133}Te by beta-decay are given in table 3.6 along with the percentage of beta-decays to each level and the log ft value. The percent beta-feeding was determined from an intensity balance at each level where the gamma-ray intensities were corrected for electron conversion [92]. The log ft values were calculated, assuming a half-life of 2.7 min for ^{133}Sb, using the tables by N. B. Gove and M. J. Martin [93]. In making the spin and parity assignments from log ft values, the empirical rules of S. Raman and N. B. Gove [94] were used. These rules state that if log ft < 5.9, the decay is allowed ($\Delta J = 0,1$; $\Delta\pi = +$), if $5.9 < \log ft < 8.5$ the decay is allowed or first forbidden non-unique ($\Delta J = 0,1$; $\Delta\pi = -$) and if log ft > 8.5 the decay could also be first-forbidden unique ($\Delta J = 2$; $\Delta\pi = -$).

The first five levels of ^{133}Te are given J^{π} assignments of $3/2^+$, $1/2^+$, $11/2^-$, $7/2^+$, and $5/2^+$, respectively, based upon the systematics of N = 81, odd-A nuclei as shown in figure 4.1. A measurement of the K/L conversion electron ratio by Alvager and Oelsner[83] indicates that the transition between the 334 keV level and the ground state is chiefly M4 multipolarity, supporting the $11/2^-$ and $3/2^+$ assignments.

Meyer[87] found that 18% of the ^{133}Sb beta decays populate the 334 keV isomeric state. In this experiment it was found that 20% of the beta decays populate the isomeric state by gamma cascading from higher levels. Consequently, the direct feeding to the 334 keV level is very small.

Levels at 2580, 2593, 2750, 2755, 2794, 3041, 3061, and 3192 keV, within the limits of the errors in the % beta-feeding, have log ft values of less than 5.9 and are therefore assumed to be fed by allowed beta transitions. From systematics (see figure 4.3), the ground state of ^{133}Sb is $7/2^+$. Consequently, ^{133}Te levels fed by allowed transitions have possible spins and parities of $5/2^+$, $7/2^+$, and $9/2^+$. Assuming these levels deexcite by E2 gamma radiation, the levels at 2755 and 3192 keV are assigned $J^\pi = 5/2^+$ because they feed the $1/2^+$ 308 keV level. Similarly, the levels at 2580, 2593, 2794 and 3041 have J^π values of $5/2^+$ or $7/2^+$ because they deexcite with a gamma-ray that feeds the $3/2^+$ ground state. Gamma-rays that excite the $11/2^-$ 334 keV level from a positive parity level are assumed to have a multipolarity of E1. Thus, the levels 2750 and 3061, have a J^π value of $9/2^+$.

The 1370, 1552, 1606, 1639, 1642, 1706, 1913, 1977, 2211, 2332, 2440, 2988, and 3005 keV levels have log ft values between 5.9 and 8.5 implying that their possible spin and parities must be $5/2^\pm$, $7/2^\pm$, or $9/2^\pm$. By making the reasonable assumption that observed gamma rays are E1, M1, or E2, further limits on the spins and parities of these levels can be made. The assumption that gamma-ray transitions are dominated by these multipolarities will be used throughout the discussion in this section.

The 1552, 2440, 2988 and the 3005 keV levels feed the 308 $1/2^+$ first excited state and are therefore given the J^π assignment of $5/2^+$. The 1642, 1977 and 2332 levels deexcite to the $3/2^+$ ground state and consequently must have possible spins and parities of $5/2^\pm$ or $7/2^+$. Levels at 1606, 1913, and 2211 have possible J^π

assignments of $9/2^{\pm}$ or $7/2^{-}$ because these states deexcite to the $11/2^{-}$ 334 keV level.

A few of the levels (308, 1500.7, 1518, 1729, and 2328) have slightly more gamma intensity entering than leaving. Within experimental errors, the intensities can be taken to be balanced. The beta feeding to these levels is therefore very small. The 1500.7 level decays to both the $11/2^{-}$ 334 keV level and the $7/2^{+}$ level and must therefore have possible spin and parity values of $11/2^{+}$, $9/2^{\pm}$, and $7/2^{-}$. Because the 1518 keV state deexcites to the $11/2^{-}$ 334 keV level, and is populated from the $5/2^{+}$, $7/2^{+}$ 2593 level, its possible J^{π} values are $11/2^{+}$, $9/2^{\pm}$, or $7/2^{-}$. The 1729 level can be assigned a spin and parity of $5/2^{+}$ because it feeds the $1/2^{+}$ 308 keV level and is fed by the $9/2^{+}$ 3061 keV state. The 2328 keV level must have possible spin and parities of $11/2^{+}$, $9/2^{\pm}$, and $7/2^{-}$ because it feeds the $11/2^{-}$ 334 keV isomeric level and is fed by the $5/2^{+}$, $7/2^{+}$ 2592 keV level.

The 1370 and 1706 levels have log ft values that imply they are populated by allowed or first forbidden non-unique beta transitions, however, the errors on the % beta feeding are large enough that other types of transitions are also possible. Because the 1369 level directly populates the $1/2^{+}$ 308 keV level, it will be assigned possible J^{π} values of $1/2^{\pm}$, $3/2^{\pm}$, and $5/2^{+}$. Likewise, the log ft for the 1906 level are consistant with spin and parity assignments of $1/2^{+}$, $3/2^{\pm}$, $5/2^{+}$ because this level is fed by the $5/2^{+}$ 2755 level and it feeds the $1/2^{+}$ 308 level.

When more than one spin and parity assignment are given in table 3.5, the first one agrees best with the shell model results.

Table 3.6 Spin and parity assignments for levels of ^{133}Te populated in beta-decay

Energy (keV)	% β^- Feeding	log ft(*)	J^π
G.S	0.0		$3/2^+$
308.0	$-.7 \pm 2.1$		$1/2^+$
334.3	0.0		$11/2^-$
1096.2	1.7 ± 3.7	(7.3)	$7/2^+$
1265.2	0.4 ± 1.4	(7.8)	$5/2^+$
1369.8	$0.6 \pm .6$	(7.5)	$3/2^+$, $3/2^-$, $1/2^\pm$, $5/2^+$
1500.7	$-.3 \pm 1.2$		$9/2^+$, $7/2^-$, $9/2^-$, $11/2^+$
1518.2	-1.1 ± 1.3		$9/2^+$, $11/2^+$, $9/2^-$, $7/2^-$
1551.8	$1.4 \pm .8$	7.0	$5/2^+$
1605.6	$2.5 \pm .5$	6.8	$9/2^\pm$, $7/2^-$
1639.4	$1.0 \pm .8$	7.1	$9/2^+$
1641.8	$1.0 \pm .7$	7.1	$5/2^\pm$, $7/2^+$
1706.1	$.85 \pm .8$	(7.3)	$3/2^+$, $3/2^-$, $1/2^+$, $5/2^+$
1728.6	-1.7 ± 2.1		$5/2^+$
1913.3	5.6 ± 2.6	6.2	$9/2^\pm$, $7/2^-$
1977.2	1.3 ± 1.0	6.7	$7/2^+$, $5/2^+$, $5/2^-$
2211.2	$4.6 \pm .9$	6.0	$9/2^\pm$, $7/2^-$
2327.5	$-.6 \pm .8$		$7/2^-$, $9/2^\pm$, $11/2^+$
2332.3	$3.4 \pm .7$	6.0	$5/2^+$, $7/2^+$
2440.4	$1.9 \pm .5$	6.1	$5/2^+$
2580.0	4.2 ± 1.0	5.6	$5/2^+$, $7/2^+$
2592.8	7.2 ± 1.4	5.3	$5/2^+$, $7/2^+$

Energy (keV)	% β^- Feeding	log ft	J^π
2750.1	26.7 ± 2.5	4.6	$9/2^+$
2755.0	14.4 ± 2.6	4.8	$5/2^+$
2794.0	7.1 ± 1.1	5.1	$5/2^+$, $7/2^+$
2988.0	$.2 \pm .1$	6.5	$5/2^+$
3005.1	$.2 \pm .1$	6.2	$5/2^+$
3041.1	6.6 ± 1.0	4.7	$5/2^+$, $7/2^+$
3060.6	$4.0 \pm .9$	4.9	$9/2^+$
3192.0	$.3 \pm .1$	5.7	$5/2^+$

(*) Parentheses indicate that types of beta-decay other than the type implied by log ft value are possible within the % beta-feeding errors.

Chapter 4

4. Nuclear Shell Model Calculations

4.1 The Vector Method

4.2 The Hamiltonian

4.3 The Basis Wavefunctions

4.4 The Lanczos Algorithm

4.5 The PMM Force

4.6 The Valence Space

4.7 Single Particle Energies

4.0 Nuclear Shell Model Calculations

In general there are no exact solutions to the nuclear many-body problem. There are, however, approximate methods by which the problem can be attacked. One such technique, known as the "shell model", postulates that the interaction of one nucleon with all of the other nucleons can be replaced by its interaction with an average central field. Thus, the problem reduces to one of solving, for each nucleon, a one-body problem in a central field, of some assumed form such as a spherical harmonic oscillator well. If this can be done, that part of the mutual interaction which has not been taken into account, called the residual interaction, must be considered. Usually the residual interaction can be treated as a perturbation.

The single particle orbits of the nucleons moving in the central field are usually highly degenerate in energy. Consider the example of a particle in a spherical harmonic oscillator well. The first energy level can be occupied by two identical fermions, the second by six and so on. The residual interaction perturbation partially breaks the degeneracies of these levels. However, the separation between levels split by the perturbation is usually small relative to the separation of the original degenerate levels. Consequently, the levels are grouped in bunches which are known as "major shells."

Because we are dealing with a system of identical fermions which obey the Pauli principle, only a certain number of nucleons can occupy the orbits of a given shell. When a shell is filled with its complement of fermions, the shell is said to be "closed". A closed shell can be described by a single wavefunction, has a total angular momentum of zero, and therefore can be considered part of an inert core.

The shell model assigns the orbitals to one of three classes. The first class is the inert core which consists of one or more closed shells. It is assumed that these orbitals are permanently occupied; no particle may be excited out of a core orbital. The second class consists of a set of orbitals which may be occupied by those particles outside of the inert core. This set of orbitals is called the valence space. The third class is the set of orbitals that are always vacant; no particle is allowed to be excited into one of these orbitals. If the core states are chosen so that the energy required to excite a particle out of one of these orbitals is relatively large and if a large amount of energy is required to excite a particle into the third class of orbitals, the problem can be successfully treated by dealing only with the particles and orbitals of the valence space.

If the valence space extended over all possible orbitals, the residual interaction could be taken to be the real two-body interaction experienced by two bound nucleons. However, since the Fock space must be severely truncated to make the calculation possible, an attempt is made to renormalize the residual interaction to compensate for the truncation. This renormalized interaction is called the effective interaction. More will be said on this subject later.

With the specification of the valence space, the number of valence particles, and the effective interaction among them, a well defined mathematical problem is formulated. The problem is to find the eigenvalues and eigenvectors of the Schrodinger equation. This is usually done by diagonalizing the Hamiltonian matrix.

The afore mentioned individual particle model approach to the

nuclear many-body problem is a reasonable one to the extent that abundant experimental evidence exists that nuclear energy levels do exhibit shell structure. Since this method was pioneered in the late 1940's by M. Mayer and H. Jensen, for which they received the Nobel prize, it has been employed extensively to explain and predict a host of nuclear properties.

In the work presented here, a novel approach called the "vector method" has been used to perform shell model calculations on nuclei having a few protons and/or neutron holes added to the doubly closed nucleus $^{132}_{50}Sn_{82}$. Various aspects of the vector method are discussed in Sections 4.1 - 4.4.

Another feature of these calculations is the use of the PMM force, a realistic effective interaction. This force has been employed successfully in other doubly-magic regions of the nuclide chart. Section 4.5 describes the PMM force and mentions other nuclear structure calculations making use of it.

The valence spaces used in these calculations will be detailed in section 4.6. Section 4.7 will discuss the determination of the single particle energies -- the energies a single valence particle or hole has in the various accessible orbits.

4.1 The Vector Method

Despite the great success of the shell model, the method suffers from severe limitations. First, the minimum size of the valence space required to represent the interesting features of the nucleus adequately is not easily determined. Obviously, the larger it is the more accurate the calculation will be. However, as the valence space grows, so do the single and multiparticle basis sets and the number of two-body matrix elements that must be dealt with. Second, as the number of valence particles is increased, the dimensionality of the multiparticle basis set grows extremely rapidly. A new technique, originated by R. Hausman and S. Bloom and dubbed the "vector method"[49], is able to handle a larger number of particles and a larger valence space than was possible with any previous shell model method. Hausman has described the vector method in detail so only a brief mention of the major points will be made here.

The name "vector method" has a multiple meaning. Firstly, it implies that the technique involves the direct manipulation of basis state vectors (Slater determinants) in a Fock space representation (occupation number representation) rather than more complicated coupled vectors. This feature follows from the second-quantization formalism and from a machine oriented representation of the Slater determinants. Two computer words are used to represent a Slater determinant; one is a real coefficient and the other is an index where each bit corresponds to a single particle orbital. A set bit indicates that that orbital is occupied. A representation like this allows implementation of efficient bit handling commands for operations such as particle annihilation and creation, and finding the

inner products of two abstract vectors. Machine language subroutines to perform these operations were written using the concept of locality. The CDC 7600, on which all calculations reported here were done, has a command stack processor that holds 100 words. If the main loop of a heavily used subroutine consists of 100 words or less, no time is expended in fetching a new set of command words.

Secondly, the word "vector" is used in the linear algebra sense. That is, the Lanczos algorithm for finding the lowest eigenvalues of a matrix is cast in a form that uses column vectors, matrix operators, and matrix algebra. Because the second-quantization formalism is used, the Hamiltonian matrix does not have to be explicitly constructed. Instead an operator representation is used as discussed in section 4.2.

The last meaning of "vector" anticipates the application of the method to the generation of computers that are able to perform many operations simultaneously. This is called vector or parallel processing and obviously results in considerable gains in computation speed for vector (in the linear algebra sense) algorithms such as the Lanczos algorithm.

4.2 The Hamiltonian

The Hamiltonian is given by

$$H = E_{core} + \sum_i \left(\frac{p_i^2}{2m} - \frac{kx_i^2}{2} + F_i\right) + \sum_{i>j} V_{ij}$$

where E_{core} is a constant equal to the self-energy of the core, the second term is a summation of single particle energies, and the last term is the sum of interaction energies between valence particles. Single particle energies arise from the interaction of the valence particles with the core. These energies are represented by the kinetic and potential energies due to motion in a spherical harmonic oscillator well added to an empirically determined factor, F_i, which represents effects such as the Coulomb and spin-orbit interactions that are not explicitly accounted for. The determination of single particle energies for the gddsh shell will be described in section 4.7. The core self-energy was obtained from experimental binding energies. The spring constant, k, was found from the relationships

$$\omega = \frac{41\text{MeV}}{A^{1/2}} \text{ and } k = m\omega^2$$

where A is the mass number and m is the mass of a nucleon. The value 41 MeV was obtained from electron scattering experiments[95].

An important tenet of the vector method is the choice of the m-scheme representation for the wavefunctions and operators. In this representation each single particle state (assuming j-j coupling and a spherical basis) is specified by the quantum numbers n, l, j, m_j, m_τ.

No unnecessary symmetries are embodied in the m-scheme representation, which results in a much larger basis set than one would have working in a coupled representation where the Hamiltonian is already partially diagonalized. Simplification of the manipulations involved in the calculation compensate for the larger basis set. In the m-scheme, the operators and wavefunctions can be expressed in a second quantized form. Annihilation and creation operators are used in the usual manner to rewrite the Hamiltonian as

$$H = \sum_{\alpha\beta} a^{+}_{\alpha} \langle \alpha | H_1 | \beta \rangle \; a_{\beta} + \frac{1}{2} \sum_{\alpha\beta\delta\gamma} a^{+}_{\alpha} \; a^{+}_{\beta} \langle \alpha\beta | H_2 | \delta\gamma \rangle \; a_{\gamma} \, a_{\delta}.$$

The summations now extend over all of the single particle valence orbitals instead of the particles. The Hamiltonian is separated into a sum of one-body and two-body parts. The one-body matrix elements, all of which are diagonal, now incorporate the single particle energies plus the core contribution. The two-body matrix elements contain the effective interaction and are defined in the following way:

$$\langle \alpha\beta | H_2 | \delta\gamma \rangle = (\alpha\beta | H_2 | \delta\gamma) - (\alpha\beta | H_2 | \gamma\delta)$$

$$(\alpha\beta | H_2 | \delta\gamma) = \int\int \phi_{\alpha}(\vec{x}_1) \quad \phi_{\beta}(\vec{x}_2) \; H_2 \; (\vec{x}_1, \vec{x}_2) \quad \phi_{\delta}(\vec{x}_1) \quad \phi_{\gamma}(\vec{x}_2) \; d\vec{x}_1 \; d\vec{x}_2$$

The Greek indices refer to single particle orbitals, the ϕ's represent the single particle wavefunctions, and H_2 is the effective interaction. The coordinate $\vec{x}$ encompases all of the appropriate coordinates (space coordinates, spin, isospin) associated with each particle.

For the details of the construction of two-body matrix elements see the series of reports by Rajasekar, Wong, and Struble.[115]

4.3 The Basis Wavefunctions

The single particle basis wavefunctions are spherical harmonic oscillator eigenfunctions[95] of the Schrodinger equation. With the inclusion of spin and isospin the wavefunctions take the form

$$\phi_{n_j l m_j m_\tau}(r) = \frac{1}{r} R_{nl}(r)\, \chi^{1/2}_{m_\tau} \sum_{\substack{m_l,\, m_s \\ m_j = m_l + m_s}} (l m_l \tfrac{1}{2} m_s | j m_j)\, Y_{l m_l}(\theta,\phi)\, \chi^{1/2}_{m_s}$$

where

$$R_{nl}(r) = \left\{ \frac{2^{l-n+3}\,(2l+2n-1)!!}{\sqrt{\pi}(n-1)!\left[(2n+1)!!\right]^2}\, \nu^{l+\frac{3}{2}} \right\}^{1/2} \exp(-\tfrac{1}{2}\nu r^2) r^{l+1} \quad X$$

$$\sum_{k=0}^{n-1} (-1)^k\, 2^k \binom{n-1}{k} \frac{(2l+1)!!}{(2l+2k+1)!!} (\nu r^2)^k \quad ,$$

where $Y_{lm}(\theta,\phi)$ are spherical harmonics, $\chi^{1/2}_{m_s}$ are spinors, $\chi^{1/2}_{m_\tau}$ are isospinors, and $(l m_l \tfrac{1}{2} m_s \mid j m_j)$ are Clebsch-Gordan coefficients. Each orbital is specified by $njm_j m_\tau$, the radial, total angular momentum, orbital angular momentum, total angular momentum projection, and isospin projection quantum numbers, respectively. The orbital angular momentum projection, m_l, and the spin projection, m_s, must, of course, sum to the total angular momentum projection, m_j.

Also, $\nu = \frac{m\omega}{\hbar}$, where m is the mass of a nucleon and ω is the classical angular frequency of the oscillator.

The multiparticle basis wavefunctions, on which the Hamiltonian acts, are Slater determinants built from the above single particle wavefunctions,

$$\Phi_{i_1,i_2,i_3,\ldots i_n}(\vec{x}_1, \vec{x}_2,\ldots.\vec{x}_n) = (n!)^{-1/2} \begin{vmatrix} \phi_{i_1}(\vec{x}_1) & \phi_{i_1}(\vec{x}_2)\ldots\phi_{i_1}(\vec{x}_n) \\ \phi_{i_2}(\vec{x}_1) & \phi_{i_2}(\vec{x}_2)\ldots\phi_{i_2}(\vec{x}_n) \\ \phi_{i_n}(\vec{x}_1) & \phi_{i_n}(\vec{x}_2)\ldots \phi_{i_n}(\vec{x}_n) \end{vmatrix}$$

where the indices, i_1, $i_2\ldots i_n$, each specify a unique set of quantum numbers $(nj\ell m_j m_\tau)$ and $\vec{x}_k$ expresses the appropriate coordinates of particle k.

In a second quantized notation, the multiparticle wavefunctions are written as

$$\Phi_{i_1, i_2,\ldots i_n} = C \; a^+_{i_1} a^+_{i_2} \ldots a^+_{i_n} |0\rangle$$

with $|0\rangle$ symbolizing the vacuum state, C is the normalizing coefficient and the a^+_i's are creation operators specifying the occupied orbitals. It is a simple device to represent this second quantized multiparticle wavefunction by a pair of computer words as mentioned before.

Since the computer used for all of the calculations done here, a CDC 7600, has a 60 bit word size the number of orbitals was limited to 59 (the sixtieth bit is a sign bit). Due to the size of the core memory the multiparticle wavefunctions are built as a superposition of

no more than 30,000 Slater determinants. It must be emphasized that these two limitations are not fundamental ones, but merely reflect the present degree of development of the computer code.

4.4 The Lanczos Algorithm

An essential component of the vector method used in this study is the symmetric Lanczos algorithm which transforms the uncoupled m-scheme basis into one in which the Hamiltonian is at least partially tridiagonal. This section will briefly discuss this algorithm emphasizing its advantages in shell model calculations over more traditional methods. For a more detailed discussion, the reader is directed to the references given herein.

The usual shell model technique for determining the eigenstates of the Hamiltonian is to find a suitable matrix representation and then diagonalize. A major difficulty arises with this approach; namely that the Hamiltonian matrix for all but the simplest problems is enormously large. For instance, the number of distinct ^{133}Te configurations in the gddsh shell is 15872. Diagonalization of a matrix of these dimensions is wholly impractical with present day computing machines. To reduce the size of this matrix, a coupled representation can be found in which the Hamiltonian is already partially diagnolized, however, for a system such as ^{133}Te, even the submatrices are too large to be dealt with.

It was first suggested by Sebe and Nachamkin[47] and by Whitehead[45, 46] that the traditional shell model formalism of group theory, fractional parentage, and angular momentum theory be abandoned and replaced by a more elementary numerical technique such as the Lanczos algorithm. As mentioned above, this algorithm is an iterative method of tridiagonalizing a real symmetric matrix. The Householder[96] tridiagonalization algorithm is the usual method of choice, but, unfortunately, the entire matrix must be tridiagonalized

before eigen-information becomes available. Because only the lowest 20 or 30 eigenstates can usually be compared with experiment, it is of no use to calculate several thousand. After r iterations the Lanczos algorithm produces an r x r tridiagonal matrix from the full n x n Hamiltonian, where $n > r$. The eigenvalues of the r x r matrix converge monotonically to the lowest r eigenvalves of the n x n matrix as a consequence of the eigenvalue separation theorem. It is therefore not necessary to tridiagonalize the complete n x n matrix, but rather only a small fraction of it. Moreover, the speed of convergence of the Lanczos algorithm is unusually fast. The first 25 eigenvalves of the ^{133}Te system, for instance, can be obtained after only 200 iterations. The computation time varies only linearly with the dimensionality of the space.

Only a brief outline of the symmetric Lanczos algorithm will be given here. For greater detail refer to Wilkinson[96]. Let A be an n x n real symmetric matrix and let $\vec{V}_1$ be an n x 1 normalized initial vector.

$$(\vec{V}_1, \vec{V}_1) = 1.$$

To obtain the second Lanczos vector, $\vec{V}_2$, let

$$H\vec{V}_1 - (\vec{V}_1, H\vec{V}_1)\vec{V}_1 = (\vec{V}_2, H\vec{V}_1)\vec{V}_2 = \vec{\alpha}_2,$$

then

$$V_2 = \frac{\vec{\alpha}_2}{\left[(\vec{\alpha}_2, \vec{\alpha}_2)\right]^{1/2}}$$

To obtain the third vector, $\vec{V}_3$, let

$$H\vec{V}_2 - (\vec{V}_2, H\vec{V}_1)\,\vec{V}_1 - (\vec{V}_2, H\vec{V}_2)\,\vec{V}_2 = \vec{V}_3, H\vec{V}_3)\vec{V}_3 = \vec{\alpha}_3$$

then

$$\vec{V}_3 = \frac{\vec{\alpha}_3}{(\vec{\alpha}_3, \vec{\alpha}_3)^{1/2}}$$

The i th vector is obtained by letting

$$H\vec{V}_{i-1} - (\vec{V}_{i-1}, H\vec{V}_{i-2})\,\vec{V}_{i-2} - (\vec{V}_{i-1}, H\vec{V}_{i-1})\vec{V}_{i-1} = \vec{\alpha}_i$$

$$(\vec{V}_i, H\vec{V}_{i-1})\vec{V}_i = \vec{\alpha}_i,$$

so

$$\vec{V}_i = \frac{\vec{\alpha}_i}{(\vec{\alpha}_i, \vec{\alpha}_i)^{1/2}}$$

If an orbitrary vector, $\vec{V}_k$, is dotted into the equation for $\vec{\alpha}_i$ one gets

$$(\vec{V}_k, H\vec{V}_{i-1}) = (\vec{V}_{i-1}, H\vec{V}_{i-2})\,(\vec{V}_k, \vec{V}_{i-2}) + (\vec{V}_{i-1}, H\vec{V}_{i-1})\,(\vec{V}_k, \vec{V}_{i-1}) + (\vec{V}_i, H\vec{V}_{i-1})\,(\vec{V}_k, \vec{V}_i) \quad .$$

It can be seen that H is tridiagonal in the new Lanczos representation.

$$(\vec{V}_k, H\vec{V}_{i-1}) = 0 \quad \text{if} \quad k \neq \begin{cases} i-2 \\ i-1 \\ i \end{cases}$$

Because this algorithm depends on the orthogonalization of the vectors, $\vec{V}_i$, and because round off errors destroy this orthogonalization, it is necessary to re-orthogonalize the vector $\vec{V}_i$ at iteration i with all of the previously constructed vectors. Once the desired tridiagonal matrix has been formed, the diagonal form is

easily obtained by using standard techniques such as bisection and inverse iteration.[96]

Note that the operator H need not be a matrix but can be an abstract operator like the second quantized Hamiltonian discussed in the last section. This is a very important point because it obviates the need to store a large Hamiltonian matrix in core; random access to matrix elements is not a requirement. Furthermore, most of the operations are vector operations and can easily be performed on a processor capable of vector arithmetic.

By applying the Hamiltonian to the initial vector, new Slater determinants are produced by the annihilation of one or two particles in occupied orbitals and the creation of one or two particles in unoccupied orbitals. Repeated application of the Hamiltonian to the vectors made of these new Slater determinants will generate vectors that span the space containing the initial vector. These new vectors reflect all of the symmetries embodied in the Hamiltonian. For instance, assume the initial vector has a definite total angular momentum, j, and a definite total angular momentum projection, m_j, then the new vectors will also have these qualities (neglecting roundoff error). Note that a judicious choice of start vector will span only the space containing the states of interest.

4.5 The PMM Force

All of the calculations reported here employed an effective interaction due to F. Petrovich, H. McManus, and V. Madsen called the PMM force.[50] This force is derived from the Kallio-Kolltveit[51] (KK) force and is also known as the "Kallio-Kolltveit equivalent force." In this section, the KK force, the PMM force, and their relationship to each other will be discussed. Also, previous calculations making use of the PMM force will be mentioned.

The KK force expressed in the triplet-singlet format is

$$V = \begin{cases} P^{01} V_t e^{-\alpha_t (r-c)} + P^{10} V_s e^{-\alpha_s (r-c)} & r > c \\ \infty & r \leqslant c \end{cases}$$

where

$V_t = -475$ MeV

$V_s = -330.8$ MeV

$\alpha_t = 2.521$ fm^{-1}

$\alpha_s = 2.402$ fm^{-1}

$c = .4$ fm

The t and s subscripts in the above equation denote the triplet spin state and the singlet spin state, respectively. The projection operators can be expressed in terms of spinors, $\vec{\sigma}$, and isospinsors, $\vec{\tau}$, in the usual way.[97]

$$P^{01} = \frac{1}{16}(3 + \vec{\sigma}_1 \cdot \vec{\sigma}_2) \cdot (1 - \vec{\tau}_1 \cdot \vec{\tau}_2) \qquad \text{Triplet - Even}$$

$$P^{10} = \frac{1}{16}(3 + \vec{\tau}_1 \cdot \vec{\tau}_2) \cdot (1 - \vec{\sigma}_1 \cdot \vec{\sigma}_2) \qquad \text{Singlet - Even}$$

Several features of this force should be noted. First of all, it is a static central force, meaning the tensor and spin-orbit portions of the most general form of the nuclear interaction are neglected. Three-body and higher order interactions play a very minor role in nuclear structure and are safely ignored for the present purposes. The KK force consists of a hard repulsive core and an exponentially long range attractive component and it is designed to work only in relative s-states.

The strengths and ranges of the triplet-even and singlet-even components were determined by fitting the effective ranges and scattering lengths of the proton-neutron system and by fitting the deuteron binding energy. The hard core radius, c, is given a value found to be reasonable by Scott and Moskowski from nuclear matter calculations.[98]

Effective interactions can be placed in three categories: phenomenological interactions, realistic interactions, and semi-realistic interactions. Phenomenological interactions are obtained from experimental level-structure information and from the microscopic analysis of inelastic scattering data. Realistic interactions, such as the KK force, are of a more fundamental nature because they are derived from the nucleon-nucleon potential. Semi-realistic interactions are constructed from a combination of phenomenological and realistic data.

Using the separation method of Scott and Moskowski[99] to avoid infinite matrix elements due to the repulsive core, Kallio and Kolltveit calculated the odd parity states of ^{16}O. Petrovich and McManus have used the KK force on the ^{90}Zr structure problem.[100] Thus, it has been demonstrated that this realistic force can be applied to shell model type calculations.

F. Petrovich, H. McManus, V.A. Madsen, and J. Atkinson showed that the KK interaction works well in a distorted-wave approximation analysis of a few transitions in the reactions $^{12}C(p,p')$ and $^{40}Ca(p,p')$ at energies of 25 MeV to 55 MeV. They also constructed an even Yukawa type force of 1 fm range, called the KK equivalent force, by adjusting the strengths to reproduce the cross-sections obtained with the KK interaction for $^{12}C(p,p')$ at 45.5 MeV and 28.05 MeV and $^{40}Ca(p,p')$ at 25 MeV and 55 MeV. Even though the KK force fit the scattering data better, the KK equivalent force (also called the PMM force) is a much easier force to work with since one doesn't have to contend with a repulsive core. The PMM force is written

$$V = \frac{e^{-\alpha r}}{r/\alpha}\left[V_t P^{01} + V_s P^{10}\right]$$

where

$V_t = -119.5$ MeV

$V_s = -73.5$ MeV

$\alpha = 1$ fm^{-1}

The symbols have the same meaning as in the previous equation. Interestingly, the triplet-even and singlet-even exchange mixture is almost identical to the KK mixture.

The PMM force has been used, without modification, in several widely separated regions of the nuclide chart. Petrovich and McManus[100] have used the force to explain the $^{90}Zr(p,p')$ reaction at 20 MeV. Bloom et al.[101] and Hausman[49] showed that structure calculations in the ^{48}Ca region could be made with PMM. The present work shows that the PMM force works well in the ^{132}Sn region.

It is surprising and rather exciting to see that a force as simple as this static central interactions, working only in even states, performs so well, at least in regions of sphericity near doubly magic nuclei.

4.6 The Valence Space

All of the calculations presented in the next chapter were performed on nuclei having a few valence protons and valence neutron holes outside of the $^{133}_{50}Sn_{82}$ inert core. The following valence spaces were used:

1) For Sn nuclei, which have no valence protons, up to four neutron holes were allowed access to the entire gddsh neutron shell.
2) ^{133}Sb, ^{134}Te, ^{135}I, and ^{136}Xe have closed neutron shells, therefore, only valence protons needed to be accounted for. The valence protons had access to the entire gddsh proton shell.
3) The gddsh shell consists of 32 proton orbitals and 32 neutron orbitals. Because the computer code could handle only 59 orbitals, non-magic nuclei had the $g_{7/2}$ neutron orbitals included in the core. That is, neutron holes had access to all of the orbitals in the gddsh neutron shell except in $g_{7/2}$ orbitals. Because it took 3 MeV to move a neutron hole from the surface of the Fermi sea to the $g_{7/2}$ orbitals, this approximation did not strongly effect the energy level calculations. On the other hand, when transition probability calculations are made, small admixtures of $g_{7/2}$ neutron hole components may be important. In this case it may be wiser to include an alternate subshell in the core.

4.7 Single Particle Energies

The single particle energies (SPEs) defined in section 4.2 for the gddsh shell were determined from the spectrum of the one neutron-hole nucleus ^{131}Sn. Unfortunately, the lack of experimental data prevents firm spin and parity assignments for ^{131}Sn. The tentative assignments shown in figure 4.1 were obtained from the work of DeGeer and Holm [43]. Nevertheless, the systematics of N=81 nuclei and Z=50 nuclei, shown in figures 4.1 and 4.2, suggest that the spin-parity assignments should be $3/2^+$, $1/2^+$, $11/2^-$, $5/2^+$, and $7/2^+$ in order of ascending energy. This proposed spectrum was fit with single particle energy differences of

$$1g_{7/2} - 2d_{5/2} = -.6757 \text{ MeV}$$
$$1g_{7/2} - 1h_{11/2} = -1.3596 \text{ MeV}$$
$$1g_{7/2} - 3s_{1/2} = -1.9355 \text{ MeV}$$
$$1g_{7/2} - 2d_{3/2} = -2.3541 \text{ MeV}$$

Absolute values for the SPEs were obtained by using the neutron separation energy of ^{131}Sn, estimated to be 5.2 MeV.[102] The set of SPEs used in most of the calculations which yield the above experimental values are

$1g_{7/2}$	-4.5030 MeV
$2d_{5/2}$	-3.8273 MeV
$2d_{3/2}$	-2.1489 MeV
$3s_{1/2}$	-2.5675 MeV
$1h_{11/2}$	-3.1434 MeV

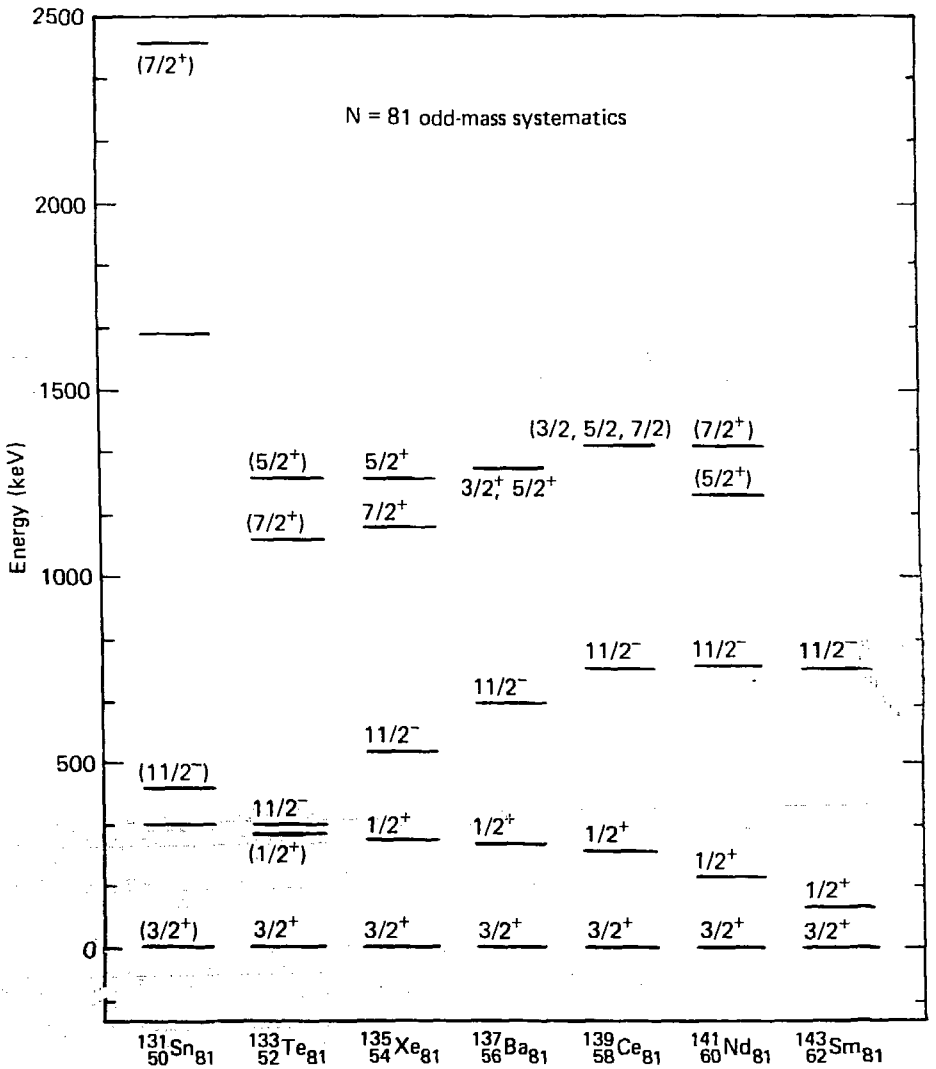

Figure 4.1. N = 81 odd-mass systematics. Tentative spin and parity assignments for ^{131}Sn were obtained from reference 43.

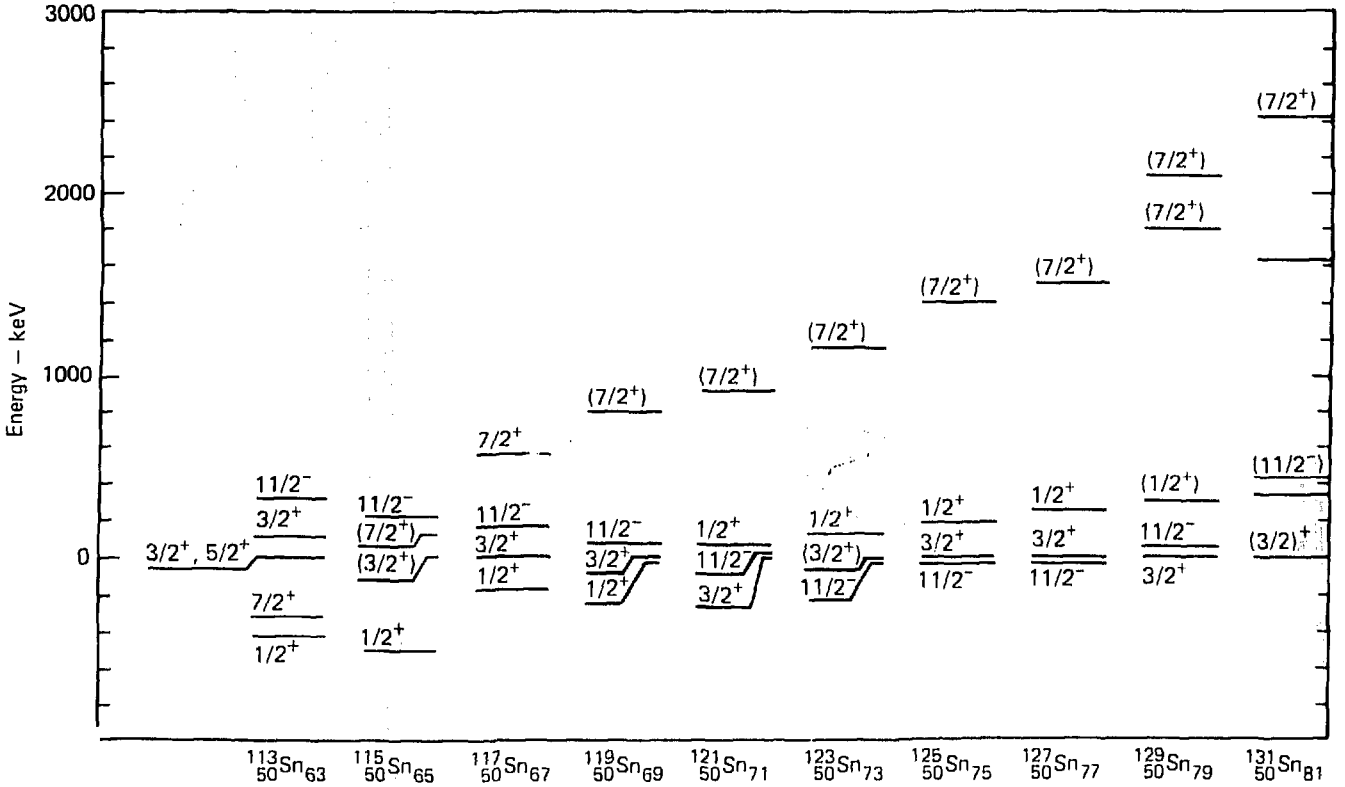

Figure 4.2. Z = 50 odd-mass systematics.

In a few cases the $1h_{11/2}$ SPE was changed to -2.9429 MeV to fit the 334 keV $11/2^-$ level in ^{133}Te. Unless otherwise mentioned, the first SPE set was used.

Using this SPE set, the levels of the single valence proton nucleus, ^{133}Sb, were calculated and compared with the ^{133}Sb experimental levels, with the systematics of Z=51 odd-mass muclei, and with the systematics of N=82 odd-mass nuclei (see figures 4.3 and 4.4). All of the calculated ^{133}Sb single-particle levels are consistent with available experimental evidence.

In contrast to other shell model calculations, the present technique used the same SPE values for both protons and neutrons as a consequence of all the neutrons in the gddsh shell being taken explicitly into account.

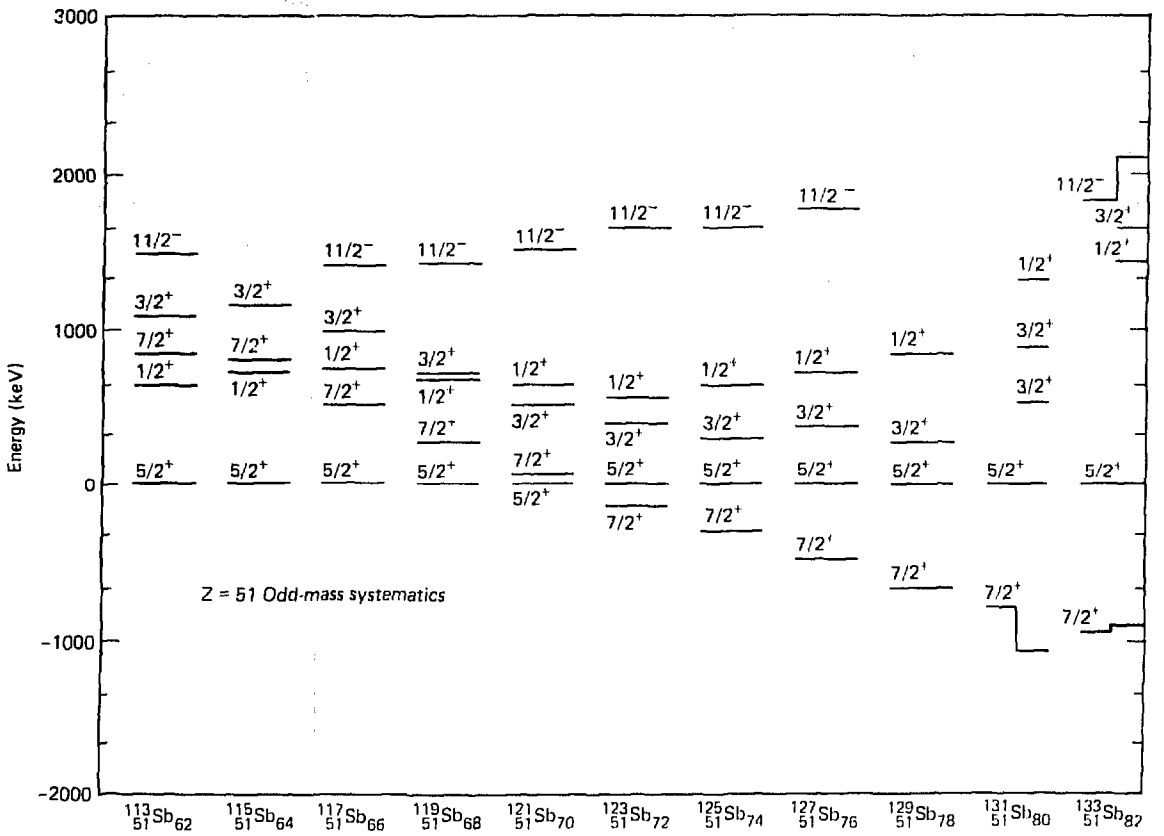

Figure 4.3. Z = 51 odd-mass systematics. Calculated levels are given to the right of the experimental ones for ^{131}Sb and ^{133}Sb. The calculated values have been normalized to the $5/2^+$ level.

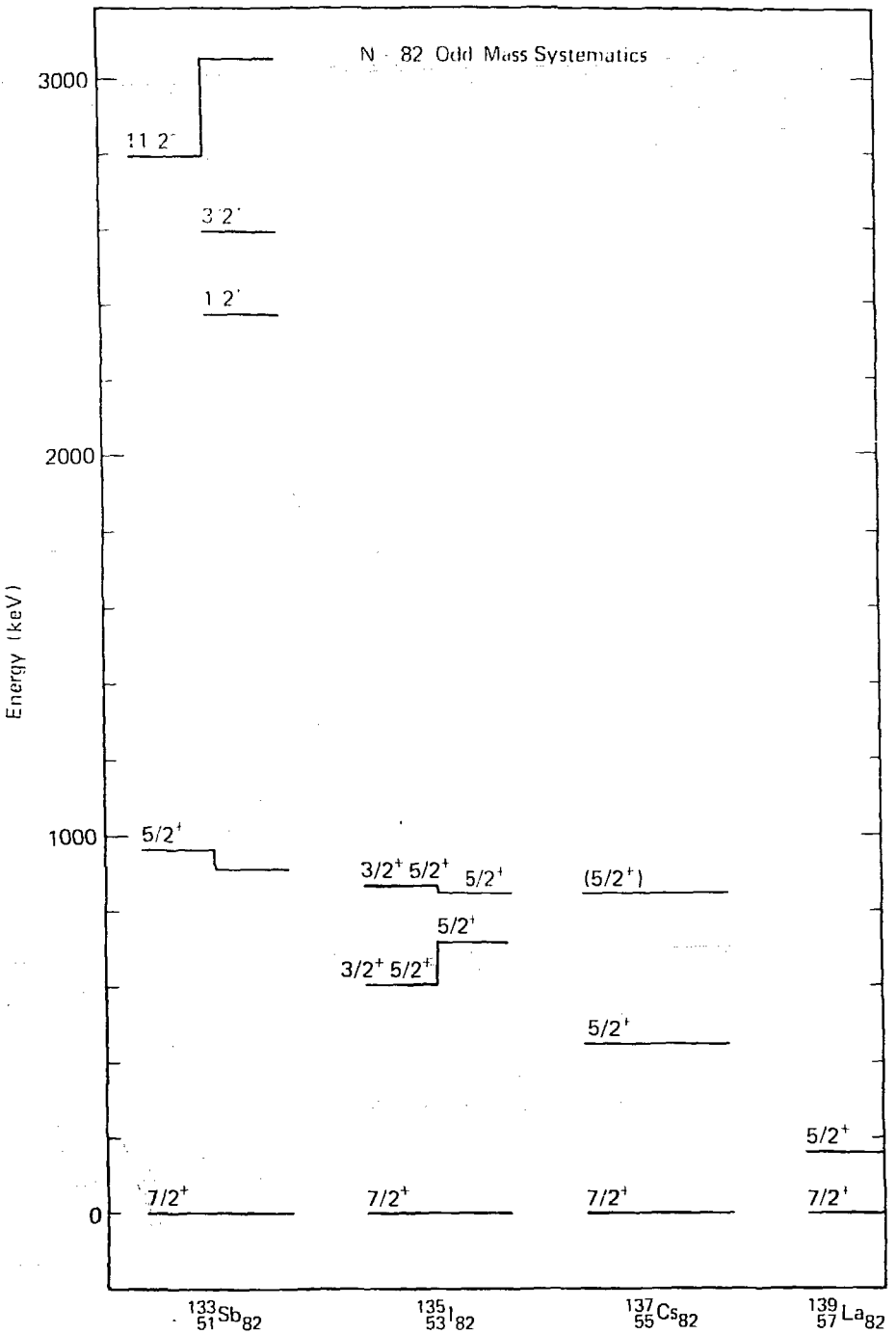

Figure 4.4. N = 82 odd-mass systematics. Calculated levels are given to the right of the experimental ones for ^{133}Sb and ^{135}I. The calculations have been normalized to the $7/2^+$ level.

Chapter 5

5. Results of Calculations Done in the ^{132}Sn Region

5.1 Neutron and Proton Separation Energies

5.2 Two Exciton Nuclei

5.3 Three Exciton Nuclei

5.4 Four Exciton Nuclei

5.5 ^{135}Xe

5. Results of Calculations Done in the ^{132}Sn Region

For those nuclei shown in figure 1.3, configuration mixing calculations using the techniques described in the previous chapter were performed. The results are presented in this chapter. There were numerous reasons for calculating properties of several nuclei: the PMM force had never been applied to the ^{132}Sb region of nuclei, the computational technique is relatively novel, and to establish the validity of this work it seemed prudent to calculate the properties of more than a single nucleus. Especially important were the calculations of the two-exciton systems whose properties can easily be calculated in closed form. Also, the effective charges and gyromagnetic ratios were found by adjusting their values to give agreement with measured branching ratios and with lifetimes of isomeric states. It obviously was desirable to have calculated levels from many different nuclei to make this comparison.

The calculation of neutron and proton separation energies is discussed in section 5.1. Sections 5.2 to 5.5 present the energy levels, spins, parities, and wavefunctions for each nucleus considered. The nuclei are grouped by exciton number -- an exciton defined for these purposes as the number of valence particles plus the number of valence holes. The more excitons, the more complex the resultant spectrum will be. For each nucleus the calculated nuclear properties are compared with experiment and, when available, with calculations done by others. Partial results for the five exciton nucleus, ^{135}Xe, are given in section 5.5

5.1 Neutron and Proton Separation Energies

The difference in binding energy between a given nucleus and the nucleus having one less neutron (proton) is defined as the neutron (proton) separation energy. This section will compare experimental separation energies[102] with those obtained from these calculations.

The neutron separation energies were obtained by subtracting the ground state energy of a nucleus with N neutrons from the ground state energy of a nucleus with N-1 neutrons. Figures 5.1 and 5.2 display the theoretical separation energies along with those obtained from measurement or from systematics. Recall that the absolute values of the single particle energies were adjusted to reproduce the ^{133}Sb neutron separation energy. The disagreement between experiment and theory for the other nuclei never exceeds 0.2 MeV.

The proton separation energies were obtained by subtracting the ground state energy of a nucleus with Z-1 protons from the ground state energy of a nucleus with Z protons and making a correction for the difference in Coulomb energy. The Coulomb correction is required since the Hamiltonian used does not account for the electrical interaction. Assuming the charge is spread uniformly throughout the nucleus, a crude estimate of the Coulomb energy difference, E_c, is given by

$$E_c = \frac{6e^2Z}{1.4A^{1/3}} \text{ MeV}$$

This expression overestimates E_c by 1.2 MeV. If one assumes that

$$E_c = K \frac{Z}{A^{1/3}}$$

where K is chosen to be 1.4 to fit the ^{133}Sb value, the Z=51 nuclei are well reproduced, but the Z=52 values are .5 MeV too high, and the Z=53,54 values are overestimated by 1-2 MeV.

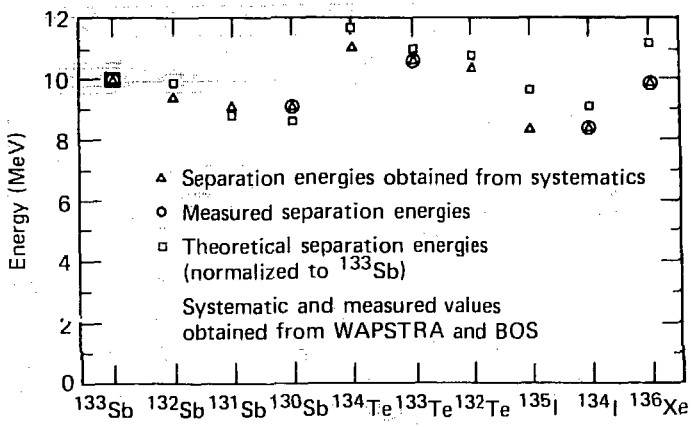

Figure 5.1. Proton separation energies.

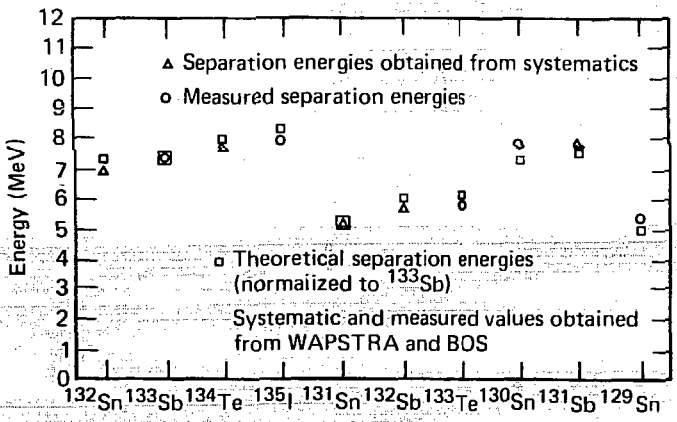

Figure 5.2. Neutron separation energies.

5.2 Two Exciton Nuclei

The nuclei described in this section are the 2 neutron hole nucleus ^{130}Sn, the two proton nucleus ^{134}Te, and the one neutron hole, one proton nucleus ^{132}Sb.

$^{130}_{50}Sn_{80}$

The measured levels of this nucleus can be explained by the coupling of its two neutron holes as they move through the gddsh shell. Using the Osiris on-line isotope separator[103] to produce ^{131}In samples, Kerek et al.[2] found four gamma-rays which were in coincidence with a beta-ray thought to belong to this system. From this information they proposed the level diagram shown in figure 5.3. Theoretical levels are also shown and the configurations giving rise to those levels are presented in tables 5.1 and 5.2.

The ground state wavefunction is comprised of a mixture of 39% $|d_{3/2}^{-2}>$, 34% $|h_{11/2}^{-2}>$ and 13% $|s_{1/2}^{-2}>$ instead of the pure $|d_{3/2}^{-2}>$ configuration one might expect. The first excited 2^+ state agrees with the experimental findings as do the 7^- and 5^- states. These odd parity states are built chiefly from the coupling of $|h_{11/2}^{-1}>$ and $|s_{3/2}^{-1}>$.

Two 0^+ levels and the 2^+ level predicted to be around 2 MeV were not seen experimentally. Kerek predicted the beta-decaying ground state of $^{130}_{49}In_{81}$ has a spin and parity of 5^+. Accordingly, the missing states would not be populated directly by beta decay.

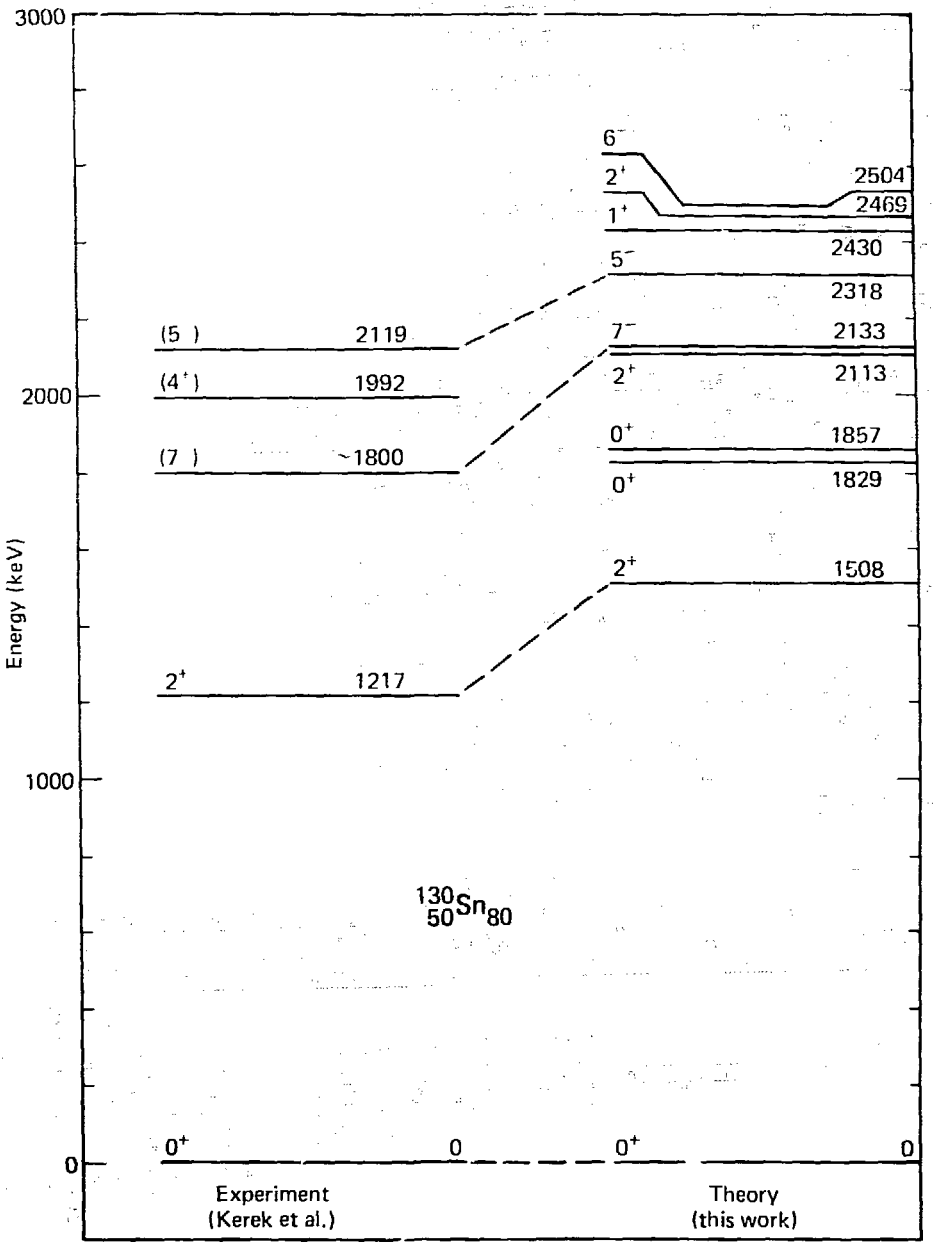

Figure 5.3. Experimental and theoretical levels of $^{130}_{50}Sn_{80}$.

Table 5.1. $^{130}_{50}Sn_{80}$ Positive Parity Model Wavefunctions*

Energy (keV)	J^π	Percent Neutron Configurations									Total
		g^{-2}	d_5^{-2}	s^{-2}	h^{-2}	d_3^{-2}	$s^{-1}d_3^{-1}$	$s^{-1}d_5^{-1}$	$d_5^{-1}d_3^{-1}$	$g^{-1}\ d_3^{-1}$	
0	0^+	4	9	13	34	39					99
1508	2^+		2		10	44	33	7	2		98
1829	0^+	2		59	37	2					100
1857	0^+	1		27	20	52					100
2113	2^+				2	51	45		2		100
2430	1^+						100				100
2469	2^+	1			80	2	15			2	100

* The following orbital notation is used in this and in subsequent tables in this chapter.

$g = 1g_{7/2}$
$d_5 = 2d_{5/2}$
$d_3 = 2d_{3/2}$
$h = 1h_{11/2}$
$s = 3s_{1/2}$

Negative superscripts indicate valence neutron holes; positive superscripts indicate valence protons.

Table 5.2. $^{130}_{50}Sn_{80}$ Negative Parity Model Wavefunctions

Energy (keV)	J	Percent Neutron Configurations				Total
		$h^{-1}d_3^{-1}$	$h^{-1}d_5^{-1}$	$h^{-1}g^{-1}$	$h^{-1}s^{-1}$	
2133	7-	98	1	1		100
2318	5-	70	2		27	99
2504	6-	100				100

Furthermore, there are lower lying 0^+ and 2^+ levels to which the decay would be preferential, causing the missing states to be only weakly populated in gamma decay. Kerek's experiment was not sensitive to the detection of weak gamma-rays due to a low fission yield for ^{133}In and a 5 s hold-up time in the separator that was comparable to the halflife. Consequently, a more sensitive experiment must be performed to prove or disprove the existence of these missing states.

The shell model also failed to predict the 4^+ level. Most predicted levels were about 300 keV higher than their experimental counterparts. Therefore the theoretical 4^+ state could have been above the cutoff energy for the calculation (2500 keV).

As is true with all of the other Sn isotopes and, for that matter, most of the nuclides discussed in this study, the validity of the experimental-theoretical comparison of level properties suffers from the large uncertainties in the measured data. Tin-130 is a typical case; only ground state and first excited state spins and parities are unambiguously known. The other spin/parity assignments are tentative at best. To make a good assessment of the quality of these calculations, much additional experimentation must be done in the ^{132}Sn region.

$^{134}_{52}Te_{82}$

Figure 5.4 shows the calculated spectrum of the two valence proton nucleus $^{134}_{52}Te_{82}$ along with the experimental spectrum.[26] Agreement with experiment is excellent; no calculated level differs from the measured value by more than 70 keV. The model wavefunctions are given in table 5.3.

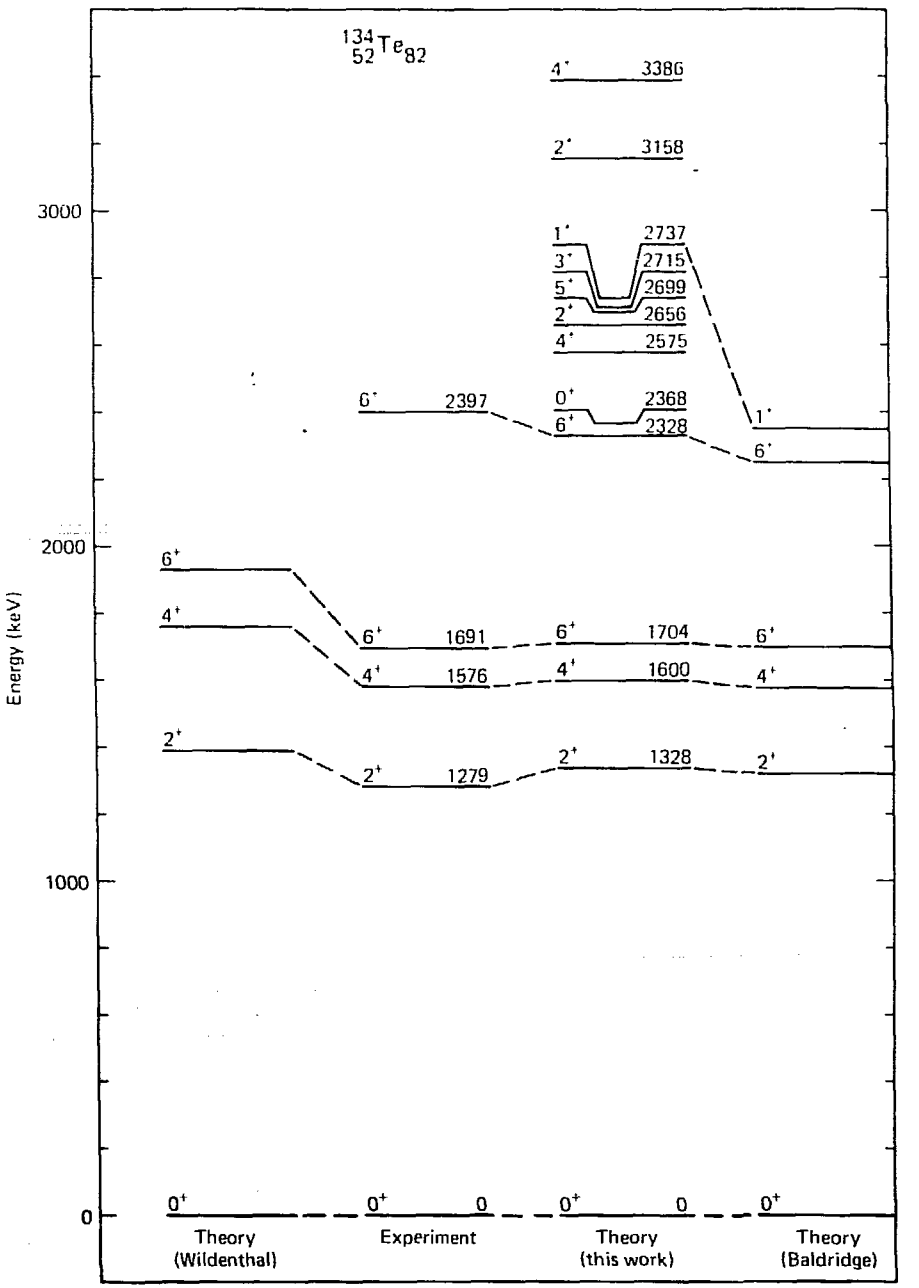

Figure 5.4. Experimental and theoretical levels of ^{134}Te.

Table 5.3. $^{134}_{52}Te_{82}$ Model Wavefunctions

Energy	J^π	Percent Neutron Configurations										Total
		g^2	d_5^2	d_3^2	s^2	gd_3	h^2	gd_5	g_5	$d_5 s$	$d_5 d_3$	
0	0^+	82	10	2	1		4					99
1338	2^+	96	1			1	1					99
1600	4^+	98						1				99
1704	6^+	97						3				100
2328	6^+	3						97				100
2368	0^+	14	80	4	2							100
2575	4^+	1				1		96	1			99
2656	2^+	1	1			2		96				100
2699	5^+							100				100
2715	3^+							100				100
2737	1^+							100				100
3158	2^+	1	85							5	2	93
3386	4^+		90						2		6	98

Note that all of the model wavefunctions are at least 80% pure and are members of the two multiplets arising from the couplings $|\pi 1g_{7/2}^2>$, $|\pi g_{7/2}, \pi 2d_{5/2}>$ and $|\pi d_{5/2}^2>$. Total spins of 0^+, 2^+, 4^+, and 6^+ are obtained by coupling two $g_{7/2}$ protons. The anti-aligned (0^+) arrangement gives the maximum overlap and therefore the lowest energy while the 2^+, 4^+, and 6^+ states have successively higher energies. The levels at 2328, 2575, 2656, 2699, 2715 and 2737 keV are due to a $|\pi g_{7/2}, \pi d_{5/2}>$ multiplet which can couple to total spins of 1^+, 2^+, 3^+, 4^+, 5^+, and 6^+. For short range forces, DeShalit and Talmi[104] show that the 6^+ state has the lowest energy followed by the 4^+ state and the 2^+ state. Odd J states are shown to have very little splitting. Finally, the levels at 2368, 2737, 3158, and 3386 keV come from the coupling of two $d_{5/2}$ protons.

Figure 5.4 also displays the results of shell model calculations by Widenthal and Larsen[10] and by Baldridge.[12] Since both these groups have calculated properties of the N=82 isotones, $^{134}_{52}Te_{82}$, $^{135}_{53}I_{82}$, and $^{136}_{54}Xe_{82}$, it will be interesting to compare their results with those obtained here. First, however, it will be useful to discuss the models that they used.

Wildenthal's valence space consisted of the full $1g_{7/2}$ and $2d_{5/2}$ proton subshells with a single particle allowed in the $3s_{1/2}$ or $2d_{3/2}$ subshells. The nucleon-nucleon force was a modified surface delta interaction (MSDI).[105] The interaction strengths and the single particle energies were obtained by a least squares fit to all of the then known positive parity levels in N=82, A=136-140 nuclei.

Baldridge, on the other hand, used a more sophisticated semi-realistic residual interaction. The Brueckner G matrix[106] from the Reid soft-core potential[107] was taken as the zeroth order proton-proton interaction and first order phenomenological corrections were made by adding two-body pairing and multipole forces. The strengths of the correction terms were determined by fitting the $^{134}_{52}Te_{82}$ spectrum. The valence space consisted of the full gddsh proton shell. Systematic trends of levels having large single particle spectroscopic factors[11] were used to obtain estimates of the SPEs. A comparison of the single particle proton energies for the three calculations is given in table 5.4. Recall that the SPE used in this work were obtained by fitting the one neutron hole, $^{131}_{50}Sn_{81}$ spectrum. There is a difference in the ordering of the $3s_{1/2}$, $1h_{11/2}$ and $2d_{3/2}$ levels between the calculations but with the sparcity of experimental data it is hard to decide which single proton energy set is correct. All three sets seem to work well in reproducing quantitative aspects of neighboring nuclei.

The three calculations correctly predict the first four states in ^{134}Te although this agreement is not particularly noteworthy in the Baldridge calculation because his correction term strengths were determined by fitting these levels. Both the present calculation and the one by Baldridge correctly predict the second 6^+ level but there is disagreement as to the location of the 1^+ level. The leading components of the model wavefunctions obtained in the three calculations are compared in table 5.5. The mixture of configurations is substantially the same for all three calculations with the Wildenthal wavefunctions

Table 5.4. Proton Single Particle Energies (MeV)

Orbit	Experimental	Baldridge	Windenthal	This Work
$1g_{7/2}$	0.0	0.0	0.0	0.0
$2d_{5/2}$	.963	.963	.88	.910
$1h_{11/2}$	2.792	2.76		3.058
$2d_{3/2}$		2.69	3.12	2.597
$3s_{1/2}$		2.99	2.95	2.377

Table 5.5. Comparison of Model Wavefunctions of $^{134}_{52}Te_{82}$

Energy[a]	J^π	Calculation[b]	Percent Proton Configuration							Total
			g^2	d_5^2	d_3^2	s^2	h^2	gd_3	gd_5	
0	0^+	L	82	10	2	1	4			99
		B	72	16	3		7			98
		W	81	18						99
1338	2^+	L	96	1			1	1		99
		B	98							98
		W	81	5			7			93
1600	4^+	L	98						1	99
		B	99							99
		W	86						7	93
1704	6^+	L	97						3	100
		B	98							98
		W	86						14	100
2328	6^+	L	3						97	100
		B							98	98
2737	1^+	L							100	100
		B							100	100

a) Energies, given in keV, refer to this work.
b) L refers to this work; B refers to reference (12); W refers to reference (10)

being slightly less pure.

The half life of the first 6^+ state, measured to be 164 nsec,[1] has been reproduced theoretically by Wildenthal and in the present work. The details are given in section 5.6.

$^{132}_{51}Sb_{81}$

The low energy excited states of $^{132}_{51}Sb_{81}$ are constructed from the coupling of the 51st proton and a single neutron hole in the otherwise closed neutron shell. The major configurations and the total spins to which they couple are

$1g_{7/2}$, $2d_{3/2}^{-1}$	$J^\pi = 5^+, 4^+, 3^+, 2^+$
$1g_{7/2}$, $3s_{1/2}^{-1}$	$J^\pi = 4^+, 3^+$
$2d_{5/2}$, $2d_{3/2}^{-1}$	$J^\pi = 4^+, 3^+, 2^+, 1^+$
$d_{5/2}$, $3s_{1/2}^{-1}$	$J^\pi = 3^+, 2^+$
$1g_{7/2}$, $1h_{11/2}^{-1}$	$J^\pi = 9^-,8^-,7^-,6^-,5^-,4^-,3^-,2^-$
$2d_{5/2}$, $1h_{11/2}^{-1}$	$J^\pi = 8^-,7^-,6^-,5^-,4^-,3^-$

Both single particle sets were used to calculate these states and the full gddsh valence space was used with the exception of the $1g_{7/2}$ neutron subshell which was placed in the inactive core. The results of these calculations, the experimental results[7] and a calculation by Kerek et al.[7] using a simple delta force interaction are displayed in figure 5.5. The experimental results were obtained by observing the beta-decay of the doubly closed ^{132}Sn nuclide and the accompanying gamma-rays. The tin samples were produced with the online isotope separator, Osiris. Table 5.6 shows that the levels at 0, 61, 292, and

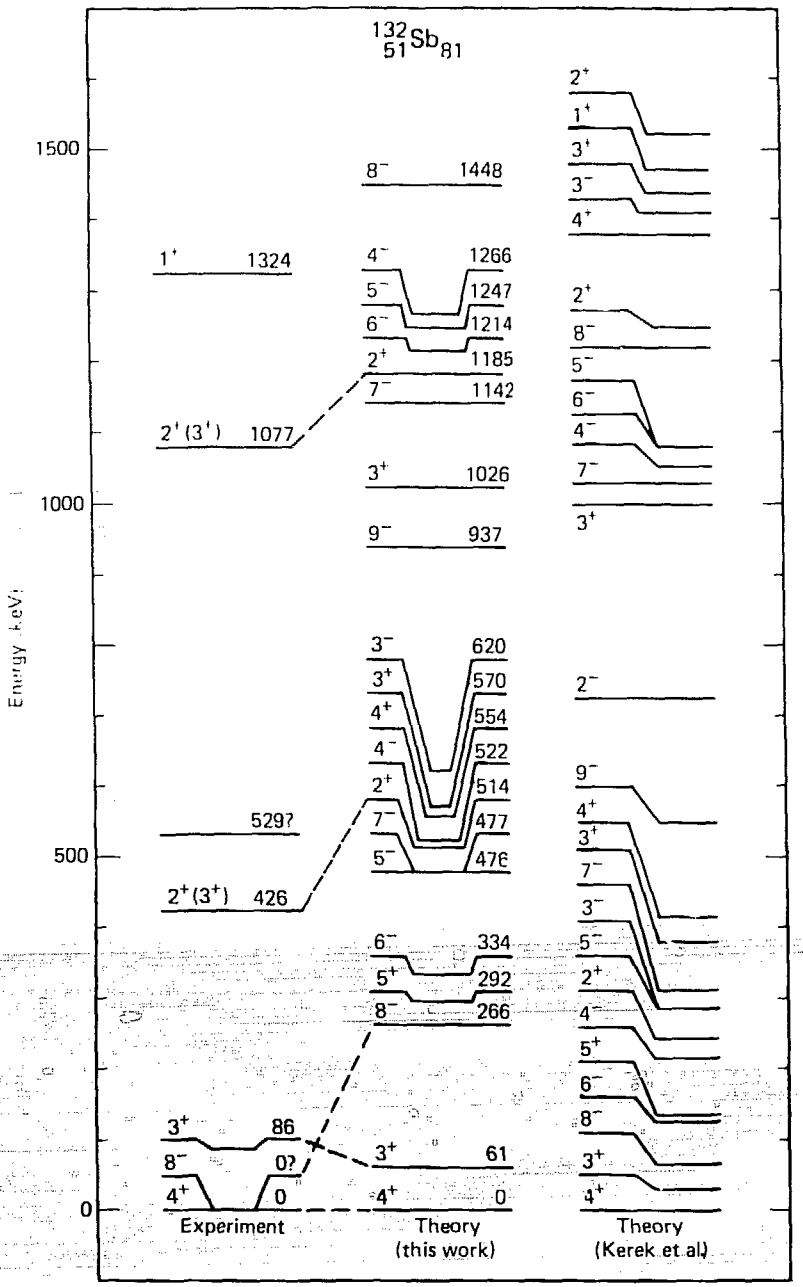

Figure 5.5. Experimental and theoretical levels of ^{132}Sb.

Table 5.6. $^{133}_{51}Sb_{81}$ Model Wavefunctions

Energy keV	J^π	Percent Configurations										Total
		gd_3^{-1}	gs^{-1}	gh^{-1}	d_5h^{-1}	gd_5^{-1}	d_3h^{-1}	$d_5d_3^{-1}$	d_5s^{-1}	sd_3^{-1}	sh^{-1}	
0	4^+	91	9									100
61	3^+	80	20									100
266	8^-			99	1							100
292	5^+	99				1						100
334	4^-			99	1							100
476	5^-			97	3							100
477	7^-			97	2		1					100
514	2^+	93				6						99
522	4^-			98	1		1					100
554	4^+	8	86			6						100
570	3^+	19	78			3						100
620	3^-			96	4							100
937	9^-			100								100
1026	3^+							93	6			99
1142	7^-			1	97		1					99
1185	2^+							78	20	1		99
1214	6^-				97						1	98
1247	5^-			4	93						3	100
1266	4^-				97		2					99
1448	8^-				99							99

514 keV are all due to the $|\pi 1g_{7/2}^{-1}, \nu 2d_{3/2}^{-1}>$ configuration. There was less than a 10% admixture of other states excepting the 20% $|\pi g_{7/2}, \nu s_{1/2}^{-1}>$ component in the 61 keV level wavefunction. The next higher multiplet of positive parity levels was due chiefly to the $|\pi g_{7/2}, \nu s_{1/2}^{-1}>$ configuration which can couple to total spins of 3^+ and 4^+. The 4^+ state had an 8% admixture of $|\pi g_{7/2}, \nu d_{3/2}^{-1}>$ and a 6% admixture of $|\pi g_{7/2}, \nu d_{5/2}^{-1}>$ while the 3^+ state at 570 KeV had a 19% admixture of $|\pi g_{7/2}, \nu d_{3/2}^{-1}>$ and a 3% admixture of $|\pi g_{7/2}, \nu d_{5/2}^{-1}>$. These two close lying levels were inverted with respect to the delta force results but were above the 2^+ from the $|\pi g_{7/2}, \nu d_{5/2}^{-1}>$ configuration as predicted by Kerek. The next positive parity multiplet was due to the $|\pi d_{5/2}, \nu d_{3/2}^{-1}>$ configuration. Only the 3^+ and 2^+ states were calculated and were found to have a 6% and a 20% mixture of the $|\pi d_{5/2}, \nu s_{1/2}^{-1}>$ configuration, respectively.

The odd parity states were due to the two configurations $|\pi g_{7/2}, \nu h_{11/2}^{-1}>$ and $|\pi d_{5/2}, \nu h_{11/2}^{-1}>$. All of the states were very pure, having admixtures of at most a few percent. As with the positive parity states, the qualitative arrangement of states is explained by the simple delta interaction. The only negative parity level found experimentally was the 8^- level. Its energy with respect to the ground state is unknown.

Again, as with the other two exciton nuclides, the qualitative aspects of the spectrum are explained by a simple delta force picture. The present calculations, however, show good quantitative agreement with the small amount of known experimental data. The lifetime of the 3^+ first excited state is known and the 3^+ to 4^+ transition is known to

be primarily M1. A theoretical lifetime, discussed in chapter 6, has been determined and it agrees well with the measured value.

5.3 Three Exciton Nuclei

The nuclei treated in this section are:

$^{135}_{53}I_{82}$, $^{129}_{50}Sn_{79}$, $^{133}_{52}Te_{81}$, and $^{131}_{51}Sb_{80}$.

$^{135}_{53}I_{82}$

$^{135}_{53}I_{82}$ consists of a 50 proton and 82 neutron core and 3 extra-core protons. Level diagrams from this calculation and from ones by Baldridge[12] and by Wildenthal[30] in addition to the three levels known experimentally[19] are displayed in figure 5.6. The models used by Baldridge and by Wildenthal have been explained in the previous section.

Model wavefunctions for the three calculations are compared in table 5.7. There is general agreement for all levels under 2 MeV. The second $5/2^+$ state and the four successive states are predicted to be almost pure $|g^3_{7/2}>$ configurations. The ground state, although chiefly a $|g^3_{7/2}>$ configuration, is much more mixed. The $7/2^+$, $9/2^+$, and $5/2^+$ levels near 2 MeV are comparatively pure $|g^2_{7/2}, d_{5/2}>$ states. The first excited state is also $|g^2_{7/2}, d_{5/2}>$ with admixtures of $|d^3_{5/2}>$ plus other small components. Wildenthal and Baldridge predict a 16% and 5% $|g^3_{7/2}>$ admixture, respectively. This calculation predicts no such component.

These results can be used as a guide for further experimental investigation of the $^{135}_{53}I_{82}$ nucleus.

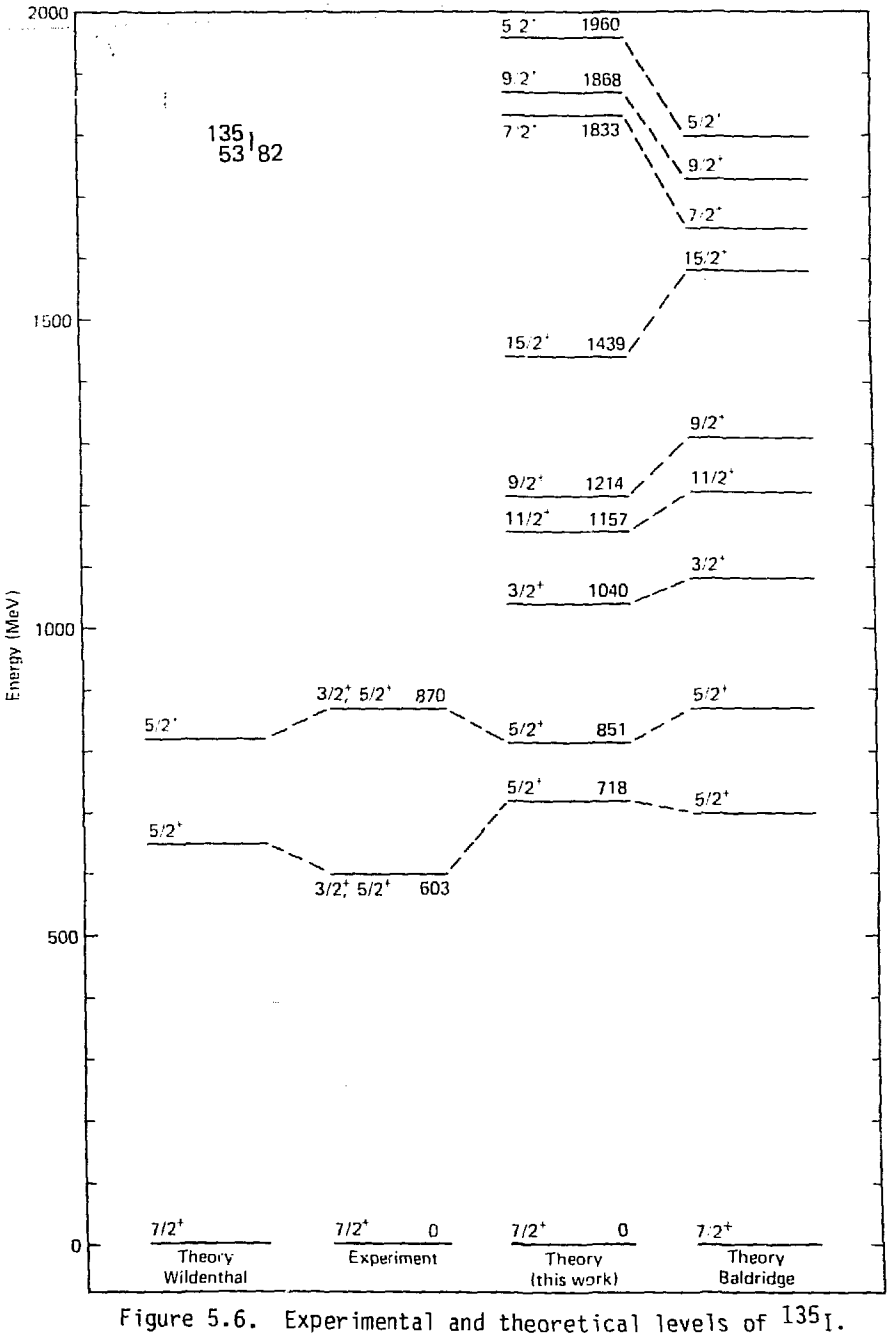

Figure 5.6. Experimental and theoretical levels of ^{135}I.

Table 5.7. $^{135}_{53}I_{82}$ Model Wavefunctions

Energy[a] (keV)	J^{π}	Calculation[b]	Percent Configuration									Total
			g^3	gd_5^2	gh^2	gd_3^2	d_5g^2	d_5^3	d_5h^2	$d_5d_3^2$	d_5h^2	
0	$7/2^+$	L	82	10	4	2						98
		B	69	19	7	3						98
		W	81	18								99
718	$5/2^+$	L					86	6	4	2		98
		B	5				76	9			6	96
		W	16				71	7				94
851	$5/2^+$	L	95	1			1					97
		B	91				4					95
		W	64				18	4				96
1040	$3/2^+$	L	96				1					97
		B	95									95
1157	$11/2^+$	L	95				2					97
		B	97									97
1214	$9/2^+$	L	97				1					98
		B	98									98
1438	$15/2^+$	L	95				4					99
		B	96									96
1833	$7/2^+$	L		12			79					91
1868	$9/2^+$	L					96					96
		B					95					95
1960	$5/2^+$	L										
		B					93	3				96

a) Energies given are those calculated here.
b) L = this calculation; B = Baldridge's calculation(12); W = Wildenthal's calculation(30).

$^{129}_{50}Sn_{79}$

There is no experimental level information for this three-neutron-hole nucleus, but, in the interest of completeness, the calculated levels and model wavefunctions are presented (see figure 5.7 and table 5.8).

Note that all of the states are highly mixed due to the close proximity of the $s_{1/2}$, $d_{3/2}$, and $h_{11/2}$ single particle levels.

$^{131}_{51}Sb_{80}$

Levels at 798.2 keV, 1226.2 keV, 1676.6 keV, and 1981.6 keV have recently been proposed by Schussler, Blachot, Bocquet, and E. Monnand[6] using gamma-gamma coincidence and fission fragment-gamma delayed coincidence information collected at the LOHENGRIN mass separator. The half-life and first excited states have been assigned spins and parities of $7/2^+$ and $5/2^+$ on the basis of systematics. The 1676.6 keV level was found to have a half-life of 50 microseconds and, by analogy with the $^{127}_{51}Sb_{76}$ decay scheme, was tentatively assigned a J^π value of $15/2^-$.

Both experimental and theoretical level diagrams are given in figure 5.8. The positive and negative parity model wavefunctions are given in tables 5.9 and 5.10, respectively. With the exception of the first excited state, all of the positive parity model wavefunctions are built chiefly by coupling a $g_{7/2}$ proton to the two-neutron-hole configurations $|d_{3/2}^{-2}>$, $|s_{1/2}^{-2}>$, $|h_{11/2}^{-2}>$, or $|d_{3/2}^{-1}, s_{1/2}^{-1}>$. The closeness in energy of the $2d_{3/2}$ and the $3s_{1/2}$ single

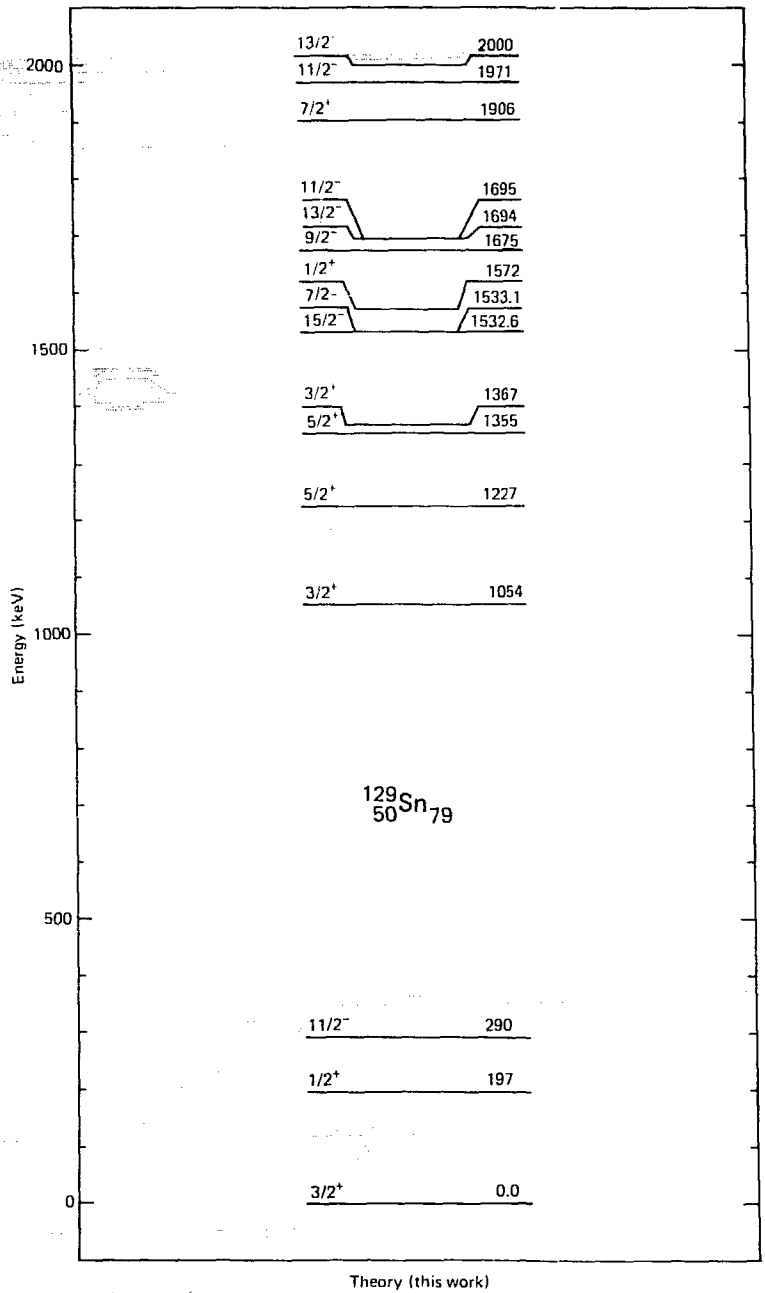

Figure 5.7. Calculated energy levels of $^{129}_{50}Sn_{79}$.

Table 5.8. $^{129}_{50}Sn_{79}$ Model Wavefunctions(*)

Energy (keV)	J^π	Neutron Configurations	Total
0	$3/2^+$	$.39\|d_3^{-1}h^{-2}> + .29\|d_3^{-3}> + .18\|d_3^{-1}s^{-2}> + .08\|d_3^{-1}d_5^{-2}> + .05\|d_3^{-1}g^{-2}>$	.99
197	$1/2^+$	$.53\|s^{-1}d_3^{-2}> + .32\|s^{-1}h^{-2}> + .08\|s^{-1}d_5^{-2}> + .04\|s^{-1}g^{-2}> + .01\|d_3^{-1}s^{-1}d_5^{-1}>$	.99
290	$11/2^-$	$.44\|h^{-1}d_3^{-2}> + .28\|h^{-3}> + .14\|h^{-1}s^{-2}> + .09\|h^{-1}d_5^{-2}> + .04\|h^{-1}d_5^{-2}>$	.99
1054	$3/2^+$	$.31\|d_3^{-3}> + .30\|d_3^{-1}s^{-2}> + .18\|s^{-1}d_3^{-2}> + .08\|d_3^{-1}s^{-1}d_5^{-1}> + .06\|d_3^{-1}h^{-2}> + .01\|s^{-1}h^{-2}> + .01\|d_5^{-1}d_3^{-2}>$	.95
1227	$5/2^+$	$.66\|s^{-1}d_3^{-2}> + .11\|d_3^{-1}h^{-2}> + .08\|d_5^{-1}d_3^{-2}> + .06\|d_3^{-1}s^{-1}d_5^{-1}> + .01\|s^{-1}h^{-2}>$	.92
1355	$5/2^+$	$.41\|d_5^{-1}d_3^{-2}> + .26\|d_5^{-1}h^{-2}> + .15\|d_5^{-1}s^{-2}> + .07\|s^{-1}d_3^{-2}> + .05\|d_5^{-3}> + .04\|d_5^{-1}g^{-2}> + .01\|d_3^{-1}h^{-2}>$	.99
1367	$3/2^+$	$.47\|d_3^{-1}h^{-2}> + .33\|d_3^{-1}s^{-2}> + .13\|d_3^{-3}> + .03\|d_3^{-1}g^{-2}> + .02\|s^{-1}h^{-2}>$	.98
1532.6	$15/2^-$	$.51\|h^{-1}d_3^{-2}> + .30\|h^{-1}d_3^{-1}s^{-1}> + .05\|h^{-1}d_5^{-1}s^{-1}> + .05\|h^{-3}>$	.91
1533.1	$7/2^-$	$.43\|h^{-1}d_3^{-1}s^{-1}> + .34\|h^{-1}d_3^{-2}> + .06\|h^{-1}d_5^{-1}s^{-1}> + .04\|h^{-3}> + .01\|h^{-1}d_5^{-1}d_3^{-1}>$	.88
1572	$1/2^+$	$.41\|s^{-1}h^{-2}> + .24\|s^{-1}d_3^{-2}> + .13\|d_3^{-1}h^{-2}> + .07\|d_5^{-1}d_3^{-1}s^{-1}> + .04\|d_5^{-1}d_3^{-2}>$	.89
1675	$9/2^-$	$.39\|h^{-1}d_3^{-1}s^{-1}> + .26\|h^{-1}d_3^{-2}> + .21\|h^{-3}> + .04\|h^{-1}d_5^{-1}s^{-1}> + .01\|h^{-1}d_5^{-1}d_3^{-1}>$	.91
1694	$13/2^-$	$.79\|h^{-1}d_3^{-2}> + .09\|h^{-1}d_3^{-1}s^{-1}> + .03\|h^{-3}> + .03\|h^{-1}d_5^{-1}s^{-1}>$	.94
1695	$11/2^-$	$.38\|h^{-1}d_3^{-2}> + .27\|h^{-1}d_3^{-1}s^{-1}> + .21\|h^{-3}> + .02\|h^{-1}s^{-2}> + .01\|h^{-1}d_5^{-1}d_3^{-1}> + .01\|h^{-1}d_5^{-1}s^{-1}> + .01\|h^{-1}d_5^{-2}>$	.91
1906	$7/2^+$	$.80\|d_3^{-1}h^{-2}> + .06\|g^{-1}d_3^{-2}> + .05\|d_3^{-1}d_5^{-1}s^{-1}> + .01\|d_5^{-1}d_3^{-2}>$	.92
1971	$11/2^-$	$.69\|h^{-1}s^{-2}> + .24\|h^{-1}d_3^{-2}> + .05\|h^{-1}d^{-1}s^{-1}> + .01\|h^{-1}d_5^{-1}s^{-1}>$	.99
2000	$13/2^+$	$.86\|h^{-1}d_3^{-1}s^{-1}> + .06\|h^{-1}d_3^{-2}> + .03\|h^{-1}d_5^{-1}d_3^{-1}> + .02\|h^{-3}>$	.97

* The format of this table is different from the previous wavefunction tables because of the large number of possible configurations. Before each configuration is the fraction that configuration is of the total mixture.

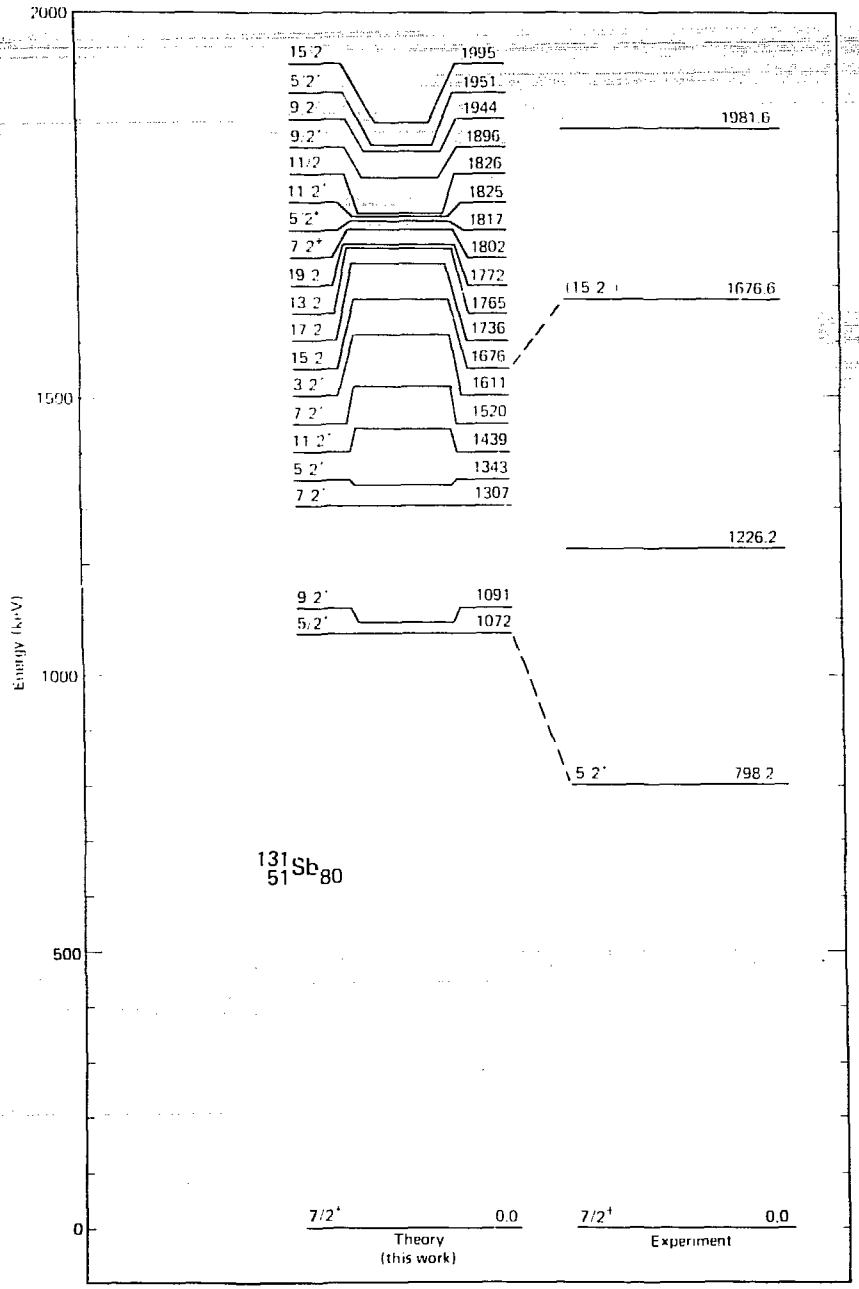

Figure 5.8. Theoretical and experimental energy levels for $^{131}_{51}Sb_{80}$.

Table 5.9. $^{131}_{51}Sb_{80}$ Positive Parity Model Wavefunctions

Energy (keV)	J^{π}	Percent Configurations												Total
		gd_3^{-2}	gs^{-2}	gh^{-2}	gd_5^{-2}	$gs^{-1}d_3^{-1}$	$gd_5^{-1}s^{-1}$	$gd_5^{-1}d_3^{-1}$	$d_5d_3^{-2}$	d_5s^{-2}	d_sh^{-2}	$d_5d_5^{-2}$	$d_5d_3^{-1}s^{-1}$	
0	$7/2^+$	46	18	21	8	4	1							98
1072	$5/2^+$	1							34	14	34	7	3	92
1091	$9/2^+$	33		1		48	9	1						92
1307	$7/2^+$	22	6	16	2	43	4	1						94
1343	$5/2^+$	33		4		33	7	4	1					82
1439	$11/2^+$	57		4		15	4	6						86
1520	$7/2^+$	43	52			3	1							99
1611	$3/2^+$	78		8				4						90
1802	$7/2^+$	20	9	59		4								92
1817	$5/2^+$	42				54	1	2						99
1825	$11/2^+$	32		2		60	2							96
1896	$9/2^+$	52				37	1							90
1951	$3/2^+$	7	1	25		50								83

Table 5.10. $^{131}_{51}Sb_{80}$ Negative Parity Wavefunctions

Energy (keV)	J^{π}	Percent Configurations $gh^{-1}d_3^{-1}$	$gh^{-1}s^{-1}$	Total
1676	$15/2^+$	75	12	87
1736	$17/2^+$	90	3	93
1765	$13/2^+$	73	13	86
1772	$19/2^+$	96		96
1826	$11/2^+$	56	29	85
1944	$15/2^+$	73	16	89
1995	$15/2^+$	93	1	94

particle energies produces substantial mixing of the two-neutron-hole configurations. The first excited state is made of a mixture of these neutron-hole configurations coupled to a $d_{5/2}$ proton.

The low lying negative parity states consist of a $g_{7/2}$ proton coupled to an $h_{11/2}$ neutron hole and either a $d_{3/2}$ or an $s_{1/2}$ neutron hole.

$^{133}_{52}Te_{81}$

Figure 5.9 shows the experimental and theoretical level structure of the one neutron-hole, 2 proton nucleus ^{133}Te which was determined here. Tables 5.11 and 5.12 give the calculated model wavefunctions. Also shown in figure 5.9 are the results of a unified model (UM) calculation by Heyde and Brussard[19] in which they coupled the motion of the single neutron-hole to quadrupole surface oscillations of the ^{134}Te even-even core.

The present calculation found the first three levels ($J^\pi = 3/2^+$, $1/2^+$, and $11/2^-$) to be ≈80% pure single hole states which agrees with UM results and with neutron pick-up reactions performed by Jolly and Kashy[109] and by Chaumeaux et al.[110] These $3/2^+$, $1/2^+$, and $11/2^-$ levels were formed from two protons in the $g_{7/2}$ orbital, coupling to zero, and the neutron hole in the $d_{3/2}$, $s_{1/2}$, or $h_{11/2}$ orbitals. Below 2 MeV, only the $5/2^+$ and $3/2^+$ positive parity states are strongly fragmented while the other states are ≈80% pure. An exception is the 1611 $11/2^+$ state which is also fragmented. Ninety percent of the mixture of all of the positive parity states, except the 1496 $5/2^+$ state, are made from the

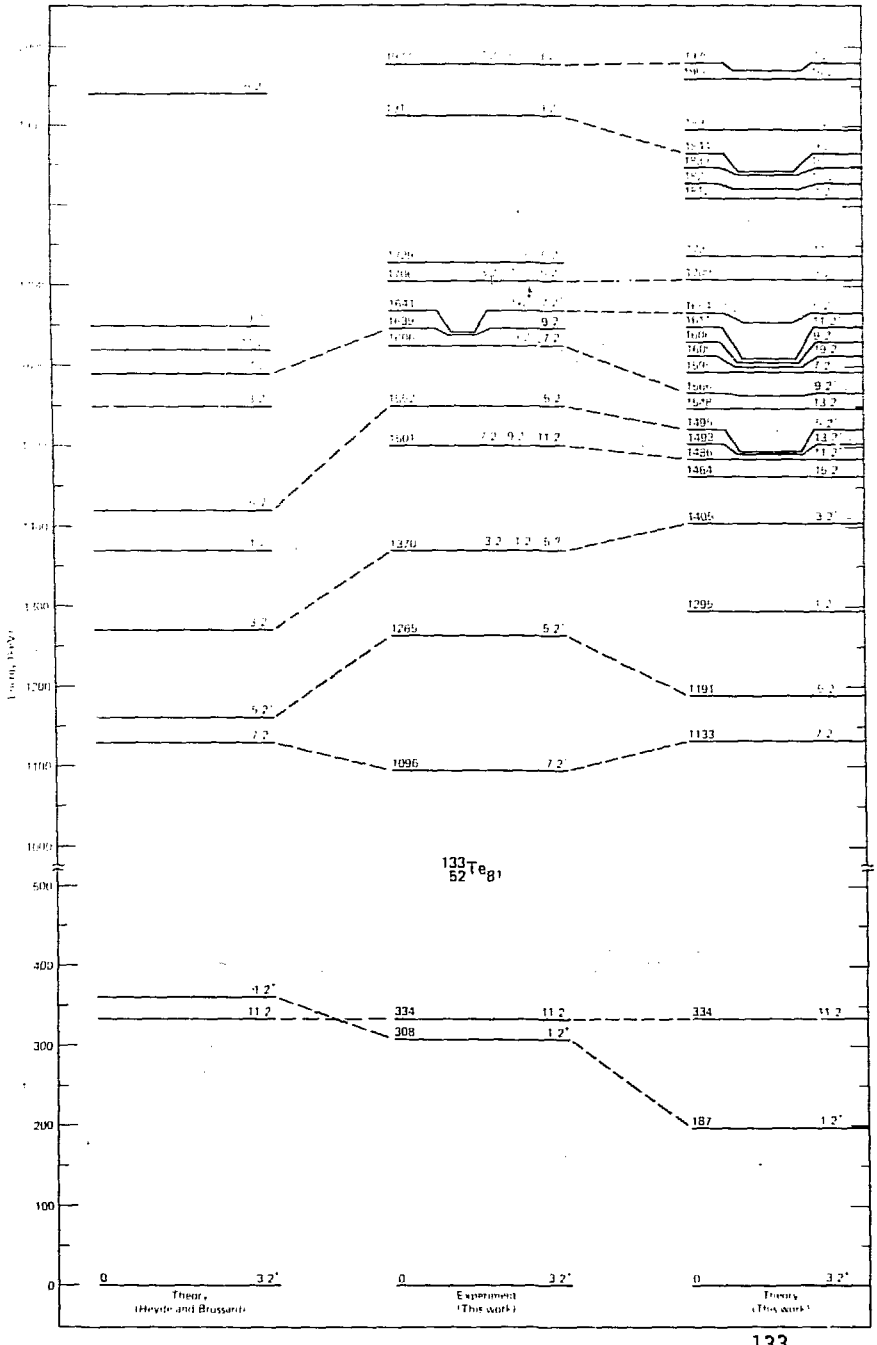

Figure 5.9. Theoretical and experimental levels of $^{133}_{52}Te_{81}$.

Table 5.11. $^{133}_{52}Te_{81}$ Positive Parity Model Wavefunctions

Energy (keV)	J^π	Percent Configuration																	Total
		$g^2d_3^{-1}$	$d_5^2d_3^{-1}$	g^2s^{-1}	$h^2d_3^{-1}$	$d_3^2d_3^{-1}$	$s^2d_3^{-1}$	$d_5^2s^{-1}$	gd_3s^{-1}	$d_3^2s^{-1}$	$d_5sd_3^1$	h^2s^{-1}	$gd_3d_3^{-1}$	$g_2d_5^{-1}$	$d_3^2d_5^{-1}$	$gd_5d_3^{-1}$	$h^2d_5^{-1}$	gd_5s^{-1}	
0	$3/2^+$	82	7	3	4	1	1							2					98
187	$1/2^+$	10		75				7		7		4		2					99
1133	$7/2^+$	86		11										1					98
1191	$5/2^+$	48	1	37										11					97
1295	$1/2^+$	85		7				1						5					98
1405	$3/2^+$	60	1	30	1									6					98
1486	$11/2^+$	95												3		1		1	100
1493	$13/2^+$	82		13										1		3			99
1496	$5/2^+$	39	4	1										51	1		2		98
1566	$9/2^+$	89		6										3		1			99
1611	$11/2^+$	59		36										1		2		1	99
1654	$5/2^+$	60	1	30					1		1		2	4					99
1709	$3/2^+$	31		57					1				1	7					97
1812	$7/2^+$	87		6										4		1			98
1839	$15/2^+$	99														1			100
1844	$9/2^+$	24		70										3		1			98
1970	$7/2^+$	16		79										3		1			99

Table 5.12. $^{133}_{52}Te_{81}$ Negative Parity Model Wavefunctions

Energy (keV)	J^{π}	Percent Configurations							Total
		g^2h^{-1}	$d^2h_5^{-1}$	$d_3^2h^{-1}$	sh^{-1}	gd_3h^{-1}	gd_5h^{-1}	d_5sh^{-1}	
334	11/2-	79	12	2	1	1	1		96
1464	15/2-	94	1			1	3		99
1548	13/2-	91	1			2	4		98
1595	7/2-	96	1						97
1600	19/2-	95					4		99
1606	9/2-	90	2			2	4	1	98
1737	11/2-	94	1			2	1		98
1822	17/2-	96				1	2		99
1897	5/2-	93	1				6		100
1960	15/2-	88				2	9		99

$|\pi g^2_{7/2}\ \nu d^{-1}_{3/2}>$ or $|\pi g^2_{7/2}\ \nu d^{-1}_{5/2}>$ configurations. The 1496 $5/2^+$ state is a mixture of $|\pi g^2_{7/2}\ \nu d^{-1}_{3/2}>$ and $|\pi g^2_{7/2}\ \nu d^{-1}_{5/2}>$. The negative parity states are all 90% $|\pi g^2_{7/2}\ \nu h^{-1}_{11/2}>$.

Heyde and Brussard's calculation also agree with the experiment. However, the UM approach adjusted the energy of the surface oscillations, the collective motion - single particle coupling constant, and the single particle energies to give a best fit to other N=81 nuclei.

None of the theoretical states with spins greater than 11/2 were experimentally detectable because these states are unlikely to be populated by beta-decay. The same is true for the $1/2^+$ state calculated at 1295 keV.

The calculation of low-lying states (below 2 MeV) agrees well with both experiment and systematics (see figure 4.1).

5.4 Four Exciton Nuclei

This section will present the results of shell model calculations on $^{128}_{50}Sn_{78}$, $^{130}_{51}Sb_{79}$, $^{132}_{52}Te_{80}$, $^{134}_{53}I_{81}$, and $^{136}_{54}Xe_{82}$.

$^{128}_{50}Sn_{78}$

The calculated and experimental level schemes are given in figure 5.10 and the model wavefunctions are given in tables 5.13 and 5.14. With the exception of the two 0^+ states, the dominant configuration for the positive parity states is one in which there are two neutron holes in both the $d_{3/2}$ and $h_{11/2}$ orbitals. The dominant configuration for the first 0^+ state has two neutron holes in both the $d_{3/2}$ and $s_{1/2}$ orbitals while the second 0^+ state is mostly made of a configuration having four holes in the neutron $d_{3/2}$ orbital. All states, including the negative parity states, are highly fragmented. Agreement with experiment is fair especially if one keeps in mind that the 0^+ states are difficult to detect experimentally when populated from beta decay.

$^{130}_{51}Sb_{79}$

The levels of $^{130}_{51}Sb_{79}$ have been independently investigated by A. Kerek et a.[17] and by L. Nunnelly.[116] Regarding the ^{130}Sn decay scheme, there is general agreement between these workers except for the absence of the 341 keV and 726 keV positive parity levels and the 85 keV and 145 keV negative parity levels in Nunnelly's scheme.

The results of the present calculations using the ^{131}Sn single particle set and the usual valence space are given in figures 5.11 and 5.12 along with Kerek's experimental spectrum. Tables 5.15 and 5.16

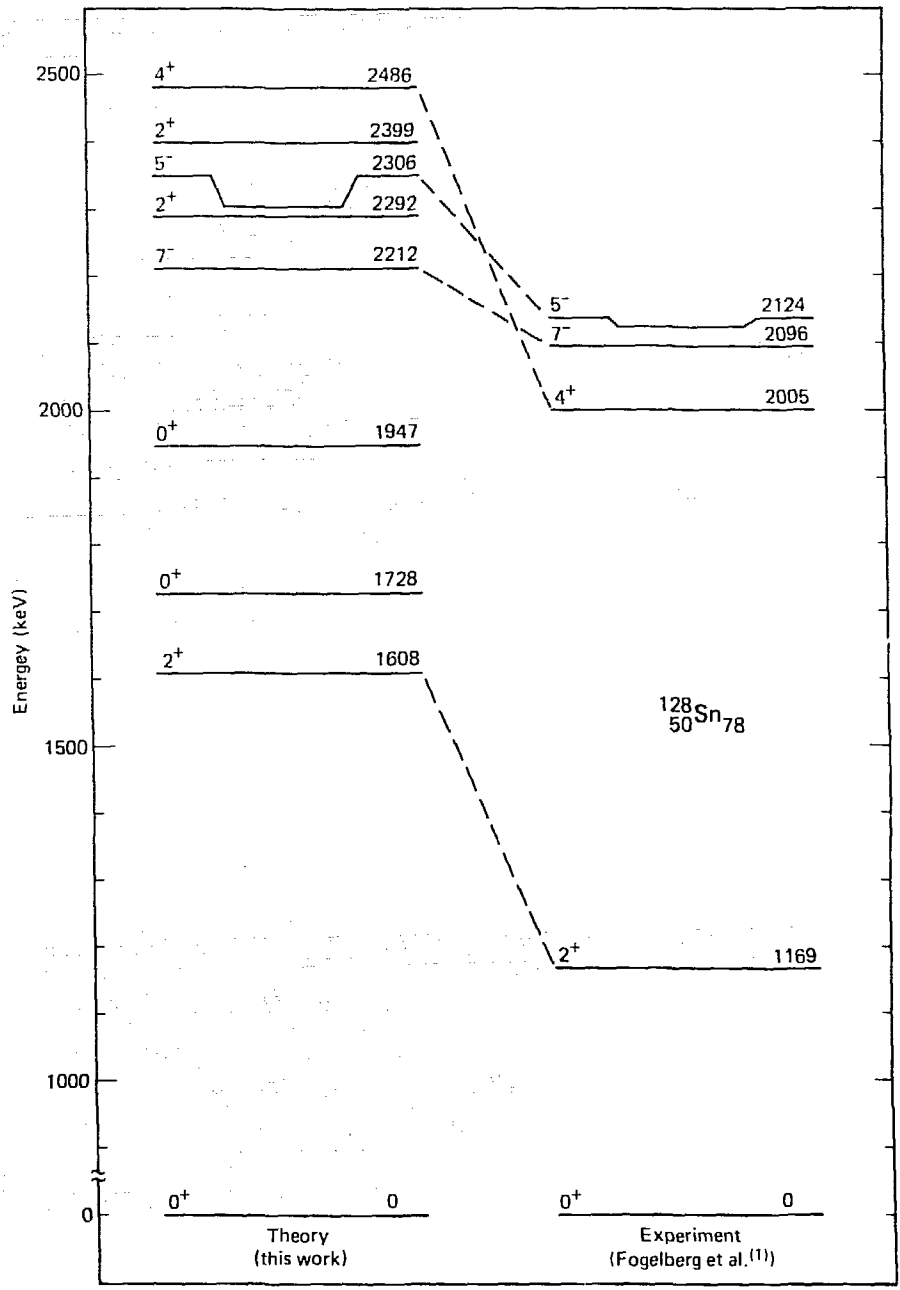

Figure 5.10. Experimental and calculated level structure of ^{128}Sn.

Table 5.13 $^{128}_{50}Sn_{78}$ Positive Parity Model Wavefunctions

Energy (keV)	J^π	Percent Configurations											Total
		$d_3^{-2}h^{-2}$	$d_3^{-2}s^{-2}$	h^{-4}	$s^{-2}h^{-1}$	d_3^{-4}	$d_5^{-2}d_3^{-2}$	$d_5^{-2}h^{-2}$	$d_3^{-1}s^{-1}h^{-2}$	$d_3^{-3}s^{-1}$	$d_5^{-2}s^{-2}$	$d_5^{-1}d_3^{-1}h^{-2}$	
0	0^+	30	13	11	11	8	7	7					87
1608	2^+	25	10						16	14			65
1728	0^+	10	48	21							5		84
1947	0^+			8	25	46	7						86
2292	2^+	34	20						12	19			85
2399	2^+	32	8	16	8			6		16			86
2486	4^+	43		18	13			8				5	87

Table 5.14. $^{128}_{50}Sn_{78}$ Negative Parity Model Wavefunctions

Energy (keV)	J^{π}	Percent Configurations							Total
		$d_3^{-1}h^{-3}$	$d_3^{-3}h^{-1}$	$d_3^{-1}s^{-2}h^{-1}$	$g^{-2}d_3^{-1}h^{-1}$	$d_3^{-2}s^{-1}h^{-1}$	$s^{-1}h^{-3}$	$d_3^{-1}s^{-2}h^{-1}$	
2212	7-	33	30	21	8				92
2306	5-	16	21			26	11	8	82

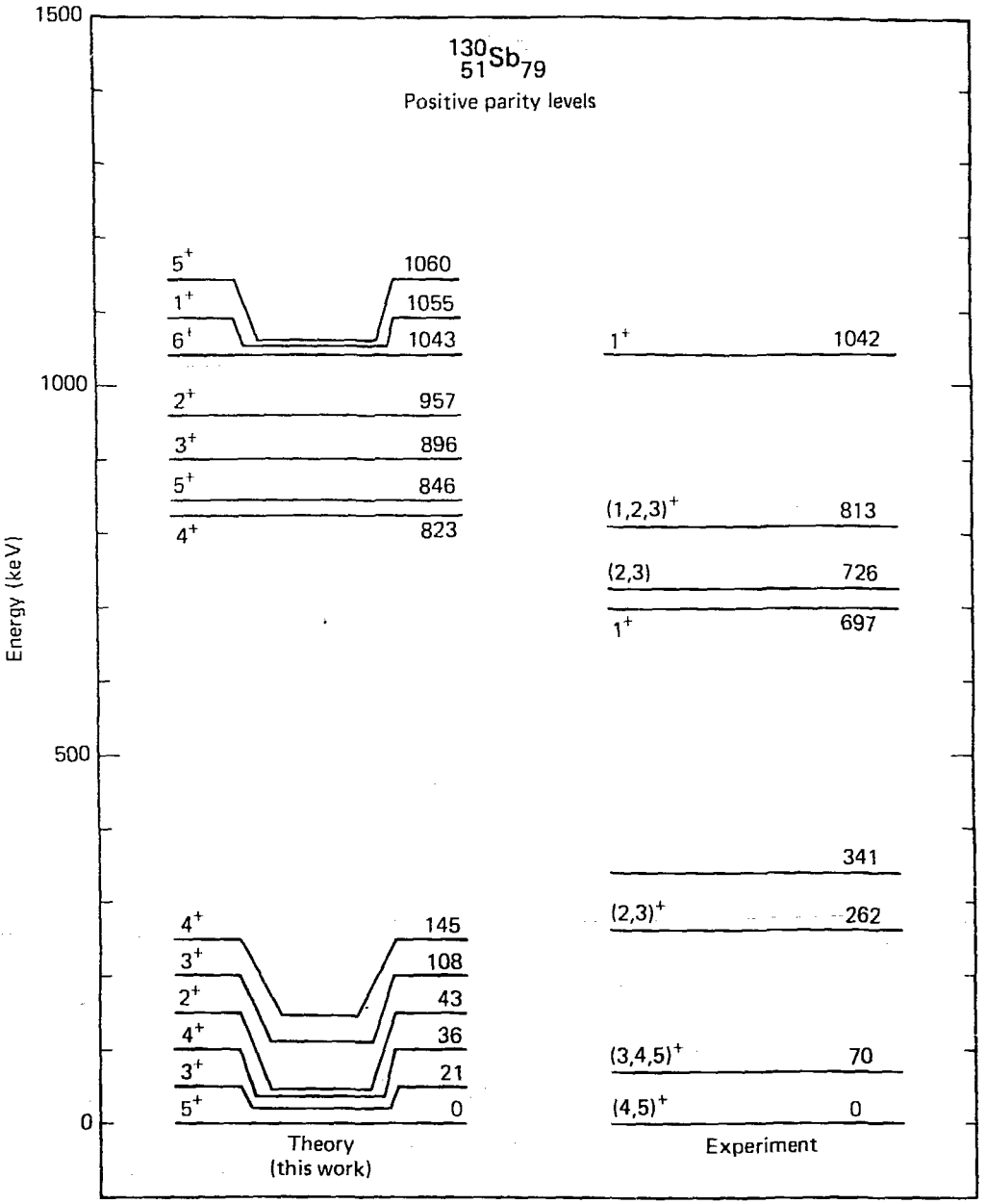

Figure 5.11. Theoretical and experimental positive parity levels for $^{130}_{51}Sb_{79}$.

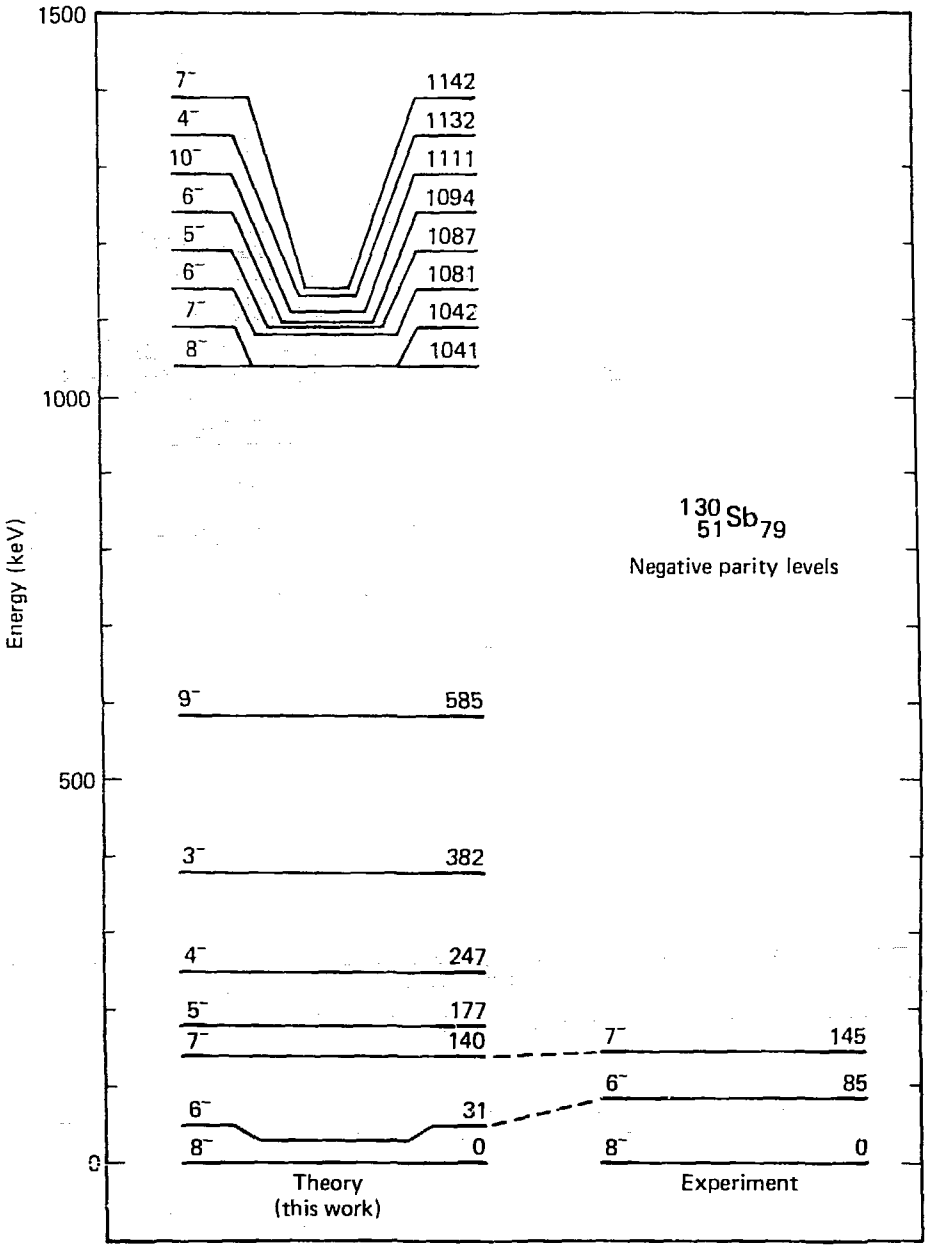

Figure 5.12. Theoretical and experimental negative parity levels for $^{130}_{51}Sb_{79}$.

Table 5.15. $^{130}_{51}Sb_{79}$ Positive Parity Model Wavefunctions

Energy (keV)	J^{π}	Percent Configurations										Total
		gd_3^{-3}	$g_{\frac{1}{2}}^{-1}s^{-2}$	$gd_3^{-1}h^{-2}$	$gd_5^{-2}d_3^{-1}$	$gd_3^{-2}s^{-1}$	$gs^{-1}h^{-2}$	$gd_5^{-2}s^{-1}$	$gd_5^{-1}d^{-2}_3$	$gd_5^{-1}d_{\frac{1}{2}}^{-1}s^{-1}$	$gd_5^{-1}h^{-2}$	
0	5^+	42	20	19	7	6						94
21	3^+	14	35	18	6	20						93
36	4^+	17	38	31	8							94
43	2^+	49	14	14	6	7						90
108	3^+	14		10		45	17	6				92
145	4^+					62	16	6	5			89
823	4^+	17	25	10		23			10	9		94
846	5^+	17	27	6					17	10		77
896	3^+	24	13	5		23	8			13		86
957	2^+	12	27	10		29				6		84
1043	6^+			10		71				6		87
1055	1^+			12		65				6		83
1060	5^+		6			41			17	9	14	88

Table 5.16. $^{130}_{51}Sb_{79}$ Negative Parity Model Wavefunctions

Energy (keV)	J^{π}	Percent Configurations										Total
		$gd_3^{-2}h^{-1}$	$gs^{-2}h^{-1}$	gh^{-3}	$gd_5^{-2}h^{-1}$	$gd_3^{-1}s^{-1}h^{-1}$	$gd_5^{-1}s^{-1}h^{-1}$	$d_5d_3^{-2}h^{-1}$	d_5h^{-3}	$d_5s^{-2}h^{-1}$	$d_5d_5^{-2}h^{-1}$	
0	8⁻	51	19	15	8							93
31	6⁻	51	19	13	8	6						97
140	7⁻	50	20	12	7	8						95
177	5⁻	49	18	14	8	6						95
247	4⁻	49	18	16	8	6						97
382	3⁻	47	17	17	8							89
565	9⁻	49	15	14	7	11						96
1041	8⁻	38				42	8					88
1042	7⁻	6					10	33	20	12	6	87
1081	6⁻	30				39	7					76
1087	5⁻	25				40	6	6				77
1094	6⁻	8				11		31	17	11		78
1111	10⁻	51				30	6					87
1132	8⁻	30		6		44	7	5				92
1142	7⁻	27		5		39	6	7				94

give the model wavefunctions calculated here. The energy of the 8^- state relative to the ground state is unknown and has arbitrarily been set to zero. It can be seen that a correspondence between theory and experiment is difficult because of the uncertainty in experimental spin and parity assignments. Again the level structure can be qualitatively described by coupling the valence proton to the three neutron holes. The first four positive parity levels (2^+, 3^+, 4^+, 5^+) are a result of a $g_{7/2}$ proton coupled to a $|d_{3/2}^{-3}>_{3/2^+}$ or a $|d_{3/2}^{-1}\ s_{1/2}^{-2}>_{1/2^+}$ state and the next two levels (3^+ and 4^+) are due to the $g_{7/2}$ proton coupling to a $|d_{3/2}^{-2}\ s_{1/2}^{-1}>_{1/2^+}$ neutron state. Because of the close proximity of the $d_{3/2}$, $s_{1/2}$, and $h_{11/2}$ single particles, substantial mixing occurs as witnessed by the model wavefunctions.

The next set of positive parity states (1^+, 2^+, 3^+, 4^+, 5^+,and 6^+) can be thought of as a result of the $g_{7/2}$ proton coupling to $|d_{3/2}^{-3}>_{3/2^+}$ or $|d_{3/2}^{-2}\ s^{-1}>_{3/2^+}$ neutron states since such a neutron configuration appears at 1 MeV in the 3 neutron-hole spectrum of ^{129}Sn. The model wavefunctions indicate that this multiplet is not due to a $d_{5/2}$ proton as Nunnelly has suggested. The last three states are probably due to a $|g_{7/2}>_{7/2^+} + |d_{3/2}^{-2}\ s_{1/2}^{-1}>_{5/2^+}$ coupling. Similarly, the first negative parity level grouping (2^-, 3^-, 4^-, 5^-, 6^-, 7^-, 8^-, and 9^-) are due to the $g_{7/2}$ proton coupled to a $|d_{3/2}^{-2}\ h_{11/2}^{-1}>_{11/2^-}$ state. The 2^- level was mysteriously absent from the computed spectrum possibly because of a faulty Lanczos start vector.

It is difficult to explain in this simplified fashion the grouping of negative parity levels between 1 MeV and 1.5 MeV. It is perhaps an oversimplification to even attempt to explain the coupling of 4 particles (or holes) by conjecturing, for example, that two of the particles (or holes) couple to zero and the remaining two couple in a way that gives the observed spectrum, without first analyzing the model wavefunctions and determining the coefficients of fractional parentage.

One glaring discrepancy in the calculation lies in the lack of a state corresponding to the first experimental 1^+ state. If this assignment is indeed correct, it indicates the presence of a phenomenon outside the scope of the present model. Another slight difficulty with the calculation is the violation of the Brennan-Bernstein rule[95] which predicts a 4^+ ground state. Since the nearest 4^+ state to the 5^+ ground state is only 36 keV away, this is not considered serious.

$^{132}_{52}Te_{80}$

The model wavefunctions of the 2-proton 2-neutron-hole nucleus, ^{132}Te, are given in tables 5.17 and 5.18 while figure 5.13 shows the experimental level structure[54] and the theoretical shell model results. Also shown are the results of a calculation by Degrieck and Vanden Berghe[14] using the unified model[108]. Up to three phonon states of the ^{130}Sn core were coupled to the motion of 2 valence protons in the Degrieck calculation. The protons had access to the entire gddsh shell and the residual interaction between them

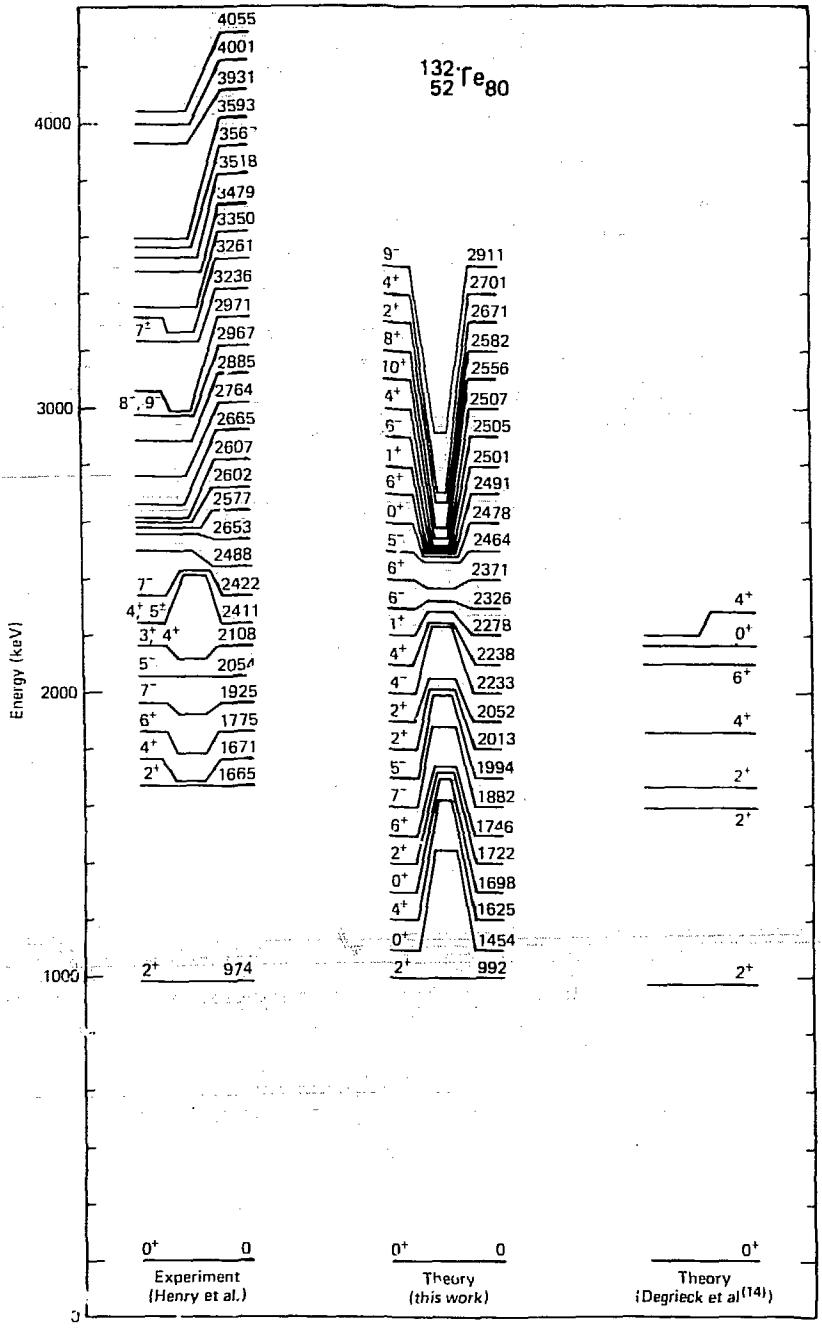

Figure 5.13. Theoretical and experimental level structure of ^{132}Te.

$^{132}_{62}Sm_{70}$ Positive Parity Model Wavefunctions

Energy (keV)	J^{π}	Percent Configuration												
		$g^2d_3^{-2}$	g^2h^{-2}	g^2s^{-2}	$g^2d_5^{-2}$	$g^2f_7^{-1}h^{-1}$	s^2h^{-2}	$g^2d_5^{-1}f_7^{-1}$	$d_5^2f_7^{-2}$	$g^2h_9^{-1}h^{-1}$	$s^2d_5^{-2}$	$d_5^2f_7^{-2}$	$g^2h_9^{-2}$	$d_5^2d_3^{-2}$	$s^2h_9^{-2}$	
0	0^+	34	22	16	7	22										78
992	2^+	34	13	11		22										80
1454	0^+		38	25		7	12									87
1675	4^+	39	24	16	7	7										93
1698	0^+	42	5	35												82
1742	2^+	31	21	5		19										76
1746	6^+	38	24	16	7											85
2013	2^+	17	31			27	6									81
2057	2^+	39	31			8	6									84
2238	4^+		53			6	9	12								80
2278	1^+					92			5							87
2331	6^+		6								35		26	5	11	83
2478	0^+		19				33					20				77
2491	6^+		69				13									91
2501	1^+	23	6			44		8		12						93
2507	4^+	12	27			25		17								81
2566	10^+		74				14									86
2582	8^+		75				14									89
2671	2^+										32		25		11	68
2701	4^+	5	5								33		19		8	70

Table 5.18. $^{132}_{52}Te_{80}$ Negative Parity Model Wavefunctions

Energy	J^{π}	Percent Configurations				Total
		$g^2d_3^{-1}h^{-1}$	$d_5^2d_3^{-1}h^{-1}$	$g^2s^{-1}h^{-1}$	$d_5^2s^{-1}h^{-1}$	
1882	7^-	78	8			86
1994	5^-	40		41		81
2233	4^-	80	8			88
2326	6^-	72	7	11		90
2464	5^-	49		32		81
2505	6^-	20		62	6	88
2911	9^-	82		11		93

was the surface delta interaction. The SPE's, the single particle-phonon coupling parameter, the amplitude of the core oscillations and the strength of the surface delta function were obtained by fitting the known energy levels of A=126-134 tellurium isotopes. Only positive parity levels were calculated. Agreement with experiment is good, which is not surprising given the number of adjustable parameters.

Agreement between experiment and the shell model calculation is also good. The shell model, however, predicts two low lying 0^+ states not observed experimentally or predicted by the unified model calculation. It may be that these levels are not populated strongly in a ^{132}Te nucleus produced in beta decay.

Of particular interest are the model wavefunctions of the levels below 2.4 MeV. The valence protons remain paired in the $g_{7/2}$ sub-shell in all of the dominant configurations in this energy region. This implies that the low energy ^{132}Te level structure is similar to the ^{130}Sn two neutron hole structures. This is indeed the case as seen in figure 5.14 where negative parity and 0^+, 1^+, and 2^+ ^{132}Te levels are compared to the ^{130}Sn levels. The 4^+ and 6^+ states are absent from the ^{130}Sn calculation probably because of a faulty start vector in the Lanczos calculation. If the ^{132}Te - ^{130}Sn analogy holds as it appears to, credence is added to the prediction of the two 0^+ levels.

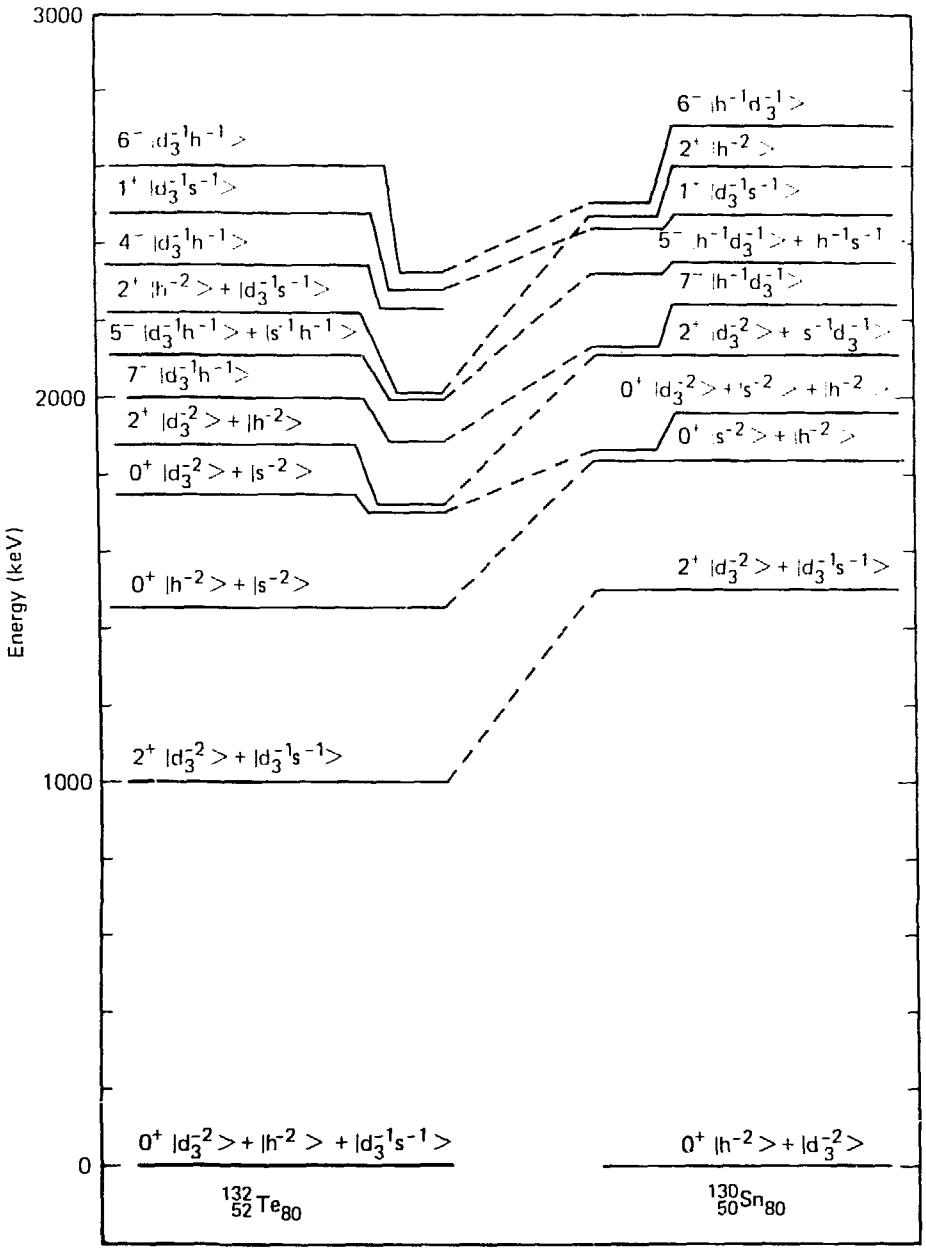

Figure 5.14. Dominant configurations of ^{132}Te are compared with those of ^{130}Sn.

$^{134}_{53}I_{81}$

Several experimental levels of the three-valence proton one neutron-hole nucleus, $^{134}_{53}I_{81}$, have been measured by Meyer et al.[29] and are shown along with the results of present calculations in figures 5.15 and 5.16. A qualitative explanation of the levels under 2 MeV can be obtained by coupling the lower levels of the three-valence-proton nucleus, $^{135}_{53}I_{82}$, to the single neutron-hole single particle states of $^{131}_{50}Sn_{81}$. For instance, the ^{135}I ground state, $|g^3_{7/2}>_{7/2^+}$, coupled to the ^{131}Sn ground state, $|d^{-1}_{3/2}>_{3/2^+}$ gives rise to the 2^+, 3^+, 4^+, 5^+ multiplet which constitute the first four states in ^{134}I. The next two states (3^+ and 4^+) result from the ^{135}I $|g^3_{7/2}>_{7/2^+}$, ^{131}Sn $|s^{-1}_{1/2}>_{1/2^+}$ couplings. The first negative parity multiplet (2^-, 3^-, 4^-, 5^-, 6^-, 7^-, 8^-, and 9^-) can be constructed from ^{135}I $|g^3_{7/2}>_{7/2^+}$ and ^{131}Sn $|h^{-1}_{11/2}>_{11/2^-}$. One can continue in this manner, identifying levels in ^{134}I as due to couplings of levels in ^{135}I and ^{121}Sn, but at higher energies the correspondence becomes more and more tenuous since several combinations can lead to the same ^{134}I level and substantial configuration mixing can be expected to occur. The basic idea, however, is corroborated by an inspection of the model wavefunctions (see tables 5.19 and 5.20).

Several features of the calculated spectrum should be pointed out. Firstly, the energy of the lowest negative parity state (8^-) relative to the ground state was not determined and was arbitrarily set equal to the experimental value. Secondly, only levels with spins 1 and 2 were calculated above the 1115 keV level; there are undoubtedly some missing levels of higher spins in the 1115 keV -

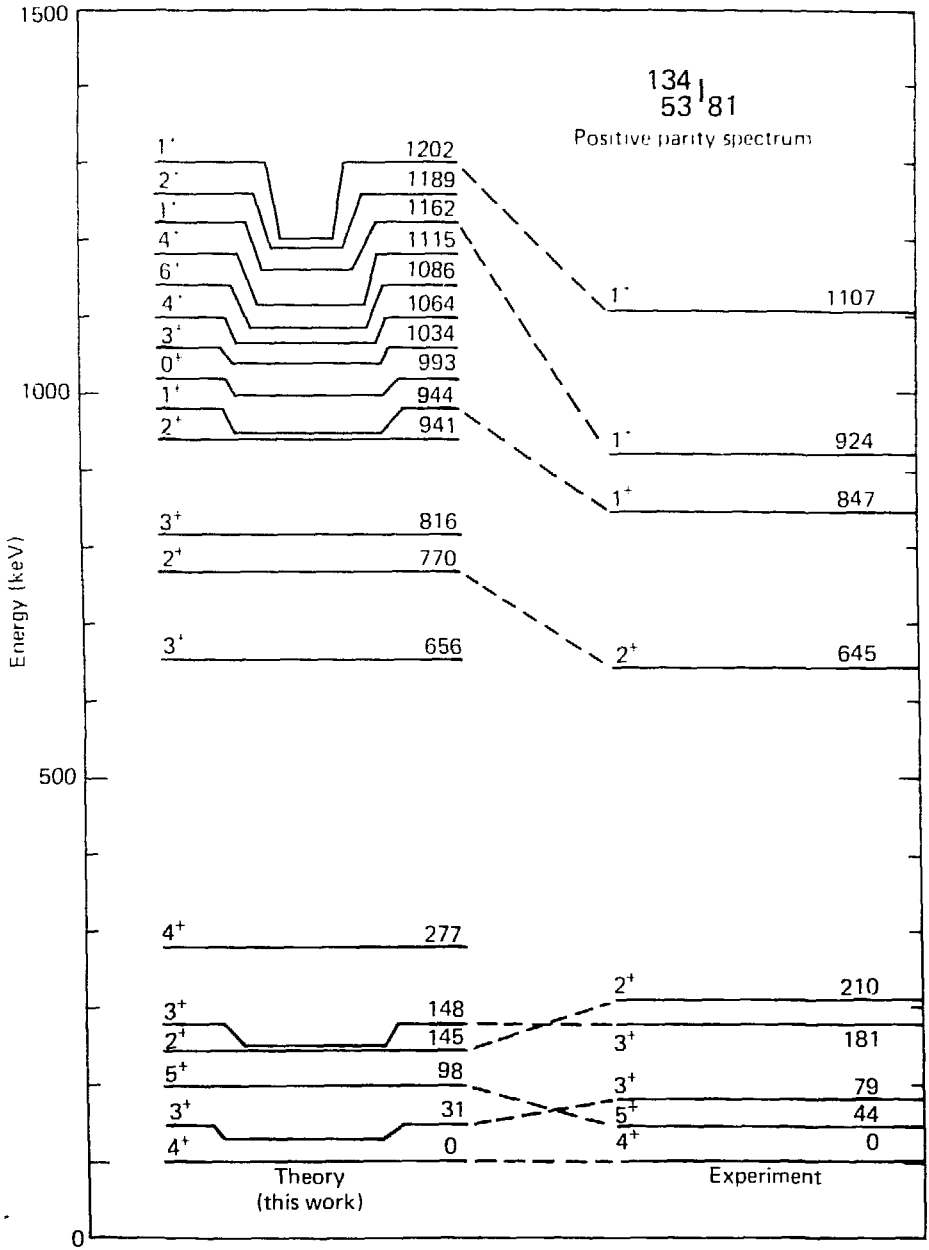

Figure 5.15. Theoretical and experimental positive parity level structure of ^{134}I.

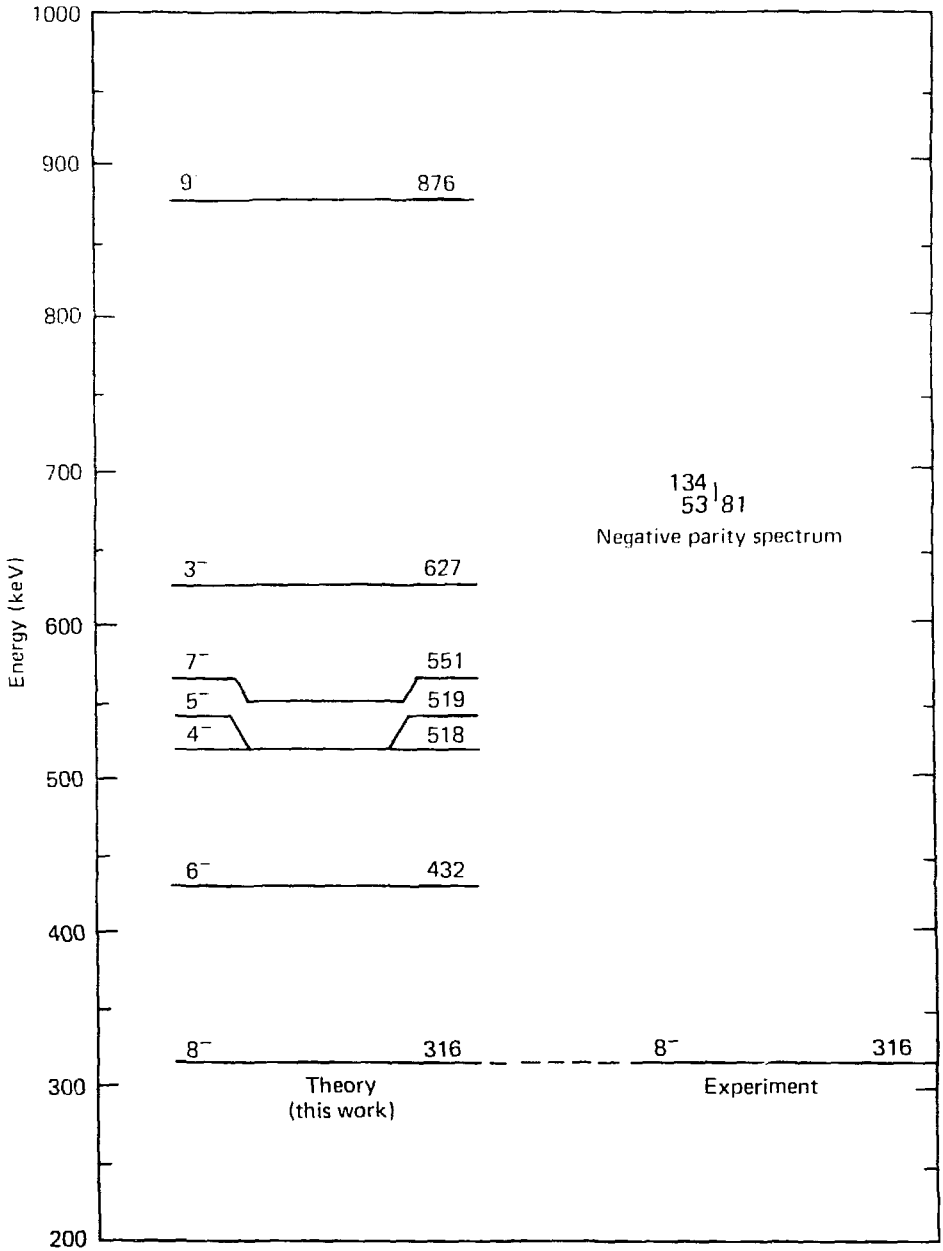

Figure 5.16. Theoretical and experimental negative parity level structure of ^{134}I.

Table 5.19. $^{134}_{53}I_{81}$ Positive Parity Model Wavefunctions

Energy (keV)	J^π	Percent Configurations									Total
		$g^3_{7/2}d^{-1}_{3/2}$	$g^3_{7/2}s^{-1}_{1/2}$	$gd^2_{5/2}d^{-1}_{3/2}$	$gd^2_{5/2}s^{-1}_{1/2}$	$g^2_{7/2}d_{5/2}d^{-1}_{3/2}$	$g^3_{7/2}d^{-1}_{5/2}$	$g^2_{7/2}d_{5/2}s^{-1}_{1/2}$	$d^3_{5/2}s^{-1}_{1/2}$	$d^3_{5/2}d^{-1}_{3/2}$	
0	4^+	74	5	4							83
31	3^+	76	6	5							87
98	5^+	81	3	5							89
145	2^+	74	9		1						84
148	3^+	18	65		5						88
277	4^+	15	67	6							88
656	3^+					74		9			83
770	2^+					56		25			81
816	3^+	68	19				1				88
941	2^+	42	40				3				85
944	1^+	80	12								92
993	0^+	93									93
1034	3^+					11		61	3		75
1064	4^+	77	8				1				86
1086	6^+	91									91
1115	4^+					69		4	2		75
1162	1^+	4	9			61				4	78
1189	2^+	44	20			7		13			84
1202	1^+	47	30	10			4				91

Table 5.20. $^{134}_{53}I_{81}$ Negative Parity Model Wavefunctions

Energy (keV)	J^{π}	Percent Configurations						Total
		g^3h^{-1}	$gd_5^2h^{-1}$	gh^2h^{-1}	$gd_3^2h^{-1}$	$g^2d_5h^{-1}$	$gd_3^2h^{-1}$	
0	8^-	79	12	3	2			96
116	6^-	77	13	3	2			95
202	4^-	79	11	3	2			95
203	5^-	77	12	3		2	2	96
234	7^-	75	13	3		2	2	95
311	3^-	76	10	3		4	2	95
560	9^-	79	12	3	2			96

1202 keV range.

Alaga and co-workers[111] have explained several features of the odd-mass iodine nuclei with a three-particle clustering. At least as far as level energies are concerned, the features of the ^{134}I spectrum are reproduced fairly well without explicit reliance on clustering.

$^{136}_{54}Xe_{80}$

Because ^{136}Xe has four extra core protons and a closed neutron shell, it is ideal for shell model calculations. Model wavefunctions shown in tables 5.21 and 5.22 and the calculated level structure shown in figure 5.17 are compared with other shell model results by Baldridge[12] and by Wildenthal and Larsen.[10] The specifics of the models used by these workers were discussed in the ^{134}Te section. Figure 5.17 also displays the results of two-quasiparticle calculations done both by Hyde, Waroquier, and Vanden Berghe[23], and by Lombard.[31]

Western et al.[33] established the experimental level scheme shown in figure 5.17 from a study of the beta decay of ^{136}I at the TRISTAN isotope separator.

The three shell model calculations predict much the same level structure below 2.5 MeV. The $(6^+)_2$ and $(4^+)_2$ ordering for this calculation and for the Wildenthal calculation agree with experiment while the Baldridge result is inverted. The $(0^+)_1$

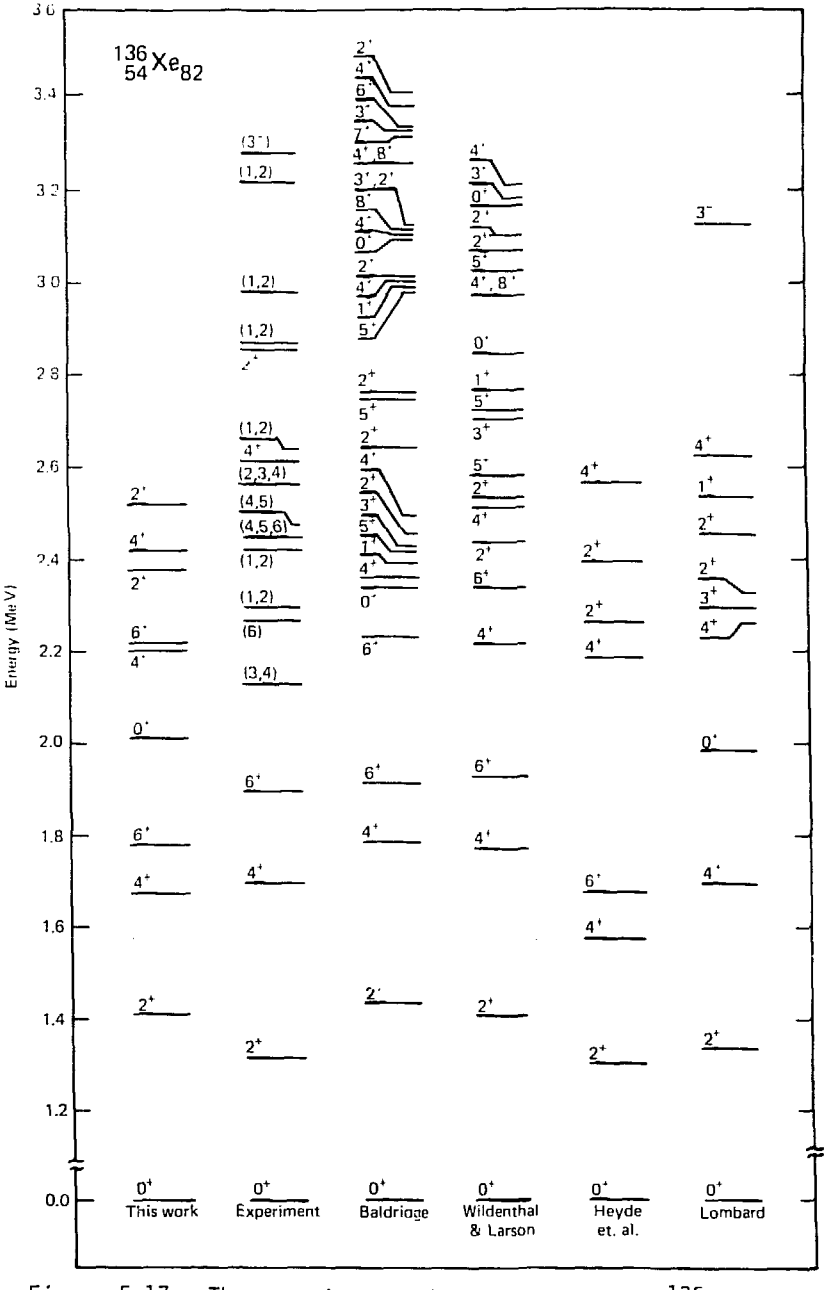

Figure 5.17. The experimental level structure of ^{136}Xe is compared to several theoretical calculations.

Table 5.21. $^{136}_{54}Xe_{82}$ Positive Parity Model Wavefunctions

Energy (keV)	J^π	Percent Configurations											Total
		g^4	$g^2d_5^2$	g^2h^2	g^3d_5	gd_5^3	$g^2d_3^2$	$d_5^2h^2$	g^3d_3	d_5^4	gd_5h^2	$d_5^2d_3^2$	
0	0^+	64	15										79
		43	30	12			4	3		2			94
		64	34										98
1403	2^+	64	12										76
		58	25	7			3						93
		64	20										84
1674	4^+	81	10										91
		63	3	7									73
		67	14		7								88
1778	6^+	80	9	1									90
		65	23	7			3						98
		62	14		19								95
2010	0^+	28	41										69
		39	35					4		11		3	92
2191	4^+	93			1								94
		59			25	4					2		90
		66			6				4				76
2217	6^+				82	4							86
					75	11						9	95
		19			64	9							73
2372	2^+	94			1								95
		7	9		53	7							76
2425	4^+				76								76
		34			44	6						4	88
2510	2^+	1			76								77

Energies are those calculated in this work. The first row of % configurations is from these calculations, the second is from Baldridge [12] and the third is from Wildenthal and Larsen [10].

Table 5.22. $^{136}_{54}Xe_{82}$ Negative Parity Model Wavefunctions

Energy (keV)	J	Percent Configurations g^3h	gd_5^2h	Total
3937	9-	79	3	81
4275	7-	69		69
4370	8-	79		79
4380	5-	76		76
4460	6-	71		71

level is 300 keV lower than the one found by Baldridge and 800 keV lower than that computed by Wildenthal. The 0^+ level was not seen experimentally.

The positive parity model wavefunctions for these calculations are compared in table 5.21. The calculations done here find the states to be generally more pure than the states calculated by Baldridge and Wildenthal, especially the $(4^+)_2$ and the $(4^+)_3$ states. A major difference occurs in the $(2^+)_2$ state in which Baldridge finds a 7% $|g^4>$ admixture while this calculation finds the state to be 94% $|g^4>$. The lowest negative parity states from the calculation done here (see table 5.22) are all $|g^3h>$ configuration.

5.5. $^{135}_{54}Xe_{81}$

^{135}Xe is a five exciton nucleus having four extra core protons and a valence neutron hole. In the code's present state, this problem represents a practical upper limit in terms of valence space size and exciton number. The valence space used was the full gddsh proton and neutron shells with the $g_{7/2}$ neutrons frozen to that subshell. To keep the multiparticle basis set less than 30,000, the Lanczos start vector used was coupled to produce good J and M_J values. That is, a different start vector was used for each spin value. Even so, the multiparticle basis set had typically 27,000 states making this the largest shell model calculation ever done. Because of computer time considerations, only the $1/2^+$, $3/2^+$, $5/2^+$, $7/2^+$, and $9/2^+$ states below 2.5 MeV have been calculated to date. Figure 5.18 compares the calculated levels with experiment.[28] The wavefunctions for the first $11/2^-$ state was also calculated to determine the $11/2^- \rightarrow 3/2^+$ M4 isomeric transition. This transition will be mentioned in the next section. Further analysis of this problem will await the completion of the calculation.

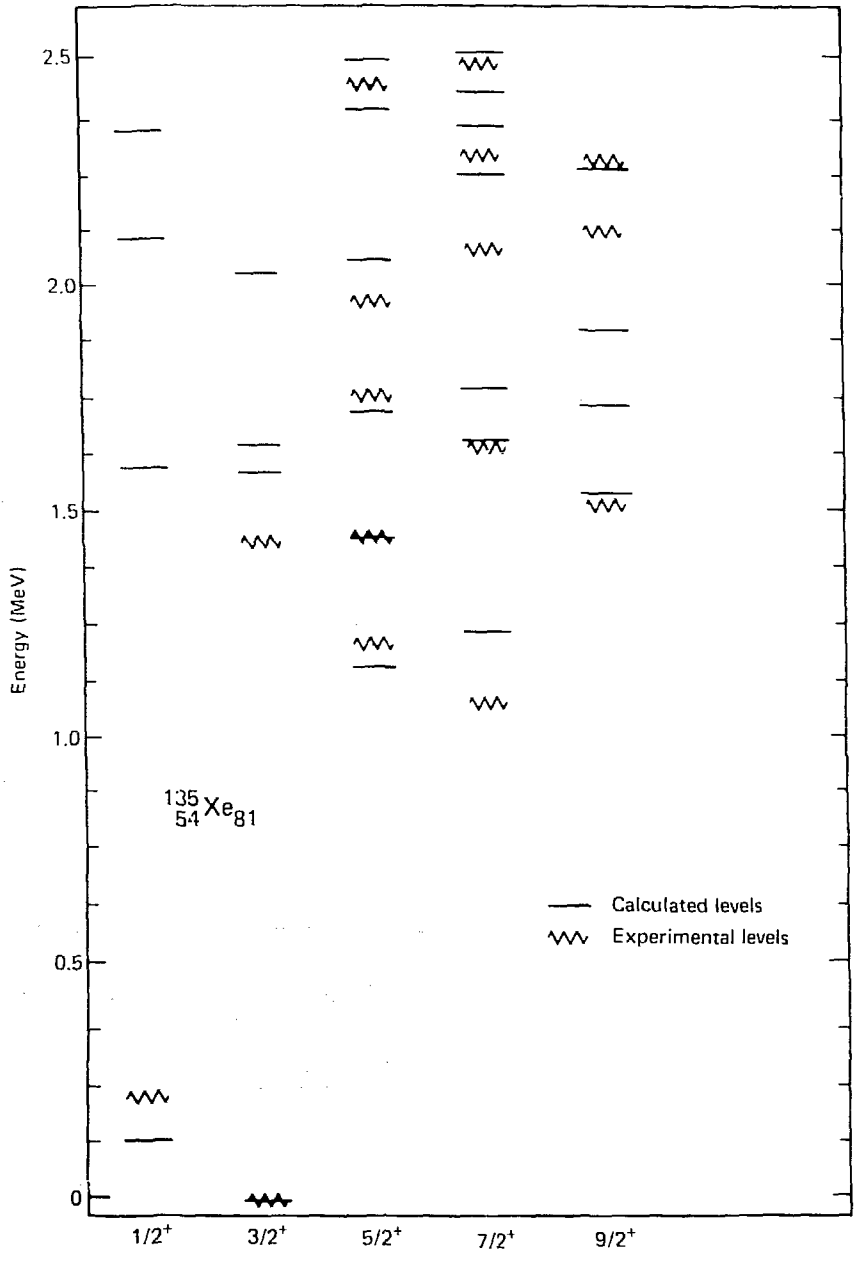

Figure 5.18. Experimental and calculated $1/2^+$, $3/2^+$, $5/2^+$, $7/2^+$, and $9/2^+$ levels in ^{135}Xe.

Chapter 6

6. Electromagnetic Transition Probabilities

This chapter will discuss the method used to calculate electromagnetic transition probabilities. The one-body operators will be given. An attempt will be made to determine the neutron and proton effective charges and gyromagnetic ratios for E2, E3, M1, and M4 multipole transitions by reproducing both measured level lifetimes and branching ratios. A unique set of parameters could not be determined from the experimental data available, consequently several simplifying assumptions were required. Once a possible set of consistent effective parameters were found, transitions in ^{134}Te and ^{133}Te were calculated and compared with experiment.

An electromagnetic one-body transition operator that connects an initial multiparticle state, Φ_i, with a final multiparticle state, Φ_f, can be written as a sum over transitions between the single particle wavefunctions, ϕ_j, that Φ_i and Φ_f are composed of. The electric single particle operator has the form

$$\langle \phi_f \,|\, EL \,|\, \phi_i \rangle = \langle j_f l_f m_f \,|\, EL \,|\, j_i l_i m_i \rangle$$

$$= (-1)^{j_f - m_f} \begin{pmatrix} j_f & L & j_i \\ -m_f & 0 & m_i \end{pmatrix} \left[\frac{(2j_f+1)(2j_i+1)(2l_f+1)(2l_i+1)(2L+1)}{4} \right]^{1/2}$$

$$\times \begin{Bmatrix} l_f & L & l_i \\ 0 & 0 & 0 \end{Bmatrix} \begin{Bmatrix} l_f & j_f & 1/2 \\ j_i & l_i & L \end{Bmatrix} \langle r^L \rangle e \, e_{eff}$$

where

n j l m are the usual single particle quantum numbers, L is the operator multipolarity, and

$\begin{pmatrix} j_f & L & j_i \\ -m_f & 0 & m_i \end{pmatrix}$ is a 3j symbol,

$\begin{Bmatrix} l_f & L & l_i \\ 0 & 0 & 0 \end{Bmatrix}$ is a 6j symbol,

$$\langle r^L \rangle = \int_0^\infty R_{n_f l_f}(r)\, r^L\, R_{n_i l_i}(r)\, dr$$

and R(r) is the radial portion of the wavefunction. The effective charge, e_{eff}, is defined by

$$e_{eff} = e_{\pi EL}(m_\tau + 1/2) - e_{\nu EL}(m_\tau - 1/2)$$

where m_τ is the isospin projection (protons: $m_\tau = +1/2$; neutrons: $m_\tau = -1/2$). $e_{\pi EL}$ ($e_{\nu EL}$) is the effective proton (neutron) charge in in units of elementary charge, e.

The magnetic single particle transition operator is given by

$$\langle j_f l_f m_f \,|ML|\, j_i l_i m_i \rangle =$$

$$(-1)^{j_f - m_f} \begin{pmatrix} j_f & L & j_i \\ -m_f & 0 & m_i \end{pmatrix} \frac{e\hbar}{2mc} \langle r^{L-1} \rangle \sqrt{L(2L+1)}\ (-1)^{l_f}$$

$$\times \left[\frac{(2l_f+1)(2L-1)(2l_i+1)}{4}\right]^{1/2} \begin{pmatrix} l_f & L-1 & l_i \\ 0 & 0 & 0 \end{pmatrix} \left[(2j_f+1)(2j_i+1)(2L+1)\right]^{1/2}$$

$$\left\{ (-1)^{l_f + j_f - 1/2}\ 2\, e_{eff}\ \frac{1}{L+1}\ \left[j_i\,(j_i+1)(2j_i+1)\right]^{1/2} \begin{Bmatrix} l_f & j_f & 1/2 \\ j_i & l_i & L-1 \end{Bmatrix} \right.$$

$$\left. \times \begin{Bmatrix} j_f & L & j_i \\ 1 & j_i & L-1 \end{Bmatrix} + \left(g_{eff} - e_{eff}\ \frac{1}{L-1}\right) 6^{1/2} \begin{Bmatrix} l_f & 1/2 & j_f \\ l_i & 1/2 & j_i \\ L-1 & 1 & L \end{Bmatrix} \right\}$$

where $\frac{e\hbar}{2mc}$ is a nuclear magneton and

$$\begin{Bmatrix} l_f & 1/2 & j_f \\ l_i & 1/2 & j_i \\ L-1 & 1 & L \end{Bmatrix} \qquad \text{is a 9j symbol}$$

and

$$g_{eff} = 2.79 g_\pi (m_T + 1/2) + 1.91 g_\nu (m_T - 1/2)$$

defines the effective gyromagnetic ratio.

The other symbols have the same meaning as defined for the electric multipole operator. The multiparticle matrix elements, (M_{if}), are related to the transition probability by

$$T(E2) = 1.22 \times 10^{9} \; E^5 \; \frac{1}{2j_i+1} \left| \frac{M_{if}}{\begin{pmatrix} j_f & 2 & j_i \\ -m_f & 0 & m_i \end{pmatrix}} \right|^2$$

$$T(E3) = 5.67 \times 10^{2} \; E^7 \; \frac{1}{2j_i+1} \left| \frac{M_{if}}{\begin{pmatrix} j_f & 3 & j_i \\ -m_f & 0 & m_i \end{pmatrix}} \right|^2$$

$$T(M1) = 1.76 \times 10^{13} \; E^3 \; \frac{1}{2j_i+1} \left| \frac{M_{if}}{\begin{pmatrix} j_f & 1 & j_i \\ -m_f & 0 & m_i \end{pmatrix}} \right|^2$$

$$T(M4) = 1.87 \times 10^{-6} \; E^9 \; \frac{1}{2j_i+1} \left| \frac{M_{if}}{\begin{pmatrix} j_f & 4 & j_i \\ -m_f & 0 & m_i \end{pmatrix}} \right|^2$$

where T is in sec^{-1}, E is the energy of the transition in MeV, j and m are the total angular momentum and projection of the initial (i) and final (f) states.

Now, two things are needed before transition probability calculations can be made: multiparticle wavefunctions for the initial

and final states and the effective charges and gyromagnetic ratios. The wavefunctions have been calculated as described in Chapter 4 and 5.

The effective charges and gyromagnetic ratios can be determined by treating them as parameters and using the calculated wavefunctions to reproduce measured level lifetimes. This assumes that the e_{eff} and g_{eff} values do not vary throughout the ^{132}Sn region. The transitions investigated will be limited to E2, E3, M1, and M4.

When determining effective parameters it is best to use pure transitions that depend on only a single parameter. For instance e_{E2} can best be found from the $(6^+)_1 \rightarrow (4^+)_1$ transition in ^{134}Te which has a measured lifetime of 164 ns[73] and is expected to be pure E2. Figure 6.1 shows the $(6^+)_1 \rightarrow (4^+)_1$ transition matrix element as a function of $e_{\pi E2}$. Theory matches experiment at $e_{\pi E2} = 1.55$. Also shown is the calculated ^{136}Xe $(6^+)_1 \rightarrow (4^+)_1$ matrix element. The Xe transition is, however, seniority forbidden[104] and depends only on small admixtures in the wavefunctions which were not reproduced in this calculation. In addition, the results of a calculation be Wildenthal[10] allowed the 4 valence protons access to only the $1g_{7/2}$ and $2d_{5/2}$ orbitals. This valence space is adequate to reproduce the ^{134}Te results but does even worse in duplicating the ^{136}Xe results than the calculation done here.

The dashed line in figure 6.1 represents a transition in which the two valence protons confined to the $g_{7/2}$ subshell recouple from a 6^+ state to a 4^+ state. As is expected, with no configuration mixing, $e_{\pi E2}$ has a larger value (1.7).

The M4 $11/2^- \rightarrow 3/2^+$ isomeric transitions in ^{133}Te and

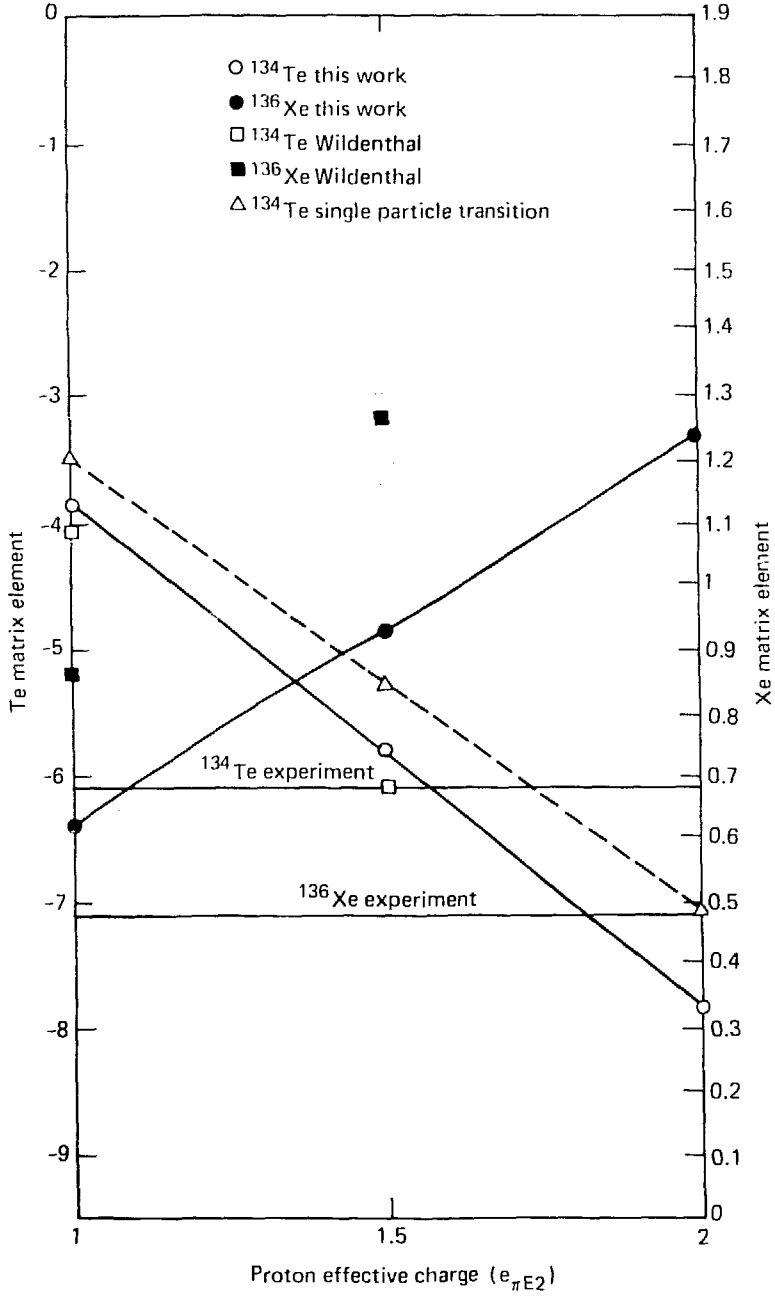

Figure 6.1. The $(6^+)_1 \rightarrow (4^+)_1$ E2 transition probability matrix elements in tellurium-134 and xenon-136 as a function of the effective proton charge.

^{135}Xe were found to be almost purely single particle transitions. The dashed line in figures 6.2 and 6.3 represent the transition of a single neutron hole from the $1h_{11/2}$ subshell to the $2d_{3/2}$ subshell. The full gddsh valence space calculation results are shown by the solid lines. These results show, for this particular case, that the transition probability is insensitive to configuration interaction. They also show that the transition probability is only weakly dependent on $e_{\pi M4}$. Theory matches experiment at $g_{\pi M4} = 0.4$.

The proton gyromagnetic ratio for M1 transitions can be found from the $(3^+)_1 \rightarrow (4^+)_1$ 14.8 nsec isomeric transition in ^{132}Sb. The K/L conversion electron ratio measured by Kerek[7] indicates this transition to be almost pure M1. Assuming effective parameters $e_{\pi M1} = 1.5$, $e_{\nu M1} = 0.5$, and $g_{\nu M1} = 0.4$, the theory agrees with experiment at $g_{\pi M1} = 0.7$ (figure 6.4).

Figure 6.5 displays the calculated $8^- \rightarrow 5^+$ E3 transition in ^{134}I as a function of $e_{\nu E3}$. The calculated transition matrix element was found to be independent of $e_{\pi E3}$. This transition was investigated by E. Achterberg[112] who measured the half-life of the level to be 3.6 min and found the K/L conversion ratio to be consistent with an E3 transition. The results of the calculation done here implies $e_{\nu E3} = 0.2$.

This exhausts the experimental data that can be used to determine the effective parameters. Several other level lifetimes have been measured but they have been found to depend in a complex fashion on the effective charges and gyromagnetic ratios, the multipolarity mixing ratio, and on the configuration mixing. Because it involves circular reasoning to test the configuration mixing by reproducing

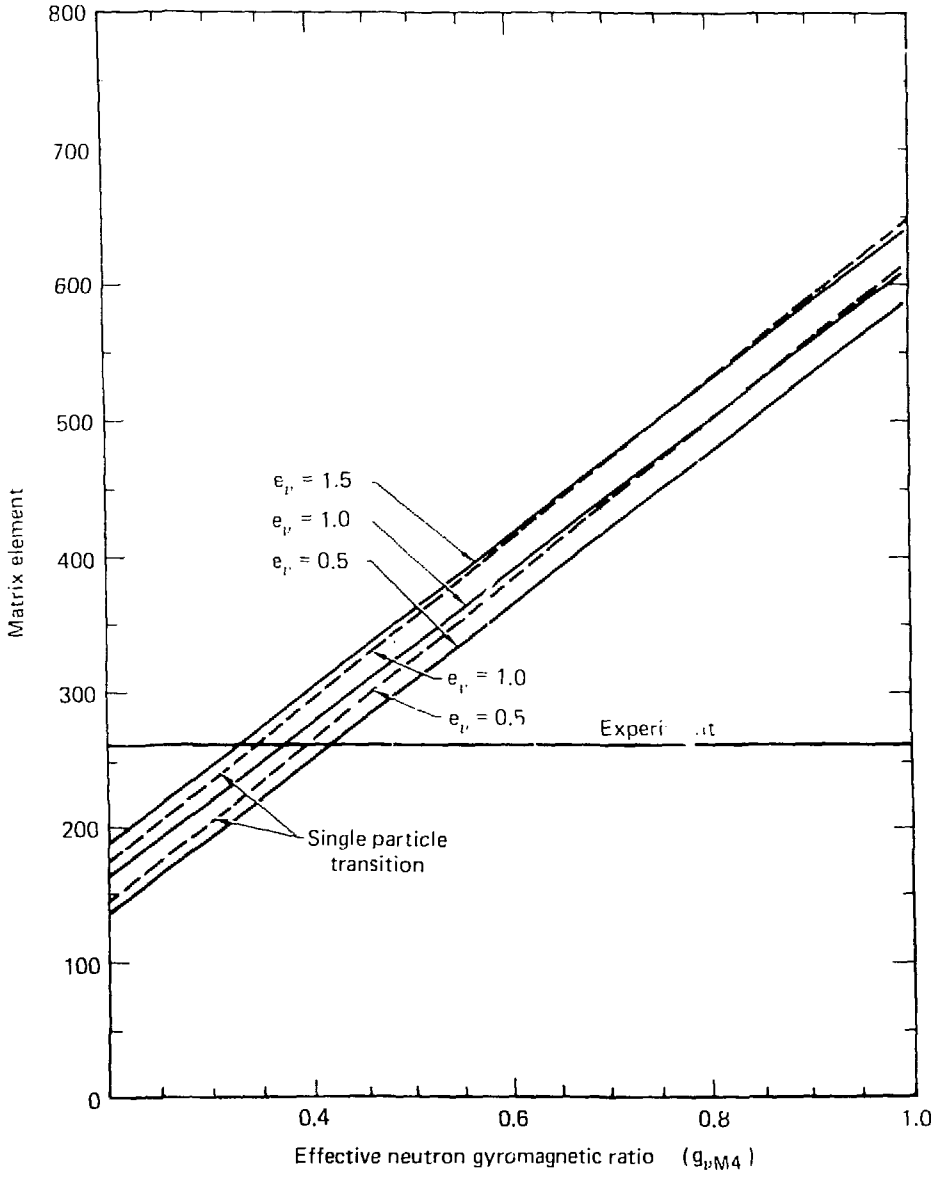

Figure 6.2. The matrix element for the $11/2^- \rightarrow 3/2^+$ M4 isomeric transition in tellerium-133 as a function of effective neutron charge and effective neutron gyromagnetic ratio.

Figure 6.3. The matrix element for the $11/2^- \rightarrow 3/2^+$ M4 isomeric transition in xenon-135 as a function of effective neutron charge and effective neutron gyromagnetic ratio.

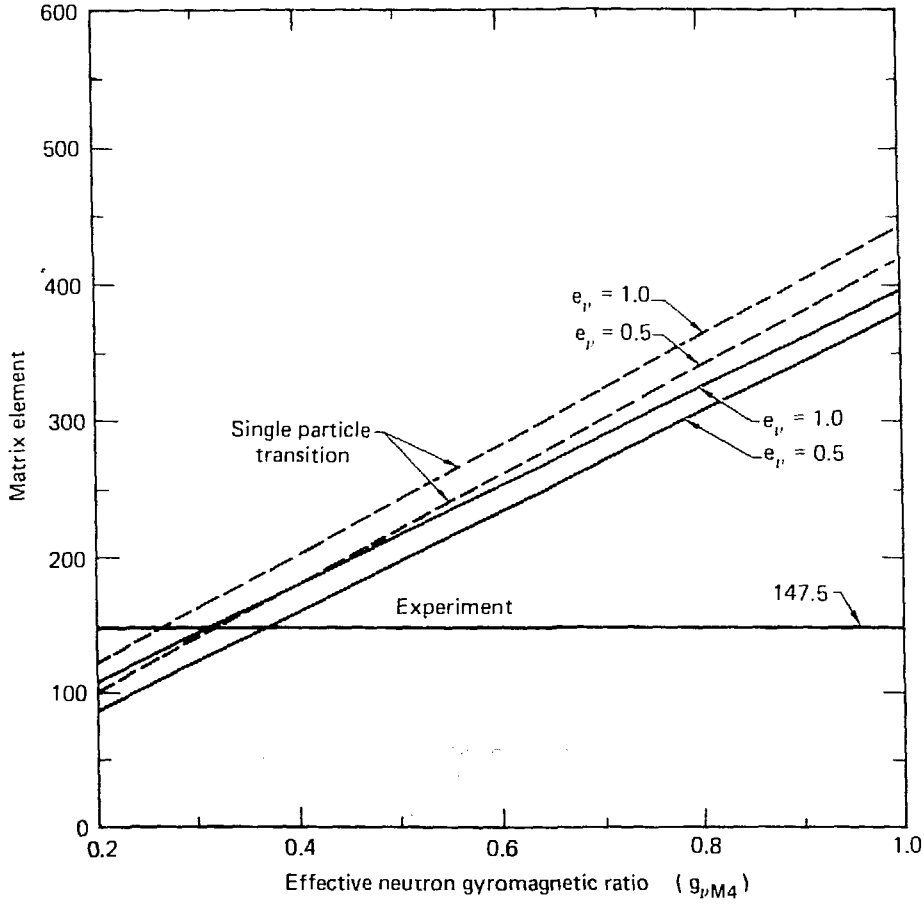

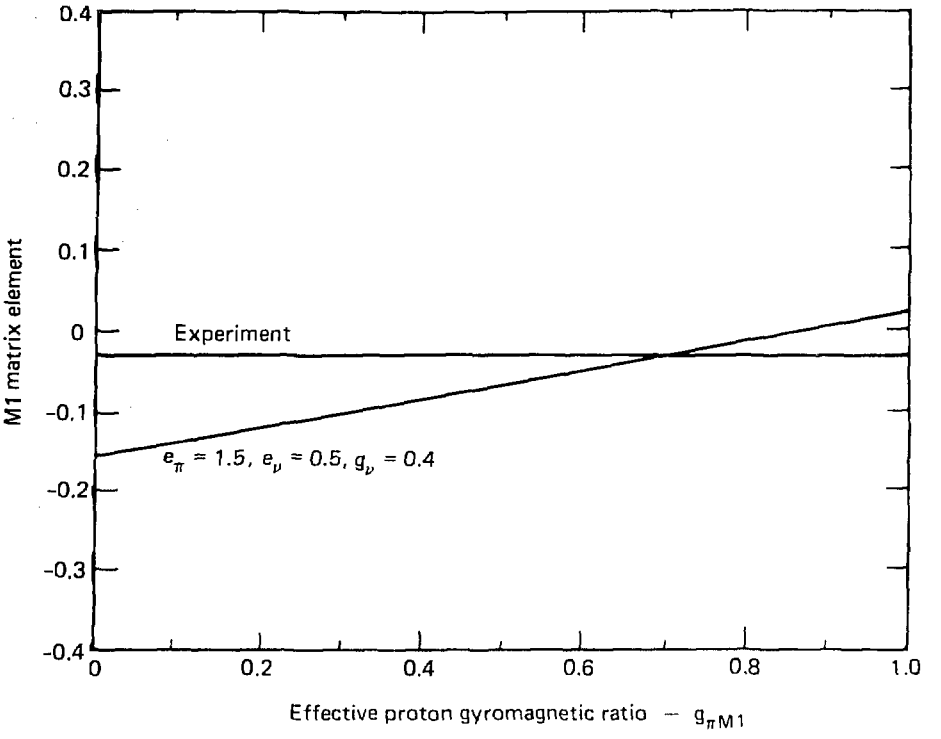

Figure 6.4. The matrix element for the $(3^+)_1 \rightarrow (4^+)_1$ M1 isomeric transition in antimony-132 as a function of the effective proton gyromagnetic ratio.

Figure 6.5. The matrix element for the $8^- \rightarrow 5^+$ E3 isomeric transition in iodine-134 as a function of the effective neutron charge.

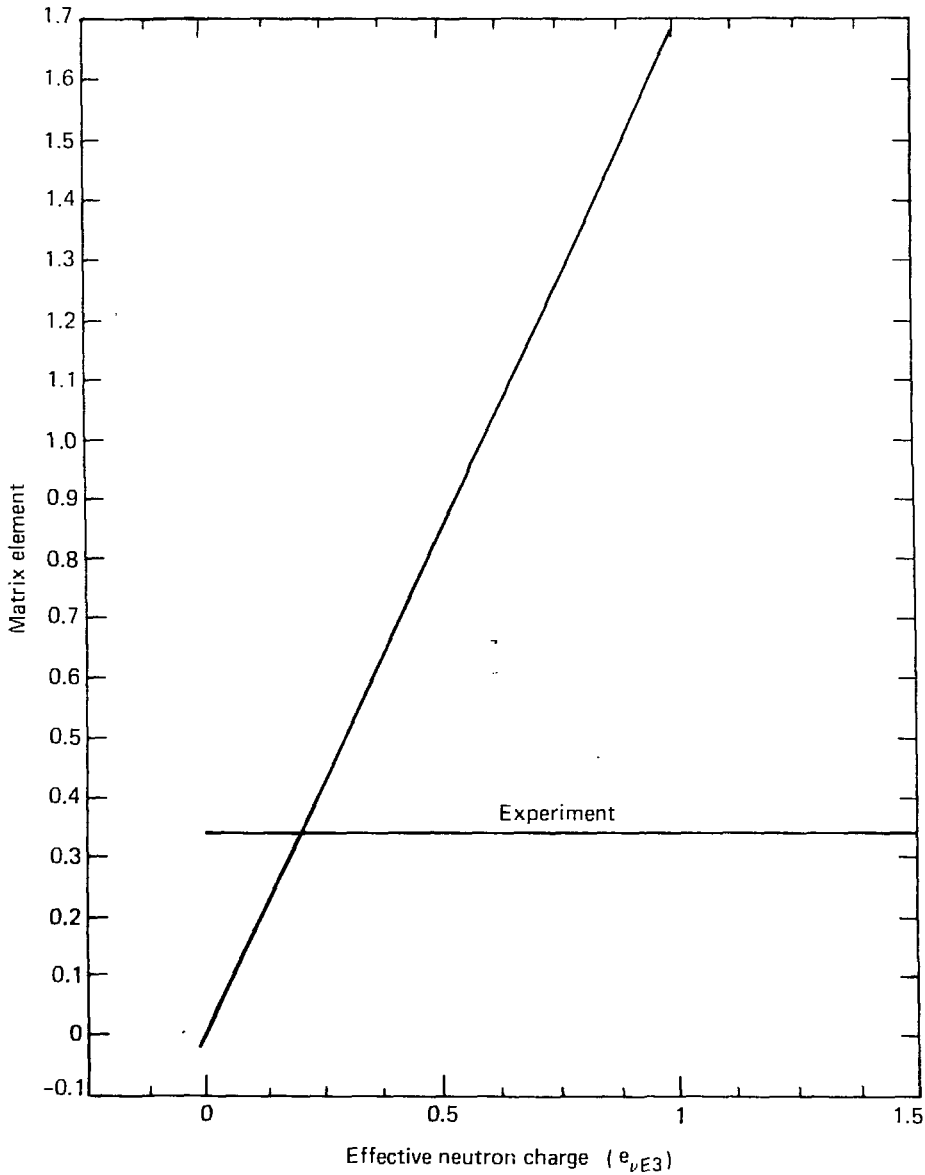

transitions rates whose values depend on parameters determined from highly mixed states, it is far more desirable to assign these parameters by using relatively pure states.

To procede further the assumption must be made that the effective charges in the operators of different multipolarities and for electric and magnetic transitions are approximately the same. This assumption plus the few effective parameters determined above yield the following set of effective parameters which will then be used to calculate branching ratios in ^{133}Te.

$$e_\pi = 1.5$$
$$e_\nu = 0.5$$
$$g_\pi = 0.7$$
$$g_\nu = 0.4$$

These parameters are consistent with parameters used by other workers[7,10,12] who have done calculations in this region.

We will first calculate two branching ratio ratios in ^{134}Te recently measured by E.A. Henry.[71] The $\frac{6_2^+ \rightarrow 6_1^+}{6_2^+ \rightarrow 4_1^+}$ ratio, R_A, was 80 and the $\frac{6_2^+ \rightarrow 6_1^+}{5_1^+ \rightarrow 6_2^+}$ ratio, R_B, was 0.5. The $6_2^+ \rightarrow 4_1^+$ was considered to be pure E2 while the other transition rates were the sum of the E2 and the M1 rates. The results using the above effective parameters give R_B= .25, a factor of 2 low, and R_A= 600, a factor of 7.5 too high.

Calculated branching ratios are compared with those determined experimentally in table 6.1 for the 1265, 1370, 1552, 1706, 1913, and 1977 keV levels in ^{133}Te. Only E2 and M1 transitions were considered. Except for two ground state transitions, agreement between experiment and theory is within a factor of 4 of experiment. Considering the simplistic determination of the effective parameters, this agreement is good. Ground state transitions in the case of the 1552 and 1913 levels are wrong by almost 3 orders of magnitude. Since other ground state transitions are in good agreement with experiment, no explanation can be offered for this behavior.

Table 6.1. Branching ratios in ^{133}Te involving M1 and E2 transitions

Transition		<f|E2|i><f|M1|i>		T(E2)	T(M1)	R_{Theory}	$R_{Exp.}$
1265($5/2^+$)	308($1/2^+$)	-7.9	0.0	1.0×10^{11}	0.0		
1265($5/2^+$)	0.0($3/2^+$)	1.8	0.21	1.4×10^{11}	2.6×10^{12}	27	28
1370($3/2^+$)	308($1/2^+$)	4.9	.072	1.6×10^{9}	1.6×10^{11}		
1370($3/2^+$)	0.0($3/2^+$)	-3.0	-.037	5.9×10^{9}	9.3×10^{11}	5.8	2.1
1552($5/2^+$)	1096($7/2^+$)	0.17	.063	2.4×10^{7}	1.5×10^{10}		
1552($5/2^+$)	308($1/2^+$)	1.85	0.0	2.1×10^{10}	0.0	1.4	4.0
1552($5/2^+$)	0.0($3/2^+$)	.78	.40	1.1×10^{9}	1.8×10^{13}	1200	32
1706($3/2^+$)	1265($5/2^+$)	-1.9	.42	1.3×10^{9}	6.7×10^{11}		
1706($3/2^+$)	308($1/2^+$)	-5.4	-.057	4.7×10^{11}	2.3×10^{11}	1.0	4.0
1706($3/2^+$)	0.0($3/2^+$)	-2.5	.020	5.5×10^{11}	5.2×10^{11}	1.6	6.5
1913($9/2^+$)	1501($11/2^+$)	.0005	.012	3.1×10^{2}	3.9×10^{8}		
1913($9/2^+$)	1265($5/2^+$)	-3.1	0.0	2.8×10^{9}	0.0	7.2	1.0
1913($9/2^+$)	1096($7/2^+$)	-.46	-.30	4.3×10^{9}	1.6×10^{12}	4100	56
1911($7/2^+$)	1096($7/2^+$)	-1.9	.039	9.8×10^{9}	4.2×10^{12}		
1911($7/2^+$)	0.0($3/2^+$)	-1.6	0.0	5.6×10^{11}	0.0	.47	1.0

For each level the theoretical branching ratios were found by dividing the sum of the E2 and the M1 rates for each transition by the sum of the E2 and M1 rates of the lowest energy transition. The 1265 keV level branching ratio for example is

$$R_{Theory} = (1.4 \times 10^{11} + 2.6 \times 10^{12}) / 1.0 \times 10^{11} = 27$$

Experimental branching ratios were obtained from the ^{133}Te scheme shown in figure 3.3.

Chapter 7.

7. Conclusions

In this dissertation the level structure of ^{133}Te was investigated via beta-decay of ^{133}Sb using singles gamma ray spectroscopy and gamma-gamma coincidence spectroscopy. The ^{133}Sb samples were isolated from a gross fission product mixture by an automated fast chemistry procedure. With these techniques, approximately 400 gamma rays were observed of which 105 were assigned to a proposed ^{133}Te level scheme containing 29 excited levels. One hundred and twenty-two of the remaining gamma-rays were assigned to the decay of other nuclei. Many of the remaining unplaced gamma-rays belong to the ^{132}Te level scheme which is currently being constructed.

The spin and parity assignments of 4 of the first 5 levels were made by appealing to systematics, with shell model results producing strongly corraborative evidence. The 334 keV level had previously been assigned a spin and parity of $11/2^-$ from conversion electron data. Spin and parity assignments for the other levels were made on the basis of log $\underline{ft}$ values obtained from the percent beta feeding to each level inferred from a gamma ray intensity balance. It would be interesting, therefore, to confirm the number of beta decays that feed each level by performing a beta-gamma coincidence experiment.

Overall, I believe that a fairly complete job has been done on the ^{133}Te decay scheme and although some small details are no doubt incorrect, the gross features of the level structure have been discovered.

Work on the shell model calculations is not as complete. Only a very cursory survey was undertaken with this very powerful tool. None of the following important physics questions have been addressed: Why

does the PMM two-body force work so well in several different regions of the nuclide chart? How well do other forces work (MSDI and Reid soft core for instance)? How sensitive are the calculated energies to the SPEs? How sensitive are specific transitions to SPEs, to effective charges and g-factors, and to the valence space? What is the connection between shell model wavefunctions and unified model or quasiparticle wavefunctions? What are the beta decay transition rates? How does center of mass motion effect the results?...etc.

Despite these many questions, much useful information has been obtained. The work here is best viewed as a demonstration of technique: a preliminary investigation of the limits and accuracy of very large shell model calculations in the ^{132}Sn region. It was found that the valence space used was sufficient to reproduce the level structure of nuclei below 1 MeV and there was fair agreement with experiment between 1 and 2 MeV. The PMM force works at least as well as more complicated G-Matrix forces. The $g_{7/2}$ neutrons could safely be frozen when calculating level energies below 2 MeV and transitions between these levels. Also, 3 exciton problems could easily be run while 4 exciton problems required a substantial amount of computation time and 5 exciton problems bordered on intractability. Neutron and proton separation energies can be easily be calculated to accuracy equal to that obtained from systematics.

Electromagnetic transition rate calculations, as shown in the previous chapter, strongly depend upon the choice of effective charges and g-factors. Without a reliable set of effective parameters, it is impossible to use branching ratios and level lifetimes to test the correctness of the wavefunction mixture. In fact, it seems

impractical to pursue transition rate calculations in this region, except for the comparison of similar transitions (M4 isomeric transitions in ^{133}Te and ^{135}Xe for instance), until more experimental information is gained. Of most value are transitions involving only protons or only neutrons (transitions in singly magic nuclei) preferably of known multipolarity. These simple transitions depend on only one or two effective parameters. In contrast, transitions of mixed multipolarity in non-magic nuclei involving both neutrons and protons depend on these parameters in a complex way. Especially lacking is information on simple neutron-hole transitions of the type expected to be found in the Sn nuclei.

I would also recommend that more experimental level information be obtained on the nuclei immediately adjacent to ^{132}Sn: ^{133}Sn, ^{134}Sb, ^{131}Sn, and ^{131}In. This is important in that it would allow a less ambiguous determination of the single particle energies on which these configuration mixing calculations depend.

Finally, the versatility of the vector method of shell model calculations must be emphasized. By dispensing with an encumbering and complicated coupling formalism, the vector method allows easy manipulation of the model wavefunctions. This provides a way to ellucidate the importance various components have on level energies and transition rates.

Appendix Contaminating Species Calculation

All the information given in figures A1 to A15 was obtained from the 1977 compilation by Meek and Rider[55]. Independent fission yields are taken from a calculated charge distribution model and merged statistically with weighted averages of measured yields. Independent yields are indicated in the figures with an arrow directly above or below the chemical symbols, half-lives are beneath the symbols, and the branching ratios are placed adjacent to the arrows connecting nuclides.

Two types of calculations were made. First, under the assumption that all fissions occurred at t=0 s, a number was calculated for each member of the decay chains which was proportional to the disintegrations undergone from t=50 s to t=230 s. This number was normalized so that the number of Sb^{133} disintegrations equaled 100. To simulate experiment, the calculation was repeated with the additional condition that a perfect Sb separation was made at t=5 s. The results are given in table A1.

Solutions to the systems of linear first order differential equations involved in these computations were obtained numerically using a subroutine package called EPISODE[113] which employs the variable-step variable-order implicit Adams method[114].

Table A1. Decay Chain Calculation Results(*)

A=89	Br	Kr	Rb	Sr				
	.045	170	24	0				
	0	0	0	0				
A=90	Kr	Rb^m	Rb^g	Sr				
	150	38	200	0				
	0	0	0	0				
A=128	In	Sn^m	Sn^g	Sb^m	Sb^g	Te		
	.014	.0001	1.0	.30	.003	0		
	0	0	0	.16	.003	0		
A=129	In^m	In^g	Sn^m	Sn^g	Sb	Te^m	Te^g	I
	0	0	17	4.3	.23	0	.003	0
	0	0	0	0	.07	0	.001	0
A=130	In	Sn	Sb^m	Sb^g	Te			
	0	37	16	4.3	0			
	0	0	8.2	1.3	0			
A=131	In	Sn	Sb	Te^m	Te^g	I		
	0	40	18	.02	1.6	0		
	0	0	14	0	.77	0		
A=132	In	Sn	Sb^m	Sb^g	Te	I	Xe	
	0	21	36	72	.11	.028	0	
	0	0	28	59	.038	0	0	
A=133	Sn	Sb	Te^m	Te^g	I^m	I^g	Xe^m	Xe^g
	0	100	11	26	.14	.07	0	
	0	100	1.5	8.6	0	.008	0	0
A=134	Sn	Sb^m	Sb^g	Te	I^m	I^g	Xe^m	Xe^g
	0	0	.89	29	12	3.9	.24	0
	0	0	.89	.83	0	.044	0	0
A=135	Sb	Te	I	Xe^m	Xe^g	Cs		
	0	49	3.0	1.9	.038	0		
	0	.38	.010	0	0	0		

Table A1. Continued

A=136	Sb	Te	I^m	I^g	Xe	
	0	23	60	164	0	
	0	.005	.016	0	0	
A=137	Te	I	Xe	Cs		
	0	71	209	0		
	0	0	0	0		
A=138	Te	I	Xe	Cs^m	Cs^g	Ba
	0	.71	76	6.1	4.9	0
	0	0	0	0	0	0
A=139	I	Xe	Cs	Ba	La	
	0	191	100	.018	0	
	0	0	0	0		
A=140	I	Xe	Cs	Ba		
	0	27	300	0		
	0	0	0	0		

(*) First row under chemical symbols gives calculated counts from t=50 sec to t=230 sec normalized so that Sb-133 is 100. Second row includes the effect of a perfect Sb separation at t=5 sec.

Figures A1-A15. Fission product decay chains containing species likely to be present in the chemically separated antimony sample.

1. A = 89

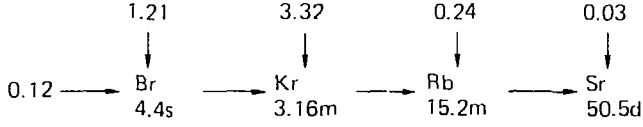

2. A = 90

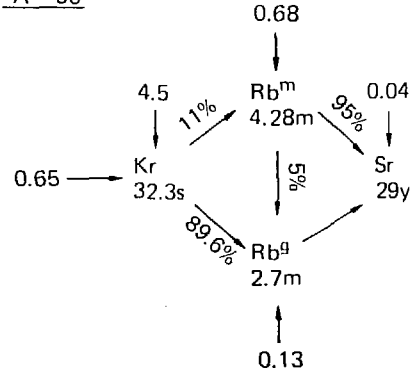

3. A = 128

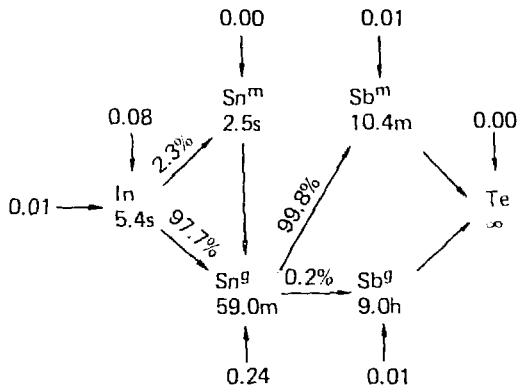
0.00
0.01
Sn^m
2.5s
Sb^m
10.4m
0.08
0.00
2.3%
In
5.4s
0.01
97.7%
99.8%
Te
∞
Sn^g
59.0m
0.2%
Sb^g
9.0h
0.24
0.01

4. A = 129

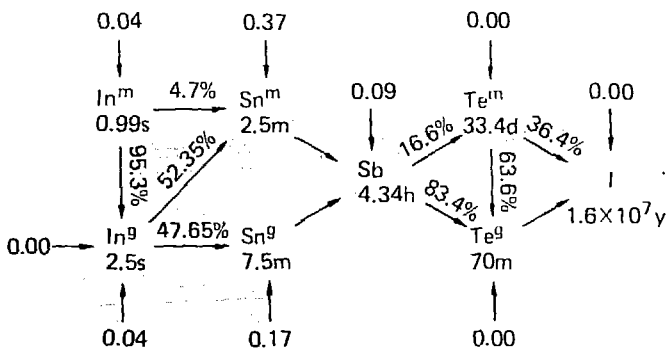
0.04
0.37
0.00
In^m
0.99s
4.7%
Sn^m
2.5m
0.09
Te^m
33.4d
0.00
16.6%
36.4%
95.3%
52.35%
Sb
4.34h
63.6%
83.4%
I
1.6X10^7y
0.00
In^g
2.5s
47.65%
Sn^g
7.5m
Te^g
70m
0.04
0.17
0.00

5. A = 130

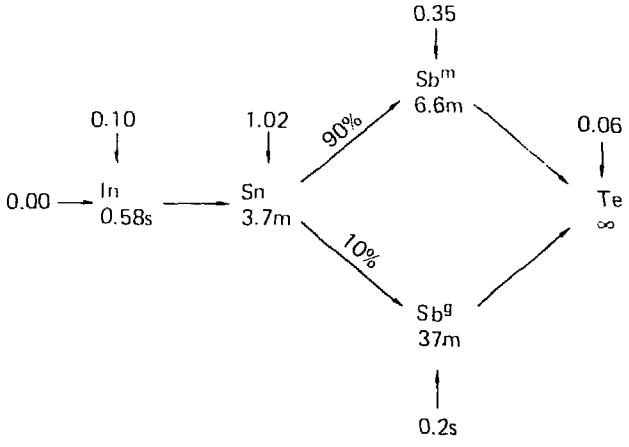
0.35
Sb^m
6.6m
0.10
1.02
90%
0.06
0.00
In
0.58s
Sn
3.7m
Te
∞
10%
Sb^g
37m
0.2s

6. A = 131

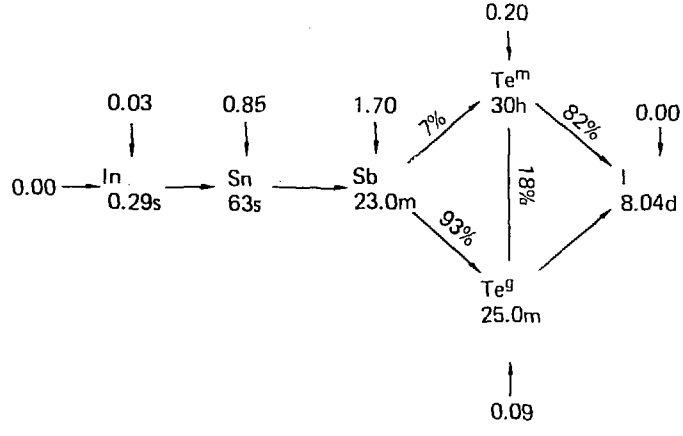
0.20
Te^m
30h
0.03
0.85
1.70
7%
82%
0.00
0.00
In
0.29s
Sn
63s
Sb
23.0m
18%
I
8.04d
93%
Te^g
25.0m
0.09

7. A = 132

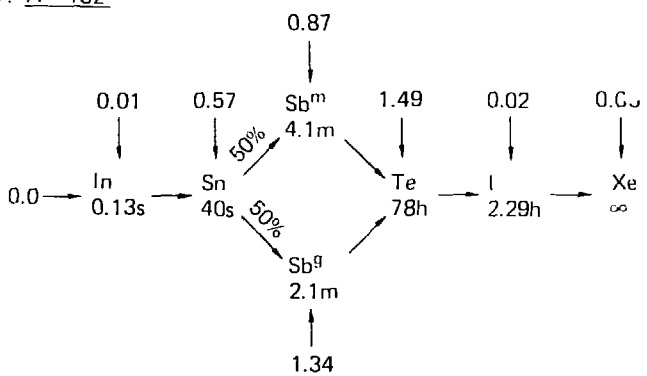
0.87
0.01
0.57
Sb^m
4.1m
1.49
0.02
0.0
50%
In
0.13s
Sn
40s
Te
78h
I
2.29h
Xe
∞
50%
Sb^g
2.1m
1.34

8. A = 133

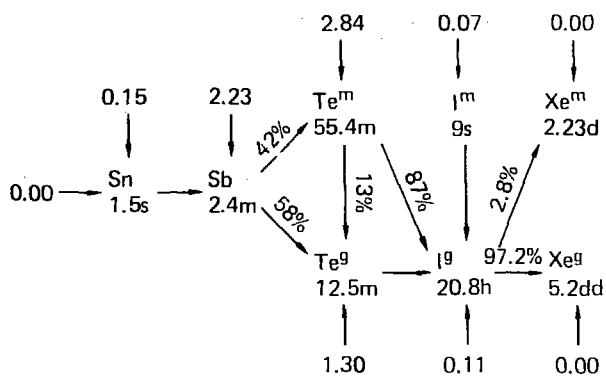
2.84
0.07
0.00
0.15
2.23
Te^m
55.4m
I^m
9s
Xe^m
2.23d
42%
0.00
Sn
1.5s
Sb
2.4m
13%
87%
2.8%
58%
Te^g
12.5m
I^g
20.8h
97.2%
Xe^g
5.2dd
1.30
0.11
0.00

9. A = 134

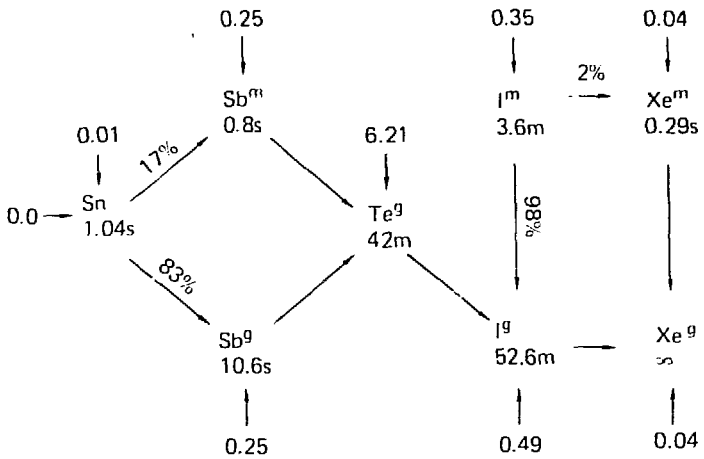

10. A = 135

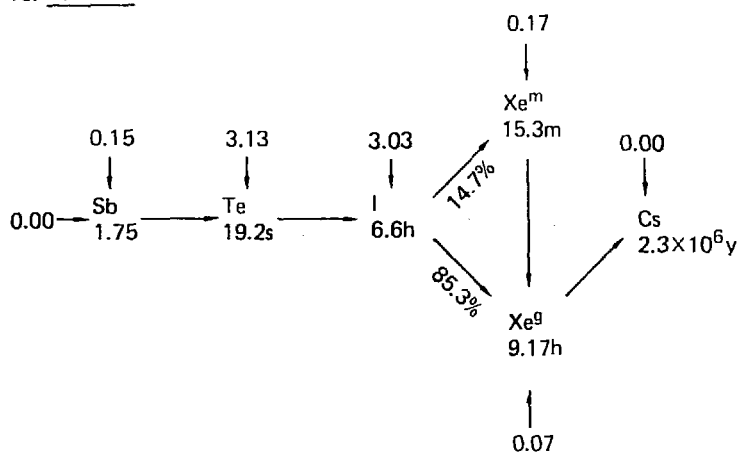

11. A = 136

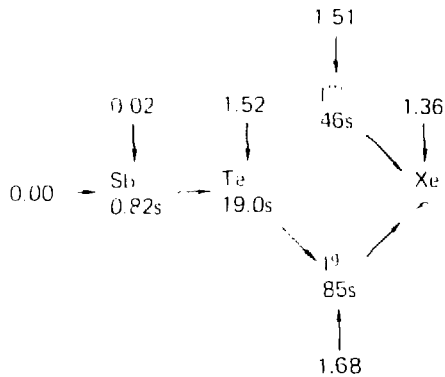

12. A = 137

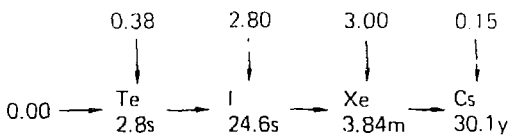

13. A = 138

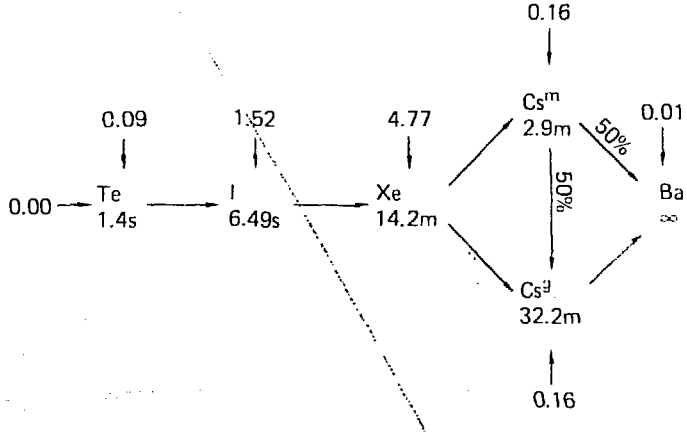

14. A = 139

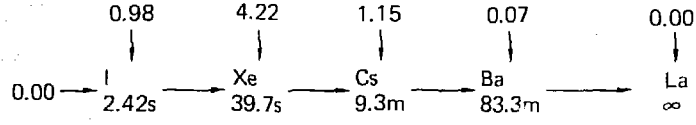

15. A = 140

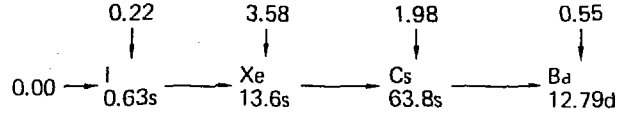

References

1. B. Fogelberg, P. Carle, and T. Nagarajan, "Energy Levels in the Heavy Even Mass Isotopes of Sn, Studied in the Decay of In Isotopes", 1976 Progress Report, CERN

2. A. Kerek, G. B. Holm, S. Borg, and P. Carle, Nuc. Phys. A209 (1973) 520

3. I. Andersson, S. Borg, L-E. DeGeer, and G. Holm, Annual Report 1970, Research Institute for Physics, Stocklolm

4. J. Blachot, private communication, CENG, Grenoble, France (1977)

5. G. Bailleul et al., Z. Physik A273 (1975) 283

6. F. Schussler, J. Blachot, J. P. Bocquet, and E. Monnond, Z. Physik A281 (1977) 229

7. A. Kerek, G. B. Holm, P. Carle, and J. McDonald, Nuc. Phys. A195 (1972) 159

8. K. Sistemich et al., Z. Physik. A285 (1977) 305

9. S. Borg, G. B. Holm, and B. Rydberg, Nuc. Phys. A212 (1973) 197

10. B. H. Wildenthal and D. Larson, Phys. Lett. 37B (1971) 266

11. B. H. Wildenthal, E. Newman, and R. L. Auble, Phys. Rev. C 3 (1971) 1199

12. W. J. Baldridge, preprint (1977)

13. B. Parsa, G.E. Gordon, and A. Wenzel, J. Inorg. Nuc. Chem. 31(1969)585

14. E. Degrieck and G. Vanden Berghe, Nuc. Phys. A231 (1974) 141

15. J. Blachot, H. N. Erten, C. D. Coryell, E. S. Macias, and W. B. Walters, Phys. Rev. C 4 (1971) 214

16. J. McDonald and A. Kerek, Nuc. Phys. A206 (1973) 417

17. A. Kerek, P. Carle, and S. Borg, Nuc. Phys. A224 (1974) 367

18. H. N. Erten and J. Blachot, Radiochimica Acta 19 (1973) 84

19. K. Heyde and P. J. Brussard, Z. Physik. 259 (1973) 15

20. W. J. Treytl, Phys Rev 188 (1969) 1831

21. J. Blachot and L. C. Carraz, Radiochimica Acta 11 (1969) 45

22. A. Kerek, G. B. Holm, S. Borg, and L-E. DeGeer, Nuc. Phys. A195 (1972) 177

23. K. Heyde, M. Waroquier, and G. Vanden Berghe, Phys. Lett. 35B (1971) 211

24. M. Rho, Nuc. Phys. 65 (1965) 497

25. K. Heyde, M. Waroquier, P. Van Isacker, and H. Vincx, Phys. Rev. C 16 (1977) 489

26. E. A. Henry, private communication (1978)

27. B. Parsa, G. E. Gordon, and W. B. Walters, Nuc. Phys. A110 (1968) 674

28. R. A. Meyer, private communication (1977)

29. R. A. Meyer, J. H. Landrum, S. V. Jackson, W. H. Zoller, and W. B. Walters, Phys. Rev. C 13 (1976) 1617

30. B. H. Wildenthal, Phys. Rev. Lett. 22 (1969) 1118

31. R. J. Lombard, Nuc. Phys. A117 (1968) 365

32. J. A. Morman, W. C. Schick, and W. L. Talbert, Phys. Rev. C 11 (1975) 913

33. W. R. Western, J. C. Hill, W. L. Talbert, and W. C. Schick, Phys. Rev. C 15 (1977) 1822

34. K. Heyde, M. Waroquier, H. Vincx, and P. J. Brussard, Nuc. Phys. A234 (1974) 216

35. M. Waroquier and K. Heyde, Nuc. Phys. A164 (1971) 113

36. W. R. Western, J. C. Hill, W. L. Talbert, and W. C. Schick, Phys. Rev. C 15 (1977) 1024

37. K. Heyde and M. Waroquier, Nuc. Phys. A167 (1971) 545

38. L. S. Kisslinger and R. A. Sorensen, Rev. Mod. Phys. 35 (1963) 853

39. The Proceedings of the International Conference on Properties of Nuclei Far from the Region of Beta-Stability, Leysin, Switzerland, vol 2 p1093

40 I. Anderson, S. Borg, L-E DeGeer and G. Holm, (Annual Report, 1970 Research Institute for Physics, Stockholm, Sweden)

41. O. Birgul and S. J. Lyle, Radiochimica Acta 8 (1967) 9

42. B. J. Dropesky and C. J. Orth, J. Inorg. Nuc. Chem. 24 (1962) 1301

43. L-E. DeGeer and G. B. Holm, Annual Report, (Research Institute of Physics, Stockholm 1975)

44. V. Hnatowicz, J. Kristak, M. Fisher, D. Venos, and J. Jursik, Czech. J. Phys. 25B (1975) 1

45. R. R. Whitehead, Nuc. Phys. A182 (1972) 290

46. R. R. Whitehead, A. Watt, B. J. Cole, and I. Morrison, Advances in Nuclear Physics, vol 10 p123 (Plenum Press, New York, 1977)

47. T. Sebe and J. Nachimkin, Ann. of Phys. 51 (1969) 100

48. J. D. Talman, Phys. Rev. 135 (1964) B1302

49. R. F. Hausman, Ph.D. Thesis, University of California, Davis

50. F. Petrovich, H. McManus, V. A. Madsen, and J. Atkinson, Phys. Rev. Lett. 22 (1969) 895

51. A. Kallio and K. Kolltveit, Nuc. Phys. 53 (1964) 87

52. P. C. Stevenson, R. A. Thomas, and S. M. Lane, Nuc. Instr. Meth. 89 (1970) 177

53. P.C. Stevenson, J. T. Larson and J. J. Leary, Inter. Conf. on Prop of Nuc. Far From the Region of Beta-Stability. Cern 70-30 (1970) 143 Vol. 1.

54. To be submitted to Phys Rev C with E. A. Henry

55. B. F. Rider and M. E. Meek, "Compilation of Fission Product Yields", (General Electric Co. NEDO-12154-2(D) 1977)

56. R. Gunnink and J. B. Niday, "Computerized Quantitative Analysis by Gamma-Ray Spectrometry. Vol. 1. Description of the GAMANAL Program", (Lawrence Livermore Laboratory, UCRL-51061 1972)

57. J. Carlson, private communication, LLL (1978)

58. W. Maeck, "The Radiochemistry of Antimony", National Academy of Sciences, Nuclear Science Series, Monograph 3033 (1961)

59. A. E. Greendale and D. L. Love, Anal. Chem. 35 (1963) 632

60. J. Landrum, private communication, LLL (1976)

61. W. L. Jolly, J. Am. Chem. Soc. 83 (1961) 335

62. H. Folger, J. V. Kratz, G. Herrmann, Radiochem. Radioanal. Letters 3 (1969) 185

63. J. V. Kratz, H. Franz, and G. Herrmann, J. Inorg. Nuc. Chem. 35 (1973) 1407

64. J. V. Kratz, H. Franz, N. Kaffrell, and G. Herrmann, Nuc. Phys. A250 (1975) 13

65. W. J. Richards, "Users Guide to the Livermore Pool-Type Reactor", (Lawrence Livermore Laboratory, M-051)

66. D. C. Kocher, Nuc. Data Sh. 16 (1975) 445

67. D. C. Kocher, Nuc. Data Sh. 16 (1975) 55

68. H. R. Hiddleston and C. P. Browne, Nuc. Data Sh. 13 (1974) 133

69. R. L. Auble, H. R. Hiddleston, and C. P. Browne, Nuc. Data Sh. 17 (1976) 573

70. H. R. Hiddleston and C. P. Browne, Nuc. Data Sh. 17 (1976) 225

71. E. A. Henry, private communication, LLL (1978)

72. E. A. Henry, Nuc. Data Sh. 11 (1974) 495

73. E. A. Henry, Nuc. Data Sh. 15 (1975) 203

74. S. C. Pancholi and M. J. Martin, Nuc. Data Sh. 18 (1976) 167

75. L. K. Peker, V. M. Sialov, and Yu. I. Kharitonov, Nuc. Data Sh. 12 (1974) 343

76. R. A. Meyer, J. Larsen, and J. Landrum, private communication, LLL (1976)

77. R. Gunnink and J. Niday, "Precise Analysis by Gamma Spectrometry", (Lawrence Livermore Laboratory, UCRL-76699 1975)

78. C. Schneider, D. Thompson, and G. Whitten, "Users Guide to the Octopus Computer Network",(Lawrence Livermore Laboratory, UCID-30048 Rev 2, 1975)

79. P. Abelson, Phys. Rev. 56 (1939) 1

80. G. B. Cook, Atomic Energy Research Establishment Report, No AERE-C/R-729, 1951 (unpublished)

81. A. C. Pappas, Mass. Inst. Technol. Res. Lab. Electron. Tech. Rept. 63 (1953) 97

82. P. O. Strom, D. L. Love, A. E. Greendale, A. A. Delucchi, D. Sam, and N. E. Ballou, Phys. Rev. 144 (1966) 984

83. T. Alvager and G. Oelsner, Arkiv Fysik 12 (1957) 319

84. V. Berg, K. Fransson, and C. E. Bemis, Arkiv Fysik 37 (1968) 213

85. S. G. Prussin and W. W. Meinke, Radiochim Acta 4 (1965) 79

86. C. E. Bemis, Ph.D. Thesis, Massachusetts Institute of Technology, Department of Chemistry, Sept 1964 (unpublished)

87. R. A. Meyer, "Proc. of Topical Conf. on Problems of Vibrational Nuclei" Zagreb, Croatia, Yugoslavia, Sept 1974

88. G. Rudstam, E. Lund, L. Westgaard, and B. Grapengiesser, "Proc. Int. Conf. Prop. Nuclei Far from Region of Beta-Stability",Leysin Switzerland, Vol. 1, p.341 (1970); CERN-70-30

89. E. Moll et al., Nucl. Instr. and Meth. 123 (1975) 615

90. H. Lawin et al., Nucl. Instr. and Meth. 137 (1976) 103

91. R. A. Meyer, private communication, LLL (1977)

92. K. Way, Editor, Internal Conversion Coefficients. (Academic Press, New York, 1973)

93. N. B. Gove and M. J. Martin, Nuc. Data Tables 10 (1971) 206

94. S. Raman and N. B. Gove, Phys. Rev. C 7 (1973) 1995

95. R. R. Roy and B. P. Nigam, Nuclear Physics. (John Wiley and Sons, New York, 1967)

96. J. H. Wilkinson, The Algebraic Eigenvalue Problem. (Oxford University Press, London, 1965)

97. A. deSahalit and H. Feshbach, Theoretical Nuclear Physics, Vol I. Nuclear Structure. (John Wiley and Sins, New York, 1974)

98. S. A. Moszkowski and B. L. Scott, Ann. Phys. 11 (1960) 6

99. B. L. Scott and S. A. Moszkowski, Nucl. Phys. 29 (1962) 66

100. V. A. Madsen, "Charge-Exchange Reactions", Nuclear Isospin (Academic Press, New York, 1969)

101. S. D. Bloom, J. B. McGrory, and S. A. Moszkowski, Nucl. Phys. A199 (1974) 369

102. A. H. Wapstra and K. Box, At. Data and Nucl. Data Tables 19 (1977) 177

103. S. Borg, I Bergstrom, G. B. Holm, B. Rydberg, L. E. DeGeer, G. Rudstam, B. Grapengiesser, E. Lund, and L. Westgaard, Nucl. Instr. 91 (1971) 109

104. A. de-Shalit and I. Talmi, Nuclear Shell Theory. (Academic Press, New York, 1963)

105. R. Arvieu and S. A. Moszkowski, Phys. Rev. 145 (1966) 830

106. K. A. Brueckner, Phys. Rev. 97 (1955) 1353

107. R. V. Reid, Ann. Phys. (N.Y.) 50 (1968) 411

108. P. J. Brussaard and P. W. M. Glaudemans, Shell-Model Applications in Nuclear Spectroscopy. (North-Holland Publishing Co., New York, 1977)

109. R. K. Jolly and E. Kashy, Phys. Rev. C 4 (1971) 887

110. A. Chaumeaux, G. Bruge, H. Faraggi, and J. Picard, Nuc. Phys. A164 (1971) 176

111. G. Alaga, V. Paar, and L. Sips, "Proceedings of the International Conference on Vibrational Nuclei", Zagreb, Yugoslavia, 1974 (unpublished)

112. E. Achterberg et al., Phys. Rev. C 4 (1971) 188

113. A. C. Hindmarsh and G. D. Byrne, "Episode: An Effective Package for the Integration of Systems of Ordinary Differential Equations",(Lawrence Livermore Laboratory, UCID-30112, 1977)

114. R. W. Hornbeck, Numerical Methods. (Quantum Publishers, New York, 1975)

115. P. S. Rajasekhar, J. Wong, and G. Struble, Lawrence Livermore Laboratory, UCRL-76007, 1974

116. L. L. Nunnelley and W. Loveland, Phys. Rev. C 13 (1976) 2017

Acknowledgements

I take this opportunity to thank:

Bob Lanier, Gene Henry, and Dick Meyer for introducing me to the world of experimental nuclear physics;

Stewart Bloom for introducing me to the world of theoretical nuclear physics;

Peter Stevenson for introducing me to the worlds of science and common sense;

and Ruth Yaffe for showing me how to survive in these worlds through persistence, self-discipline, and hard work.

A special thanks also goes to Jill MacFarland who helped with the typing.

U.S.GPO:1979-689-060/2038